

The construction of TRIGA-TRAP and direct high-precision
Penning trap mass measurements
on rare-earth elements and americium

Dissertation
zur Erlangung des Grades
“Doktor der Naturwissenschaften”
am Fachbereich 08 Physik, Mathematik und Informatik
der Johannes Gutenberg-Universität in Mainz

Jens Ketelaer

geboren in Bingen am Rhein

Mainz, den 14.06.2010

1. Gutachter: Prof. Dr. Klaus Blaum
2. Gutachter: Prof. Dr. Jochen Walz

Tag der mündlichen Prüfung: 23.09.2010

The construction of TRIGA-TRAP and direct high-precision Penning trap mass measurements on rare-earth elements and americium:

Nuclear masses are an important quantity to study nuclear structure since they reflect the sum of all nucleonic interactions. Many experimental possibilities exist to precisely measure masses, out of which the Penning trap is the tool to reach the highest precision. Moreover, absolute mass measurements can be performed using carbon, the atomic-mass standard, as a reference. The new double-Penning trap mass spectrometer TRIGA-TRAP has been installed and commissioned within this thesis work, which is the very first experimental setup of this kind located at a nuclear reactor. New technical developments have been carried out such as a reliable non-resonant laser ablation ion source for the production of carbon cluster ions and are still continued, like a non-destructive ion detection technique for single-ion measurements. Neutron-rich fission products will be available by the reactor that are important for nuclear astrophysics, especially the r-process. Prior to the on-line coupling to the reactor, TRIGA-TRAP already performed off-line mass measurements on stable and long-lived isotopes and will continue this program. The main focus within this thesis was on certain rare-earth nuclides in the well-established region of deformation around $N \sim 90$. Another field of interest are mass measurements on actinoids to test mass models and to provide direct links to the mass standard. Within this thesis, the mass of ^{241}Am could be measured directly for the first time.

Der Aufbau von TRIGA-TRAP und direkte Hochpräzisions-Penningfallen-Massenmessungen an seltenen Erden und Americium:

Kernmassen sind eine wichtige Größe zur Untersuchung der Kernstruktur, da sie die Summe aller Wechselwirkungen im Atomkern widerspiegeln. Es gibt viele Möglichkeiten zur präzisen Massenmessung unter denen die Penningfalle die höchste Präzision erreicht. Darüber hinaus können damit absolute Massenmessungen unter Verwendung des atomaren Massenstandards Kohlenstoff als Referenz durchgeführt werden. Im Rahmen dieser Arbeit wurde das neue Doppel-Penningfallen-Massenspektrometer TRIGA-TRAP aufgebaut und in Betrieb genommen. Diese Anlage stellt die erste dieser Art an einem Kernreaktor dar. Zahlreiche technische Neuentwicklungen wurden getätigt, darunter eine verlässliche nicht-resonante Laser-Ablations-Ionenquelle zur Erzeugung von Kohlenstoff-Cluster-Ionen, und werden fortgeführt, wie z.B. ein zerstörungsfreier Ionennachweis für Messungen mit einzelnen Teilchen. Durch den Forschungsreaktor TRIGA Mainz erhält TRIGA-TRAP Zugang zu neutronenreichen Spaltprodukten, die in der Kern-Astrophysik im Rahmen des r-Prozesses von Bedeutung sind. Vor der Ankopplung an den Reaktor sind an TRIGA-TRAP bereits Massenmessungen an stabilen und langlebigen Isotopen durchgeführt worden und werden fortgesetzt. Im Rahmen dieser Arbeit lag der Schwerpunkt auf Nukliden der seltenen Erden im Bereich starker Deformation für $N \sim 90$. Daneben werden Aktinoide im Hinblick auf Tests von Massenmodellen untersucht und um direkte Verknüpfungen zum Massenstandard zu bilden. Hier konnte zum ersten Mal direkt die Masse von ^{241}Am gemessen werden.

Contents

1	Introduction and motivation	1
I Theory		
2	Nuclear structure and nucleosynthesis processes	7
2.1	Overview on the mass models	11
2.1.1	The liquid-drop model and shell-corrections	12
2.1.2	Microscopic mass models	15
2.1.3	The Nilsson model of deformed nuclei	18
2.1.4	Other mass formulas	19
2.2	Impact of shell-effects on heavy and superheavy elements	21
2.3	Nucleosynthesis by neutron-capture	23
3	Storage, manipulation and detection of ions in a Penning trap	29
3.1	The Penning trap	29
3.1.1	Penning-trap basics: the ideal trap	29
3.1.2	Imperfections of the real trap	33
3.2	Manipulation of the ion motion	36
3.2.1	Dipolar and quadrupolar excitation	37
3.2.2	Cooling of the ion motion	38
3.3	Ion detection techniques for mass spectrometry	39
3.3.1	Destructive time-of-flight detection	40
3.3.2	Non-destructive image current detection	43
3.3.3	Comparison between destructive and non-destructive ion detection	48
3.4	Carbon clusters as reference masses	50
II Experimental Setup		
4	The double-Penning trap mass spectrometer TRIGA-TRAP	55
4.1	The TRIGA reactor and extraction of fission products	57
4.2	The TRIGA-TRAP setup	61
4.3	The off-line ion sources of TRIGA-TRAP	63
4.4	Ion transport	68
4.5	The cryogenic Penning traps and the superconducting magnet	70

4.6	Ion detection systems	75
4.7	Measurement procedure	81
4.8	The TRIGA-TRAP control system	83
III	Results and discussion	
5	Commissioning of the mass spectrometer	89
5.1	Simulation studies and electric field optimisation	89
5.2	Stability of the magnetic field	94
5.3	Data analysis procedure and accuracy studies	96
5.4	Phase shift in the Ramsey excitation	102
6	First direct mass measurements at TRIGA-TRAP	105
6.1	Investigation of stable isotopes in the rare-earth region	105
6.1.1	Ion production	105
6.1.2	Measurements and results	108
6.1.3	The Atomic-Mass Evaluation in the rare-earth region	112
6.1.4	Discussion of the new mass values with respect to nuclear structure studies	119
6.2	First direct mass measurement of ^{241}Am	124
6.2.1	Mass measurements and results	124
6.2.2	Discussion	127
7	Conclusion and Outlook	129
	Bibliography	133

List of Tables

2.1	Parameters for the Bethe-Weizsäcker mass formula.	13
3.1	Frequencies of singly charged ions in the Penning trap.	33
4.1	Candidates for mass measurements on neutron-rich nuclides.	59
4.2	Alkali nuclides as mass references.	64
5.1	List of all voltages used for the transport and trap electrodes.	92
5.2	Best tuning voltages of the precision trap.	94
5.3	Result of the mass measurement of ^{197}Au	101
6.1	Natural abundances of stable rare-earth nuclides.	106
6.2	Results of the mass measurements in the rare-earth region.	111
6.3	Influence of the TRIGA-TRAP mass measurements on the AME mass excesses.	118
6.4	Nilsson ground-state orbits of gadolinium and hafnium isotopes.	123
6.5	Result of the mass measurement of ^{241}Am	125

List of Figures

1.1	Uncertainties of experimental mass values in the Atomic-Mass Evaluation.	2
2.1	Binding energy per nucleon for stable nuclides.	8
2.2	Two-neutron separation energies for elements between $Z = 30$ and $Z = 50$	8
2.3	Comparison of different mass models for barium and americium.	10
2.4	Contributions to the Bethe-Weizsäcker mass formula.	12
2.5	Deviations from experimental masses for the Bethe-Weizsäcker formula.	13
2.6	Deviations from experimental masses for the Finite-Range-Liquid-Droplet model.	15
2.7	Illustration of Nilsson-model basics.	18
2.8	Nuclear energy as a function of the quadrupolar deformation.	21
2.9	Quadrupolar deformation calculated by the FRDM model.	22
2.10	Calculated microscopic corrections for heavy and superheavy nuclides.	23
2.11	Solar-system abundances as a function of the mass number A	24
2.12	Sketch of the r-process.	26
3.1	Electrode configurations for Penning traps.	30
3.2	Ion motion in a Penning trap.	31
3.3	Energy levels of a spinless charged particle in a Penning trap.	34
3.4	Application of rf fields for the excitation of the ion motion in a Penning trap.	36
3.5	Conversion from magnetron into cyclotron motion.	37
3.6	Damping of the magnetron and the modified cyclotron motion.	38
3.7	Principle of TOF-ICR measurements.	40
3.8	Time-separated oscillatory fields.	42
3.9	Simple signal model for the image current.	43
3.10	Principle of the image current detection.	44
3.11	Equivalent circuit for the broad-band FT-ICR detection.	45
3.12	Equivalent circuit for the narrow-band FT-ICR detection.	46
3.13	Impedance of a tuned circuit used for narrow-band FT-ICR detection.	47
3.14	Ion number dependence of the statistical uncertainty using TOF-ICR.	49
3.15	Carbon cluster reference masses.	51
4.1	TRIGA-SPEC layout at beam port B of the TRIGA Mainz reactor.	56
4.2	Production rates of fission nuclides.	57
4.3	Extraction of fission products by the gas-jet system.	58
4.4	Schematic drawing of the ECR ion source.	60

4.5	Principle of an RFQ cooler and buncher.	61
4.6	The TRIGA-TRAP setup.	62
4.7	Surface ion source.	64
4.8	Sketch of the laser-ablation ion source.	65
4.9	Carbon cluster ion spectrum.	66
4.10	Radiographic images of targets.	67
4.11	Overview of ion optics at TRIGA-TRAP.	69
4.12	Function principle of a Bradbury-Nielsen-Gate.	70
4.13	Magnetic field of the superconducting magnet on axis of the magnet bore.	71
4.14	Purification trap including the electric potentials.	72
4.15	Trap electrode stack including differential pumping stage.	73
4.16	Segmentation of the ring electrode.	74
4.17	Hyperbolic precision trap and magnetic field distortion.	75
4.18	Time-of-flight section with electric and magnetic field.	76
4.19	Time-of-flight contrast example.	78
4.20	Drawing of the superconducting helical resonator.	79
4.21	Signal processing for the narrow-band FT-ICR detection.	80
4.22	Typical measurement cycle for a time-of-flight mass measurement.	81
4.23	Simplified FT-ICR measurement procedure.	82
4.24	Sample screenshot of the voltage control.	84
4.25	Part of the control system architecture.	85
5.1	Ion transport simulation.	90
5.2	Optimisation of the capture delay time in the precision trap.	93
5.3	Shift of the modified cyclotron frequency as a function of the correction voltages.	94
5.4	Cyclotron frequency fluctuations in the precision trap.	95
5.5	Relative deviation of the interpolated from the true cyclotron frequency.	96
5.6	Ramsey TOF-ICR resonance for $^{12}\text{C}_{20}^+$	97
5.7	Ideograms of the cluster cross-reference measurements.	98
5.8	Relative deviation between known and measured frequency ratios of carbon clusters.	99
5.9	Ramsey TOF-ICR resonance for $^{197}\text{Au}^+$	102
5.10	Results of the mass measurement of ^{197}Au	103
5.11	TOF-ICR resonances with phase shifted Ramsey excitation pulses.	104
6.1	TOF-ICR resonance of $^{152}\text{Gd}^{16}\text{O}^+$ and obtained frequency ratios.	108
6.2	TOF-ICR resonance of $^{175}\text{Lu}^{16}\text{O}^+$ and obtained frequency ratios.	109
6.3	Network of experimental links between masses of nuclides.	112
6.4	Deviations between measured mass excesses and literature values for rare-earth nuclides.	114
6.5	Comparison of neutron separation energies for gadolinium isotopes.	115
6.6	Comparison of neutron separation energies for hafnium isotopes.	116
6.7	Shift of the mass surface due to the TRIGA-TRAP results.	117
6.8	Comparison between mass models and TRIGA-TRAP results.	119

6.9	Two-neutron separation energies as a function of N in the rare-earth region.	120
6.10	Two-neutron separation energies for europium, gadolinium, lutetium, and hafnium.	121
6.11	δV_{pn} values in the rare-earth region.	122
6.12	Comparison between experimental and theoretical δV_{pn} values.	123
6.13	TOF-ICR resonance of $^{241}\text{Am}^{16}\text{O}^+$ and obtained frequency ratios.	125
6.14	Result of the mass measurement of ^{241}Am	126
6.15	Comparison of the ^{241}Am mass excess with theoretical calculations.	127
6.16	Part of the mass network around ^{241}Am	128

1 Introduction and motivation

High-precision mass measurements pave the way for a deeper understanding of nuclear structure across the entire chart of nuclides, since the mass is directly linked to the binding energy via Einstein's famous relation $E = mc^2$. Nuclear binding energies in turn reflect the sum of all nucleonic interactions leading to nuclear structure in all its variations. Most of the information has to be searched among radionuclides since only less than 10% of the presently known 3200 nuclides are stable, explaining the huge interest in new radioactive-beam facilities. Theoretical models have been and are still developed to reproduce experimental masses and other observables like half-lives for a basic understanding [Lunn2003]. However, present global models fight with uncertainties in the order of hundreds of keV, which is far behind the performance of experiments.

Besides nuclear structure studies, mass values are important in many fields of science with different requirements on the accuracy ranging from $\delta m/m = 10^{-11}$ in atomic physics, $10^{-8} - 10^{-6}$ in astro- and nuclear physics, to 10^{-5} in chemistry. The highest precision can be achieved turning the mass into a frequency measurement on stored ions in Penning traps [Blau2006a]. The charged particle is stored in a superposition of a strong homogeneous magnetic field and a weak electric quadrupole potential, which enables isolation against environmental influences as well as long observation times only limited by the half-life of the species under investigation. Penning traps have been successfully employed for mass measurements on very short-lived nuclides (^{11}Li with $t_{1/2} = 8.8$ ms [Smit2008]) as well as with impressively high precision (e.g. ^{14}N with $\delta m/m < 10^{-11}$ [Rain2004]). Only between 2003 and 2010 more than 600 Penning trap mass measurements entered the Atomic-Mass Evaluation (AME) [Audi2010]. Fig. 1.1 shows the presently achieved uncertainties for all known nuclides within the framework of the AME [Audi2009].

Within this thesis work TRIGA-TRAP, a new double-Penning trap mass spectrometer, has been installed and commissioned at the research reactor TRIGA Mainz [Kete2008]. The main physical goal of this new facility is to provide highly precise and accurate mass values of neutron-rich fission products and actinoids. While most of the neutron-deficient nuclides have been thoroughly investigated at other setups like SHIPTRAP (GSI, Darmstadt) and JYFLTRAP (Jyväskylä, Finland) (see e.g. [Webe2008]), the very neutron-rich part of the nuclear chart especially above $Z = 50$ has not been and will not be available soon to experiments until new radioactive-beam facilities like FAIR start their operation. However, the most important nucleosynthesis process regarding the creation of more than half of the heavy elements evolves exactly in this region, which is the rapid-neutron capture process (r-process). Astrophysical calculations mainly have to rely on the predictions of theoretical mass formulas and would require more experimental input data to test and improve the present knowledge about the r-process. Moreover, nuclear structure studies need to be extended towards the neutron drip-line searching for new subshell closures, shell quenching, or deformed nuclei (see e.g. [Doba1994, Stoi2000]). TRIGA-TRAP will provide valuable mass values on neutron-rich nuclides and bridge the time until FAIR starts to deliver beams.

Another field of interest at TRIGA-TRAP deals with the transuranium elements up to californium, which can be investigated employing off-line samples without the reactor. In this region of the nuclear chart in the past

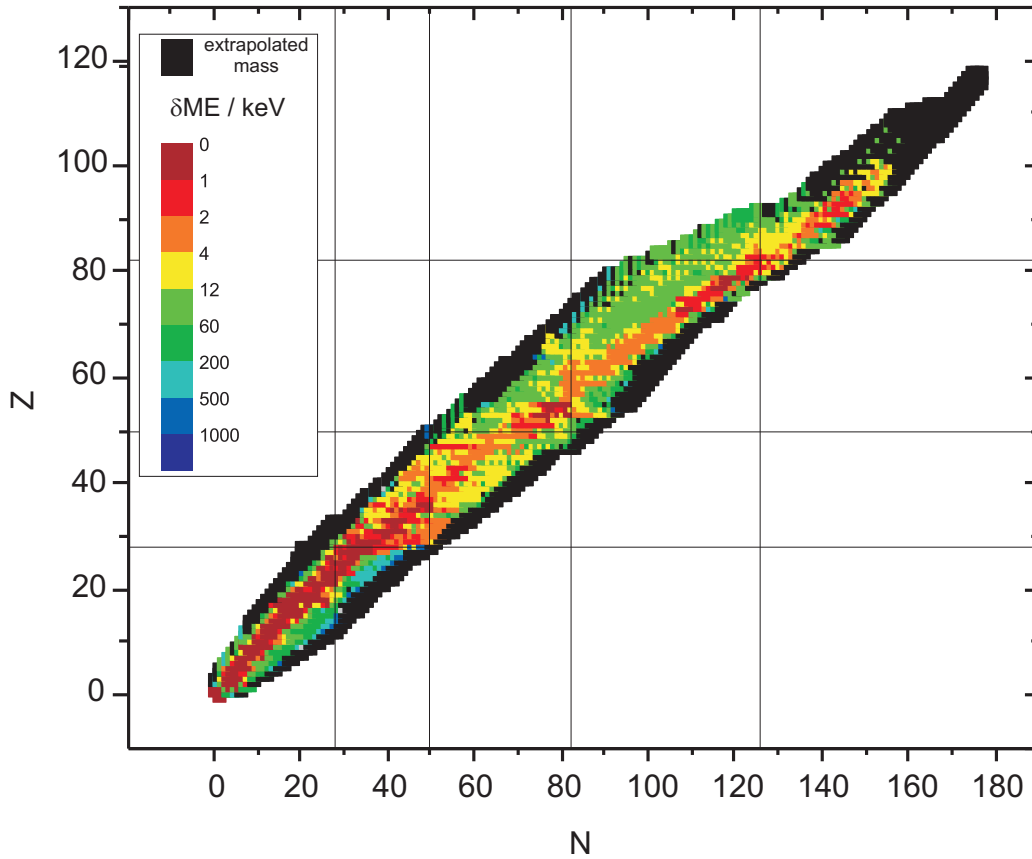


Figure 1.1: (Colour) Uncertainties of experimental mass values in the Atomic-Mass Evaluation from 2009 [Audi2009]. The smallest uncertainties are achieved for nuclides along the valley of stability, whereas the uncertainties increase when going to more exotic nuclides. Black squares mark nuclides with the mass determined through extrapolations.

all mass values have been only determined by decay energies, mainly α decays, leading to an accumulation of uncertainties in each step with the risk of a single wrong value effecting all subsequent masses in a chain. To this end new anchorpoints are required, and there have been first successful mass measurements performed beyond uranium on the three nobelium isotopes $^{252-254}\text{No}$ at SHIPTRAP [Bloc2010a] in close collaboration with members from TRIGA-TRAP. Due to very low production rates of less than one particle per hour, the commonly used Time of Flight-Ion Cyclotron Resonance (TOF-ICR) detection technique requiring at least one hundred ions for a single measurement is no longer suited when going over to superheavy elements. A new detection system based on the image currents induced by a single singly charged stored ion in the electrodes of the Penning trap is presently under development at TRIGA-TRAP and some parts of the electronics have been already successfully tested. This detection system will be later moved to SHIPTRAP.

A new non-resonant laser ablation ion source has been developed to provide carbon cluster ions as references, enabling absolute mass measurements based on the atomic mass standard ^{12}C [Smor2009]. This reliable source based on a rather simple design is routinely used at TRIGA-TRAP. Besides carbon clusters, also ions of certain stable rare-earth elements and the long-lived α -emitter ^{241}Am have been successfully produced and transferred to the Penning trap setup. Part of this thesis discusses all technical developments and steps during the commissioning phase, like design and simulation of the electrostatic ion optics before and after the Penning

traps, investigations about the stability and homogeneity of the magnetic field, installation of the vacuum and cryogenic system to cool down the trap region, and the assembly of the complete electrode structure. The experimental setup of TRIGA-TRAP is presented in Chap. 4, also including a distributed control system to monitor and set over 150 different parameters of the experiment via a graphical user interface as well as to partly automatise the measurement process. This system is based on a development from GSI [Beck2004] and has been implemented to TRIGA-TRAP within this thesis work.

The last step of the commissioning phase contained detailed studies of all contributions of the apparatus to the uncertainty of mass measurements, which have been carried out employing carbon cluster ions since their binding energies can be neglected and, thus, their mass is exactly known by definition. After identifying the influence of magnetic field fluctuations as well as a mass-dependent systematic effect, the accuracy was tested by a very first mass measurement on ^{197}Au . The result also served as an important confirmation of the present literature value with an uncertainty of only 600 eV since $^{197}\text{Au}^+$ was used as a reference ion for the investigation of short-lived nuclides at ISOLTRAP (CERN) and its accuracy had to be checked (see Chap. 5).

First mass measurements at TRIGA-TRAP dedicated to nuclear structure studies in the region of well-deformed rare-earth nuclei have been performed with relative uncertainties as low as 3×10^{-8} and are reported in Chap. 6. The investigation of 15 isotopes of the elements europium, gadolinium, lutetium, and hafnium is discussed with respect to the important derivatives of the binding energy, the two-neutron separation energy and δV_{pn} values quantifying the p-n interaction among valance nucleons. At the end of Chap. 6 the very first direct mass measurement on ^{241}Am is presented, which has been already performed during the commissioning phase of the experimental setup.

Part I

Theory

2 Nuclear structure and nucleosynthesis processes

The mass of a nucleus is one of its most fundamental properties and has a tremendous impact not only in the field of nuclear physics. It is known for a long time that the nuclear mass differs from the sum of the masses of the constituent nucleons [Asto1920] by the so called binding energy

$$B(N, Z) = [Nm_n + Zm_p - M(N, Z)]c^2, \quad (2.1)$$

which is an important measure for many nuclear effects since it reflects all interactions involved (the strong, the weak, and the electromagnetic interaction) and determines the stability of the nucleus. Here, m_n , m_p denote the neutron and proton masses, N , Z the neutron and proton numbers, respectively, and $M(N, Z)$ the nuclear mass being the experimental access to the binding energy¹. Fig. 2.1 shows the binding energy per nucleon $B(N, Z)/A$ as a function of the mass number A for stable nuclides, which exhibits a clear maximum at $A \approx 56$. For most nuclides, $B(N, Z)/A$ has a value between 8 and 9 MeV, which in combination with the almost constant nuclear densities gave rise to the concept of the saturation of nuclear forces. The analogy to a liquid drop led to a first and very successful model, the semi-empirical Bethe-Weizsäcker formula [Weiz1935, Beth1936]. Two important quantities that can be derived from binding energies, and thus, from mass measurements, are the two-neutron and the two-proton separation energies, respectively,

$$S_{2n}(N, Z) = B(N, Z) - B(N - 2, Z), \quad (2.2)$$

$$S_{2p}(N, Z) = B(N, Z) - B(N, Z - 2). \quad (2.3)$$

Due to pairing effects which are also accounted for by the Bethe-Weizsäcker formula, two-particle separation energies are used instead of one-particle separation energies S_n and S_p . Two-neutron separation energies are plotted for elements between zinc and tin in Fig. 2.2. A continuous decrease of $S_{2n}(N, Z)$ for fixed Z and increasing N is visible which can be explained by the liquid drop model. However, at $N = 50$ and $N = 82$, sudden drops of the separation energy point to an analogy to the atomic shells. At first glance, this seems to be contradictory to the liquid drop characteristics of nuclei, since a shell model requires independent particles in a common field, like the electrons in the electromagnetic field of the nucleus in case of an atom. Nevertheless, the experimental data manifested a higher stability for certain nuclides with so called magic neutron or proton numbers ($N_0, Z_0 = 8, 20, 28, 50, 82, 126$) which could be finally explained by an independent-particle model including spin-orbit coupling [Goep1950, Haxe1950]. It turned out that a generalisation of the mean-field approach allowing for a deformation of the potential from spherical symmetry and a time variation could reproduce the liquid-drop features as well [Brow1971].

Today, a large variety of theoretical models exists to explain experimentally determined nuclear masses and to predict masses of nuclides which are not available in laboratories up to now. A coarse classification

¹Since the nuclear mass and the binding energy are connected by Eq. (2.1), the two expressions are used synonymously within the text.

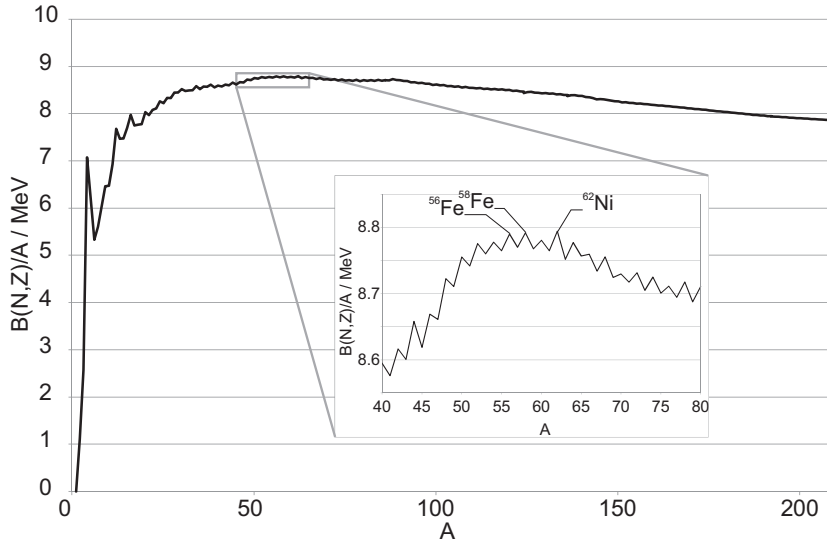


Figure 2.1: Binding energy per nucleon for stable nuclides as a function of the mass number A . In case more than one stable nuclide exists for a certain mass number, the largest binding energy was taken. The most strongly bound nuclides are $^{56,58}\text{Fe}$ and ^{62}Ni with about 8.8 MeV per nucleon. Data taken from [Waps2003b].

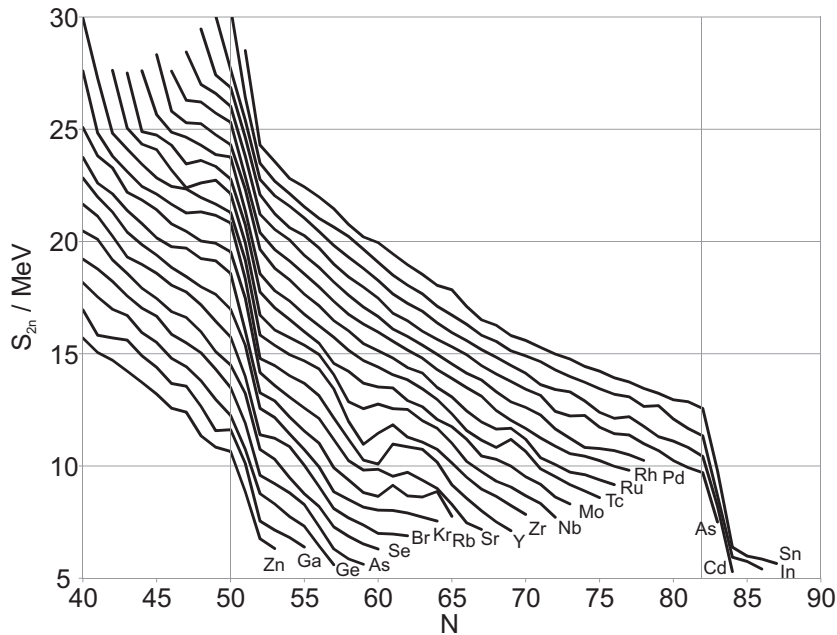


Figure 2.2: Two-neutron separation energies S_{2n} for elements with proton numbers between $Z = 30$ and $Z = 50$ around the neutron shell closures at $N = 50$ and $N = 82$. A continuous decrease in S_{2n} is visible for more neutron-rich nuclides. In addition, a sudden drop characterises the neutron shell closures. A region of deformation is visible around yttrium ($Z = 39$) and $N \sim 63$. Data taken from [Waps2003b].

of global models that are applicable over the entire nuclear chart can be done into macroscopic-microscopic (mac-mic) and microscopic approaches, where the semi-empirical Bethe-Weizsäcker formula is still outstanding [Lunn2003]. The mac-mic models are based on the macroscopic liquid-drop analogy describing the global trends of nuclear binding energies modified by an additional microscopic shell-correction employing a phenomenologically adjusted single-nucleon potential [Möll1988]. Microscopic mass formulas determine nuclear binding energies from single-particle levels for both neutrons and protons in a mean field defined by the given interactions. Due to the complexity of the many-body systems and the lack of knowledge on the strong interaction, *ab initio* calculations strictly employing realistic nucleon-nucleon potentials so far can only describe light nuclei reaching about as far as ^{12}C [Navr2000]. Thus, effective interactions and phenomenological contributions to account for specific effects are used instead in mass formulas to numerically calculate the binding energies [Lunn2003, Bend2003]. The free parameters of the effective potentials are fixed by a comparison of the predicted mass values to experimental data. Other models use systematic trends or special relations to derive the mass of a certain nuclide from its neighbours and, thus, represent local approaches. Masses predicted by several formulas are compared to the experimental values in Fig. 2.3(a) for barium isotopes from which the neutron-rich species are available as fission products at TRIGA-TRAP, and in Fig. 2.3(b) for americium isotopes where ^{241}Am is under investigation. In the region of known masses the different models agree within about 1 MeV. However, the discrepancies increase up to several MeV for nuclides far away from stability.

A measure for the quality of a mass model is the rms error

$$\sigma_{\text{rms}} = \left[\frac{1}{N} \sum_{i=1}^N \left(M_i^{\text{exp}} - M_i^{\text{theo}} \right)^2 \right]^{1/2} \quad (2.4)$$

comparing the predicted masses M_i^{theo} to the experimental values M_i^{exp} for N nuclides. The values for σ_{rms} reported here are taken from [Lunn2003] obtained by a fit to the 2001 Atomic-Mass Evaluation or in case of the most recent Hartree-Fock-Bogoliubov (HFB) calculations from the given references. The mass formula by Duffo and Zuker (dark blue line) [Duff1995] so far performs best as far as global approaches are concerned ($\sigma_{\text{rms}} = 0.373$ MeV). So called Garvey-Kelson relations (red line) [Jane1988] have the smallest rms error ($\sigma_{\text{rms}} = 0.319$ MeV) but can be applied only locally. Other models like the one from Koura *et al.* (orange line) [Kour2000] ($\sigma_{\text{rms}} = 0.682$ MeV), the Finite-Range-Droplet-Model (FRDM, green line) [Möll1995] ($\sigma_{\text{rms}} = 0.676$ MeV), or the HFB approaches (purple and turquoise lines) [Gori2007, Gori2009a] ($\sigma_{\text{rms}} = 0.729$ MeV, 0.581 MeV) already differ more from the experimental values (light blue line) [Waps2003b]. Finally, mass values calculated from a modified Bethe-Weizsäcker formula including deformation and shell corrections (pink line) [Span1988] are included for completeness. It has to be mentioned that the free parameters of this model are fitted only to experimental values with $Z > 50$ and $N > 50$ due to problems with the deformation terms. The original Bethe-Weizsäcker formula would completely fail to reproduce the experimental mass values for americium in Fig. 2.3(b), since shell effects play an important role in the stabilisation of heavy elements (see Sect. 2.2). It should be mentioned that there is a discussion among theorists whether quantum chaos can set a limit to the achievable accuracy in the prediction of nuclear masses but so far no evidence has been found [Bare2005].

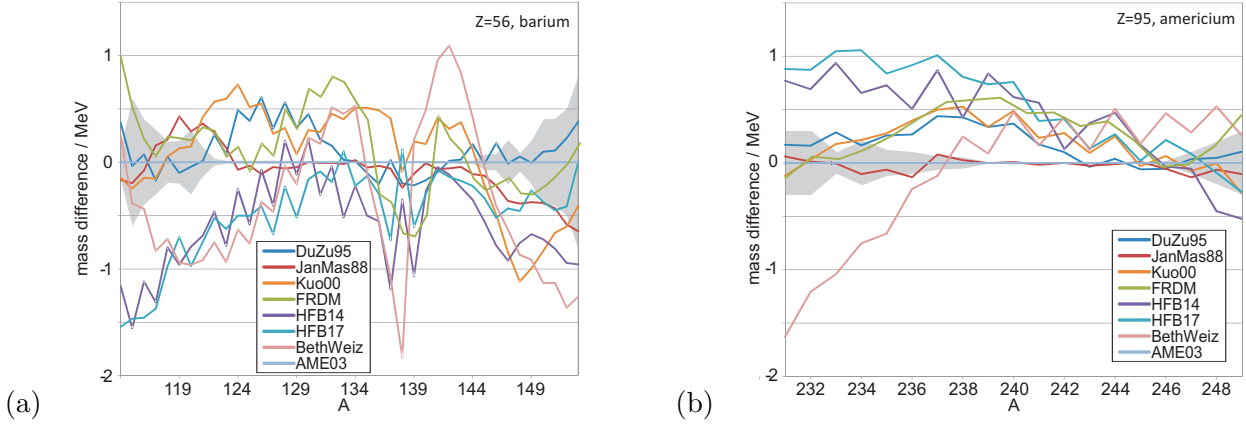


Figure 2.3: Comparison of different mass models for (a) barium ($Z = 56$) and (b) americium ($Z = 95$). Shown is the difference of the calculated mass excess from the experimental values (AME 2003 [Waps2003b]). The grey shaded area represents the uncertainty of the experimental values. For details see text.

The shell gaps

$$\Delta_n(N_0, Z) = S_{2n}(N_0, Z) - S_{2n}(N_0 + 2, Z), \quad (2.5)$$

$$\Delta_p(N, Z_0) = S_{2p}(N, Z_0) - S_{2p}(N, Z_0 + 2), \quad (2.6)$$

are commonly defined by the two-particle separation energies (Eqs. (2.2,2.3)). In terms of a mean-field description, shell closures are large gaps in the spectrum of the single-particle Hamiltonian. These single-nucleon states are not directly equivalent to the separation energies $S_{n,p}$ due to residual interactions such as pairing and rearrangement effects [Bend2002]. The shell gaps defined in Eqs. (2.5,2.6) already cancel out the pairing effects and provide a strong signature of shell closures in many cases, where the rearrangement influences on the mean field are negligible. To this end, nuclear masses through the binding energies are a frequently used observable for shell effects [Lunn2003] since high-precision measurement techniques are available here [Blau2006a].

At this point one might ask the question whether the magic numbers established when binding energy data was only available for nuclides close to stability also hold for more exotic species approaching the proton or neutron drip lines². The weakening or the vanishing of a shell gap for a large neutron or proton excess is referred to as 'shell quenching' [Doba1994, Naya1999]. Experimental evidence for neutron shell quenching is available for $N = 20$ [Thib1975] and $N = 28$ [Sara2000] as well as hints on possible new magic numbers [Ozaw2000]. However, the disappearance of certain experimental indications for shell closures might be independent from the underlying spherical shell structure as it is the case for the $Z_0 = 82$ magic proton number for lead isotopes. Here, all mean-field models predict a stable spherical shell gap in the single-particle spectrum but additional deformation effects reduce Δ_p which was mistaken to be a sign for a breakdown of the magic proton number [Bend2002]. In case of the magic number $N_0 = 82$, recent direct mass measurements

²Beyond the proton (neutron) drip line which is defined by $S_p = 0$ ($S_n = 0$), the unstable nucleus will emit free protons (neutrons). Nuclides beyond the neutron drip line cannot exist whereas nuclides beyond the proton dripline can still have half-lives in the order of a few hundred milliseconds due to the Coulomb barrier and are accessible for mass measurements [Raut2007b].

at ISOLTRAP revealed a discrepancy of the mass values determined from Q_β data and, thus, restored this neutron shell gap for the doubly-magic nucleus ^{132}Sn [Dwor2008]. The last two examples show the need for further high-precision data from direct mass measurements and further modifications to the existing theoretical models to improve our understanding of nuclear structure. The predictive power of models is very important as nuclides far away from stability are concerned which are presently not available in radioactive beam laboratories.

Since transfermium elements ($Z \geq 104$) have been synthesised, the ‘island of stability’ seems to be within reach for experiments [Hofm2000]. This is a region of superheavy nuclides which owe their pure existence to shell stabilisation effects against Coulomb repulsion due to the large number of protons [Myer1966]. Here, new magic numbers and a spherical doubly-magic nucleus around $^{298}114$ are predicted. Direct mass measurements in this region of the nuclear chart most likely will not be possible due to the short half-lives and the very low production rates of those nuclei. However, experimental mass data on actinoids can be used to better understand the nuclear structure and to improve model predictions on the stability of superheavy nuclides. A discussion on the island of stability and the nuclear structure in this region is given in Sect. 2.2. The following section gives an overview and a short discussion on different mass models which are on the market today.

In nuclear astrophysics, the rapid-neutron capture process (r-process) is discussed which is attributed to be responsible for the creation of about half of the nuclei in nature heavier than iron [Burb1957]. Model predictions of nuclear masses and β -decay properties are important input parameters for the calculation of nuclide abundances, since the r-process evolves mainly outside the limit of accessible nuclides. However, the discrepancies between different models for neutron-rich nuclides in the region of the r-process are several MeV [Blau2006b]. Solar-abundance calculations using neutron-separation energies S_n from four mass formulas have been performed in [Pfei2001] using identical astrophysical conditions. It turned out that the discrepancies in the model predictions of neutron shell gap sizes result in totally different abundances of heavy nuclides. Thus, more direct high-precision mass data is needed to test and improve theoretical models for neutron-rich nuclei. The r-process and the influence of nuclear masses is discussed in more detail in Sect. 2.3. Some of the nuclides involved will be available for high-precision mass measurements at TRIGA-TRAP (see Fig. 4.2).

2.1 Overview on the mass models

This section briefly discusses the existing models used to predict masses of nuclides presently not available for experiments. A comprehensive and more detailed overview can be found in the review by Lunnay et al. [Lunn2003]. We shall follow the historical development mentioned in the introduction to this chapter beginning with the semi-empirical Bethe-Weizsäcker formula (Sect. 2.1.1) inspired by the analogy of the nucleus to a liquid drop. Historically, the struggle to combine liquid drop features and shell-effects led to the macroscopic-microscopic (mac-mic) models, whereas physically this is nothing else than an approximation of the more fundamental Hartree-Fock method (Sect. 2.1.2) which is employed for about 10 years. Models which do not fit into this classification are discussed separately: on the one hand this is the very successful approach by Duflo and Zuker [Duf1995] and on the other hand certain algebraic relations used to calculate the mass of a nucleus from the masses of its neighbours in the chart of nuclides [Garv1966, Garv1969a] (Sect. 2.1.4).

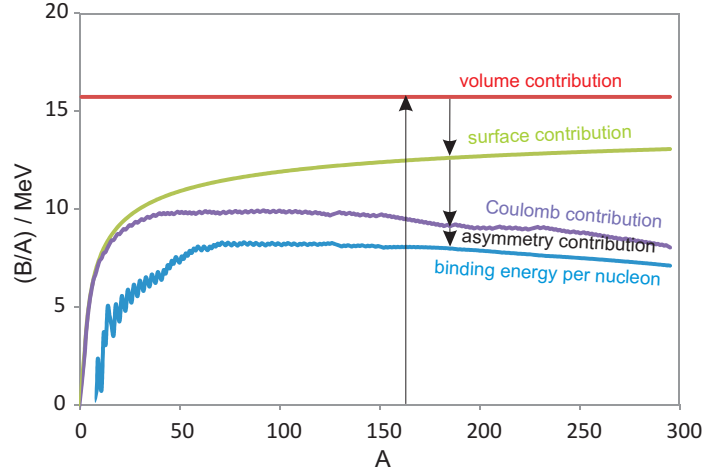


Figure 2.4: Different contributions to the nuclear binding energy in the Bethe-Weizsäcker mass formula (Eq. (2.10)).

2.1.1 The liquid-drop model and shell-corrections

It has been already mentioned how the concept of the saturation of nuclear forces evolved. The fact that a nucleon only interacts with its closest neighbours is consistent with the known short range of nuclear forces. In 1935 von Weizsäcker developed a model for nuclear binding energies $B(N, Z)$ based on this concept [Weiz1935] as illustrated in Fig. 2.4. Thus, the main contribution to $B(N, Z)$ is proportional to the number of nucleons A or, due to the almost constant nucleon density, to the volume of the nucleus. The binding energy must be lower for the nucleons at the surface of the liquid drop, which is proportional to the radius and, thus, to $A^{2/3}$. Coulomb repulsion between protons also reduces the binding energy. If one assumes a homogeneously charged sphere with radius $r_0 A^{1/3}$ and charge Ze , this contribution to the energy can be written as

$$\frac{3e^2}{5r_0} \frac{Z^2}{4\pi\epsilon_0} A^{-1/3}, \quad (2.7)$$

where r_0 is a free parameter and e is the elementary charge. A further reduction of the binding energy can be explained by the Pauli principle stating that two fermions cannot be in the same quantum state. The energy $E_0(Z, N)$ of Z protons and N neutrons in a three-dimensional box potential can be expressed in terms of the Fermi energy ϵ_F which is proportional to $(Z/A)^{2/3}$ or $(N/A)^{2/3}$:

$$E_0(Z, N) \propto \frac{Z^{2/3} + N^{2/3}}{A^{2/3}}. \quad (2.8)$$

A series expansion finally leads to the binding energy reduction for nuclei with $Z \neq N$ [Beth2008]:

$$\Delta E_0(Z, N) \propto \frac{(N - Z)^2}{A}. \quad (2.9)$$

The Bethe-Weizsäcker formula sums up all of the previously mentioned contributions. Weizsäcker also accounted for the fact that nuclei with even Z and even N are more strongly bound than even-odd or odd-odd nuclei. This pairing effect, which is clearly visible as a staggering in the inset of Fig. 2.1, is omitted here for simplicity, since only the macroscopic aspects are considered³. Within this chapter, the Bethe-Weizsäcker

³The pairing contribution has been empirically determined to be $a_p A^{-1/2} \delta$, where a_p is a free parameter and $\delta = 1$ (0, -1) for even-even (even-odd, odd-odd) nuclei.

$a_{\text{vol}} / \text{MeV}$	15.73
$a_{\text{sym}} / \text{MeV}$	-26.46
$a_{\text{sf}} / \text{MeV}$	-17.77
$a_{\text{ss}} / \text{MeV}$	17.70
r_0 / fm	1.2185

Table 2.1: Parameters used in Eq. (2.10) are taken from [Lunn2003].

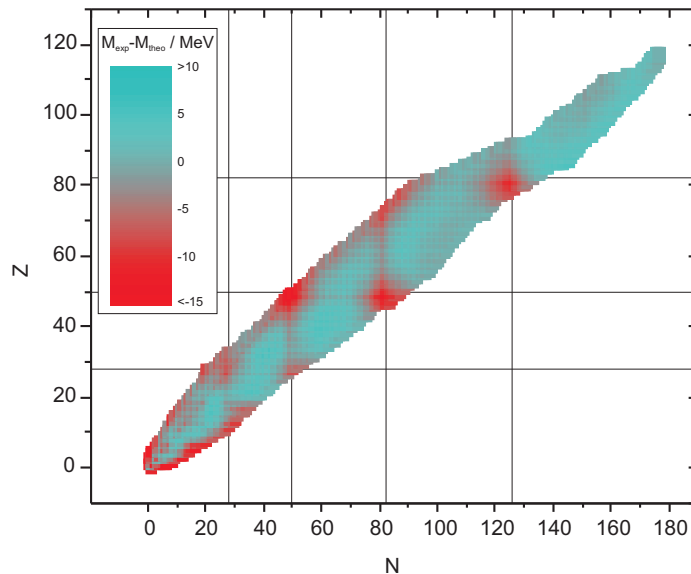


Figure 2.5: Deviations of the atomic masses predicted by the Bethe-Weizsäcker formula (see Eq. (2.10)) M_{theo} from the experimental values M_{exp} [Audi2009] for all presently known nuclides. The mass formula clearly underestimates the binding energy for magic nuclides marked by lines since shell effects are not included.

formula presented in [Lunn2003] is used:

$$B = a_{\text{vol}}A + a_{\text{sf}}A^{2/3} - \frac{3e^2}{5r_0} \frac{Z^2}{4\pi\epsilon_0} A^{-1/3} + \left(a_{\text{sym}}A + a_{\text{ss}}A^{2/3} \right) \left(\frac{N - Z}{A} \right)^2, \quad (2.10)$$

with the parameters given in Tab. 2.1 obtained in a fit of Eq. (2.10) to experimental mass values of nuclides with $N, Z \geq 8$. The surface-symmetry term with the coefficient a_{ss} has not been part of the original Bethe-Weizsäcker formula but was introduced in [Myer1966]. In principle, one could already consider it to be part of the modifications that lead to the Finite-Range-Droplet model.

Fig. 2.5 shows the differences between experimental mass values from the 2009 Atomic-Mass Evaluation [Audi2009] and the values calculated by Eq. (2.10) for all presently known nuclides. At first sight it is obvious that shell-effects are not considered in Eq. (2.10) since the binding energy for magic nuclides is systematically underestimated by several MeV. This is especially true in the vicinity of doubly-magic nuclei. To this end, the original macroscopic Bethe-Weizsäcker formula has been modified and microscopic shell-corrections have been added to remove this discrepancy from the liquid-drop model, leading to so-called mac-mic approaches.

The macroscopic term in these mac-mic models can be expressed as a sum of volume, surface and Coulomb

contributions similar to Eq. (2.10). The first modification was to introduce a compressibility coefficient K_{vol} , which describes how the finite nucleus is squeezed by the surface tension and bloated by the Coulomb repulsion. In addition, the proton and neutron surfaces are now treated independently. The result can be interpreted as an expansion of the energy in powers of $A^{-1/3}$ motivating two additional purely phenomenological terms $a_{\text{cv}}A^{1/3}$ and a_0A^0 . The total expression for the macroscopic contribution to the binding energy is then according to [Lunn2003]:

$$\begin{aligned}
E_{\text{mac}} = & - \left(a_{\text{vol}} + a_{\text{sym}}\delta^2 - \frac{1}{2}K_{\text{vol}}\epsilon^2 \right) A \\
& - \left(a_{\text{sf}} + \frac{9a_{\text{sym}}}{4Q}\delta^2 \right) A^{2/3} \\
& - \frac{3e^2}{5r_0} \frac{Z^2}{4\pi\epsilon_0} A^{-1/3} + \frac{9e^4}{400r_0^2Q} \frac{Z^4}{16\pi^2\epsilon_0^2} A^{-2} \\
& - a_{\text{cv}}A^{1/3} - a_0A^0,
\end{aligned} \tag{2.11}$$

where δ and ϵ are determined through a minimisation of E_{mac} . Q describes the surface stiffness as introduced by Myers and Swiatecki [Myer1969]. A further generalisation was done by taking deformation of the nucleus into account by correction factors multiplied to each term except the ones scaling with A , which are proportional to the volume. Moreover, the effect of the short range of the nucleon-nucleon interactions on the surface energy contribution is finally accounted for by adding another correction factor B_1 to the surface term which finally becomes $a_{\text{sf}}B_1A^{2/3}$ [Möll1981]. Further refinements of the macroscopic energy expression have been performed to eliminate certain deficiencies in the model's predictions.

So far only modifications of the droplet model's macroscopic part have been considered which certainly cannot influence the failure at magic nuclei. To this end, microscopic shell-corrections were added using a method proposed by Strutinsky [Brac1973]: the aim is to separate a single-particle field Φ into a smooth liquid-drop energy $\tilde{\Phi}$ and remaining oscillating shell-corrections $\delta\Phi$. These corrections are obtained by means of an energy-averaging of the single-particle spectrum $\{\epsilon_i^{(\tau)}\}$ for protons and neutrons:

$$\delta\Phi_\tau = 2 \sum_i \epsilon_i^{(\tau)} - 2 \int_{-\infty}^{\lambda_\tau} E \tilde{g}_\tau(E) dE, \quad \tau \in (\text{p}, \text{n}), \tag{2.12}$$

where $\tilde{g}_\tau(E)$ is the average level density obtained by smearing out the spectrum with Gaussian functions [Brac1973], and λ_τ is the Fermi energy. For the FRDM, the single-particle potential used is

$$\Phi = \Phi_1 + \Phi_{\text{s.o.}} + \Phi_{\text{Coul}}, \tag{2.13}$$

with the spin-independent nuclear contribution Φ_1 , the spin-orbit term $\Phi_{\text{s.o.}}$, and the Coulomb term Φ_{Coul} . Further information on the application of the Strutinsky method and shell-corrections in the FRDM can be found in [Möll1995]. In addition, pairing corrections and a charge-asymmetry term scaling with $(Z - N)$ are added but not discussed here. Also a Wigner term reflecting an additional binding in case neutrons and protons occupy the same shell-model orbitals is taken into account, similar to the microscopic mass models to be discussed in the following section. The results of the FRDM are shown in Fig. 2.6 as mass differences between experimental [Audi2009] and calculated [Möll1995] values in comparison to Fig. 2.5. Obviously, the implementation of microscopic shell corrections removed the striking discrepancy previously mentioned for magic nuclides. The FRDM is frequently used as a reference for experimentalists and had the largest impact

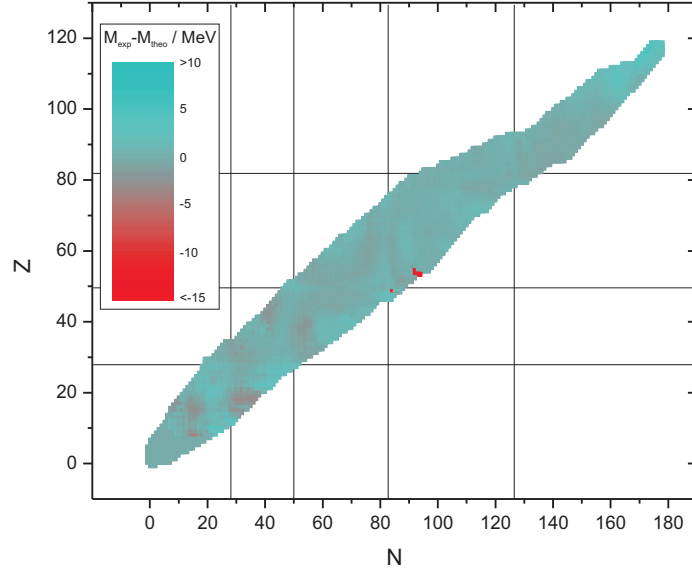


Figure 2.6: Deviations of the atomic masses calculated by the FRDM model M_{theo} from the experimental values M_{exp} [Audi2009] for all presently known nuclides. In comparison to Fig. 2.5 the large discrepancies for magic nuclides are removed by the implementation of microscopic shell-corrections to the macroscopic liquid droplet characterisation.

as far as mac-mic mass formulas are concerned. Nevertheless, there have been other approaches classified as mac-mic models like the mass formula by Myers and Swiatecki [Myer1966], the TF-FRDM⁴ [Myer1996], and the ETFSI⁵ [Gori2000]. The last example is already based on an effective force, which will be the central object in the discussion of microscopic models (Sect. 2.1.2).

2.1.2 Microscopic mass models

In principle nuclear properties should be derived from the basic nucleonic interactions. Those *ab initio* approaches start from a realistic nucleon-nucleon potential V_{ij} obtained from nucleon-nucleon scattering experiments [Mach2001]. The non-relativistic Hamiltonian of a nucleus can be written as

$$H = -\frac{\hbar^2}{2M} \sum_i \nabla_i^2 + \sum_{i>j} V_{ij}. \quad (2.14)$$

The special short-range characteristic of the strong interaction with a repulsive core makes it quite difficult to solve the corresponding Schrödinger equation by common perturbation methods. Brueckner and co-workers introduced a transformation of the original problem based on the Hamiltonian in Eq. (2.14) to a simpler system where the Hartree-Fock technique can be applied [Brue1955]. This technique has been primarily developed to solve eigenvalue problems with weak long-range interactions: the wave-function is approximated by a fully anti-symmetrised product of the single-particle wave-functions expressed as a Slater determinant. Starting from this approach, the energy eigenvalues are obtained through the variational method in a self-consistent field. Even the more developed framework reviewed in [Beth1971] had only limited success in describing the properties of finite nuclei and is mainly applied to the theoretical concept of a simple many-body problem

⁴TF-FRDM = Thomas Fermi-Finite Range Liquid Droplet.

⁵ETFSI = Extended Thomas Fermi plus Strutinsky Integral.

called ‘infinite nuclear matter’. This contains infinite nuclei with a certain ratio between neutrons and protons and the Coulomb repulsion switched off. The theoretically interesting extreme of infinite nuclear matter can be used to benchmark the *ab initio* calculations of nuclear properties. Within this context, it has to be mentioned that frameworks strictly applying two-nucleon forces as briefly discussed above so far fail to reproduce the so-called point of nuclear saturation, referring to an empirical saturation density of about 0.17 nucleons/fm³ obtained from high-energy electron scattering experiments on heavy nuclides and a corresponding binding energy per nucleon of $B/A \approx 16$ MeV [Li2006]. This discrepancy can be improved by the introduction of three-nucleon forces [Li2006], but their microscopic origin is still under discussion. Besides the non-relativistic calculations, relativistic many-body theories also exist (see e.g. [Dick1992]). Other approaches to solve the *ab initio* problem are based on the Green’s-function Monte Carlo method, but it seems like the increasing complexity with the mass number presently sets a limit at $A = 12$ for finite nuclei. Developments in computational techniques enabled to calculate the properties of the ¹²C nucleus [Navr2000] but the problem of three-body forces persists.

After this very brief introduction of the complexity of *ab initio* calculations, it is obvious that such approaches are presently not suited to predict the properties of unknown finite nuclides. To this end, the realistic nucleon-nucleon interactions are replaced by effective forces with phenomenological parameters (see, e.g., the reviews [Lunn2003, Bend2003]). In this case the effective Hamiltonian can be written as

$$H^{\text{eff}} = -\frac{\hbar^2}{2M} \sum_i \nabla_i^2 + \sum_{i>j} v_{ij}^{\text{eff}}. \quad (2.15)$$

The effective interaction does not have to fit the scatter data which is true for the *ab initio* calculations. Moreover, a big step forward in the performance of mass models based on effective forces has been made when the connection to the realistic nucleon-nucleon interaction has been abandoned. The interactions used in the calculations are primarily tuned to serve their purpose and they are directly adjusted to the observables, e.g. the known masses of finite nuclides. A more detailed discussion on the derivation of those effective forces based on energy-density functionals and a motivation for this procedure can be found in the review by Bender et al. [Bend2003].

In principle two parametrisations of forces are available today: a minority of the mass algorithms employs the Gogny force [Dech1980] but the approach adopted from Skyrme is widely used [Vaut1972], thus, also discussed here. Once the effective interaction is specified, the Hartree-Fock variational principle can be applied similar to *ab initio* calculations starting from the nuclear ground-state wave function given as a Slater determinant Φ of single-particle states ϕ_i

$$\Phi(\vec{x}, \sigma, T) = \frac{1}{\sqrt{A!}} \det [\phi_i(\vec{x}_j, \sigma_j, T_j)], \quad (2.16)$$

where (\vec{x}, σ, T) denote the spatial coordinates, the spin, and the isospin⁶ of all A nucleons. The total energy

$$E = \langle \Phi | H^{\text{eff}} | \Phi \rangle = \int d^3x \mathcal{H}(\vec{x}) \quad (2.17)$$

with the energy-density functional $\mathcal{H}(\vec{x})$ must be stationary with respect to variations of the single-particle states [Vaut1972]

$$\frac{\delta}{\delta \phi_i} \left[E - \sum_i \epsilon_i \int d^3x |\phi_i(\vec{x})|^2 \right] = 0. \quad (2.18)$$

⁶For protons (neutrons) the isospin is $T = +1/2$ ($-1/2$).

Inserting the Skyrme effective interaction, the following set of equations has to be solved iteratively [Lunn2003]:

$$\left[-\vec{\nabla} \frac{\hbar^2}{2m_T^*(\vec{x})} \vec{\nabla} + U_T(\vec{x}) + V_T^{\text{coulomb}}(\vec{x}) - i\vec{W}_T(\vec{x}) (\vec{\nabla} \times \vec{\sigma}) \right] \phi_i = \epsilon_i \phi_i, \quad (2.19)$$

where $m_T^*(\vec{x})$ is the density-dependent effective mass, $U_T(\vec{x})$ the single-particle field determined by the effective force, $V_T^{\text{coulomb}}(\vec{x})$ the Coulomb interaction, $\vec{W}_T(\vec{x})$ the form-factor of the single-particle spin-orbit potential, and $\vec{\sigma}$ the spin operator. $U_T(\vec{x})$ does not need to have spherical symmetry but can be deformed as well. With the self-consistent solutions ϕ_i the energy E in the Hartree-Fock approximation can be calculated. To obtain the binding energies, and thus, the nuclear masses, a rearrangement term

$$E_R = -\frac{t_3}{8} \int d^3x \rho_n(\vec{x}) \rho_p(\vec{x}) \rho(\vec{x}) \quad (2.20)$$

has to be added to the total single-particle energies ϵ_i due to the density dependence of the nuclear interaction, where t_3 is a free parameter of the Skyrme force [Vaut1972, Bend2002]. The remaining parts still to be included in the calculations are pairing effects. In the first place the p-p and n-n pairing is taken into account, corresponding to an isospin of $T = 1$ ($|T_z| = 1$). Early models took a general approach adopted from the theory of superconductors [Bard1957], where an additional pairing energy of the form

$$E_{\text{pair}} = -G \left[\sum_{i>0} (n_i [1 - n_i])^{1/2} \right]^2 \quad (2.21)$$

has to be introduced⁷ into (2.18) [Vaut1973], where G is the pairing strength and n_i the occupation probability for the single-particle state ϕ_i . Another treatment of the pairing interaction can be done using the Bogolyubov transformation, which is a standard procedure in many-body theory. Here, the single-particle states are connected to quasiparticle states by a unitary transformation. Thus, the pairing energy is fully included in the variation procedure of the Hartree-Fock-Bogolyubov method⁸. An extensive discussion on these calculations can be found in [Bend2003]. The most recent microscopic mass tables, HFB-17 ($\sigma_{\text{rms}} = 0.581 \text{ MeV}$) and HFB-18 ($\sigma_{\text{rms}} = 0.585 \text{ MeV}$), are based on this technique [Gori2009a, Cham2009] and a mass model using the mentioned Gogny force ($\sigma_{\text{rms}} = 0.798 \text{ MeV}$) has been developed as well [Gori2009b].

After taking the p-p and n-n pairing into account, the binding energies of $N = Z$ nuclides, corresponding to a vanishing isospin $T = 0$, are systematically underestimated by the microscopic Hartree-Fock models so far. To address this problem, an additional energy contribution has been proposed by Myers and Swiatecki [Myer1966]. Due to a similarity to the supermultiplet theory founded by Wigner, this is often referred to as Wigner term. Another striking problem in the microscopic mass models is the so-called mutually enhanced magicity, which means nothing else than the systematic underbinding of the doubly-magic nuclei with $N \neq Z$ and their direct neighbours by the mass formulas. There are some starting points for an investigation of this problem but so far the origin is not understood. Despite the fact that binding energies of finite nuclei are only in the order of MeV/u, a relativistic Hartree-Fock approach has been investigated as well [Bogu1977], where the nucleons are represented by Dirac spinors and the interaction mesons appear explicitly in the calculation⁹. For further details on the relativistic calculations the reader is referred to a review article on this topic by Reinhard [Rein1989].

⁷Mass models based on this approach are called HF-BCS (=Hartree Fock-Bardeen Cooper Schrieffer), to account for the pairing treatment adopted from the theory of superconductors.

⁸Models employing the Bogolyubov transformation are labeled HFB (=Hartree Fock Bogolyubov).

⁹This approach is usually called RMF (=Relativistic Mean Field).

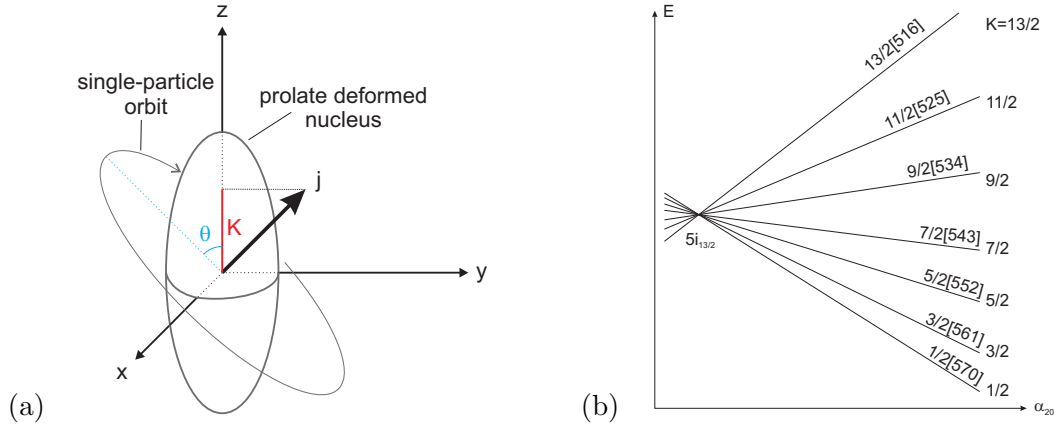


Figure 2.7: (a) Illustration of a single-particle orbit for a prolate deformed nucleus. In the Nilsson model, the projection of the total angular momentum j on the symmetry axis is labelled K . Θ is the classical orbit angle. (b) Changes in the single-particle energies stemming from $i_{13/2}$ as a function of the quadrupolar deformation α_{20} with different projections K . For details see text.

2.1.3 The Nilsson model of deformed nuclei

The Nilsson model is a rather simple but powerful approach to enclose the variation of standard (spherical) shell-model energies as a function of the deformation of the nucleus (see e.g. [Cast2000]). To derive the exact level energies detailed calculations are needed, but a qualitative understanding is straight forward. Contrary to spherical nuclides, the energy of an orbit depends on its inclination with respect to the symmetry axis of a deformed nucleus. Fig. 2.7(a) shows an illustration for the example of a prolate shape. The orbit angle is described by the quantum number K being the projection of the total angular momentum j on the symmetry axis z . A nucleon in an orbit closer to the remaining nuclear matter (symbolised by the prolate) will be stronger bound leading to a lower level energy. Thus, the level energy will increase with increasing K . Moreover, a similar trend is observed for the quadrupolar deformation parameter $\alpha_{20} > 0$, which parametrises compression or expansion of the sphere along the symmetry axis z to obtain an oblate or a prolate shape. Fig. 2.7(b) illustrates the variation of the energy for the shell-model level $i_{13/2}$ as a function of α_{20} for different projections K . Nilsson model orbits are labelled

$$K[Nn_z\Lambda], \quad (2.22)$$

where N is the principal quantum number for the major shell, n_z the number of nodes in the wave function in direction of the z axis, and Λ the projection of the orbital angular momentum along this axis (see Fig. 2.7(b)). The single-particle Hamiltonian for a deformed nucleus with a harmonical oscillator potential can be written as [Cast2000]

$$H = \frac{\hat{p}^2}{2m} + \frac{1}{2}m\omega_0^2\hat{r}^2 - m\omega_0^2\hat{r}^2\delta\frac{4}{3}\frac{\pi}{5}\hat{Y}_{20}(\theta, \phi) + C\hat{l} \cdot \hat{s} + D\hat{l}^2, \quad (2.23)$$

using the deformation operator $\delta\hat{r}^2\hat{Y}_{20}$ in spherical coordinates. The deformation parameter δ is proportional to α_{20} . For small δ , the contribution of $\delta\hat{r}^2\hat{Y}_{20}$ can be regarded as a distortion to the isotropic harmonic oscillator including $\hat{l} \cdot \hat{s}$ and \hat{l}^2 terms. So the energy is proportional to δ and depends quadratically on K (compare Fig. 2.7(b)). For a large deformation, an anisotropic harmonic oscillator remains.

2.1.4 Other mass formulas

This section briefly summarizes other existing mass formulas which do not fit into the previous classification but still play an important role. In particular this is the microscopic approach by Duflo and Zuker which is often regarded as the benchmark for theoretical models and a powerful tool to predict unknown masses [Mend2008]. However, it is somewhat different from the models discussed above as it will be shown in the following. At the end of this section, mass predictions utilising the masses of surrounding nuclides or of members of an isospin multiplet by systematic trends and algebraic relations are introduced.

The approach by Duflo and Zuker: Duflo and Zuker started with the assumption that a smooth pseudopotential exists allowing Hartree-Fock calculations [Duf1995]. In this case, the effective Hamiltonian (which is similar to Eq. (2.15)) can be separated into a monopole and a multipole term [Abzo1991]

$$H = H_m + H_M. \quad (2.24)$$

H_M acts as a residual interaction and is fully determined by realistic nucleon-nucleon potentials, which, however, do not appear explicitly in the calculations. Pairing and Wigner effects are also covered by the multipole term [Lunn2003]. H_m , in turn, includes the single-particle properties and saturation, in general, the liquid-drop features. The explicit form is given by [Duf1995]

$$H_m = \sum_{k,l} a_{kl} m_k (m_l - \delta_{kl}) + b_{kl} \left(T_k \cdot T_l - \frac{3m_k}{4} \delta_{kl} \right) \quad (2.25)$$

including only up to quadratic terms in the number m_k and isospin operators T_k . The parametrisation of Eq. (2.25) is finally done extracting the dominant terms by scaling and symmetry arguments. The result is a mass algorithm based on 28 parameters with excellent extrapolation features [Mend2008]. To test the predictive power, the parameters of the mass model are fitted only to a subset of the available data and the mass values of the remaining nuclides are obtained through extrapolation. The rms error of the model predictions is only about 500 keV if the parameters are fixed to 1760 known masses¹⁰ from the Atomic-Mass Evaluation 2003 [Waps2003b] and the remaining 389 masses are predicted by the model. Also other subsets of the available mass data were taken and the remaining values predicted. In most of these tests, the rms deviation for the predictions stays between 500 and 800 keV. However, in case the subset $A \leq 200$ is taken for the fit, the error of the calculated heavier masses is about 1.4 MeV, which is still superior to other models. When dealing with such tests of the predictive power of mass formulas, the problem of possible wrong experimental data in the Atomic-Mass Evaluation has to be always considered. For completeness, it should be mentioned that Duflo and Zuker also developed a mass model based on only 10 parameters.

Local mass formulas: The atomic mass can in principle be interpreted as a parametrization of a three-dimensional surface in N and Z , and, thus, the ‘mass surface’ is often referred to. Fig. 2.2 shows the two-neutron separation energy S_{2n} being a derivative of the mass surface, similar to the two-proton separation energy S_{2p} , the α -decay Q_α , and the β -decay energy Q_β . The variation of these quantities is quite regular apart from the regions of shell-closures and nuclear deformations. Already in the early days of the Atomic-Mass Evaluation, the regularity has been used to predict missing mass values by interpolating with the

¹⁰To fit the model, the masses of those 1760 nuclides were taken from [Waps2003b] which were already known in [Audi1995].

constraint that all derivatives of the mass surface vary as smoothly as possible. The smoothness condition is checked here graphically as described in [Borc1993]. Meanwhile, this method is also used to extrapolate to mass values of three to four nuclides further away from stability than the last known one. These predictions proved to be very accurate when comparing new experimental data to the extrapolations in older mass evaluations [Lunn2003].

Algebraic relations between neighbouring nuclides have been established by Garvey and Kelson by constructing a difference equation of the general form [Garv1969b]

$$0 = \sum_{i=1}^{\alpha} (-1)^{\gamma_i} M(N_i, Z_i). \quad (2.26)$$

To get such a difference equation for a particular choice of the linear combination, the nucleonic interactions must cancel in first order. This requires α to be an even integer, which cancels out all neutron-neutron and proton-proton interactions. A further constraint to Eq. (2.26),

$$0 = \sum_{i=1}^{\alpha} (-1)^{\gamma_i} N_i Z_i, \quad (2.27)$$

ensures that all neutron-proton interactions vanish as well. Behind this approach is the interpretation of a nucleus in the single-particle picture, where nucleons are described in a smoothly varying self-consistent mean-field. The corrections due to different proton numbers and the resulting variations in the Coulomb interaction are omitted, since they are small in the set of masses of only a few nuclides entering the difference equation. The simplest choice of a linear combination obeying the constraints given above leads to the relation

$$\begin{aligned} & M(N+2, Z-2) - M(N, Z) \\ &= M(N+1, Z-2) - M(N, Z-1) \\ &+ M(N+2, Z-1) - M(N+1, Z) \end{aligned} \quad (2.28)$$

linking six masses [Garv1966]. If one takes a closer look, Eq. (2.28) includes three pairs of mass numbers $\{A, A \pm 1\}$, where the pair members differ in the isospin projection T_z , i.e. in the ratio between neutrons and protons. Eq. (2.28) can be used recurrently to determine unknown masses away from stability where the error certainly increases in each iteration step. Barea and co-workers tested the predictive power of Garvey-Kelson relations by comparing calculated to experimentally known masses and found rms deviations of only about 100-200 keV [Bare2008]. Unlike the original publication, Janecke and Masson interpreted Eq. (2.28) as a third-order partial differential equation with the general solution [Jane1988]

$$M(N, Z) = G_1(N) + G_2(Z) + G_3(N+Z), \quad (2.29)$$

where the functions G_i can be determined by a fit to known masses. Moreover, neutron-rich and neutron-deficient nuclides are treated independently to overcome the problems with long-range extrapolations. In Fig. 2.3, the masses calculated by this approach can be seen for barium and americium isotopes.

As a last example of local mass formulas, the Isobaric Multiplet Mass Equation (IMME) is briefly discussed. It is assumed for a multiplet with isospin T that the interactions are approximately charge-independent and that charge-dependent perturbations are only due to two-body interactions. In this case, the mass relation

$$M(T, T_z) = a(T, T_z) + b(T, T_z)T_z + c(T, T_z)T_z^2 \quad (2.30)$$

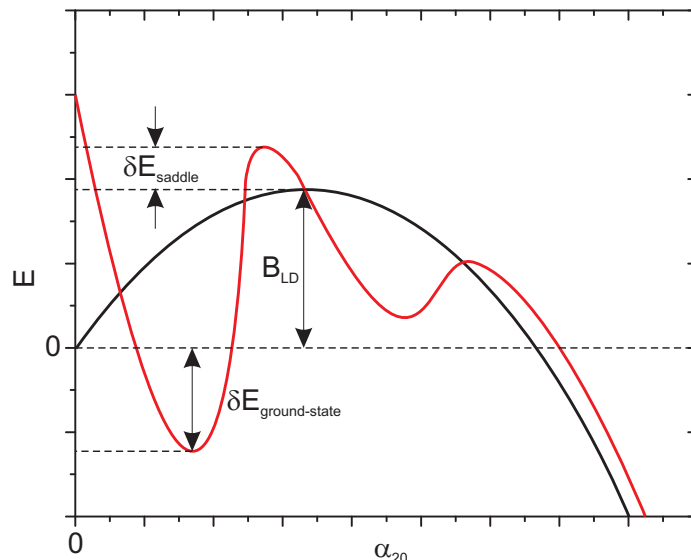


Figure 2.8: Sketch of the sum of surface and Coulomb energy in the liquid-drop model (black line) as a function of the quadrupolar deformation α_{20} . The red line demonstrates how the energy is changed due to shell corrections in microscopic-macroscopic models. In this case, the nuclear ground state would be deformed with a shell effect of $\delta E_{\text{ground-state}}$. The saddle point has an additional energy of δE_{saddle} over the fission barrier B_{LD} obtained in the liquid-drop model.

is obtained [Garv1969a], where a, b, c are coefficients specific for each multiplet. A validation of the assumptions leading to the IMME (Eq. (2.30)) can be made by any multiplet with $T > 1$. A mass measurement of ^{33}Ar at ISOLTRAP led to the conclusion that a cubic term is needed in case of the $T = 3/2$ multiplet [Herf2001b], but the problem was resolved by identifying in another experiment that the mass of ^{33}Cl was wrong [Pyle2002]. More recent stringent tests on the level of ~ 100 eV (see e.g. [Blau2003a], which is the most stringent test so far) showed that so far there is no indication of a breakdown of Eq. (2.30). Thus, it is frequently used to predict levels and masses within an isospin multiplet especially for applications in nuclear astrophysics. However, the relation is limited to multiplets with known coefficients.

2.2 Impact of shell-effects on heavy and superheavy elements

Great efforts have been made to discover new elements at the upper end of the nuclear chart. The question of how many elements may exist always went along with this struggle. Experiments at GSI and in Dubna managed to identify a few transfermium nuclides by their alpha-decay chains [Hofm2000]. The existence of heavy and superheavy elements cannot be explained by a pure liquid-drop model. Here, the calculated barriers for spontaneous fission decrease with Z^2/A due to the competition between the attractive nuclear surface tension and the Coulomb repulsion. Fig. 2.8 shows a sketch of the variation of these two dominating contributions to the liquid-drop energy of the nucleus (compare Eq. (2.10)) under a quadrupolar deformation. The obtained fission barrier B_{LD} vanishes for $Z^2/A \gtrsim 50$ and leads to a scission of the nucleus [Bohr1939]. The pure existence of nuclei beyond this fission limit is due to quantum stabilisation by shell effects. Fig. 2.8 illustrates how these microscopic contributions alter the shape of the nuclear energy as a function of the quadrupolar deformation α_{20} . One remarkable thing here is that due to shell corrections the energy mini-

mum can correspond to a deformed nucleus, going along with an additional binding energy $\delta E_{\text{ground-state}}$. In case of Fig. 2.8 the nuclear ground state would be prolate. Within the FRDM model, the quadrupole deformations of the ground states have been calculated as a function of N and Z [Möll1995] (see Fig. 2.9). Magic and doubly-magic nuclei, such as ^{208}Pb , are spherical, whereas nuclei inbetween the magic numbers exhibit strong deformations. As already indicated in the introduction to this chapter, this effect also changes the observable shell-structure. Enhanced stability away from the magic numbers referred to as a deformed-shell closure is found for example at $(N, Z) = (152, 100)$. Besides the deformation of the ground state, shell-corrections also influence the height of the fission barrier for heavy and superheavy nuclides. The additional energy contribution δE_{saddle} (see Fig. 2.8) enhances the stability of certain nuclei against spontaneous fission. Thus, the fission limit $Z^2/A \gtrsim 50$ predicted by a purely liquid-drop oriented nuclear structure model is no longer valid. Fig. 2.10 displays the microscopic corrections mainly due to shell effects obtained in an FRDM calculation by subtracting the macroscopic liquid-droplet contribution from the total binding energy [Möll1995]. Again, the largest stability enhancement is observed at doubly-magic nuclei. However, there are two regions of strongly deformed nuclides with a microscopic binding-energy gain of several MeV. In this region, several actinoid isotopes are available for mass measurements at TRIGA-TRAP indicated in Figs. 2.9 and 2.10 and the first direct mass measurement on ^{241}Am has been performed within this thesis work. In addition, direct mass measurements of the three nobelium isotopes $^{252-254}\text{No}$ with production rates of one particle per second have been recently performed at SHIPTRAP and are also marked [Dwor2009, Bloc2010a]. Also self-consistent mean-field models employing several effective interactions can be used to calculate shell-effects [Bend2001]. In case the fission barrier is large enough due to shell-effects to stabilise the nucleus against spontaneous fission, other radioactive decays limit the half-life. For the actinoids of interest at TRIGA-TRAP the emission of an alpha-particle is dominant. The alpha-decay half-life is dependent on the Q_α -value [Viol1966] and can

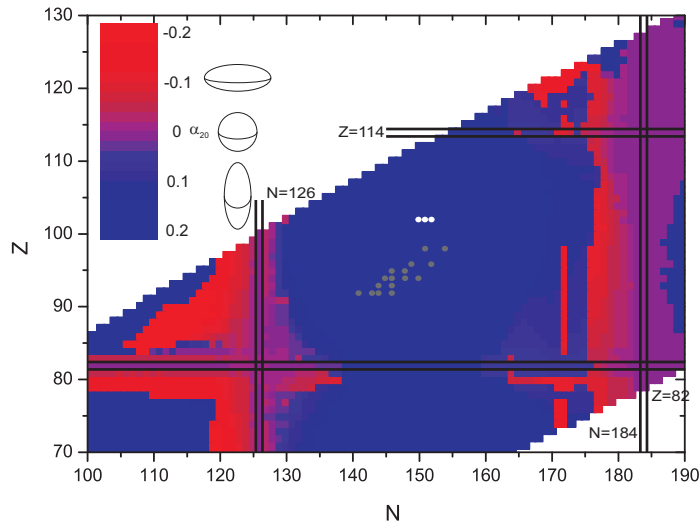


Figure 2.9: (Colour) Calculated quadrupolar deformations α_{20} of heavy and superheavy nuclides obtained with the FRDM model [Möll1995]. The grey circles indicate the actinoid nuclides easily available for mass-measurements at TRIGA-TRAP, the white circles mark the three nobelium isotopes $^{252-254}\text{No}$ measured at SHIPTRAP. As indicated, $\alpha_{20} > 0 (= 0, < 0)$ corresponds to prolate (spherical, oblate) nuclei.

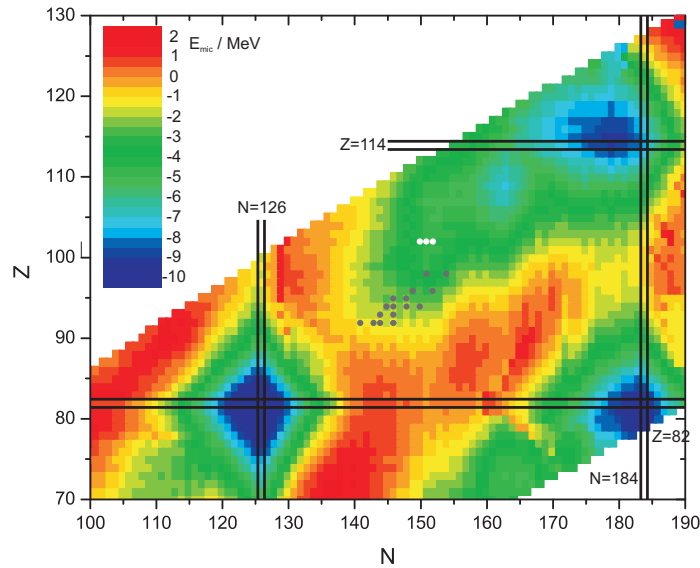


Figure 2.10: (Colour) Calculated microscopic corrections to the ground-state energy of heavy and superheavy nuclides obtained with the FRDM model [Mö11995]. A minimum (blue colour) corresponds to a shell-stabilised region, as for the doubly-magic nucleus ^{208}Pb (lower left corner). The grey circles indicate the actinoid nuclides easily available for mass-measurements at TRIGA-TRAP, the white circles mark the three nobelium isotopes $^{252-254}\text{No}$ measured at SHIPTRAP. For details see text.

be estimated as well from the model's mass predictions.

All of these attempts focus on the prediction of the next spherical neutron and proton shell-closures beyond ^{208}Pb corresponding to the so-called 'island of stability'. Up to date, the predictions vary between $Z \approx 114$ and $N = 184$ for the mac-mic models [Mö11994] and a complete region around $Z \approx 120$ and $N \approx 180$ in self-consistent mean field calculations [Bend2001, Bend2003]. The shell-corrections presented in Fig. 2.10 obtained through FRDM calculations indicate a slightly different position of the neutron-shell closure at $N \approx 180$ compared to previous mac-mic results cited above.

For a better understanding of the nuclear structure at the upper end of the nuclear chart and to come closer to an answer about the border of existence of nuclei, more experimental input data are certainly needed. However, besides the measurements within this work at TRIGA-TRAP and the values for three nobelium isotopes obtained at SHIPTRAP no direct mass measurements have been performed for nuclides heavier than uranium so far [Dwor2009, Dwor2010].

2.3 Nucleosynthesis by neutron-capture

Light nuclides up to iron are created in charged-particle induced nuclear reactions, such as



which is the hydrogen-burning with an energy release of about 27 MeV. Due to the increasing Coulomb repulsion with higher Z , the element abundance in the solar system drops rapidly between hydrogen and iron. The so-called iron-peak is an exception to this trend since it includes the nuclides with the highest binding

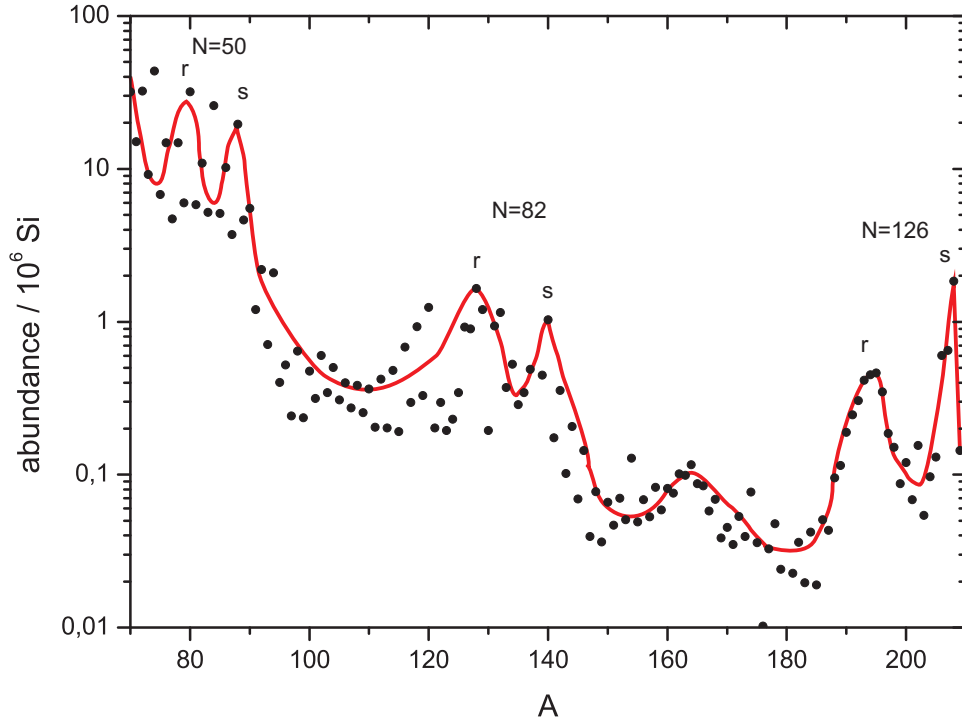


Figure 2.11: Solar-system abundances of elements beyond the iron-peak as a function of the mass number A taken from [Ande1982]. The red line is to guide the eye. Double-peaks in the abundance pattern appear for nuclides with magic neutron numbers ($N_0 = 50, 82, 126$) produced by two different neutron-capture processes indicated by the letters r and s. For details see text.

energy per nucleon (compare Fig. 2.1). However, the general trend is not continued to heavy elements which can only be explained by different astrophysical processes responsible for the element creation in this region [Rolf1988]. Fig. 2.11 displays the abundance pattern for mass numbers $A \geq 70$, exhibiting three double-peaks for the abundance of nuclides with magic neutron numbers ($N_0 = 50, 82, 126$). This fact and the increasing Coulomb barrier avoiding charged-particle reactions point to two different neutron-capture processes as the source of heavy elements [Burb1957]. At this point it should be mentioned that neutron-capture is not the only possibility to produce heavier elements but solely responsible for the creation of elements above bismuth. Processes involving protons such as the p-, rp- [Rolf1988], and ν p-process [Fröh2006] are not considered here, since these nuclides are anyhow not available at the TRIGA reactor.

The nucleosynthesis proceeds by neutron captures and subsequent beta-decays, where the environmental conditions mainly determine the capture rates $\Gamma_{n\gamma}$, and the lifetimes τ_β are limited by nuclear properties. According to $\Gamma_{n\gamma}$ the slow neutron-capture process (s-process) evolving close to the line of beta-stability is distinguished from the rapid neutron-capture process (r-process), which follows a path close to the neutron drip-line. The nuclides involved in the s-process are easily accessible in experiments and, thus, their mass values are well-known [Audi2009]. The s-process occurs most likely inside stars with typical neutron densities in the order of 10^8 n/cm^3 [Rolf1988]. A seed nucleus which is part of the iron peak (e.g. ^{56}Fe) and, thus, produced by charged-particle induced burning reactions, captures neutrons until a beta-unstable nucleus is reached. If one assumes an immediate decay¹¹ of the unstable nuclide to the next Z , the abundance evolution

¹¹This assumption neglects the branching of the s-process path which happens for a few nuclides involved, where the beta-decay

for any stable nuclide with mass number A is governed by [Ili2007]

$$\frac{dN(A, t)}{dt} = -N_n N(A, t) \Gamma_{n\gamma}(A) + N_n N(A - 1, t) \Gamma_{n\gamma}(A - 1), \quad (2.32)$$

where $N(A, t)$ and N_n are the number densities of nuclides with mass number A and the neutrons, respectively¹². The reaction rate $\Gamma_{n\gamma}(A)$ can be written as a product of an energy-averaged cross-section $\langle\sigma\rangle_A$ and the velocity of the thermalised neutrons v_T given by a Maxwell-Boltzmann distribution for a certain temperature T . After some simple mathematics one obtains the ‘local equilibrium approximation’ for abundances within the s-process [Burb1957]

$$\langle\sigma\rangle_A N(A) \approx \text{const.} \quad (2.33)$$

This approximation is certainly only valid for nuclides between magic neutron numbers. Since the cross-sections for neutron capture are very small for closed shells, the constant in Eq. (2.33) drops to a new value at each magic neutron number. A more detailed discussion of the s-process abundances can be found in the literature [Burb1957, Rolf1988, Ili2007]. The s-process terminates at ^{209}Bi , since a further neutron capture leads to an alpha-unstable nucleus. For this reason and to explain the first maximum of each double-peak in Fig. 2.11, a second process has to exist which is solely responsible for the production of trans-bismuth elements. Unlike the nucleosynthesis mechanism briefly discussed until here, the r-process evolves far away from the valley of stability towards the neutron drip-line. Nuclides in this region are not yet accessible by experiments with just a few exceptions [Blau2006b, Scha2006]. For this reason, astrophysical calculations in this field must rely on predictions by theoretical models as far as nuclear properties are concerned.

As displayed in Fig. 2.12 the seed nucleus (e.g. ^{56}Fe) captures a number of neutrons until an equilibrium is reached between neutron capture (n, γ) and photodisintegration reactions (γ, n), which is referred to as a waiting point. The exact location of the waiting point in the isobaric chain is dependent on the neutron capture reaction energy¹³ Q_n and the environmental conditions, such as temperature T and neutron density N_n . The coarse dependence on these parameters can be seen in [Rolf1988]

$$\Gamma_{\gamma n} \propto \frac{T^{2/3}}{N_n} \exp\left(-\frac{Q_n}{kT}\right) \Gamma_{n\gamma}, \quad (2.34)$$

where $\Gamma_{\gamma n}$ ($\Gamma_{n\gamma}$) is the photodisintegration (neutron capture) rate. The astrophysical site of the r-process is not known. Likely, it occurs in explosive stellar environments, such as supernovas, with neutron densities around 10^{20} n/cm^3 or higher and temperatures of about 10^9 K . These conditions are required to enable multiple neutron captures since the stability against beta-decay decreases rapidly when approaching the drip-line. Typical energies for the waiting point nuclides are $Q_n \approx 2 - 3 \text{ MeV}$ [Rolf1988, Ili2007]. At a waiting point in the isobaric chain characterised by Z , the nucleosynthesis can only continue after a beta-decay leads to the next isobaric chain with $Z + 1$. For nuclides with magic neutron numbers the beta-decay is much faster than the capture process due to the favourable nucleon configuration characterised by Q_n dropping below the limit of $2 - 3 \text{ MeV}$. Thus, these nuclides become waiting points and the r-process proceeds along an isotonic

is delayed enough to compete with a further neutron capture.

¹²Within the s-process, the abundances are commonly discussed only as a function of the mass number, since for most cases only a single isobar participates for a certain A .

¹³The Q -value is commonly used in the discussion of nuclear reactions. In this case $Q_n(N, Z)$ is identical to the neutron-separation energy $S_n(N + 1, Z)$ of the following isotope.

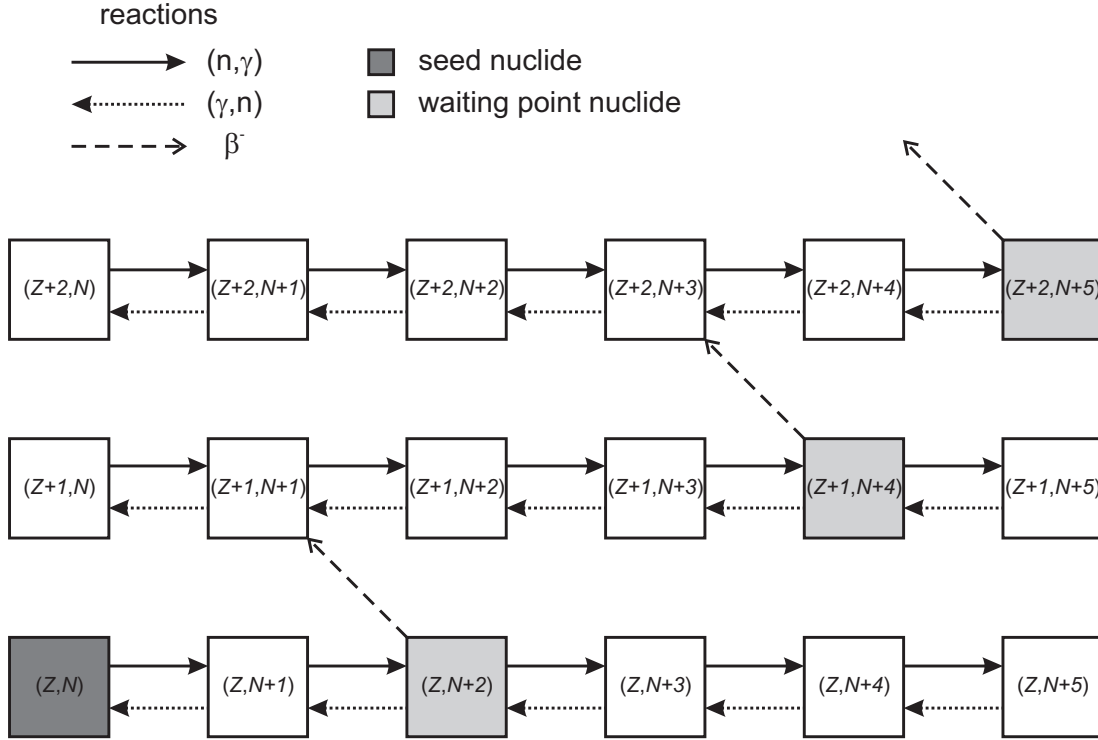


Figure 2.12: Sketch of the r-process. Starting from a seed nucleus (dark gray box) a waiting point (light gray boxes) is reached for each isotopic chain with an equilibrium between (n, γ) and (γ, n) reactions. After a subsequent beta-decay to the next Z , the neutron-capture process continues.

chain until a nuclide with longer half-life against beta-decay is reached closer to the valley of stability. Here, a further neutron capture becomes energetically possible to overcome the border given by the magic N . This hampered neutron capture is the reason for the first maximum in the abundance-double peaks visible in Fig. 2.11. They are shifted to lower masses A since the r-process proceeds far away from the valley of stability and, thus, crosses a magic neutron number at lower Z compared to the s-process. Moreover, the r-process abundance peaks are slightly broader due to the long isotonic chains for magic N causing a significant delay in the abundance flow. The maximum for $A \approx 160$ shown in Fig. 2.11 is a consequence of enhanced stability due to nuclear deformation as discussed in Sect. 2.2.

The abundance for a nucleus with mass number A and charge Z in the so-called ‘waiting point approximation’ is only governed by neutron-capture processes to the nuclide with $A + 1$ and photo-disintegration reaction back to A [Iliu2007]

$$\frac{dN(A, Z, t)}{dt} = -N_n N(Z, A, t) \Gamma_{n\gamma}(A, Z) + N(A + 1, Z, t) \Gamma_{\gamma n}(A + 1, Z). \quad (2.35)$$

The beta-decay is assumed to be much faster than the other reactions, so that it does not disturb the $(n, \gamma) \leftrightarrow (\gamma, n)$ equilibrium. Once the equilibrium abundance distribution in an isotopic chain $N_0(Z, A)$ has been determined using Eq. (2.35), the flow between different elements has to be calculated by the beta-decay probability

$$\Gamma_\beta(Z) = \frac{\sum_A N_0(Z, A) \Gamma_\beta(Z, A)}{\sum_A N_0(Z, A)}, \quad (2.36)$$

leading to the time evolution of the total abundance N_Z of element Z described by [Iliu2007]

$$\frac{dN_Z}{dt} = -\Gamma_\beta(Z)N_Z + \Gamma_\beta(Z-1)N_{Z-1}. \quad (2.37)$$

Finally, the equilibrium is reached meaning $\Gamma_\beta(Z)N_Z \approx \text{const.}$, which is referred to as the ‘steady flow approximation’.

An expected path of the r-process is illustrated in the nuclear chart in Fig. 4.2. It should be mentioned that the flow along this path can be also interrupted if the environmental conditions change, mainly if the neutron density drops dramatically. In this case, the process will continue by subsequent beta-decays until a stable nuclide is reached. To this end, the r-process contributes to the abundance of certain stable medium-mass nuclides which are also produced via the s-process. However, beta-decay is not the only mechanism for r-process nuclides to reach the valley of stability. In case, a neutron-unbound state is reached in the beta-daughter nuclide, beta-delayed neutron-emission occurs. Besides this, alpha-decay, spontaneous and beta-delayed fission compete with the beta-decay especially for large A [Iliu2007]. Fission finally terminates the r-process even in case the environmental conditions do not change. A lack of experimental data makes it difficult to predict the exact limit which lies around ($A_{\text{max}} \approx 260, Z_{\text{max}} \approx 94$) [Pano2005]. This nuclide will decay by fission feeding back the reaction products as new seeds into the r-process.

To fully understand the nucleosynthesis of heavy elements by the r-process, more experimental data, such as nuclear masses and half-lives, are certainly needed. As shown in Fig. 4.2, with the help of the TRIGA Mainz reactor, more neutron-rich nuclides are available. Therefore, TRIGA-TRAP can provide new direct mass measurements for some r-process nuclides and also other data points to test and improve the theoretical models which have to be considered for the extrapolation of mass values to the neutron drip-line.

3 Storage, manipulation and detection of ions in a Penning trap

Frequencies are the physical quantities which can be measured with the highest precision. Therefore, atomic and nuclear masses are also determined by a frequency measurement of ions in a Penning trap. The ion motion in this setup is well understood and will be briefly addressed in Sect. 3.1. In order to achieve the highest resolution, the ions have to be carefully prepared in the trap, which includes cleaning away of contaminants as well as cooling, i.e. the reduction of motional amplitudes to minimise the effect of field imperfections. The mass measurement is carried out by an excitation of the ions with a variable frequency and the determination of a resonance profile. Cooling and excitation techniques applied in Penning traps are discussed in Sect. 3.2 with a focus on the methods used at TRIGA-TRAP. The ion detection can be carried out basically in two different ways, where one method keeps the ions stored in the trap (non-destructive detection method) and the other one requires ejection of the ions (destructive detection method). Both are employed at TRIGA-TRAP and will be addressed in Sect. 3.3.

3.1 The Penning trap

In 1989 the Nobel Prize in physics was partially awarded to Hans Dehmelt for the development and introduction of the Penning trap to atomic precision spectroscopy [Dehm1990]. He was inspired by the magnetron trap described in the book of Pierce [Pier1954] and the ion gauge of Penning [Penn1936]. Ion storage for further experiments is achieved by the superposition of a strong homogeneous magnetic field responsible for the radial confinement and a weak electrostatic quadrupole field for the axial confinement. Penning traps are nowadays widely used for high-precision measurements in many fields of physics. Besides mass measurements [Blau2006a], also other fundamental quantities like magnetic moments (g -factors) are determined in such devices [Wert2006]. The magnetic field can be replaced by a time-varying electric field leading to a Paul trap, for which Wolfgang Paul shared the Nobel Prize in 1989 as well [Paul1990]. However, to date only Penning traps are employed for precision mass measurements due to the superb magnetic field stability of superconducting magnets. The following section deals with the principles of ion storage in an ideal Penning trap prior to a discussion of imperfections present in a real Penning trap. Further information beyond this brief introduction can be found in [Brow1986, Majo2004].

3.1.1 Penning-trap basics: the ideal trap

The electrostatic potential in an ideal Penning trap can be written in cylindrical coordinates as

$$V(\rho, z) = \frac{V_0}{2d^2} \left(z^2 - \frac{\rho^2}{2} \right), \quad (3.1)$$

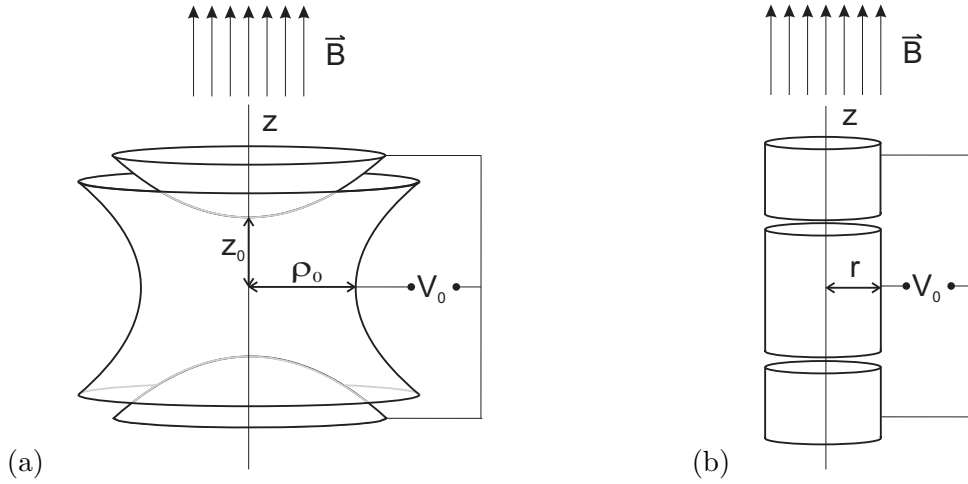


Figure 3.1: Two different electrode configurations used as Penning traps. The magnetic field defines the z -axis. (a) Hyperbolically shaped ring and endcap electrodes, which come the closest to the ideal Penning trap configuration. (b) Cylindrical electrode configuration, which is easier to machine and provides more access to the trap through the open endcaps. Therefore, it is frequently used, especially for ion preparation. In both cases, the trapping potential V_0 is applied between the endcaps and the ring electrode.

where V_0 is the trapping potential and d the trap parameter given by

$$d^2 = \frac{1}{2} \left(z_0^2 + \frac{\rho_0^2}{2} \right). \quad (3.2)$$

The parameters ρ_0 and z_0 are defined as in Fig. 3.1(a), representing the minimal distance between the centre of the trap and the ring electrode or the endcaps. For cylindrical electrodes as shown in Fig. 3.1(b) an analogue trap parameter \tilde{d} can be extracted from an expansion of the electrostatic potential.

The equation of motion for an ion with charge-to-mass ratio q/m in an electric field $\vec{E} = -\vec{\nabla}V$ and a homogeneous magnetic field $\vec{B} = B\vec{e}_z$ in the z -direction is given by

$$\begin{aligned} m\ddot{\vec{r}} &= q \left(\vec{E} + \dot{\vec{r}} \times \vec{B} \right) \\ &= q \left(-\vec{\nabla}V + \dot{\vec{r}} \times \vec{B} \right). \end{aligned} \quad (3.3)$$

Thus, the three one-dimensional differential equations of the problem are

$$\ddot{x} = \frac{\omega_z^2}{2}x + \omega_c \dot{y}, \quad (3.4)$$

$$\ddot{y} = \frac{\omega_z^2}{2}y - \omega_c \dot{x}, \quad (3.5)$$

$$\ddot{z} = -\omega_z^2 z, \quad (3.6)$$

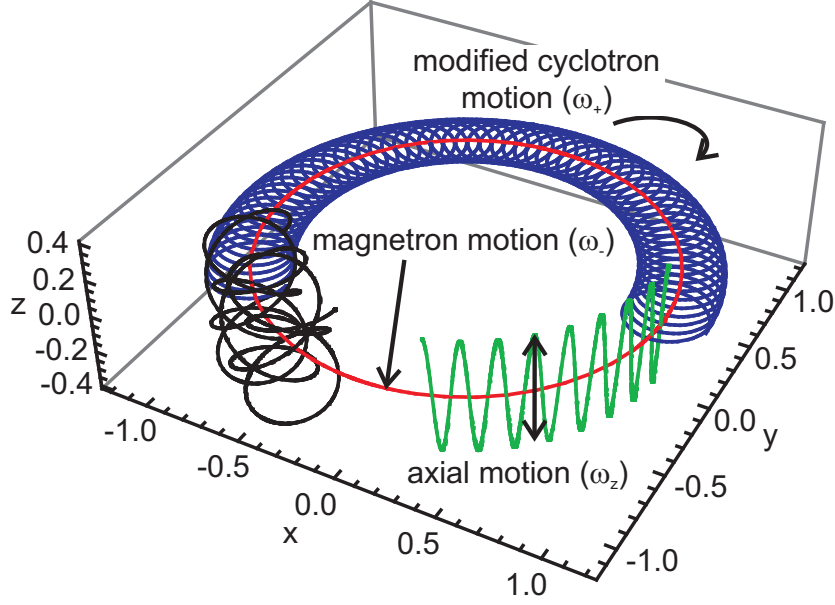


Figure 3.2: Ion motion in a Penning trap with the magnetic field aligned versus the z -axis. The ion motion in an ideal Penning trap decomposes into three independent harmonic oscillations. Red: pure magnetron motion with frequency ω_- . Blue: magnetron motion and modified cyclotron motion with frequency ω_+ superimposed. Green: axial motion with frequency ω_z . The frequency ratio is $\omega_+ : \omega_z : \omega_- = 100 : 40 : 1$, similar to an ion of mass number $A = 250$ in the TRIGA-TRAP precision trap. The black curve shows the superposition of all three eigenmotions.

with the true cyclotron frequency¹ ω_c and the axial frequency ω_z as given by

$$\omega_c = \frac{q}{m} B, \quad (3.7)$$

$$\omega_z = \sqrt{\frac{qV_0}{md^2}}. \quad (3.8)$$

Introduction of a complex variable $u = x + iy$ into Eqs. (3.4) and (3.5) leads to

$$\ddot{u} = \frac{\omega_z^2}{2} u - i\omega_c \dot{u}. \quad (3.9)$$

Thus, the solution of the system of differential equations in Eqs. (3.4), (3.5), and (3.6) is

$$\begin{aligned} x(t) &= \rho_+ \cos(\omega_+ t + \Phi_+) + \rho_- \cos(\omega_- t + \Phi_-), \\ y(t) &= -\rho_+ \sin(\omega_+ t + \Phi_+) - \rho_- \sin(\omega_- t + \Phi_-), \\ z(t) &= \hat{z} \cos(\omega_z t + \Phi_z). \end{aligned} \quad (3.10)$$

It has to be mentioned that a periodic solution requires

$$\begin{aligned} \omega_c^2 - 2\omega_z^2 &> 0, \\ qU &> 0. \end{aligned} \quad (3.11)$$

¹Since the experimental quantity is not an angular frequency but a frequency, in the following chapters ν is mostly used instead of ω . ω is used in theoretical considerations for simplicity.

The second requirement means that positively charged particles have to be trapped in a positive potential and vice versa. Eq. (3.10) indicates that the ion motion in an ideal Penning trap can be separated into three independent harmonic oscillations [Kret1991] as illustrated in Fig. 3.2: the modified cyclotron motion with amplitude ρ_+ , frequency ω_+ , and phase Φ_+ , the magnetron motion $(\rho_-, \omega_-, \Phi_-)$, and the axial motion $(\hat{z}, \omega_z, \Phi_z)$. The eigenfrequencies of this problem are

$$\omega_{\pm} = \frac{1}{2} \left(\omega_c \pm \sqrt{\omega_c^2 - 2\omega_z^2} \right) \quad (3.12)$$

and the axial frequency given in Eq. (3.8). Frequency values calculated for the conditions in the TRIGA-TRAP precision trap are listed in Tab. 3.1. Several useful relations can be derived:

$$\omega_c = \omega_+ + \omega_-, \quad (3.13)$$

$$\omega_c^2 = \omega_+^2 + \omega_-^2 + \omega_z^2, \quad (3.14)$$

$$\omega_z^2 = 2\omega_+\omega_-, \quad (3.15)$$

and the frequencies show a hierarchy of $\omega_- < \omega_z < \omega_+ < \omega_c$. Eq. (3.14) is called the invariance theorem and it holds as well for a real Penning trap with a tilting angle between the magnetic field and the trap axis and an unharmonic imperfection in the electric field [Brow1982]. In the case of the most precise mass measurements of stable nuclides with $\delta m/m \leq 10^{-11}$ [Rain2004, Dyck2004], all three eigenfrequencies are determined and this invariance theorem leads to the true cyclotron frequency. However, in mass measurements on short-lived nuclides, a special detection technique called Time Of Flight-Ion Cyclotron Resonance (TOF-ICR, see Sect. 3.3.1) is used, which is very fast and therefore well suited for the short half-lives. Here, Eq. (3.13) gives the cyclotron frequency, which can be proven to be correct within the best uncertainty limits reported so far by the invariance theorem [Gabr2009]. Another important fact for Penning trap mass spectrometry is the first-order mass independence of the magnetron frequency, which can be seen in a series expansion of Eq. (3.12):

$$\omega_- \approx \frac{V_0}{2d^2B}, \quad (3.16)$$

and with Eq. (3.13)

$$\omega_+ \approx \omega_c - \frac{V_0}{2d^2B}. \quad (3.17)$$

The mean potential energy of an ion in a Penning trap is given by

$$\begin{aligned} \bar{E}_{\text{pot}} &= - \lim_{T \rightarrow \infty} \frac{q}{T} \int_0^T V(x(t), y(t), z(t)) dt \\ &\approx - \frac{qV_0}{4d^2} (\rho_+^2 + \rho_-^2 - \hat{z}^2). \end{aligned} \quad (3.18)$$

Using Eq. (3.15) this leads to the total ion energy

$$\begin{aligned} E_{\text{total}} &= \frac{m}{2} (\rho_+^2 \omega_+^2 + \rho_-^2 \omega_-^2 + \hat{z}^2 \omega_z^2) + \bar{E}_{\text{pot}} \\ &= \frac{m}{2} \rho_+^2 (\omega_+^2 - \omega_+ \omega_-) + \frac{m}{2} \hat{z}^2 (\omega_z^2 + \omega_+ \omega_-) + \frac{m}{2} \rho_-^2 (\omega_-^2 - \omega_+ \omega_-). \end{aligned} \quad (3.19)$$

typ. nuclide	A	ν_c / kHz	ν_+ / kHz	ν_z / kHz	ν_- / kHz
^1H	1	107529.30	107526.15	822.44	3.15
^{85}Rb	85	1265.05	1261.90	89.21	3.15
^{87}Rb	87	1235.97	1232.82	88.18	3.15
^{133}Cs	133	808.49	805.33	71.31	3.16
^{238}U	238	451.80	448.64	53.31	3.17
^{241}Am	241	446.18	443.01	52.98	3.17
^{252}Cf	252	426.70	423.53	51.81	3.17

Table 3.1: True cyclotron frequency $\nu_c = \omega_c/(2\pi)$ and the three eigenfrequencies $\nu_i = \omega_i/(2\pi)$ for singly charged ions of different mass numbers A in the TRIGA-TRAP precision trap with $V_0 = 7\text{ V}$, $B = 7\text{ T}$, and $d = 5.03\text{ mm}$. The magnetron frequency ν_- is approximately mass-independent.

Eq. (3.19) indicates that the contribution of the magnetron motion to the total energy is always negative due to the fact that $\omega_+ \gg \omega_-$, which has an impact on the buffer gas cooling of the ion's motion as addressed in Sect. 3.2.2.

For completeness, it should be mentioned that a quantum mechanical treatment of the ion motion in a Penning trap leads to three uncoupled harmonic oscillators and a total energy for a spinless particle of [Brow1986]

$$E_{\text{total}} = \hbar\omega_+ \left(n_+ + \frac{1}{2} \right) + \hbar\omega_z \left(n_z + \frac{1}{2} \right) - \hbar\omega_- \left(n_- + \frac{1}{2} \right). \quad (3.20)$$

The so called Landau levels are displayed in Fig. 3.3.

3.1.2 Imperfections of the real trap

In the previous section ideal quadrupole potentials and magnetic fields were assumed to analyse the ion motion. Deviations from the ideal electric field arise from the fact that the electrodes of a real hyperbolic Penning trap are finite, sometimes segmented, and have to have holes for the ion injection and ejection. In addition, tolerances in machining and assembling the electrode stack contribute to the imperfections, which result in higher order terms of the electric potential. Cylindrical electrodes are also very common since they offer a direct access to the trap content. Besides these imperfections inhomogeneities in the magnetic field and a tilt of the field versus the trap axis cause deviations from the ideal situation. All these imperfections manifest themselves in shifts of the eigenfrequencies dependent on the amplitudes of the ion motion. For a detailed discussion of the imperfections in the electric and magnetic fields of a real Penning trap see [Brow1986, Majo2004]. The most important ones in the context of this thesis will be briefly discussed in the following.

- *Imperfections of the electric field:* The perturbation of the electric potential in a real Penning trap ΔV can be expressed by a multipole expansion in polar coordinates [Gabr1983]

$$\Delta V = \frac{V_0}{2} \sum_{k=0}^{\infty} C_{2k} \left(\frac{r}{d} \right)^{2k} P_{2k}(\cos \Theta), \quad (3.21)$$

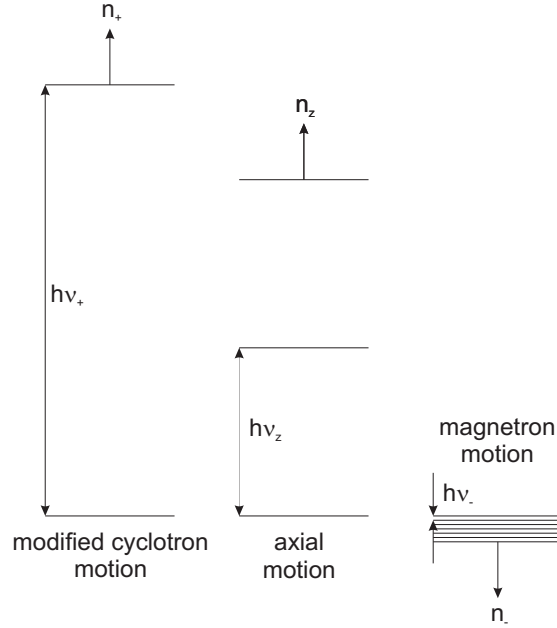


Figure 3.3: Energy levels (Landau levels) of the three eigenmotions of a spinless charged particle in a Penning trap. The frequency ratio is 100:40:1 similar to an ion of mass number $A = 250$ in the TRIGA-TRAP precision trap. Note the negative sign of the contribution of the magnetron motion. The centre of the trap is set to zero potential.

where the odd terms vanish due to a symmetry about the mid-plane of the trap. Solving the equations of motion in the perturbed potential leads to amplitude dependent shifts of the eigenfrequencies. For mass spectrometry, especially the sideband frequency $\omega_c = \omega_+ + \omega_-$ is important (see Sect. 3.3.1). The shift of this frequency arising from the multipole components² $k = 4, 6, 8$ is

$$\begin{aligned} \Delta\omega_c^{\text{el}} &= \frac{3\omega_z^2}{4d^2(\omega_+ - \omega_-)} (\rho_-^2 - \rho_+^2) [C_4 \\ &+ \frac{5C_6}{2d^2} (\rho_+^2 + \rho_-^2 - 3\hat{z}^2) \\ &+ \frac{35C_8}{8d^4} (\rho_+^4 + 3\rho_+^2\rho_-^2 + \rho_-^4 - 8\rho_+^2\hat{z}^2 - 8\rho_-^2\hat{z}^2 + 6\hat{z}^4)], \end{aligned} \quad (3.22)$$

where

$$\frac{\omega_z^2}{2(\omega_+ - \omega_-)} \stackrel{(3.15)}{=} \frac{1}{1 - \omega_-/\omega_+} \approx \omega_- \approx \frac{V_0}{2d^2B}. \quad (3.23)$$

This approximately mass-independent shift $\Delta\omega_c^{\text{el}}$ is minimised by the use of additional correction electrodes (see Sect. 4.5).

- *Magnetic field inhomogeneities and fluctuations:* Due to the limited size of the superconducting coil generating the magnetic field (in the case of TRIGA-TRAP $B = 7$ T), there is only a very limited region where a homogeneity of $\delta B/B \leq 10^{-6}$ is achieved (at TRIGA-TRAP on a circle of less than 5 mm radius around the trap centre). For the correction and stabilisation of the magnetic field amplitude additional coils are used. The materials of the trap electrodes, insulators, and holder structures induce

²The term for C_2 vanishes since the shifts in ω_+ and ω_- cancel each other in the sideband frequency $\omega_+ + \omega_-$.

inhomogeneities to the magnetic field due to their susceptibilities as well. This effect can be minimised by the use of high-purity materials with low susceptibilities, especially oxygen-free copper. Furthermore, temperature and pressure fluctuations in the environment and in the cryogenic-liquid dewars of the solenoid have an impact on the magnetic field, which can be reduced by a temperature and pressure stabilisation system, as it is done for example at ISOLTRAP [Dwor2006, Mari2008]. In the experimental hall of the research reactor TRIGA Mainz, the temperature is stabilised to better than 0.05 K/h and the atmospheric air pressure fluctuations are typically lower than 0.5 mbar/h. The perturbation of the magnetic field ΔB can be expressed in another series expansion

$$\Delta B = B_0 \sum_{k=1}^{\infty} \beta_{2k} \left(\frac{r}{d}\right)^{2k} P_{2k}(\cos \Theta), \quad (3.24)$$

leading to a frequency shift in the next multipole order of

$$\Delta\omega_c^{\text{mag}} = \frac{\omega_c \beta_2}{2(\omega_+ - \omega_-) d^2} [(\omega_+ - \omega_-) \hat{z}^2 + \omega_- \rho_+^2 - \omega_+ \rho_-^2]. \quad (3.25)$$

In addition to field fluctuations the magnetic field strength of a superconducting magnet decreases steadily with time, which is known as the *flux-creep-effect* [Ande1962]. In the case of the TRIGA-TRAP magnet, a special coil is used to minimise the field drift for the time of a measurement (see Sect. 4.5).

- *Misalignment of the trap axis and ellipticity in the electric field:* When a trap is installed in the bore of a superconducting magnet, a crucial point is the alignment of the trap axis versus the axis of the magnetic field. A tilt, which can be expressed in polar coordinates by

$$\vec{B} = B_0(\sin \Theta \cos \phi, \sin \Theta \sin \phi, \cos \Theta) \quad (3.26)$$

leads to a frequency shift. Another unavoidable imperfection is an ellipticity of the electric field, meaning that projections of equipotentials onto the x - y -plane are not circles but ellipses. The ellipticity can be treated by a parameter ϵ which is the fractional difference in length of the axes of these ellipses [Brow1986]. Taking both a small ellipticity ($\epsilon \ll 1$) and a small tilt ($|\sin \Theta| \ll 1$) into account leads to a shift in the sideband frequency $\omega_c = \omega_+ + \omega_-$ of [Majo2004]

$$\Delta\omega_c^{\text{ellip,tilt}} \approx \omega_- \sin^2 \Theta (3 + \epsilon \cos(2\phi)). \quad (3.27)$$

The invariance theorem Eq. (3.14) is still valid, since the shift in ω_z cancels the shifts of the radial frequencies.

- *Space charges and image charges:* Coulomb interaction between stored ions leads to line broadening and shifts of the eigenfrequencies. In case of two different ion species present in the trap, it depends on the resolving power of the mass spectrometer how the resulting resonance will look like: if both ion species can be resolved, two resonances at the sideband frequencies $(\omega_+ + \omega_-)_{1,2}$ will be determined where the centres of the resonances will be shifted to lower values. If both lines cannot be resolved, one resonance is observed at the centre-of-mass frequency. In case all stored ions are of the same species, no frequency shift but line broadening due to a change in the electric potential occurs [Boll1992, Köni1995]. These effects are accounted for in the data evaluation by grouping the events by ion numbers considering the detection efficiency and extrapolating the frequency to a single stored ion (see Chap. 6).

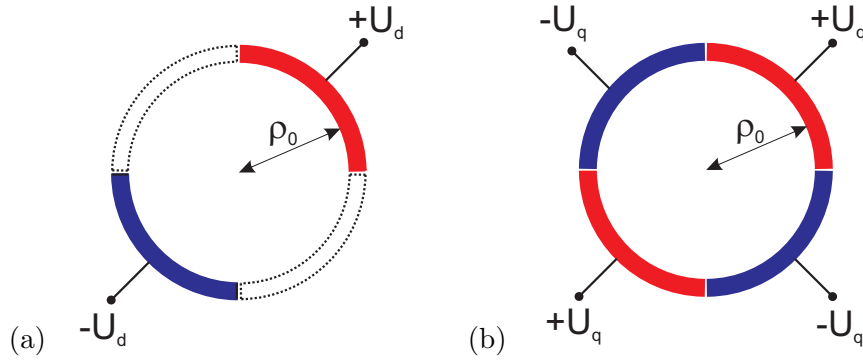


Figure 3.4: Illustration of the application of (a) dipolar and (b) quadrupolar rf fields to excite the ion motion. The sketch shows the top view of a four-fold segmented ring electrode. At TRIGA-TRAP the segmentation is asymmetric and only two smaller segments will be used for the excitation, the larger ones are reserved for image current detection (see Fig. 3.10).

The image charges induced by a single ion in the trap electrodes alter the electric field and, thus, effect the ion motion. A shift in the axial frequency scales with the ion number and is only significant for small traps. Since the origin of this frequency shift is purely electrostatic, the sideband frequency $\omega_+ + \omega_-$ is not affected [Majo2004].

3.2 Manipulation of the ion motion

For a mass measurement, the eigenfrequencies of the ions stored in the Penning trap need to be determined to as high precision as possible. Therefore, manipulation techniques such as excitation and cooling of the ion motion are needed. Excitation means the increase of energy or quantum number of one of the independent harmonic oscillators (see Fig. 3.3) by applying a resonant rf field at the corresponding eigenfrequency. Note that the negative sign of the magnetron contribution to the total energy leads to a decrease of energy in case the magnetron quantum number n_- or magnetron radius ρ_- is increased. Commonly, dipolar and quadrupolar rf fields are used for excitation. The first acts only on the eigenmotion it is in resonance with, while the second is applied at the sum frequency of two eigenmotions. Thereby, these two motions are coupled leading to a periodic energy conversion between them. The ring electrodes as well as the endcaps of the Penning trap are segmented to apply the rf fields. For completeness, the octupolar excitation has to be mentioned, which is a further development to improve the uncertainty of a frequency measurement without the need to increase the measurement time [Elis2007, Ring2007].

Another important step in a mass measurement is the cooling of the ion motion. Here, the motional amplitudes are reduced so that the ions probe less field imperfections (see Sect. 3.1.2). In radioactive beam facilities, the nuclides are typically produced in reactions at energies of a few MeV/u. To ensure a good beam transport, ion sources are usually operated at some kV. Most of the ion potential energy is removed by means of pulsed drift tubes, which can create ion pulses of a few 10 eV. In order to minimise the kinetic energy spread and the motional amplitudes, stored ions are further cooled in the Penning trap. Several techniques are applicable here [Majo2004, Blau2006a]. At TRIGA-TRAP buffer-gas cooling is applied and will be discussed in Sect. 3.2.2. Other techniques are laser, sympathetic, evaporative and electron cooling. Resistive cooling

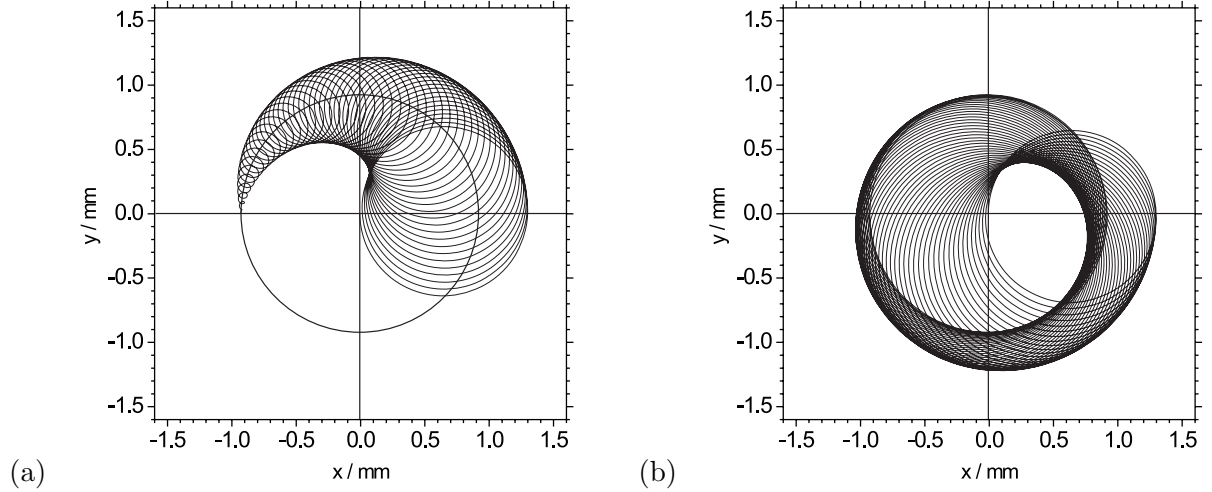


Figure 3.5: (a) First half of the conversion from a pure magnetron motion into a pure cyclotron motion by a quadrupolar rf field at $\nu_q = \nu_c$. (b) Second half of the conversion. The radii $\rho_+(t=0)$ and $\rho_-(t=T_{\text{conv}})$ are identical. For details see text.

based on the dissipation of electric energy in an equivalent resistance attached to the trap electrodes could be in principle applied at TRIGA-TRAP as well but is not feasible for short-lived heavy singly charged ions. The cooling time constant would be already in the order of seconds (see Sect. 2.4.2 in [Kete2006]).

3.2.1 Dipolar and quadrupolar excitation

In case only one eigenmotion should be manipulated a dipolar rf field at the corresponding eigenfrequency has to be applied (Fig. 3.4(a)). Since ν_+ is mass dependent, an excitation at the modified cyclotron frequency can be used to remove unwanted ion species mass selectively from the Penning trap. In contrast, a dipolar rf field at the magnetron frequency ν_- influences the magnetron radius of all trapped ion species simultaneously, which is a key ingredient of the mass-selective buffer-gas cooling described in Sect. 3.2.2. The rf field for a dipolar excitation in the x -direction can be written as

$$\vec{E}_x = \frac{U_d}{a} \cdot \cos(2\pi\nu_d + \Phi_d) \vec{e}_x, \quad (3.28)$$

where U_d is the rf voltage amplitude at radius a , ν_d the excitation frequency, and Φ_d the excitation phase. With an appropriate phase Φ_d , the amplitude of the corresponding eigenmotion increases linearly with the excitation time T_d [Blau2003b]. In principal, the phase of the ion motion is unknown. Even in the worst case (180° phase shift between ion motion and rf field), the amplitude first decreases but then starts to increase again. In this case, T_d has to be sufficiently long.

A quadrupolar excitation at the sum frequency of two eigenmotions is used to couple these two motions leading to a periodic energy conversion. Most important in Penning trap mass spectrometry is the coupling of the two radial eigenmotions at $\nu_q = \nu_c = \nu_+ + \nu_-$ [Köni1995] (see Fig. 3.5) used in a TOF-ICR frequency measurement (Sect. 3.3.1) and as part of the buffer-gas cooling process (Sect. 3.2.2). In this case an azimuthal quadrupolar field is applied to the segments of the ring electrode (see Fig. 3.4(b)) which can be expressed

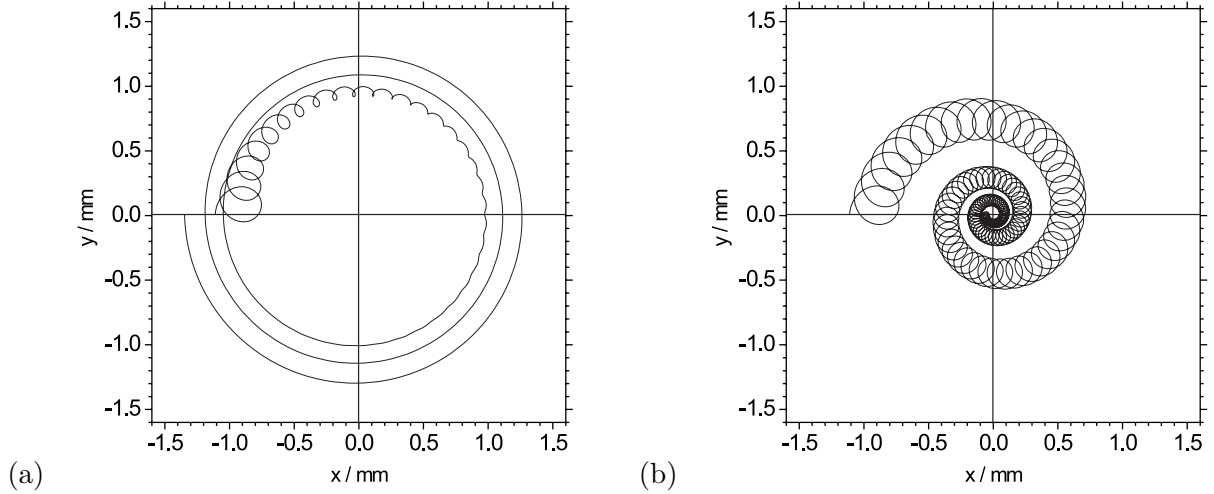


Figure 3.6: Illustration of the buffer-gas cooling mechanism by calculated ion trajectories. A velocity dependent damping force has been included in the equations of motion. (a) The amplitude of the modified cyclotron motion decreases very fast whereas the magnetron amplitude increases slowly. (b) By the additional application of an azimuthal quadrupolar rf field at the sideband frequency $\nu_c = \nu_+ + \nu_-$ energy is transferred from the magnetron into the cyclotron motion and, thus, the total radius decreases. This centering is mass dependent due to the mass dependence of ν_c .

similar to the dipolar field by

$$\begin{aligned}\vec{E}_x &= \frac{2U_q}{a^2} \cdot \cos(2\pi\nu_q t + \Phi_q) y \vec{e}_x, \\ \vec{E}_y &= \frac{2U_q}{a^2} \cdot \cos(2\pi\nu_q t - \Phi_q) x \vec{e}_y.\end{aligned}\quad (3.29)$$

The amplitudes ρ_- and ρ_+ are periodically converted into each other [Köni1995] with the conversion time

$$T_{\text{conv}} = \pi^2 \frac{m}{q} \frac{a^2}{U_q} (\nu_+ - \nu_-) \approx \pi \frac{a^2}{2U_q} B, \quad (3.30)$$

making use of $\nu_+ \gg \nu_-$ and $\nu_+ \approx \nu_c$. The radial kinetic energy

$$E_{\text{rad}} \propto \nu_+^2 \rho_+^2(t) - \nu_-^2 \rho_-^2(t) \approx \nu_+^2 \rho_+^2(t) \quad (3.31)$$

changes with $2T_{\text{conv}}$.

3.2.2 Cooling of the ion motion

In 1991 Savard *et al.* introduced a new cooling technique for ions in a Penning trap, which is commonly used in Penning trap mass spectrometry of short-lived nuclides [Sava1991]. It is a relatively fast technique and can be efficiently applied to a wide range of nuclides. Cooling is achieved by collisions of the stored ions with atoms of a light buffer-gas, in most cases helium. Information going beyond the following brief discussion can be found in [Kret2008]. A velocity dependent damping force

$$\vec{F} = -\delta m \dot{\vec{r}} \quad (3.32)$$

is introduced, where m is the mass of the stored ion, $\dot{\vec{r}}$ its velocity, and δ the damping coefficient given by [Köni1995]

$$\delta = \frac{q}{m} \frac{1}{M_{\text{ion}}} \frac{p/p_{\text{N}}}{T/T_{\text{N}}}. \quad (3.33)$$

M_{ion} is the reduced ion mobility in the buffer-gas, and pressure p as well as temperature T are given in terms of their normal values ($p_{\text{N}} = 1013 \text{ mbar}$, $T_{\text{N}} = 300 \text{ K}$). Eq. (3.3) becomes

$$m\ddot{\vec{r}} = q \left(-\vec{\nabla}V + \dot{\vec{r}} \times \vec{B} \right) - \delta m \dot{\vec{r}}, \quad (3.34)$$

leading to the trajectories

$$\begin{aligned} x(t) &= \rho_+ e^{-\alpha_+ t} \cos(\omega'_+ t + \Phi_+) + \rho_- e^{-\alpha_- t} \cos(\omega'_- t + \Phi_-), \\ y(t) &= \rho_+ e^{-\alpha_+ t} \sin(\omega'_+ t + \Phi_+) + \rho_- e^{-\alpha_- t} \sin(\omega'_- t + \Phi_-), \\ z(t) &= \hat{z} e^{-\frac{\delta}{2} t} \cos(\omega'_z t + \Phi_z), \end{aligned} \quad (3.35)$$

with

$$\omega'_{\pm} = \omega_{\pm} \pm \left(\frac{\delta}{4} \right)^2 \frac{8\omega_z^2 + \delta^2}{(\omega_c^2 - 2\omega_z^2)^{\frac{3}{2}}}, \quad (3.36)$$

$$\omega'_z = \sqrt{\omega_z^2 - \left(\frac{\delta}{2} \right)^2}, \quad (3.37)$$

$$\alpha_{\pm} = \frac{\delta}{2} \left[1 \pm \left(1 + \frac{1}{8} \frac{8\omega_z^2 + \delta^2}{\omega_c^2 - 2\omega_z^2} \right) \right]. \quad (3.38)$$

The frequency shifts are usually neglected since they are very small and the buffer-gas cooling is only applied in a trap used for beam preparation. The pressure in the Penning trap used for the actual mass measurement is much lower, leading to a small damping coefficient. The amplitudes of all three eigenmotions change exponentially with time. While $\rho_+(t) = \rho_+ e^{-\alpha_+ t}$ and $\hat{z}(t) = \hat{z} e^{-(\delta/2)t}$ decrease, the magnetron amplitude $\rho_-(t) = \rho_- e^{-\alpha_- t}$ increases due to $\alpha_- < 0$ (here: $\omega_c \gg \omega_z$ is used). To achieve a reduction of the magnetron amplitude as well and, thus, to centre the ions in the trap, an azimuthal quadrupole excitation at the cyclotron frequency ν_c is used to couple modified cyclotron and magnetron motion (Sect. 3.2.1). Fig. 3.6(a) shows the calculated trajectory of an ion in the presence of a buffer gas. Since $\nu_+ \gg \nu_-$, the modified cyclotron amplitude decreases fast, whereas the increase of the magnetron radius is slow. By an additional coupling field, a centering of the ions in the trap can be achieved (Fig. 3.6(b)) depending on the excitation amplitude U_q , the excitation time T_q , and the buffer-gas pressure p [Sava1991]. This process is mass-selective due to the mass-dependence of the sideband frequency ν_c and is used to eject only ions of certain mass from a mixture in a first (purification) trap into a second Penning trap where the mass measurement is performed.

3.3 Ion detection techniques for mass spectrometry

Ion detection for Penning trap mass spectrometry means the measurement of the true cyclotron frequency (Eq. (3.7)) related to the mass. Two techniques are frequently used for this purpose which principally differ in the question if the ion is lost during the detection procedure or not (so-called non-destructive or destructive methods). Presently, only the Time of Flight-Ion Cyclotron Resonance (TOF-ICR) technique is applied

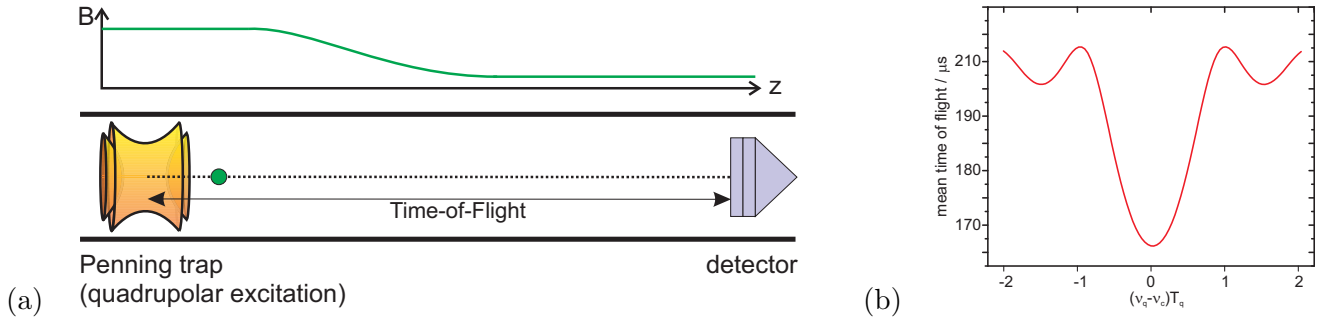


Figure 3.7: (a) Principle of the Time of Flight-Ion Cyclotron Resonance technique. Ions are probed in the trap by rf fields and sent through the B -field gradient (green line) towards an ion detector. (b) The calculated resonance profile shows the mean flight time as a function of the frequency detuning, with a minimum for $\nu_q = \nu_c$. The line shape is caused by the single finite-length pulse of the quadrupolar excitation.

for high-precision mass measurements on short-lived nuclides. The method is based on the determination of the flight time of the stored ions from the trap to a detector as a function of the frequency ν_q of a quadrupolar excitation field. The time of flight has a minimum in case the excitation frequency ν_q matches the true cyclotron frequency ν_c of the ion of interest (see Sect. 3.3.1). In Sect. 3.3.2 the detection of image currents induced by the oscillating ion in the trap electrodes is described, which enables measurements without the need to eject the ions from the trap. This technique in principal makes all eigenfrequencies of the ion motion as well as the true cyclotron frequency available. The obtained frequency is just dependent on the electrodes used for the current detection [Schw1989]. Since Penning trap mass spectrometers for short-lived nuclides besides TRIGA-TRAP are operated at room-temperature, the detection limit for the image current detection technique would be about $N \approx 100$ stored singly charged ions [Mars1998]. This so-called Fourier Transform-Ion Cyclotron Resonance (FT-ICR) technique originates from chemistry where it is used with larger numbers of simultaneously stored ions [Comi1974] and many different electrode geometries [Guan1995]. A modification of this technique reaching single-ion sensitivity is the detection system developed, e.g., at the g -factor experiment in Mainz [Häff2003]. A different scheme also based on the detection of image currents is applied at Penning trap mass spectrometers for stable nuclides, e.g. MIT-TRAP (now: FSU, Tallahassee, USA) [Rain2004, Shi2005] and the UW-MPIK-PTMS (Washington, USA, now: MPIK, Heidelberg, Germany) [Dyck2004, Pine2007], and in Penning traps for the determination of magnetic moments [Odom2004, D'Ur2005]. It will be applied at TRIGA-TRAP for the first time for mass measurements on short-lived nuclides.

3.3.1 Destructive time-of-flight detection

The radial motion of an ion in a Penning trap leads to a magnetic moment

$$\vec{\mu}(t) = \frac{1}{2} \int d^3r \left[\vec{r} \times \vec{j}(\vec{r}, \vec{r}'(t)) \right]. \quad (3.39)$$

With the current density $\vec{j}(\vec{r}, \vec{r}'(t)) = q \frac{d\vec{r}'(t)}{dt} \delta(\vec{r} - \vec{r}')$ of a moving point charge, one gets

$$\vec{\mu}(t) = \frac{q}{2} \vec{r}'(t) \times \frac{d\vec{r}'(t)}{dt} = -\frac{q}{2} (\rho_+^2 \omega_+ + \rho_-^2 \omega_- + \rho_+ \rho_- \omega_c \cos[(\omega_+ - \omega_-)t + \Phi_+ - \Phi_-]) \vec{e}_z. \quad (3.40)$$

In the last step, $\hat{z} = 0$ and Eq. (3.10) were used. Finally, the mean magnetic moment is given by

$$\vec{\mu} = \lim_{T \rightarrow \infty} \frac{1}{T} \int_0^T \vec{\mu}(t) dt = -\frac{q}{2} (\rho_+^2 \omega_+ + \rho_-^2 \omega_-) \vec{e}_z. \quad (3.41)$$

In case of a pure cyclotron motion with $\omega_+ \approx \omega_c$ one gets

$$\vec{\mu} = -\frac{E_{\text{rad}}}{B} \vec{e}_z \equiv -\bar{\mu} \vec{e}_z, \quad (3.42)$$

where E_{rad} is the radial energy of the ion motion. The radial amplitudes and, thus, the magnetic moment are dependent on the excitation frequency ν_q , the excitation time T_q , and the excitation amplitude U_q [Kret2007]. In case the ion is ejected from the Penning trap, the magnetic moment causes a force in the gradient of the magnetic field of the superconducting magnet (Fig. 3.7(a))

$$\vec{F} = -\vec{\nabla} (-\vec{\mu} \vec{B}) = -\bar{\mu} \frac{dB}{dz} \vec{e}_z, \quad (3.43)$$

directed towards a detector. Thus, the flight time to this detector is dependent on the amplitudes of the radial eigenmotions in the trap. Since $\omega_+ \gg \omega_-$, the modified cyclotron motion dominates the magnetic moment, leading to a much shorter time of flight for an ion in a pure cyclotron motion than for ions in a magnetron or any mixed radial motion.

This effect is used in a TOF-ICR measurement [Gräf1980]. After trapping of the ions, a dipolar magnetron excitation is applied to increase the magnetron amplitude ρ_- . In the next step, a quadrupolar excitation is applied to couple both radial eigenmotions (Sect. 3.2.1). Depending on the excitation parameters ν_q , U_q , and T_q , the magnetron motion is converted into cyclotron motion. U_q is fixed in a way that one full conversion from magnetron into cyclotron motion is performed within³ T_q (see Eq. (3.30)). The excitation frequency ν_q is detuned leading to a typical resonance shape for a single rectangular excitation pulse shown in Fig. 3.7(b). The global minimum in this resonance curve is located exactly at the sideband frequency $\nu_c = \nu_+ + \nu_-$ [Gräf1980]. The time of flight T from the trap to the detector as a function of the excitation frequency ν_q can be expressed by

$$T(\nu_q) = \int_0^{z_{\text{det}}} \sqrt{\frac{m}{2(E_0 - qV(z) - \bar{\mu}(\nu_q)[B(z) - B(0)])}} dz, \quad (3.44)$$

where E_0 is the initial kinetic energy of the ions in the trap⁴. $V(z)$ and $B(z)$ are the electric and magnetic fields along the ion path from the trap center at $z = 0$ to the detector position at z_{det} . The excitation time T_q is limited by the half-life of the ion of interest and the pressure inside the trap, but determines the mass resolving power \mathfrak{R}

$$\mathfrak{R} = \frac{m}{\Delta m} = \frac{\nu_c}{\Delta \nu_c} \approx \nu_c T_q, \quad (3.45)$$

where $\Delta \nu_c$ is the FWHM of the resulting cyclotron resonance. The last approximation has been done according to [Köni1995] and is given by the Fourier limit.

³After choosing an appropriate excitation time T_q , a quadrupolar excitation is applied resonantly to an ion of well-known mass ($\nu_q = \nu_c$). While detuning the excitation amplitude, a full conversion and, thus, a minimum in the flight time after ejection is obtained for the optimal value of U_q .

⁴The total initial energy in the trap consists of an initial axial energy E_{ax} , and the contributions from the electric ($qU(0)$) and magnetic fields ($\bar{\mu}B(0)$). All terms independent from ν_q are summarised in E_0 .

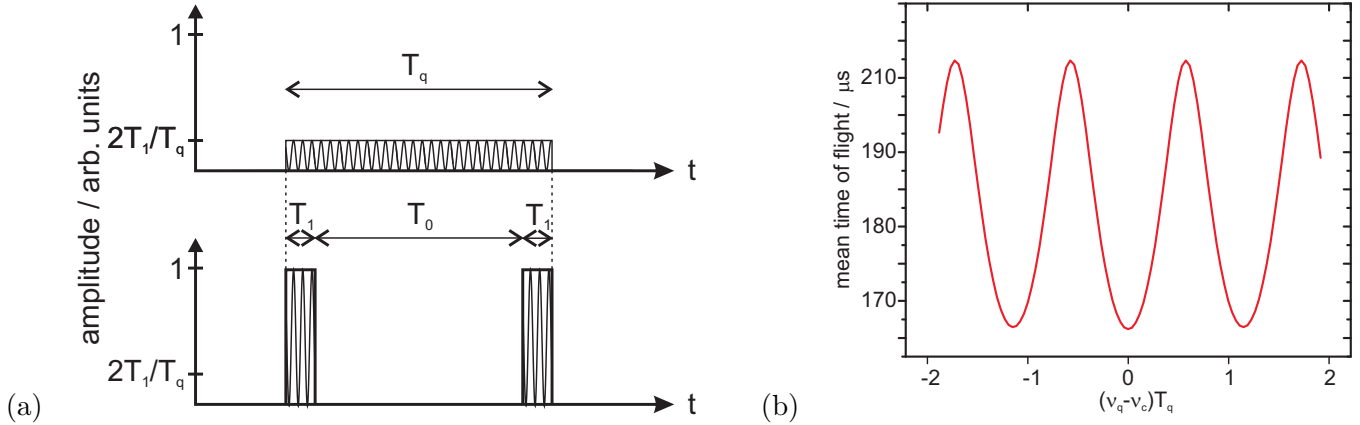


Figure 3.8: (a) Single finite-length pulse excitation and time-separated oscillatory fields. By introducing a waiting time T_0 and appropriately adjusting the amplitude to obtain one full conversion from pure magnetron into pure cyclotron motion in resonance, the line-width of the resonance curve detected with the Ramsey technique (b) is reduced and the sidebands pronounced in comparison to the single-pulse excitation (Fig. 3.7(b)).

A detailed description of the line-shape and the TOF-ICR technique can be found in [Köni1995]. To obtain the atomic mass from the frequency value ν_c , the magnetic field B has to be calibrated by an ion of well-known mass⁵, commonly alkali ions. The atomic mass of the nuclide under investigation is given by

$$\begin{aligned} m_{\text{atom}} &= r(m_{\text{ref}} - m_e) + m_e, \\ r &= \frac{\nu_{c,\text{ref}}}{\nu_c}, \end{aligned} \quad (3.46)$$

where $\nu_{c,\text{ref}}$ is the cyclotron frequency of the reference ion with mass m_{ref} , and m_e is the electron mass. Carbon cluster ions of different atom numbers C_n are ideally used as reference ions, since the atomic mass unit is defined as 1/12th of the mass of ^{12}C leading to an absolute mass measurement if the cluster binding energy is neglected. The latter approximation is justified within the present precision limit of Penning trap mass spectrometers. Moreover, carbon cluster ions are available over the entire nuclear chart, generating a 'mass comb' [Blau2002] for calibration purposes (see Sect. 3.4).

Recently, the Ramsey technique has been introduced to TOF-ICR measurements to reduce the line-width and, therefore, the uncertainty of the frequency measurement⁶ without the need to increase the excitation time [Geor2007a, Kret2007]. Improvements up to a factor of 3 have been demonstrated. The idea behind this technique is illustrated in Fig. 3.8(a). The single finite-length excitation pulse in the standard scheme is replaced by time-separated oscillatory fields, while the product between the amplitude and the total time the excitation field is applied is kept constant. As shown in the figure, the total excitation time T_q stays the same.

At TRIGA-TRAP the Ramsey excitation scheme will be used with two pulses as shown in Fig. 3.8(a), which leads to a reduction of the line-width of the centroid of about 36% in case of a total excitation time T_q of about 300 ms and a waiting time T_0 of about 240 ms [Geor2007b]. A typical resonance profile for this case is

⁵The ion species used to calibrate the magnetic field are from now on referred to as reference ions.

⁶Besides the reduction in line-width, the slope of the centroid in the resonance profile becomes steeper and the sidebands get deeper, which also improves the uncertainty of the fit.

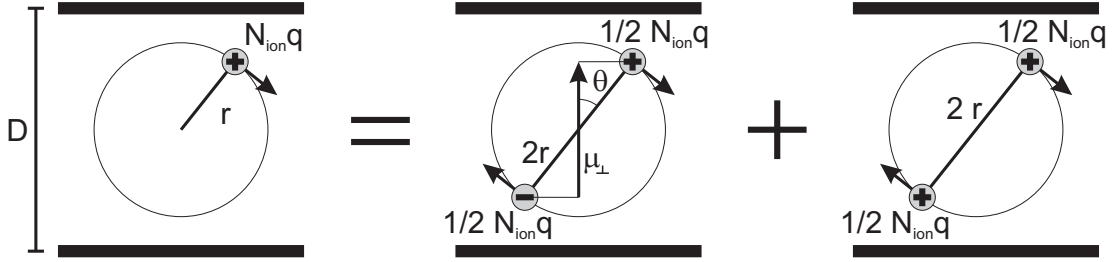


Figure 3.9: Simple model for the oscillating ion cloud between two infinitely long parallel plates. The rotating electric monopole is decomposed into an electric dipole and two electric monopoles, all rotating with the same velocity as the original monopole.

shown in Fig. 3.8(b), in comparison to the standard single-pulse excitation of $T_q = 300$ ms in Fig. 3.7(b). For more information about the Ramsey technique in Penning trap mass spectrometry the reader is referred to [Geor2007a, Geor2007b, Kret2007].

3.3.2 Non-destructive image current detection

An ion moving inside a Penning trap induces image charges on the surfaces of the electrodes, which can be detected using an appropriate circuit attached to those. Many references are available on the signal modelling for different trap geometries [Shoc1938, Dunb1984, Niko1985, Remp1986]. For a basic understanding, the model developed by Comisorow is briefly discussed here [Comi1978]. As shown in Fig. 3.9, the rotating monopole of the ion cloud is decomposed into a rotating dipole and two rotating monopoles. The detection electrodes are approximated by two infinitely extended parallel plates. The electric dipole moment μ_{\perp} normal to the plate surfaces is given by

$$\mu_{\perp} = N_{\text{ion}} q r \cos \theta, \quad (3.47)$$

leading to the charge density σ on the top plate of

$$\sigma = -\frac{\mu_{\perp}}{V} = -\frac{N_{\text{ion}} q r}{V} \cos \theta, \quad (3.48)$$

where $V = AD$ is the total volume between both plates of surface A and distance D . The charge induced in the top plate is,

$$Q(t) = \sigma(t)A = -\frac{N_{\text{ion}} q r}{D} \cos(2\pi\nu t + \phi), \quad (3.49)$$

where the angle has been expressed in terms of the ion frequency ν . The induced image current is

$$i_{\text{ion}}(t) = 2\pi\nu \frac{N_{\text{ion}} q r}{D} \sin(2\pi\nu t + \phi) \quad (3.50)$$

with an effective value of [Schw1991]

$$i_{\text{eff,ion}} = \sqrt{2\pi} N_{\text{ion}} \frac{r}{D} q \nu. \quad (3.51)$$

The two monopoles left from the decomposition of the original monopole do not contribute to the image current since their signals cancel each other. In Eq.(3.50) it can be seen that the image current signal

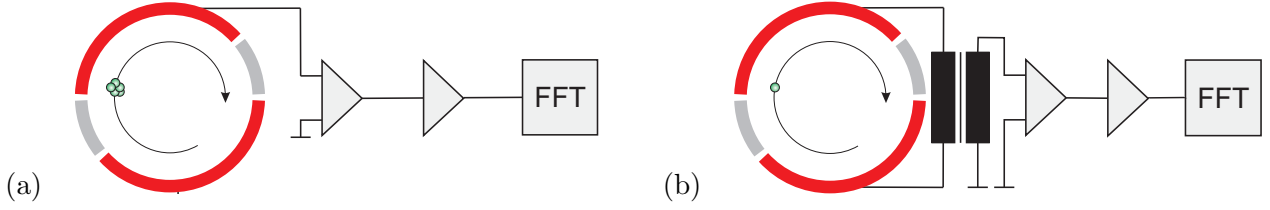


Figure 3.10: Principle of the image current detection as performed at TRIGA-TRAP. The signal induced in two 140°-segments of the ring-electrode can either be directly fed to an amplifier as done in the broad-band detection scheme (a), or a high- Q inductor can be used to reach single-ion sensitivity in the narrow-band mode (b). Several amplifier stages process the signal before the Fourier Transformation (FFT) is performed.

contains the ion frequency ν , which can be revealed by a Fourier Transformation. The signal strength scales with the charge state q , the number of ions N_{ion} and the radius of the ion motion r in terms of the spacing between the detection electrodes⁷ D .

Typically, the ions are prepared in a pure modified cyclotron motion with $(r, \nu) = (\rho_+, \nu_+)$ leading to the problem that two reference measurements are needed to calibrate the magnetic field B and the trapping potential V_0 . From Eq. (3.12) one gets

$$2\nu_+ = \frac{q}{m}a + \sqrt{\left(\frac{q}{m}\right)^2 a^2 - 4\frac{q}{m}b} \quad (3.52)$$

with $a = B/(2\pi)$ and $b = V_0/(8\pi^2 d^2)$. Some standard transformations lead to

$$\frac{q}{m} = \frac{\nu_+^2}{\nu_+ a + b}. \quad (3.53)$$

Thereby, the mass can be determined by the measurement of the modified cyclotron frequency ν_+ , if two reference measurements with different reference ions of masses $(m_{\text{ref},1}, m_{\text{ref},2})$ and modified cyclotron frequencies $(\nu_{+,1}, \nu_{+,2})$ are performed to calibrate B and V_0 before and after the measurement of the ion of interest. The atomic mass of the nuclide of interest is then given by

$$m_{\text{atom}} = \left[\frac{\nu_{+,1}^2 (\nu_+ - \nu_{+,2})}{\nu_{+,1}^2 (\nu_{+,1} - \nu_{+,2})} (m_{\text{ref},1} - m_e) + \frac{\nu_{+,2}^2 (\nu_{+,1} - \nu_+)}{\nu_{+,2}^2 (\nu_{+,1} - \nu_{+,2})} (m_{\text{ref},2} - m_e) \right] + m_e. \quad (3.54)$$

An exact calculation of the image charges induced by the ion motion in the trap electrodes can be carried out by the Green's-function formalism [Gros1991]. So far, Green's functions for the tetragonal as well as the cylindrical Penning traps have been found. Recently, a Green's function solution to the image charge problem in a hyperbolic trap as used at TRIGA-TRAP has been developed, with which it is shown that the sideband frequency $\nu_c = \nu_+ + \nu_-$ can be directly determined by the non-destructive detection technique [Kret2009].

Signal-to-noise ratio for the broad-band image current detection:

Fig. 3.10(a) shows the principle of the broad-band image current detection system used at the TRIGA-TRAP

⁷The approximation of infinitely extended parallel plates can be used to calculate the image current in segments of a ring electrode by modifying the spacing parameter D .

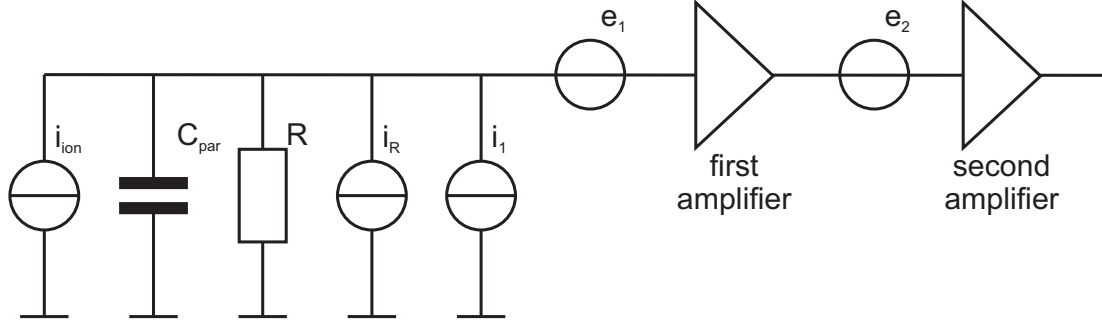


Figure 3.11: Equivalent circuit model of the broad-band FT-ICR detection system in the TRIGA-TRAP purification trap with two low-noise amplifiers. C_{par} is the parasitic capacitance due to the trap and the input field-effect transistor of the first amplifier with input resistance R . i_R is the thermal noise due to the resistance, i_1 the current noise of the first amplifier, and e_k ($k = 1, 2$) the corresponding voltage noise for each amplifier. i_2 is neglected.

purification trap. Here, one 140° -segment of the ring electrode is AC wise grounded while the opposite segment is connected to an ultra-low noise cryogenic amplifier (for details see Sect. 4.6). The equivalent circuit including the signal and noise sources is displayed in Fig. 3.11 [Repp2008]. The signal current i_{ion} generates a voltage drop across the impedance $Z(\omega)$, which is formed by the parasitic capacitance of the trap and the first field-effect transistor in the amplifier chain C_{par} , as well as the input resistance of the first amplifier⁸ R :

$$Z(\omega) = \frac{1}{\frac{1}{R} + \hat{i}\omega C_{\text{par}}}. \quad (3.55)$$

The thermal noise (Johnson noise) [John1928, Nyqu1928] due to the present resistance is given by $i_R = \sqrt{4k_B T/R}$. Together with the gain G_k ($k = 1, 2$) and the noise sources of both amplifiers, the signal-to-noise ratio is given by (according to [Spie2005])

$$\left(\frac{S}{N}\right)_{\text{broad-band}} = \frac{i_{\text{ion}}|Z(\omega)|G_1}{\sqrt{[(i_R^2 + i_1^2)|Z(\omega)|^2 + e_1^2]G_1^2 + e_2^2}} \Delta\nu, \quad (3.56)$$

where $\Delta\nu$ is the band-width of the detection system. For a realistic case with $R \gg 1/(\omega C_{\text{par}})$ Eq. (3.56) simplifies to

$$\left(\frac{S}{N}\right)_{\text{broad-band}} = \frac{i_{\text{ion}}G_1}{\sqrt{\left[\left[\frac{4k_B T}{R} + i_1^2 + \omega^2 C_{\text{par}}^2 e_1^2\right]G_1^2 + \omega^2 C_{\text{par}}^2 e_2^2\right]} \Delta\nu}. \quad (3.57)$$

In this calculation, the current noise of the second amplifier has been neglected. The voltage noise e_2 can be neglected as well, in case the gain G_1 is in the order of 10 or larger.

Signal-to-noise ratio for the narrow-band image current detection:

The narrow-band image current detection differs from the case discussed above principally in the way the current signal is read out. To reduce the noise background, a tuned circuit is used as a very narrow band-pass filter around the expected ion frequency (Fig. 3.10(b)). The equivalent circuit is shown in Fig. 3.12. It has

⁸Note: $\hat{i} = \sqrt{-1}$ is used not to get confused with the current i .

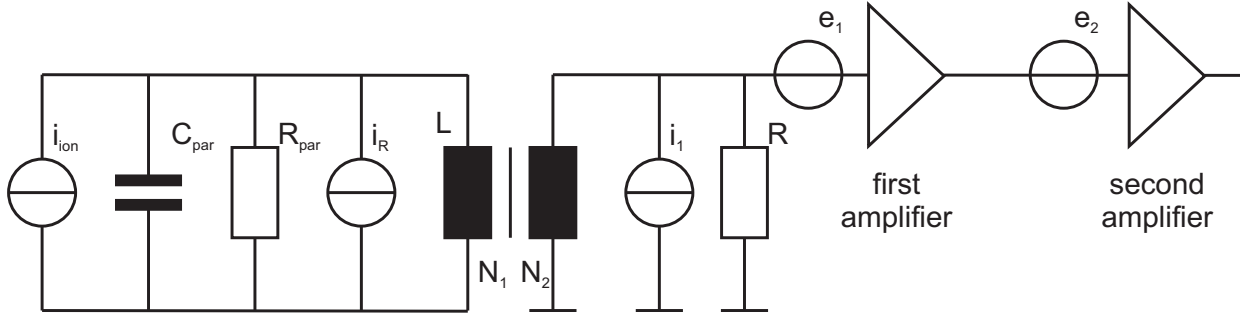


Figure 3.12: Equivalent circuit model of the narrow-band FT-ICR detection system in the TRIGA-TRAP precision trap with a high- Q inductor and two low-noise amplifiers. C_{par} is the parasitic capacitance due to the trap, R_{par} is the resistance in resonance of the tuned circuit formed by C_{par} and L . R is the input resistance of the first amplifier. i_R represents the thermal noise, i_1 the current noise of the first amplifier, and e_k ($k = 1, 2$) the corresponding voltage noise for each amplifier. N_1 and N_2 are the winding numbers of the transformer coils. i_2 is neglected again.

to be mentioned that the capacitance C_{par} and the resistance R_{par} are no hardware components but due to imperfections and parasitic effects. The absolute value of the impedance $|Z(\omega)|$ with

$$Z(\omega) = \frac{1}{\frac{1}{R_{\text{par}}} + \hat{i} \left(\omega C_{\text{par}} - \frac{1}{\omega L} \right)} \quad (3.58)$$

of such a tuned circuit is displayed in Fig. 3.13, showing a sharp maximum around the frequency⁹

$$\omega_{LC} = \frac{1}{\sqrt{LC_{\text{par}}}}. \quad (3.59)$$

The quality factor Q is defined by

$$Q \equiv \frac{\omega_{LC}}{\Delta\omega}, \quad (3.60)$$

where $\Delta\omega$ is the width within which the voltage across the LC circuit drops to $1/\sqrt{2}$ of the maximum value. Assuming a constant current amplitude this leads to

$$\begin{aligned} \left| \frac{Z(\omega)}{Z(\omega_{LC})} \right| &= \frac{1}{R_{\text{par}} \sqrt{\frac{1}{R_{\text{par}}^2} + \left(\omega C_{\text{par}} - \frac{1}{\omega L} \right)^2}} \\ &= \frac{1}{\sqrt{2}} \\ \Rightarrow \frac{1}{R_{\text{par}}^2} &= \left(\omega C_{\text{par}} - \frac{1}{\omega L} \right)^2. \end{aligned} \quad (3.61)$$

⁹The relative frequency shift $\Delta\omega_{LC}/\omega_{LC}$ of the damped tuned circuit has been estimated and is in the order of a few times 10^{-6} . Thus, a shift is neglected.

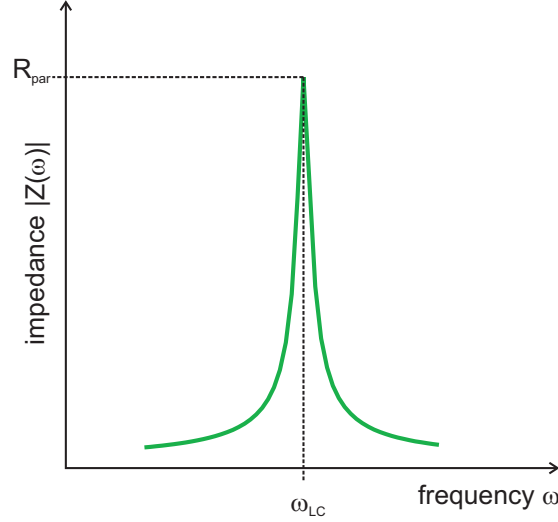


Figure 3.13: Impedance of a tuned circuit used for narrow-band FT-ICR detection. This type of frequency response can be used as a band-pass filter around the expected ion frequency to suppress noise.

A Taylor expansion around ω_{LC} of the right term to second order yields

$$\begin{aligned}
 \frac{1}{R_{\text{par}}^2} &= 4C_{\text{par}}^2 (\omega - \omega_{LC})^2 \\
 \frac{1}{2C_{\text{par}}R_{\text{par}}} &= \pm (\omega - \omega_{LC}) \\
 \omega_{1,2} &= \omega_{LC} \pm \frac{1}{2C_{\text{par}}R_{\text{par}}} \\
 \Delta\omega &= \omega_1 - \omega_2 = \frac{1}{C_{\text{par}}R_{\text{par}}}.
 \end{aligned} \tag{3.62}$$

This leads to the resistance of the tuned circuit in resonance, expressed by the Q -value and the parasitic capacitance:

$$|Z(\omega_{LC})| = R_{\text{par}} = \frac{Q}{\omega_{LC}C_{\text{par}}}. \tag{3.63}$$

Now the effective parallel resistance responsible for the voltage drop of the ion current can be calculated. It is a parallel circuit of the tuned circuit resistance $|Z(\omega_{LC})|$ and the input resistance R of the first amplifier via the transformer. Therefore, a transformation coefficient $\gamma = k \times (N_2/N_1) \times \sqrt{l_1/l_2}$ has to be introduced depending on the winding ratio (N_2/N_1) and the length ratio (l_2/l_1) between both coils. k is a constant specifying the coupling between primary and secondary side of the transformer. The effective parallel resistance for frequencies close to ω_{LC} is

$$\hat{R}_p \approx \frac{Q}{\omega C_{\text{par}}} \frac{\frac{R}{\gamma^2}}{\frac{Q}{\omega C_{\text{par}}} + \frac{R}{\gamma^2}}. \tag{3.64}$$

The signal-to-noise ratio for the narrow-band detection circuit as shown in Fig. 3.12 is given by

$$\left(\frac{S}{N}\right)_{\text{narrow-band}} = \frac{i_{\text{ion}} \hat{R}_p \gamma G_1}{\sqrt{\left([4k_B T \hat{R}_p \gamma^2 + e_1^2] G_1^2 + e_2^2\right) \Delta\nu}}, \tag{3.65}$$

where all quantities are defined similar to Eq. (3.57). As one can see from Eqs. (3.64) and (3.65), the main parameters to optimise the signal-to-noise ratio are a low temperature T , a high quality factor Q , an ultra-low voltage noise e_1 of the first amplifier, and the detection bandwidth $\Delta\nu$. Therefore, a narrow-band image current detection system is always connected to a cryogenic Penning trap and has a superconducting inductor together with an amplifier at 4 K. As an example, the experiment to determine the g -factor of the proton at the University of Mainz uses a similar cryogenic detection system [Krac2007].

Mass resolving power of the image current detection:

The mass resolving power \mathfrak{R} defined in Eq. (3.45) will be calculated in the following, requiring the line-width $\Delta\nu_c$ of the Fourier spectrum of the ion current i_{ion} (Eq. (3.50)). A current transient of length T yields a frequency spectrum given by

$$\begin{aligned} I(\omega) &= \int_{-\infty}^{+\infty} dt i_{\text{ion}}(t) \Theta(t) \Theta(t-T) \\ &= \hat{i} \frac{N_{\text{ion}} q r}{D} \left[\frac{\sin([\omega - \omega_{\text{ion}}]T/2)}{\omega - \omega_{\text{ion}}} e^{-\hat{i}(\omega - \omega_{\text{ion}})T/2} - \frac{\sin([\omega + \omega_{\text{ion}}]T/2)}{\omega + \omega_{\text{ion}}} e^{-\hat{i}(\omega + \omega_{\text{ion}})T/2} \right], \end{aligned} \quad (3.66)$$

where the phase ϕ of the ion motion has been neglected. Taking only positive frequencies $\omega > 0$ into account, the absolute value is

$$|I(\omega)| = \frac{N_{\text{ion}} q r}{D} \left| \frac{\sin([\omega - \omega_{\text{ion}}]T/2)}{\omega - \omega_{\text{ion}}} \right|. \quad (3.67)$$

The frequency $\omega > \omega_{\text{ion}}$, where the amplitude of the spectrum is reduced to 1/2 of the maximum (which is $|I(\omega_{\text{ion}})| = N_{\text{ion}} q r / D \times T/2$), can be found via

$$\begin{aligned} \frac{\sin([\omega - \omega_{\text{ion}}]T/2)}{\omega - \omega_{\text{ion}}} &= \frac{T}{4} \\ \sin([\omega - \omega_{\text{ion}}]T/2) &= \frac{T}{4} (\omega - \omega_{\text{ion}}). \end{aligned} \quad (3.68)$$

With $\sin(x) \approx x - x^3/6$, one gets

$$\frac{T}{2} (\omega - \omega_{\text{ion}}) \approx \sqrt{3}. \quad (3.69)$$

Thus, the FWHM of the centroid in the frequency spectrum is $\Delta\omega \approx 4\sqrt{3}/T$, or in terms of the measurable frequency

$$\Delta\nu \approx \frac{1.1}{T}. \quad (3.70)$$

So the mass resolving power of the non-destructive image current detection technique is

$$\mathfrak{R} = \frac{m}{\Delta m} = \frac{\nu_c}{\Delta\nu_c} \approx 0.9\nu_c T. \quad (3.71)$$

3.3.3 Comparison between destructive and non-destructive ion detection

From the discussion above the question might arise which of the two basic detection techniques is the better one for precision Penning trap mass spectrometry. Since Penning traps are widely applied for high-precision mass measurements in each region of the nuclear chart with differing demands on the sensitivity of the

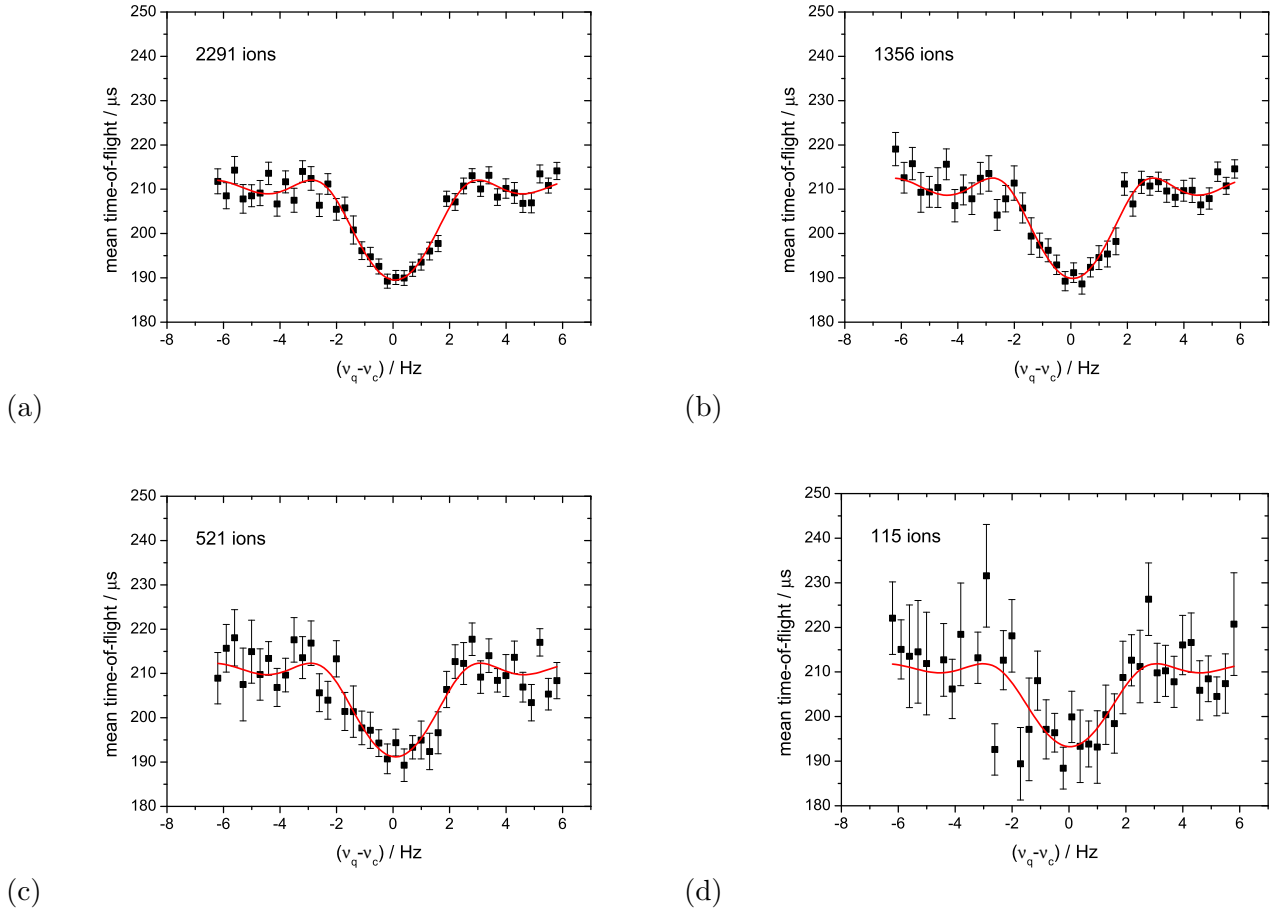


Figure 3.14: Illustration of the dependence of the statistical uncertainty on the number of recorded ions. The data showing spectra of $^{12}\text{C}_{20}^+$ ions with $T_q = 300$ ms taken at TRIGA-TRAP is evaluated with (a) 2291, (b) 1356, (c) 521, and (d) 115 ions in the spectrum. The solid lines are fits of the theoretical line shape [Köni1995]. The uncertainties of the centre frequency $\nu_c = 447838$ Hz are (a) $\delta\nu_c = 0.053$ Hz, (b) $\delta\nu_c = 0.071$ Hz, (c) $\delta\nu_c = 0.113$ Hz, and (d) $\delta\nu_c = 0.223$ Hz.

detection system and the resulting mass uncertainty, there cannot be a general answer. The applicability of one or the other technique depends on the nuclide of interest and the rate with which it can be produced. The mass resolving power of both techniques depends only on the observation time T and the cyclotron frequency of the ion of interest ν_c as it can be seen from Eqs. (3.45) and (3.71). Observation time means the total excitation time in case of a time-of-flight measurement, and the transient length if the FT-ICR technique is chosen. The statistical uncertainty is inversely proportional to the mass resolving power and the squareroot of the number of ions N_{ion} in a time-of-flight resonance [Boll2001]

$$\left(\frac{\delta m}{m}\right)_{\text{stat}} \propto \frac{1}{\Re\sqrt{N_{\text{ion}}}}. \quad (3.72)$$

The proportionality constant has been found at ISOLTRAP to be close to unity [Kell2003]. For FT-ICR measurements, the ion number can be replaced by the number of transients. Here, it has to be still experimentally verified that the proportionality constant is one, but no change to the TOF technique is expected.

As already mentioned above, the image current detection technique in high-precision mass spectrometry is presently only used for stable nuclides in so called closed systems. Here, the ion production region and the trap are located within the same rather small vacuum chamber. Very low production rates of interesting nuclides on the neutron-rich side of the valley of stability as well as of transuranium nuclides demand for the application of the image current detection technique for mass measurements on short-lived species as well if the half-life of the nuclide of interest is still in the order of seconds. A typical TOF spectrum for $^{12}\text{C}_{20}^+$ ions taken at TRIGA-TRAP is shown in Fig. 3.14, where it can be seen that the uncertainty of the centroid in the fit to a spectrum with less than 100 ions cannot reach the 10^{-7} range. Dealing with production rates of less than one per minute and taking into account a typical overall efficiency of 1-5%, a TOF-ICR measurement is no longer feasible since this would demand for extended measurement durations of more than a day. The conditions of the experimental setup cannot be stabilised to the required level for such a long time frame to still reach the required mass precision. Therefore, the non-destructive image current detection technique providing a full spectrum with a single ion can be used. Repeated measurements on the same trap content are possible until the nuclide of interest decays. Thus, the FT-ICR technique is ideally suited for high-precision mass spectrometry on transuranium isotopes, which often have half-lives in the order of minutes or much longer.

3.4 Carbon clusters as reference masses

The previous discussion showed the need for reference ions to calibrate the magnetic field B and the electric potential V_0 for TOF-ICR and FT-ICR measurements. In order not to limit the uncertainty of the resulting mass value, the uncertainty in the mass of the reference ions has to be about 1 ppb or less. This condition is fulfilled for only 23 of more than 3200 nuclides [Waps2003b]. In Penning-trap mass spectrometry on short-lived nuclides commonly alkali ions are used as references (Tab. 4.2). Recently, the use of carbon cluster ions $^{12}\text{C}_n^+$ has been introduced, since the atomic mass unit is defined by 1/12 of the mass of ^{12}C [Blau2002]. Neglecting the binding energy of the atoms in the cluster, not only direct but absolute mass measurements are possible like this. In the following discussion it will be shown that reference ions with masses as close as possible to the mass of the ion of interest minimise systematic shifts. Thus, the measurement of a mass doublet is favourable [Lind1991].

Mass independent frequency shifts $\Delta\nu_c$ introduced by imperfections of the electric (Eqs. (3.22,3.23)) and misalignments of the magnetic field (Eq. (3.27)) lead to a shift of the resulting mass. Starting from Eq. (3.46)) the mass shift in case of a TOF-ICR measurement can be calculated as follows:

$$\begin{aligned}\Delta m_{\text{atom}} &= \frac{\nu_{c,\text{ref}} + \Delta\nu_c}{\nu_c + \Delta\nu_c} (m_{\text{ref}} - m_e) - (m_{\text{atom}} - m_e) \\ &\approx \frac{\Delta\nu_c}{\nu_c + \Delta\nu_c} (m_{\text{ref}} - m_{\text{atom}}).\end{aligned}\quad (3.73)$$

Thus, the relative mass shift

$$\begin{aligned}\frac{\Delta m_{\text{atom}}}{m_{\text{atom}}} &\approx \frac{\Delta\nu_c}{m_{\text{atom}}\nu_c} (m_{\text{ref}} - m_{\text{atom}}) \\ &\propto (m_{\text{ref}} - m_{\text{atom}})\end{aligned}\quad (3.74)$$

is proportional to the difference between the reference mass and the mass of the ion of interest [Boll1996]. Of course, the proportionality is also given for the relative shift of the frequency ratio $\Delta r/r$ (see Eq. (3.46))

which can be seen as follows.

$$\begin{aligned}
 \Delta r &= \frac{\nu_{c,\text{ref}} + \Delta\nu_c}{\nu_c + \Delta\nu_c} - \frac{\nu_{c,\text{ref}}}{\nu_c} \\
 &= \frac{\Delta\nu_c (\nu_c - \nu_{c,\text{ref}})}{\nu_c (\nu_c + \Delta\nu_c)} \\
 &\approx \frac{\Delta\nu_c}{\nu_c^2} (\nu_c - \nu_{c,\text{ref}}) \\
 &\propto r (m_{\text{ref}} - m_{\text{atom}}).
 \end{aligned} \tag{3.75}$$

In case of an FT-ICR measurement a similar calculation starting from Eq. (3.54) with $\nu_+ \approx \nu_c$ leads to [Smor2008]

$$\Delta m_{\text{atom}} = -\frac{\Delta\nu_c^2}{(m_{\text{atom}} - m_e)(\nu_c + \Delta\nu_c)^2} (m_{\text{atom}} - m_{\text{ref},1}) (m_{\text{atom}} - m_{\text{ref},2}), \tag{3.76}$$

$$\tag{3.77}$$

$$\frac{\Delta m_{\text{atom}}}{m_{\text{atom}}} \approx -\frac{\Delta\nu_c^2}{m_{\text{atom}}^2 \nu_c^2} (m_{\text{atom}} - m_{\text{ref},1}) (m_{\text{atom}} - m_{\text{ref},2}) \tag{3.78}$$

$$\propto (m_{\text{atom}} - m_{\text{ref},1}) (m_{\text{atom}} - m_{\text{ref},2}). \tag{3.79}$$

Carbon clusters $^{12}\text{C}_n^+$ of different atom number n provide reference ions over the entire chart of nuclides in steps of 12 mass units (Fig. 3.15). Thus, the maximum difference $m_{\text{ref}} - m_{\text{atom}}$ is 6 u. Especially for actinoids and transactinoids, no other reference nuclide heavier than ^{133}Cs is available besides carbon clusters. The proportionality constants in (3.74), (3.75) and (3.79) can be experimentally determined to allow for a correction of this mass dependend shift.

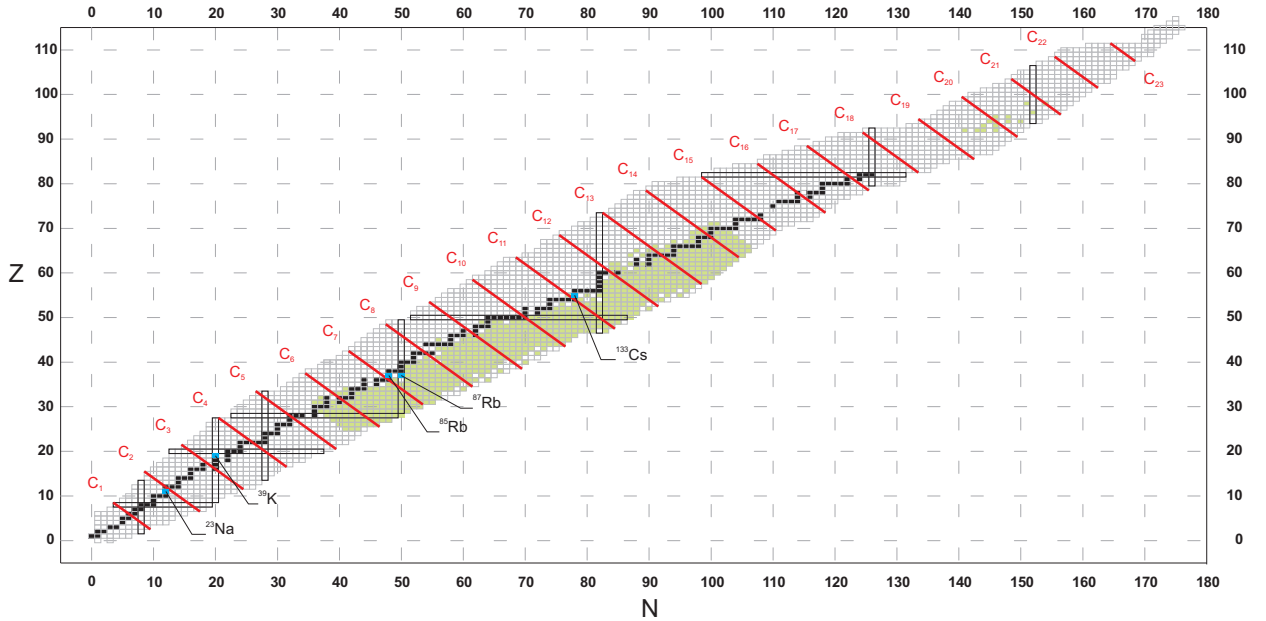


Figure 3.15: (Colour) Nuclear chart of all presently known nuclides [Audi2003]. Stable isotopes are coloured in black. Isobaric lines of carbon clusters are marked by red lines indicating the availability of reference masses over the entire chart. In addition, commonly used alkali reference nuclides are marked in blue. The nuclides of interest for TRIGA-TRAP are coloured in green.

Part II

Experimental Setup

4 The double-Penning trap mass spectrometer

TRIGA-TRAP

In 2008, the TRIGA-SPEC project was launched at the research reactor TRIGA Mainz for the investigation of ground-state properties of neutron-rich nuclides and actinoides [Kete2008]. The experimental setup consists of a section for the production of the radioactive ion beams, the collinear laser spectroscopy beamline TRIGA-LASER, and the double-Penning trap system TRIGA-TRAP (see Fig. 4.1). The research reactor TRIGA Mainz provides access to neutron-rich nuclides, which partly are not available at other radioactive beam facilities to date. Thereby, the border of knowledge on nuclear ground state properties can be pushed further out towards the neutron drip-line. The neutron-rich nuclides are produced by thermal-neutron induced fission of actinoids in a target close to the reactor core. The radioactive beam production will be discussed in Sect. 4.1, including ionisation, mass separation, bunching, and deceleration of the continuous beam.

Mass spectrometry is performed by the measurement of the true cyclotron frequency (Eq. (3.7)) of a charged particle stored in a Penning trap. At TRIGA-TRAP two techniques are available for this purpose (see Sect. 4.6), which can be applied on a wide range of nuclides: starting from very short-lived ones with production rates higher than a few per second, to nuclides with half-lives in the order of seconds which are produced in amounts of less than one particle per minute. The mass spectrometry part is discussed in detail in this chapter.

Collinear laser spectroscopy (CLS) is a well-established tool for high-precision in-flight laser spectroscopy on short-lived nuclides [Kauf1976, Anto1978]. The TRIGA-LASER setup installed for this purpose is similar to COLLAPS at CERN [Neug1981] and to the laser spectroscopy experiment at Jyväskylä [Bill2005]. A fast radioactive or stable ion beam at energies typically between 30 and 60 keV is overlapped with a laser in collinear or anti-collinear geometry. This concept allows for the use of fixed frequency lasers, since the ion velocity can be varied to obtain an appropriate Doppler shift to tune the ionic transitions into resonance with the laser light. The ions can also be neutralised in an alkali vapour to perform spectroscopy on the neutral atoms depending on whether the transitional frequencies are more favourable for the atom or the ion. At TRIGA-LASER fluorescence detection will be applied to determine the isotope shifts and hyperfine splittings of the nuclide of interest. The spectroscopic resolution also benefits from a compression of the velocity spread in CLS experiments. Measured isotope shifts and hyperfine structure lead to the determination of differences of charge radii in isotopic chains, nuclear spins, magnetic dipole and electric quadrupole moments. For more information, the reader is referred to the literature [Otte1989, Klug2003].

Besides mass measurements and laser spectroscopy on neutron-rich fission products, experiments can be performed as well on available actinoid samples. In addition, both parts of the project, TRIGA-TRAP and TRIGA-LASER, serve as well as test benches for the development of new techniques, which can be applied later at other future facilities like MATS and LaSpec at FAIR (GSI Darmstadt) [Rodr2010].

The following sections concentrate on the parts relevant for mass spectrometry including the production of radioactive beams at TRIGA. The main focus is put on the new developments at TRIGA-TRAP including

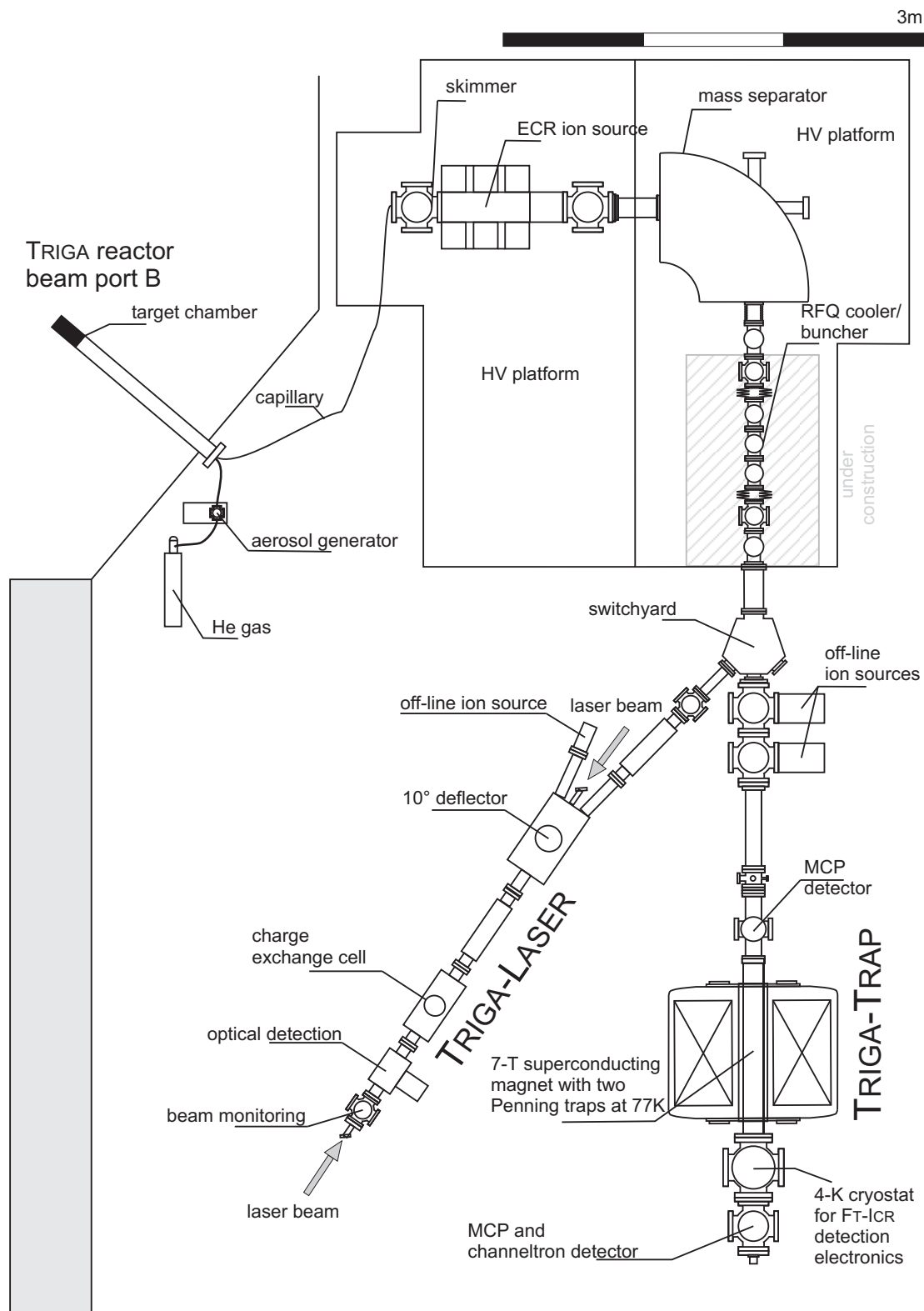


Figure 4.1: Layout of the final TRIGA-SPEC setup. The fission products from an actinoid target at the reactor core are transported to an ECR ion source by a gas-jet system. After a mass separator, an RFQ cooler and buncher will be installed to provide low-emittance ion bunches either for the mass spectrometer TRIGA-TRAP, or for the collinear laser spectroscopy beamline TRIGA-LASER. For details see text.

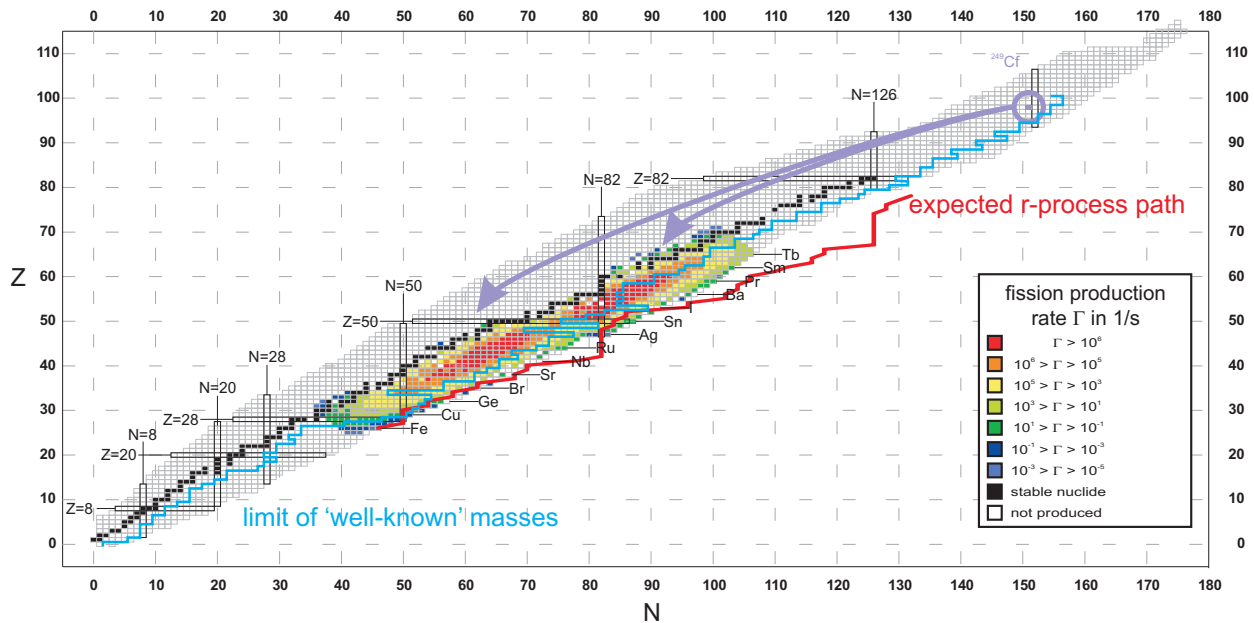


Figure 4.2: (Colour) Production rates of fission nuclides with a $300 \mu\text{g}$ ^{249}Cf target and a neutron flux of $1.8 \times 10^{11} \text{n}/(\text{cm}^2\text{s})$ as obtained at TRIGA in the steady state mode. The present mass uncertainty δm of all nuclides below the blue line is larger than 10 keV [Audi2009]. The expected r-process path has been taken from [Cowa2004]. For details see text.

a laser-ablation ion source for off-line measurements and mass calibration as well as a new non-destructive detection system with single-ion sensitivity. It will be shown that TRIGA-TRAP is a unique system among the Penning trap mass spectrometers worldwide.

4.1 The TRIGA reactor and extraction of fission products

The research reactor TRIGA Mainz offers unique possibilities for fundamental research in physics and chemistry [Eber2000, Hamp2006]. A special fuel element composed of a uranium-zirconium-hydrogen alloy with about 20% ^{235}U enrichment enables pulsed operation of the reactor. Each of the 76 cylindrical elements has a diameter of 3.5 cm and a length of 72.2 cm. They are placed in a 20m^3 light water tank surrounded by the concrete biological shield. In case the control rods are promptly removed to obtain a pulse, the rapid temperature increase reduces the moderation capability of the hydrogen and, thus, leads to a self-regulation of the fission rate. The thermal peak power of 250 MW is reached within a pulse duration of about 30 ms. In steady-state operation, a thermal power of 100 kW is obtained. The neutron flux at beam port B, where TRIGA-SPEC is located, amounts to about $1.8 \times 10^{11} \text{n}/(\text{cm}^2\text{s})$. Pulsed operation with about three orders of magnitude higher flux enhances the production of very short-lived neutron-rich fission products.

The production rates for a ^{249}Cf target have been calculated using the yields for thermal-neutron induced fission from [Engl1993], assuming a target mass of $300 \mu\text{g}$ and the above given neutron flux. The results are displayed in Fig. 4.2. The masses of all nuclides below the blue line have not been determined with an uncertainty better than 10 keV so far [Audi2009]. Fig. 4.2 clearly indicates that at TRIGA very neutron-rich nuclides are available with comparably large production rates. Some nuclides that are part of the expected

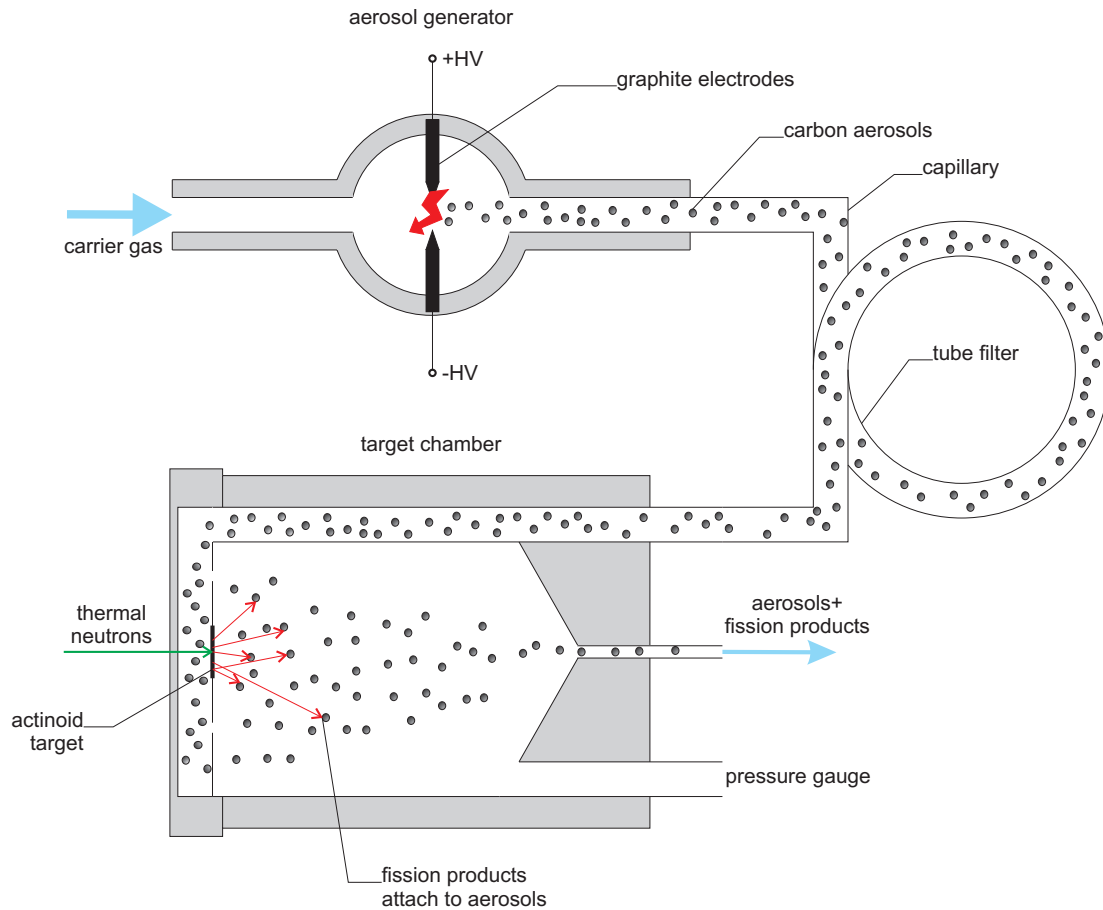


Figure 4.3: Gas-jet system for the extraction of fission products. A carrier gas (helium or argon) is flushed through the aerosol generator. Carbon nano-particles are created in a spark discharge between two graphite electrodes [Eiba2010]. The carrier gas loaded with the aerosols is guided to the target chamber. Thermal neutrons originating from the reactor core induce fission of an actinoid target. The fission products thermalise in the gas atmosphere at a pressure of about 1.7 bar and attach to the aerosols, by which they are transported to the ion source. For details see text.

r-process path [Cowa2004] can be reached as well, especially around the magic neutron numbers $N = 50$ and $N = 82$. Other targets with ^{235}U or ^{239}Pu can be used as well, leading to a shift of the two fission peaks towards lighter nuclides. A comparison of the fission yields for ^{235}U and ^{249}Cf can be found in [Eiba2009].

For the extraction of fission products a gas-jet arrangement is used, which is quite common in nuclear chemistry applications [MacF1969]. The setup used for TRIGA-SPEC is shown in Fig. 4.3. A carrier gas (helium or argon) is flushed through the aerosol generator, consisting of two graphite electrodes. Thereby, carbon nano-particles with a certain size distribution are produced and guided through a capillary to the target chamber. Here, the fission products thermalise in the gas atmosphere at a pressure of about 1.7 bar and attach to the carbon particles. Fission products and nanoparticles are then guided to the ion source through another capillary. Detailed investigations on the generation of the carbon aerosols and the transport properties of the gas-jet system for fission products under different conditions have been recently performed [Eiba2009].

nuclide	half-life	extraction rate $k_{\text{extr}}^{\text{ind}}/(10^3/s)$	mass uncertainty $\delta m / \text{keV}$	ref. for mass value
^{102}Mo	11.3 min	1.4	10	[Hage2006]
^{103}Mo	67.5 s	2.2	10	[Hage2006]
^{104}Mo	60.0 s	2.5	10	[Hage2006]
^{105}Mo	35.6 s	1.5	10	[Hage2006]
^{104}Tc	18.2 min	0.2*	25	[Audi2010]
^{105}Tc	7.6 min	0.1	35	[Audi2010]

Table 4.1: Candidates for mass measurements on neutron-rich fission products, which have been identified by γ -spectroscopy in an off-line setup [Eiba2009]. The target consisted of $310 \mu\text{g } ^{235}\text{U}$ and was covered with a $13 \mu\text{m}$ thick aluminium foil. The rate of particles per second extracted by the gas-jet system has been measured for $^{104}\text{Tc}^*$ and calculated for the remaining nuclides assuming a constant transport efficiency. Half-lives taken from [Reus1983].

Important quantities for the characterisation of the extraction system are the transport time and efficiency since both limit the available nuclides for experiments at TRIGA-SPEC. Using the pulsed mode of the TRIGA reactor, the transport time under test conditions has been determined to be $390 \pm 90 \text{ ms}$, which is defined as the duration between the creation of fission products and the time when half of the maximum activity reaches a γ -detector at the position of the ion source [Eiba2010]. It has to be mentioned that the transport time depends on the gas flow and, thus, might vary under different experimental conditions. The TOF-ICR technique will allow for mass measurements on short-lived nuclides with half-lives down to about 200 ms depending on the production yield. In this estimation, the gas-jet transport time is the main limiting factor since all other parts of the cycle, like ion transfer, cooling and the actual mass measurement, are either very short anyhow or can be shortened with a loss of resolution. For the FT-ICR technique, half-lives starting at about 5 s are of interest since the transient recording has to be sufficiently long. In this case, the gas-jet transport time is not limiting at all.

Transport efficiencies between 50% and 70% have been determined. Here, a drawback of the gas-jet technique became visible, namely the efficiency decreases with time. This might be due to the fact that aerosol particles get stuck to the inner walls of the capillary and, thus, reduce the cross-section. It has been demonstrated that a stable transport efficiency of about 50% can be maintained for at least eight hours of constant operation, which is by far sufficient for a high-precision mass measurement assuming the yields listed in Tab. 4.1 [Eiba2009].

Some candidates for mass measurements on neutron-rich fission products have been already extracted and identified by γ -spectroscopy in an off-line setup. Here, the target consisted of $310 \mu\text{g } ^{235}\text{U}$ and was covered with a $13 \mu\text{m}$ thick aluminium foil. For the identification, fission products were collected on a filter, which was moved to the detector after a decay time. Therefore, only longer-lived species are visible. Nevertheless, it is expected that TRIGA-TRAP can improve the present mass uncertainty of the nuclides given in Tab. 4.1.

The gas-jet extraction system is connected to a subsequent skimmer (see Fig. 4.4), where the heavy aerosols with the attached fission products get separated from the light carrier gas. Separation is obtained by the formation of a supersonic jet facing a conical aperture, so that the gas can be pumped away by a $270 \text{ m}^3/\text{h}$

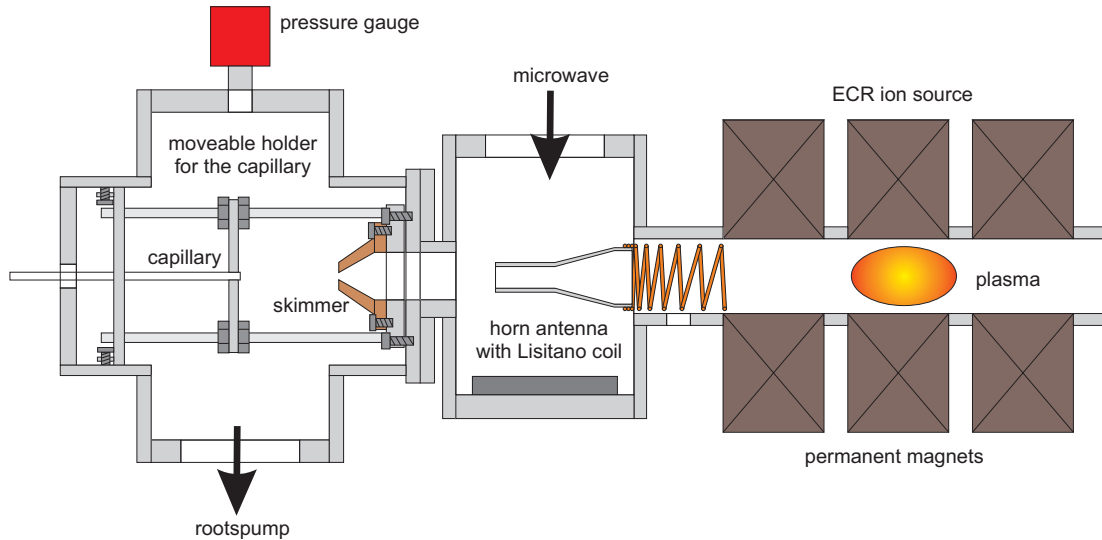


Figure 4.4: Schematic drawing of the ECR ion source with the skimmer system. The end of the gas-jet capillary is placed opposite to a conical skimmer at a tunable distance. In the left vacuum chamber, the carbon aerosols with the fission products are separated from the gas. They enter the ECR ion source and get ionised in a microwave heated plasma. The ions are extracted to the right.

roots pump. The aerosols and fission products enter an ECR ion source with a microwave heated plasma [Gell1990]. The microwave at a frequency of $\nu_{HF} = 2.45$ GHz and a power of up to 300 W is generated by a magnetron. A horn antenna couples the wave to a Lisitano coil facing the plasma region. 18 permanent magnets arranged in three rings of 6 magnets create the magnetic field for plasma confinement, both axially and radially. A closed surface of 87.5 mT is obtained in the central region of the magnetic field to match the electron cyclotron resonance condition $\nu_{HF} = eB/(2\pi m_e)$ for the given microwave frequency ν_{HF} . The ion source has been already operational at the University of Giessen [Lieh1992]. In the TRIGA-SPEC facility, the carbon aerosol particles will be cracked in the plasma to release and ionise the fission products. Due to the comparably low heating power, mainly singly charged ions will be created. The coupling of the ECR ion source to the gas-jet system and systematic studies of the performance under a gas pressure of about 10^{-4} mbar and aerosol mass flows of several microgram per minute are presently going on [Smor2011]. The complete ion source is operated on a high-voltage platform to allow for ion energies up to 60 keV when extracted to the ground level. For beam diagnosis after the extraction, either a Faraday cup can be used to monitor the absolute ion beam intensity or a fork scanner to determine the beam profile.

Mass separation will be achieved by a 90° magnetic sector field (see Fig. 4.1) with a spacial homogeneity of $\Delta B/B = 10^{-3}$ and a maximum field strength of $B = 1.12$ T subsequent to the ECR ion source. The bending radius of the dipole magnet is 500 mm. Slits in the focal planes can be used to adjust the mass separator to either high transmission or a large mass resolving power up to $m/\Delta m \approx 1000$.

For high-precision mass measurements, the application of the COLETTE RFQ cooler and buncher is also planned [Lunn2009] and will be carried out within a further PhD work [Beye2012]. Such devices are already in operation at other Penning trap mass spectrometers, like ISOLTRAP [Herf2001a], JYFLTRAP [Niem2001], and SHIPTRAP [Rodr2003]. The principle is explained in Fig. 4.5: ions from the ECR source enter a gas

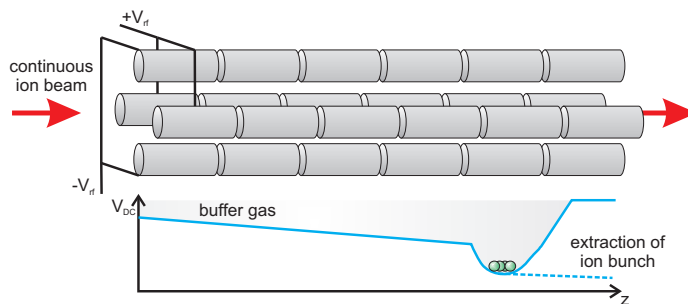


Figure 4.5: Principle of an RFQ cooler and buncher. Ions from a continuous beam are stored in a linear Paul trap and lose energy by collisions with the buffer gas. The axial potential has a minimum close to the end of the structure to accumulate cold ions. An ion bunch is released by switching down the last electrodes quickly.

filled linear Paul trap¹ in a continuous beam and are accumulated in an axial potential minimum. In order to stop the ions, the complete RFQ structure is floated at the same potential as the ECR ion source. Ion bunches of a few μs length can be finally extracted by pulsing down the last electrode segments [Herf2001a]. For TRIGA-TRAP, the RFQ is needed to improve the beam emittance, i.e. the transversal momentum, to be able to use a pulsed drift tube to reduce the ion energy from several 10 keV from the ECR ion source to a few 10 eV electrostatically. The low energy is mandatory for a highly efficient injection into the Penning trap system since the traps are on ground potential. Before and after the RFQ, an MCP and a Faraday cup are installed for beam diagnosis.

4.2 The TRIGA-TRAP setup

The TRIGA-TRAP setup is shown in Fig. 4.6. Two off-line ion sources provide carbon clusters as well as alkali ions for mass calibration, and are used to ionise transuranium elements for high-precision mass measurements (Sect. 4.3). Both of them are placed in a CF160 six-way cross chamber and evacuated by a 300-l turbomolecular pump (EBARA *ET300WS*, LEIBOLD *Turbovac 340M*). A CF160 gate valve inbetween the source chambers and another one towards the switchyard can be used to separate different sections of the vacuum system. The ion optics in front of the magnet (Sect. 4.4) are mounted in a CF100 tube and a CF100 six-way cross, where a moveable MCP detector can be used for inspection of the beam. Another 300-l turbomolecular pump (EBARA *ET300WS*) is connected here as well. A short CF100 chamber in this section provides the electric feedthroughs as well as the buffer gas inlet for the purification trap, which is regulated by a PFEIFFER *EVR 116* valve. The part making TRIGA-TRAP unique among Penning trap mass spectrometers for short-lived nuclides apart from its location at a nuclear reactor is the vacuum and cryogenic system starting with the trap tube, which has been designed within the PhD thesis of C. Weber [Webe2004]. As discussed later, two independent ion detection systems can be implemented. The design of the trap tube was chosen as a compromise between an optimal environment for a high signal-to-noise ratio of the non-destructive image

¹A linear Paul trap consists of four electrode rods where an oscillating electric potential is applied as shown in Fig. 4.5 with a static component. Depending on the potential parameters, ions of certain masses have stable motions along the axis, whereas others are lost (mass filter). The rods can be segmented to apply a static potential for axial confinement. For more details, see [Majo2004].

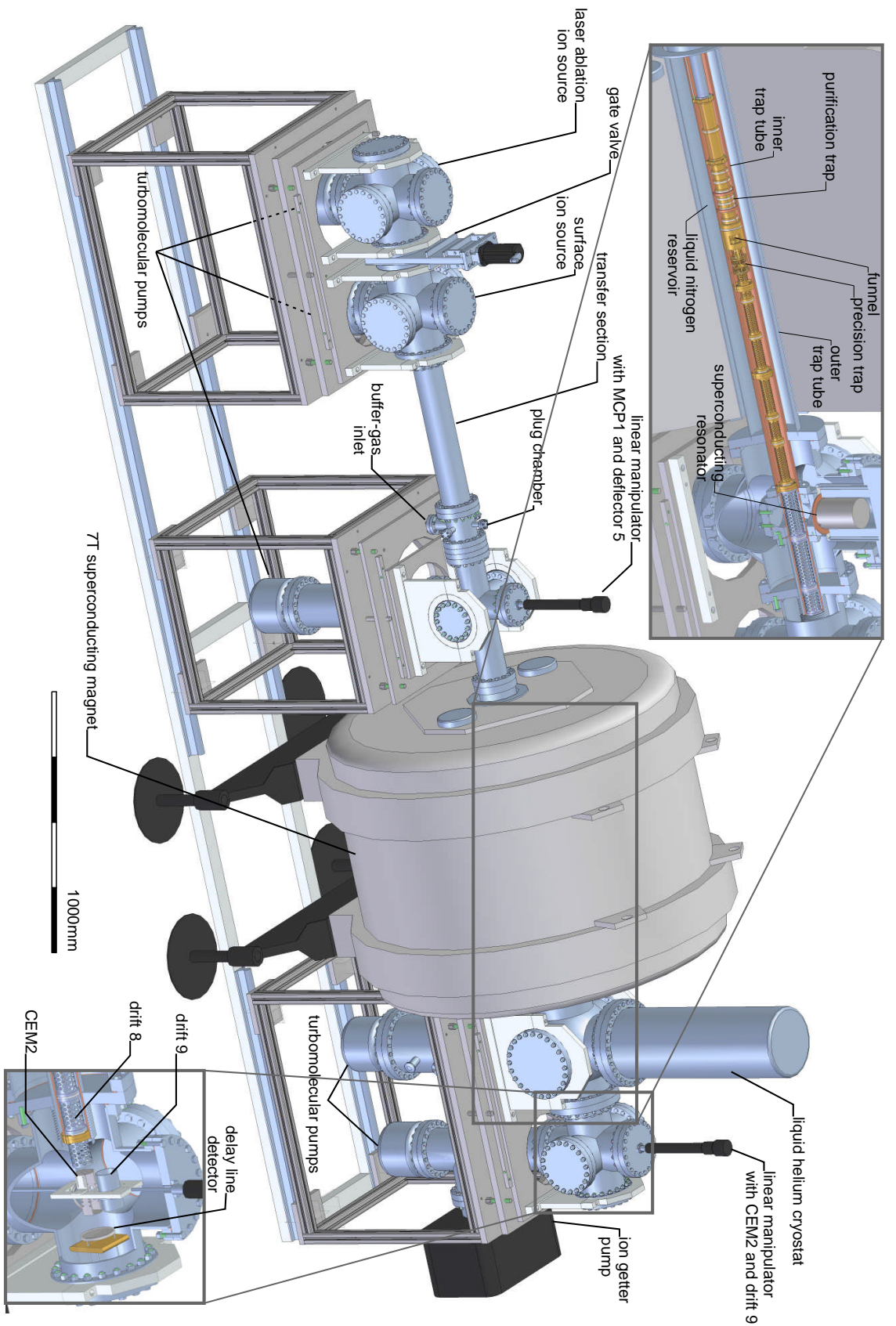


Figure 4.6: The TRIGA-TRAP setup. The two off-line ion sources are placed on the left. A transfer section guides the ions to the trap system situated inside in a 7-T environment inside a 7-T superconducting magnet. The upper inset shows the trap section including the drift electrodes required for the injection and the ejection of the ions. The superconducting resonator for the non-destructive imaging-current detection is also shown. The lower inset shows the time-of-flight ion detectors.

current detection technique (Sect. 4.6) and the available space in the magnet bore (Sect. 4.5). The tube with an outer diameter of $d = 134$ mm and a length of $l = 1150$ mm has a double wall to be able to cool the inner copper tube ($d = 60$ mm) to 77 K by liquid nitrogen. Thermal insulation is provided by a vacuum region ($p \approx 1 \cdot 10^{-7}$ mbar). The copper tube is connected to the room-temperature regions with a short stainless-steel tube at the ion injection side and with a stainless-steel bellow at the ejection side. The latter compensates for length contractions at low temperatures. A CF63 stainless-steel cube interrupts the inner trap tube to provide the electrical feedthroughs to the traps and to hold the electronics boards required for filtering and signal processing. It is placed inside a CF200 six-way cross with the 4-K liquid helium cryostat on top and a 100-l tubomolecular pump (LEIBOLD *Turbovac 150CSV*) for the insulation vacuum at the bottom. This arrangement guarantees a short distance between the precision trap and the superconducting resonator needed for the image current detection (Sect. 4.6). The liquid nitrogen dewar of the cryostat also supplies the trap tube. At the end of the vacuum system another CF160 six-way cross is placed connecting the pumps for the trap vacuum. At this point two 1300-l turbomolecular pumps (BOC EDWARDS *STP1300*) as well as a 240-l ion getter pump (VARIAN *VacIon Plus 300*) are used to provide a pressure for the precision trap as low as a few times 10^{-9} mbar. In addition, this chamber houses the detectors used for the time-of-flight measurements (Sect. 4.6).

4.3 The off-line ion sources of TRIGA-TRAP

TRIGA-TRAP uses two off-line ion sources for test and calibration purposes. The surface ion source (similar to [Kirc1981]) shown in Fig. 4.7 is used to create positively charged ions of alkali elements, which can be used as references in high-precision mass measurements (Tab. 4.2). Therefore, a cavity is filled with zeolite², providing the desired alkali atoms. The tungsten cavity surface is heated by electrons emitted by a tungsten filament, leading to a continuous release of the alkalis from the compound. They get ionised by the interaction with the hot surface, due to the work-function of tungsten ($\Phi_s = 6$ eV). The probability for this process is described by the Langmuir-Saha equation [Lang1925]

$$p_i = \frac{n_i}{n_i + n_a} = \left(1 + \frac{g_a}{g_i} \exp \left[-\frac{e(\Phi_i^{1+} - \Phi_s)}{k_B T} \right] \right)^{-1}, \quad (4.1)$$

where $n_{i,a}$ are the numbers of ions and atoms, respectively, leaving the surface in a thermal equilibrium at temperature T . $g_{i,a}$ denote the statistical weights of the ionic and the atomic state. The cavity increases the ionisation probability due to an increased number of contacts with the hot surface [Kirc1990]. The ions are extracted through a hole with 0.5 mm diameter in the front plate of the cylinder. With a typical heating power between 30 and 50 W, the source emits ion currents of up to a few nA. These high intensities are favourable to optimise the ion transport. For capturing in the Penning traps, ion currents of a few 100 pA are sufficient. In addition, the ion beam is pulsed by a fast switching extraction electrode directly after the cavity to obtain ion bunches of about 10-20 μ s.

The second off-line source is a new laser ablation ion source which has been developed at TRIGA-TRAP [Smor2008, Smor2009]. This type of source is commonly used to create carbon cluster ions for Penning trap mass spectrometry [Blau2002, Chau2007, Elom2008]. The frequency-doubled light of a pulsed Nd:YAG laser

²Sodium zeolite is a crystalline aluminium-silicate structure ($\text{Na}_{12}[(\text{AlO}_2)_{12}(\text{SiO}_2)_{12}] \cdot (27\text{H}_2\text{O})$), where the sodium can be substituted with the desired alkali element, e.g. caesium [Ohsh2006].



Figure 4.7: Surface ion source for alkali ions. During operation, the cavity part is mounted over the tungsten filament, which is heated with an electric power of about 30 W. The emitted electrons are accelerated by an adjustable DC voltage and heat up the ionisation surface of the cavity filled with the supply material. Ions are extracted through a 0.5 mm hole at the front plate.

nuclide	Φ_i^{1+} / eV	m / u
^{23}Na	5.139	22.9897692809(29)
^{39}K	4.341	38.96370668(20)
^{41}K	4.341	40.96182576(21)
^{85}Rb	4.117	84.911789738(12)
^{87}Rb	4.117	86.909180527(13)
^{133}Cs	3.893	132.905451933(24)

Table 4.2: Properties of alkali nuclides used as mass references: first ionisation potential Φ_i^{1+} [Stöc2000] and atomic mass m [Waps2003b].

(CONTINUUM *Minilite*) with a wavelength of $\lambda = 532 \text{ nm}$ and a pulse length of 5 ns is focussed onto the target surface. As shown in Fig. 4.8 the laser beam enters the vacuum chamber through a window opposite to the target. To increase the power density on the surface, an optical lens with a focal length of $f = 45 \text{ cm}$ reduces the beam diameter to about 0.85 mm. The laser power is constantly monitored by a pyroelectric detector mounted behind a beam splitter. Thereby, about 80 % of the initial intensity is transmitted to the target and about 11 % is reflected to the detector. The remaining fraction is lost in the beam splitter due to multiple reflections.

By absorbing energy from the laser, the target spot is heated leading to a vaporisation of target material. The power density is between $120\text{-}250 \text{ MW cm}^{-2}$. The vaporised material forms a plasma plume in front of the target where the atoms get ionised. Many different ion species independent from which element can be produced. The target is biased to a voltage of 80 V which defines the ion energy. They are extracted by an electrode in Pierce-like geometry [Pier1954] and guided by a system of a deflector and an einzel lens. The following 90° bender bends the ions into the main beam line where they are transported to the Penning traps.

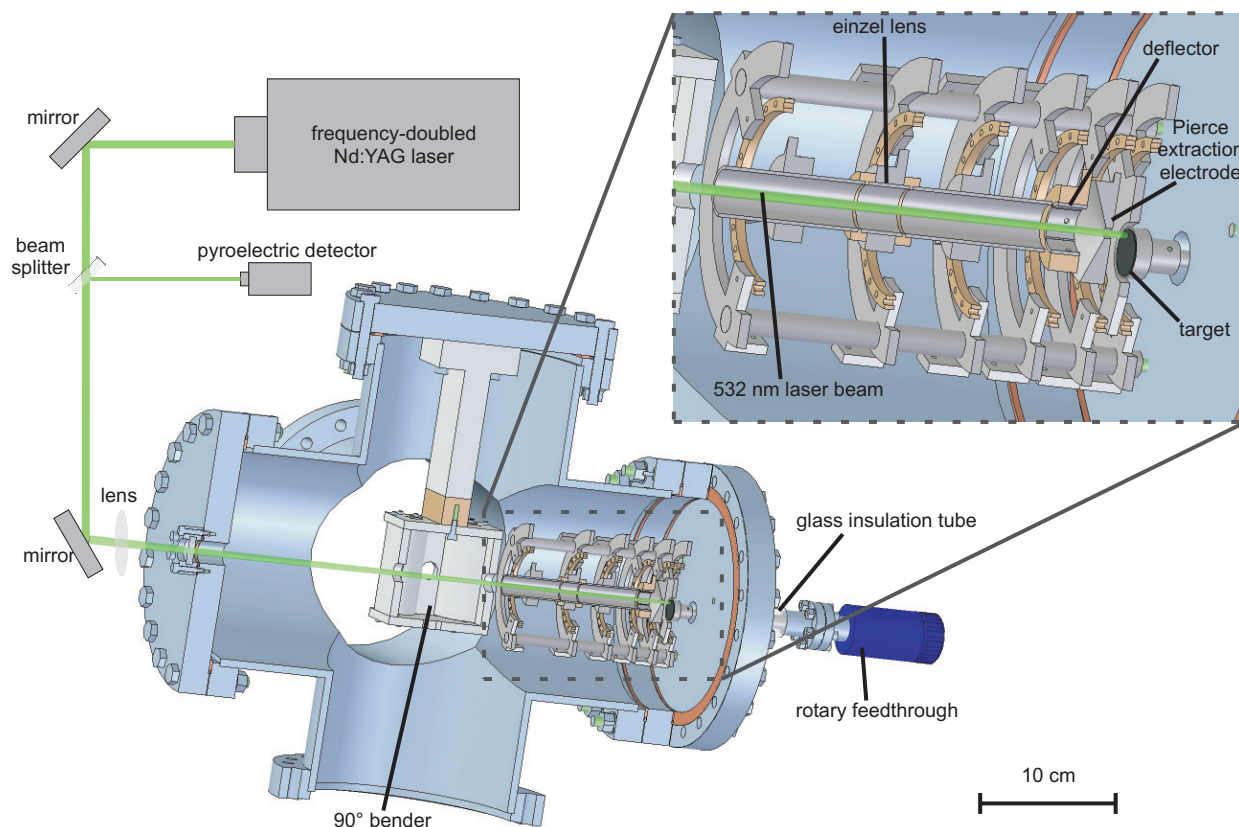


Figure 4.8: Sketch of the laser-ablation ion source. The target is mounted on a rotary feedthrough with an offset to the axis of the laser beam and the ion optics. Ions are created in the plasma plume after the impact of a pulsed laser beam ($\lambda = 532 \text{ nm}$) on the target surface. They are extracted by an electrode with Pierce-like geometry, steered and focussed by the following ion optical elements. A 90° bender is used to deflect the ions into the main beamline of TRIGA-TRAP towards the Penning traps.

Two different target materials have been tested for the production of carbon cluster ions [Smor2008]. A solid pellet with a diameter of 7 mm was created by pressing C_{60} powder with a small amount of isopropanol into a recess at a pressure of about 1.3 kN mm^{-2} . During operation of the laser ion source, the pellet showed some problems: the structure was not perfectly conducting, leading to an undefined electric potential at the target surface and, thus, an undefined ion energy. In addition, the pellet was unstable and large amounts of carbon were deposited inside the source. A better choice is Sigradur^{®3}, a glassy solid state configuration of fullerene-like carbon with a high mechanical, chemical and thermal stability, as well as good electrical conducting properties. Circular plates of this material with a diameter of 14 mm and a thickness of 2 mm are used as targets instead. Time-of-flight spectra of singly charged carbon cluster ions captured in the gas-filled purification trap and ejected towards the detector are shown in Fig. 4.9. Due to the large mass range not all cluster sizes can be stored simultaneously but the delay time between the ion creation and the capture pulse can be adjusted. Fig. 4.9 shows the results for four different capture delay times t_{cap} . The identification of each ion species was done relative to the time-of-flight information for C_{20}^+ and C_{21}^+ obtained by the mass

³Sigradur[®] is a trading label of the HTW Hochtemperatur-Werkstoffe GmbH.

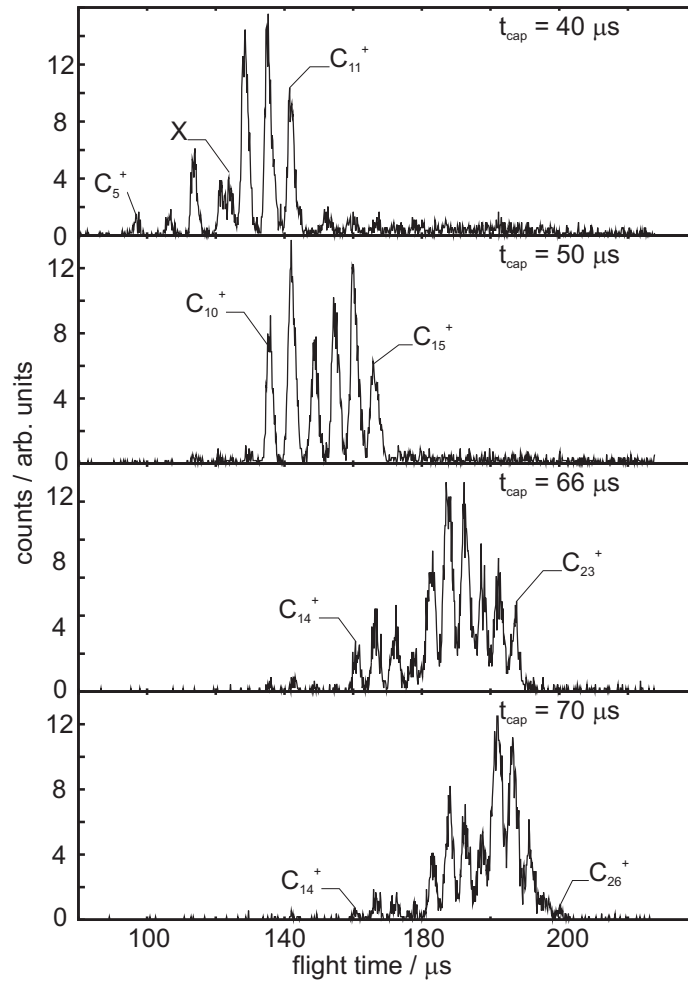


Figure 4.9: Time-of-flight spectra of carbon clusters ejected from the purification trap. The four plots correspond to four different delay times t_{cap} between the ion creation and the capture pulse of the trap. $t_{\text{cap}} = 66 \mu\text{s}$ is the optimal value for mass 240 u. The cluster species were assigned using the time-of-flight information for C_{20}^+ and C_{21}^+ obtained by a mass-selective ejection. The counts have been normalised to the total number of ions. For $t_{\text{cap}} = 40 \mu\text{s}$ a contamination (X) with $m/q \approx 100$ appears.

selective ejection from the purification trap after buffer-gas cooling has been performed (see Sect. 3.2.2). Clusters from C_5 to C_{26} corresponding to a mass range from 60 to 312 u are detected behind the trap.

Besides bare Sigradur[®], other targets for the production of certain rare-earth and americium ions have been used already. In first tests, about 10 μl of a solution of gadolinium nitrate ($\text{Gd}(\text{NO}_3)_3$) or the actinoid compound in 0.1 molar nitric acid (HNO_3) has been evaporated on a Sigradur[®] plate⁴. A sample of 10^{15} Gd atoms was sufficient to get 5-6 ions of $^{157}\text{GdO}^+$ per laser shot into the purification trap. Monoxides of the six stable isotopes $^{154,155,156,157,158,160}\text{Gd}$ were observed with a count-rate resembling the natural abundances, which is about 15 % in case of ^{157}Gd . For ^{152}Gd with a natural abundance of 0.2 % the amount was too low to perform a measurement in a suitable time, so an enriched target with about 34% abundance was used. The

⁴Tungsten and titanium substrates have also been tested, but Sigradur[®] plates can be used to produce carbon cluster ions simultaneously without the need to change the target.

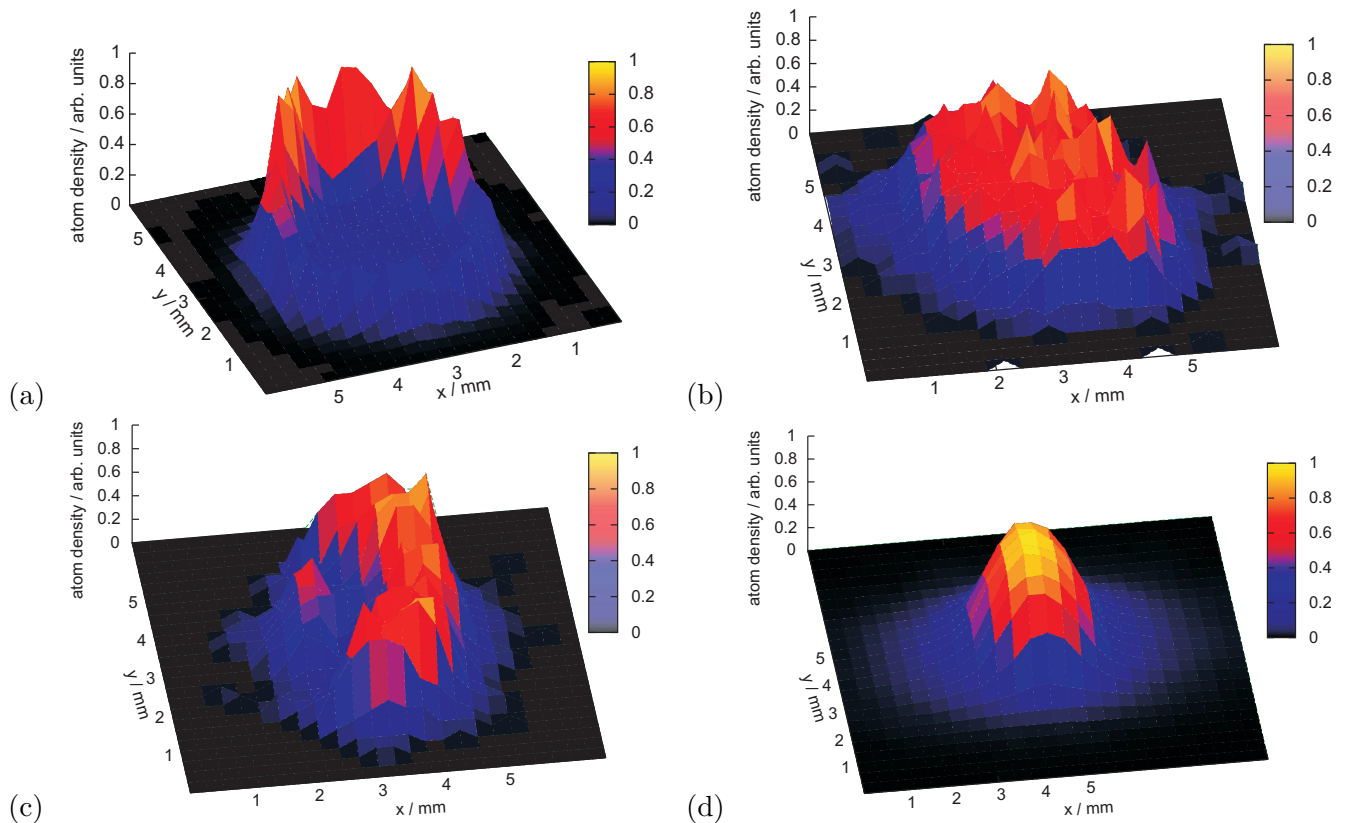


Figure 4.10: Radiographic images of several targets based on Sigradur[®] plates. (a) A drop of the $\text{Gd}(\text{NO}_3)_3$ solution has been evaporated on the surface. The Gd is mainly deposited at the border line of the spot whereas the atom density is close to zero in the center. (b) A homogeneous density of Gd atoms is achieved by electrolytical deposition. (c) The target shown in (b) has been used in the ion source. The trace of the laser spot is clearly visible. (d) A first Am target has been prepared by molecular plating as well.

laser intensity used was $40\text{--}85 \text{ MW cm}^{-2}$. More information on the individual targets and the ion production is given in Sects. 6.1.1 (for rare-earth elements) and 6.2.1 (for americium).

The distribution of the deposited material on the target surface can be monitored by radiographic imaging (RI) [Lieb2008]. Therefore, a radioactive tracer is needed, which can be provided by the β^+ -emitter ^{153}Gd obtained in the nuclear reaction $^{152}\text{Gd} + n \rightarrow ^{153}\text{Gd} + \gamma$ during irradiation of the Gd solution with neutrons from the TRIGA reactor. An imaging plate sensitive to the radiation is exposed to the target before the dose can be read out position-sensitively with an imager (FUJIFILM *FLA 7000*). The RI result shows the problem of the target production (Fig. 4.10(a)): the element of interest, in this case Gd, is mainly concentrated along the border of the deposited spot. Thus, electrolytical deposition (molecular plating) has been also tested to obtain a more homogeneous atom distribution: the conductive Sigradur[®] plate is placed below a PEEK⁵ mask defining the geometry of the Gd-plated surface. A constant current between the plate and the anode is adjusted, which enables the deposition of Gd on the Sigradur[®] backing material. Targets produced by molecular plating provide a homogeneous atom density of the desired element (Fig. 4.10(b)). Moreover, the

⁵Polyether-etherketone.

geometry has been adapted to the track of the laser spot while rotating the target. Figs. 4.10(b,c) show the RI images of the same target before and after irradiation by the laser.

Besides Gd, targets have been plated with americium (Fig. 4.10(d)) using both methods, proving the capability of the TRIGA-TRAP laser ablation ion source to produce ions of lanthanoids and actinoids. The results of the mass measurements performed on those ion species are reported in Chap. 6.

4.4 Ion transport

Penning-trap mass measurements on short-lived nuclides require ion optics to transport the externally produced charged particles to the traps with high efficiency. Moreover, in case of a TOF-ICR measurement, the ions need to be ejected and guided to a detector. An overview of the ion optics at TRIGA-TRAP is given in Fig. 4.11. Only electrostatic elements, mainly cylindrical electrodes grouped to einzel lenses and drift sections are used. An einzel lens consists of three cylinders of the same diameter, where the first and the last part are equal in length. Adjusting the potential of the central element with respect to the neighbouring ones creates a lens with variable focal length [Adam1971]. However, at TRIGA-TRAP the voltages of the outer elements of the einzel lenses differ as well, which turned out to improve the transport efficiency. To correct for tilts and parallel shifts of the ion beam versus the optical axis, several deflectors are used. These are cylinder electrodes cut longitudinally into four equal segments to apply electric fields perpendicular to the beam axis. All potentials of the ion transport were first simulated and later optimised with respect to the number of transmitted ions (Sect. 5.1). In principle, the ion sources are operated on voltages between 80-100 V to define the ion energy. The ion optics between the sources and the purification trap are biased with -1 kV to ensure a high efficiency in the ion transport.

Both off-line ion sources have similar optics: after the extraction electrode, a deflector (LIS deflector/SIS deflector) is used to correct for a possible tilt of the ion beam with respect to the optical axis. The following einzel lens (LIS lens 1-3/SIS lens 1-3) collimates the beam and focusses into the 90° bender (bender 1/bender 2). 90° bending is achieved by applying a suitable voltage to four circular rod segments, which create a quadrupole field in the bending plane. The rods are enclosed in a metallic housing with four circular apertures of 13 mm diameter to inject and eject the ions. Inbetween the benders, a system of two einzel lenses (source deflectors 1+6 and source lenses 2-5) with the diameter adapted to the apertures is used. In addition, one of the outer elements of each lens is sliced to serve as a deflector.

An ion gate is directly mounted behind the exit hole of bender 2. It can be used to pulse the continuous beam from the surface ion source for trapping in the purification trap. The second purpose is to reduce the background of unwanted ion species in case the on-line ion source or the laser ablation ion source are used. Therefore, the gate should transmit ions only for a short time and block them else. Bradbury and Nielsen introduced a grid of parallel wires with an alternating DC potential $\pm V$ to deflect the incoming ion beam [Brad1936] (Fig. 4.12). By this technique, transmitted ion pulses as short as 1 μs should be possible in case the voltage on the wires is quickly switched between $\pm V$ and zero. At TRIGA-TRAP a gate with about 1 mm wire spacing and about 0.1 mm wire diameter has been tested. Due to the fact that the ions are not really blocked but deflected, the suppression in the closed state was only a factor of 10. Thus, the wire grid has been replaced by a mesh which is switched to about 600 V to block all ions. The drawback of this solution is the low time resolution of 5-10 μs . In case of carbon cluster ions, this is not crucial since the time-of-flight

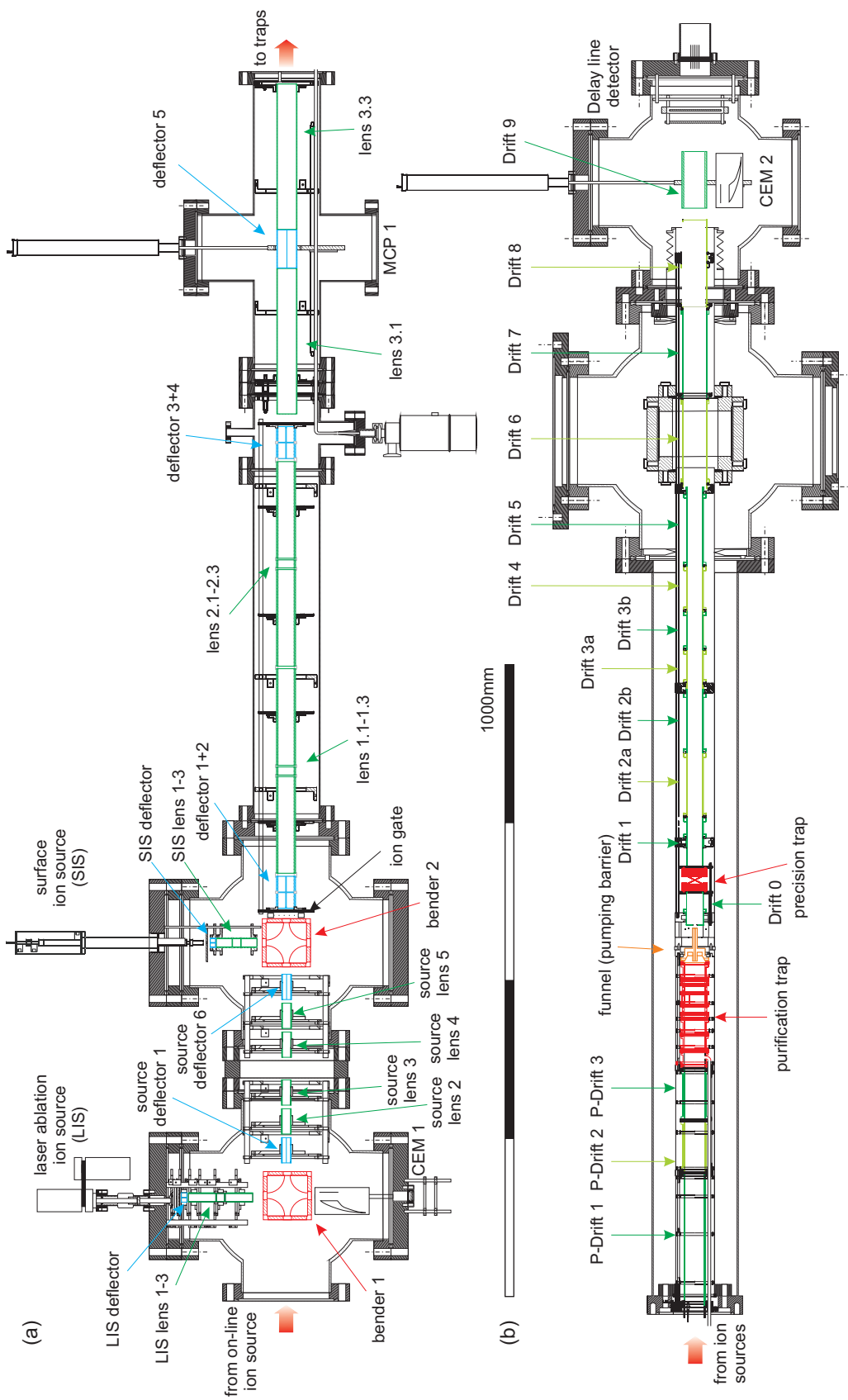


Figure 4.11: (Colour) Overview of the ion optical elements used at TRIGA-TRAP. (a) The ion source part consisting of the laser ablation and the surface ion source. Lens elements are marked in green, deflectors in blue, and the 90° benders in red. (b) The trap part with drift tubes coloured in green, and the traps in red. In addition the funnel electrode serving as a differential pumping barrier is marked in orange. Four ion detectors can be used in the setup: channeltron 1 (CEM1), microchannelplate 1 (MCP1), CEM2, and the position-sensitive delay line detector.

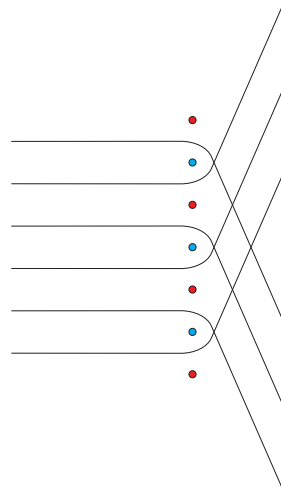


Figure 4.12: (Colour) Function principle of a Bradbury-Nielsen-Gate. An alternating DC voltage $+V$ (red circles) and $-V$ (blue circles) is applied to a wire grid. Incoming ions are deflected.

distributions of different cluster sizes are not sufficiently separated at this point anyhow. With the present configuration, the ion number can be reduced depending on the length of the transmission pulse with hundred percent suppression in the closed state. Tests with ions trapped in the purification trap showed that always 4-5 cluster sizes are simultaneously transmitted within a $1 \mu\text{s}$ pulse (see Fig. 4.9).

To inject the ions into the trap tube, a system of five deflectors and three einzel lenses is used. Two pairs of deflectors correct for parallel shifts and tilts of the ion beam versus the trap axis. For beam diagnostics an MCP detector can be moved in by a linear manipulator. At the same position, another deflector is placed in case of an ion transport to the traps. At the beginning of the trap tube, which is already located inside the superconducting magnet, three drift tubes decelerate the ion beam again from about 1 keV to about 100 eV to enable trapping in the purification trap. Subsequent to the precision trap, a system of ten drift tubes is used to guide the ions to the detector. This drift section is crucial for the TOF-ICR detection technique and is discussed in more detail in Sect. 4.6. Besides CEM2, a position-sensitive ion detector [Eite2009] can be used to utilise not only the time-of-flight information of the ions but also the position of the impact (see Sect. 4.6).

4.5 The cryogenic Penning traps and the superconducting magnet

The major components of the TRIGA-TRAP mass spectrometer are the two Penning traps [Sick2003, Webe2004]: the first trap (purification trap) is used for the cooling of the ion cloud and isobaric separation, the second one (precision trap) for the high-precision mass measurement. The vacuum tube (see Fig. 4.11) housing the complete electrode stack including both traps as well as injection and ejection drift sections can be cooled down to 77 K by liquid nitrogen, but has been used at room-temperature for all studies reported here. Therefore, all electrodes inside the cryogenic region of the trap tube starting from ‘P Drift 2’ up to ‘Drift 5’ are made of OFHC⁶ copper with a purity of at least 99.99%. This material is used due to the high thermal (519 W/(m K) at $T = 73 \text{ K}$) and electric ($\approx 0.002 \Omega \text{ mm}^2/\text{m}$ at $T = 73 \text{ K}$) conductivity as well as the low sus-

⁶Oxygen Free High Purity.

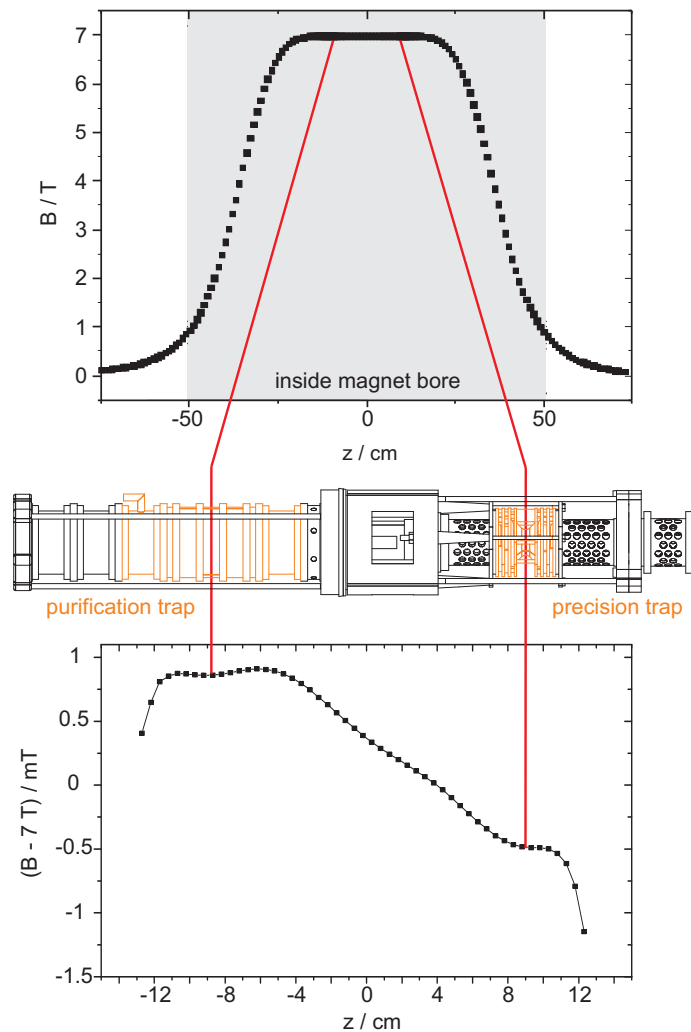


Figure 4.13: Magnetic field of the superconducting magnet on axis of the magnet bore. The region where the Penning traps are placed is enlarged in the graph below the sketch of the electrode geometry. The homogeneity for the purification trap position at $z = -9$ cm is $\Delta B/B = 0.6$ ppm and for the precision trap position at $z = +9$ cm it is $\Delta B/B < 0.3$ ppm.

ceptibility ($-8 \cdot 10^{-7}$ at $T = 293$ K) [Deu2009], which causes minimal distortions to the magnetic field. The insulator rings of the purification trap and the drift sections are made of the aluminium-oxide (Al_2O_3) configuration ‘alumina’, which is an electric insulator but still provides a good heat conductivity. The insulation at the precision trap is done by another aluminium-oxide material called sapphire.

In the following paragraphs, the superconducting magnet providing the highly homogeneous magnetic field and the two Penning traps are described.

The superconducting magnet: The Penning traps are both placed inside the bore of the same superconducting magnet. The device produced by MAGNEX SCIENTIFIC LTD. is similar to the ones used at SHIPTRAP [Raha2006], JYFL-TRAP [Joki2006], and MLL-TRAP [Kolh2008]. It provides a horizontal 160-mm room temperature bore and a maximum field strength of 7 T. To reduce the fringe field and to minimise environmental impact, the magnet is actively shielded by internal bucking coils. Fig. 4.13 shows the plot of the magnetic

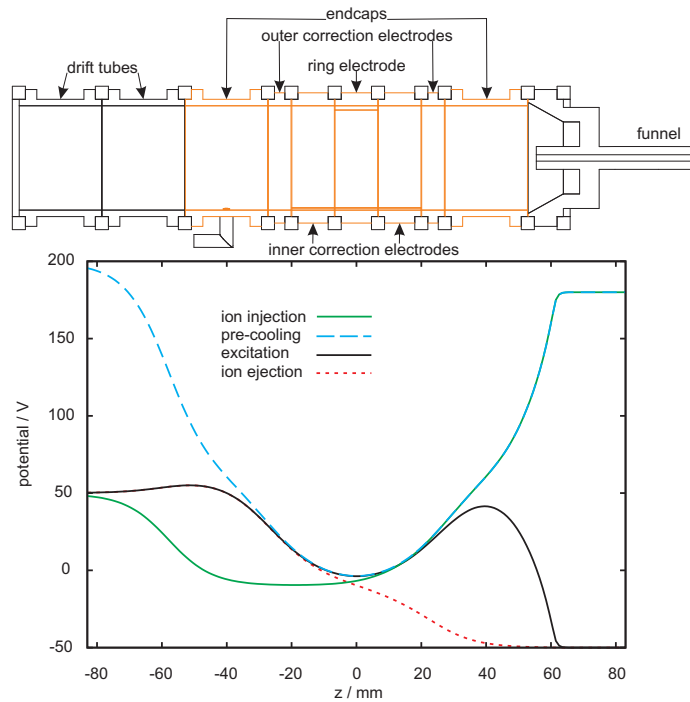


Figure 4.14: (Colour) Purification trap including the electric potentials which have been simulated in SIMION 8.0. Ions enter the trap from the left and are ejected to the right. For details see text.

field on axis of the magnet bore. The Penning traps are located in two very homogeneous regions at distances of -9 cm and +9 cm from the geometrical centre of the magnet. The homogeneity $\Delta B/B$ has been determined on a circle with 5 mm radius around the centre of both traps with an NMR probe [Repp2008]. The value for the purification trap is about 0.6 ppm and for the precision trap better than 0.17 ppm. Due to the flux creep effect [Beas1969] the magnetic fields of all superconducting magnets decrease steadily with time. This effect is corrected for by an internal superconducting field lock coil [MAG2006]. In case of TRIGA-TRAP, the field decrease is slightly overcompensated resulting in a field drift of $\Delta B/(B \cdot \Delta t) = 1.3(4) \cdot 10^{-9} \text{ h}^{-1}$. This value has been determined by measuring the cyclotron frequency of $^{12}\text{C}_{20}^+$ carbon cluster ions in the precision trap continuously for more than 110 hours (see Fig. 5.4). Of course, the current in the compensation coil has to be limited due to the force acting on the main coils. This is done by discharging the field lock coil completely once per month, thus leading to a stepwise decrease in the magnetic field of about $7.5 \mu\text{T}$ [Repp2008]. For high-precision mass measurements, only the compensated value is of interest, since the total measurement time amounts typically to only a few hours.

The purification trap and differential pumping: The purification trap is used to capture, cool, and clean an incoming ion pulse. It is a cylindrical seven-electrode Penning trap with an inner diameter of 32 mm and a total length of 110.57 mm. It consists of two endcaps, two outer and two inner correction electrodes, and the ring electrode. The inner correction electrodes are sliced into two 180° segments to enable different excitation and detection schemes for future applications which are presently not in use. The ring electrode has two 40° and two 140° segments. The smaller ones are used for the excitation of the radial eigenmotions and the larger ones for the non-destructive image current detection (see Sect. 4.6). Fig. 4.14 shows a sketch of the trap

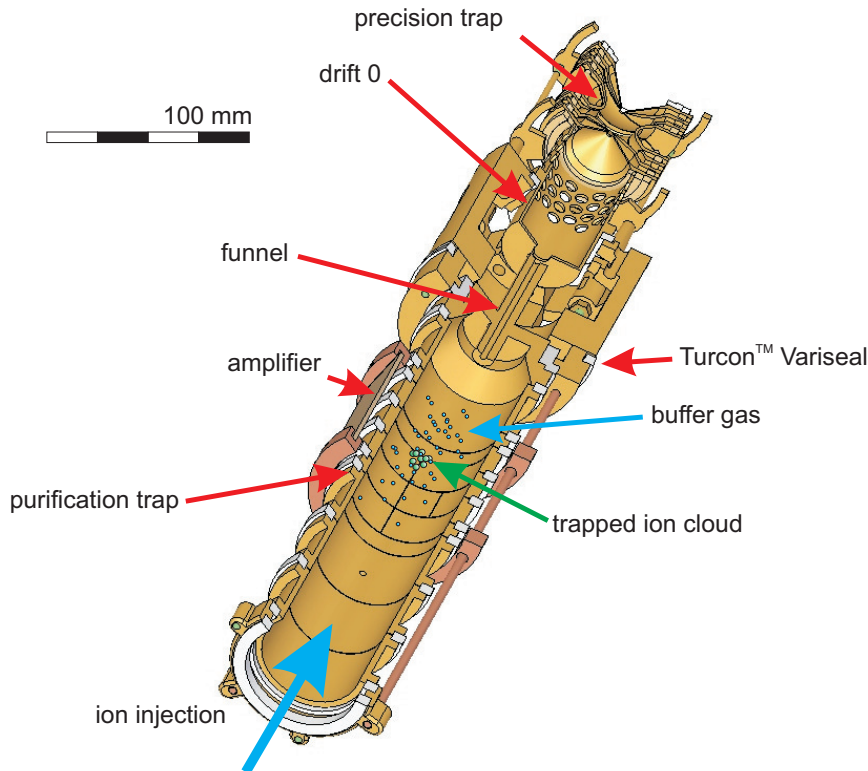


Figure 4.15: Drawing of the Penning trap setup. The purification trap is filled with helium buffer gas for ion cooling. After mass-selective centering, the desired ions are ejected through the funnel with an inner diameter of 1.5 mm. This channel also serves as a differential pumping stage. A short drift tube guides the ions to the precision trap. The amplifier for the broad-band image current detection in the purification trap is also shown.

electrode stack including the electric potentials in different phases of operation. The endcap at the injection side has a buffer-gas inlet through which the trap is flushed with helium at a flow of about $1 \cdot 10^{-5} \text{ mbar l s}^{-1}$ leading to a pressure of about 10^{-6} mbar . The funnel is pulsed to a potential sufficiently high to block the ions with about 100 eV (green line) and to capture them with the help of the second drift tube (dashed blue line). After a pre-cooling time of about 100 ms, the ions have lost a large fraction of their initial kinetic energy by collisions with the buffer-gas so that they are finally trapped in the potential minimum between both endcaps and the voltage on the drift tube and the funnel can be pulsed down (black line) to perform the mass-selective buffer-gas cooling (see Sect. 3.2.2). To eject the ions, the potentials on the corresponding electrodes are pulsed down (red line). The voltages on the correction electrodes for ion trapping are adjusted according to the trap described in [Sick2003]. The effective trap parameter has been determined through a measurement of the magnetron frequency ν_- to be $\bar{d} = (29.0 \pm 0.5) \text{ mm}$.

Subsequent to the purification trap, a differential pumping stage provides the required suppression of helium flow into the precision trap (Fig. 4.15). Therefore, the funnel is formed as a channel with 1.5 mm inner diameter and a length of 50 mm. The sealing against the vacuum tube is done with a commercial ring,

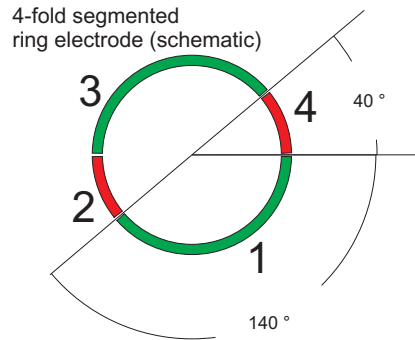


Figure 4.16: Sketch of the segmented ring electrode of the precision trap. The two larger segments are used for the image current detection, whereas the excitation of the ion motion is done via the smaller segments.

called TURCONTM *Variseal*. It consists of a PTFE⁷ body around a metallic spring, which counteracts the shrinking of the PTFE at low temperatures. This special seal has been found to work best at 77 K when the trap tube is cooled down. Tests on the gas flow suppression capability of such channels have been reported in [Neid2006, Ferr2007b, Neid2008]. Due to the long distances of the positions of pressure gauges to the trap centres, it is impossible to measure the suppression directly, but a value of about 1000 is expected. The shape of the resonance curve in a TOF-ICR measurement for different excitation times will give a hint on the residual pressure in the precision trap (see Chap. 6). A similar approach of differential pumping is used at SHIPTRAP, JYFLTRAP, and MLL-TRAP.

The precision trap: The precision trap at TRIGA-TRAP has been designed to get an optimal signal-to-noise ratio for the non-destructive image current detection technique (Eq. (3.65)). As one can see in Eq. (3.51), the image current for single singly charged ions is determined by the ratio r/D between the amplitude of the ion motion r and the effective distance of the detection electrodes D . Thus, a hyperbolic geometry has been chosen to minimise the distortions of the electric field even close to the ring electrode. The total size of the trap is kept small to ensure that the ions are still confined in the very homogeneous region of the magnetic field for $r/D \approx 0.4$. Moreover, according to [Gabr1983] the optimal ratio $\rho_0/z_0 \approx 1.16$ has been chosen to create an orthogonalised trap, which makes the eigenfrequencies practically independent from the motional amplitudes. These constraints lead to the final values of the ring electrode diameter of $2\rho_0 = 12.76$ mm and the endcap distance of $2z_0 = 11$ mm. The endcaps have holes with a diameter of 1.8 mm for the ion injection and ejection. They are sliced into two 180° segments to enable axial excitation and detection for future experiments, which is presently not applied. The distortion of the electric field due to the holes is corrected by two additional endcap correction electrodes. Two ring correction electrodes compensate for the finite size of the trap. The potential on the correction electrodes is experimentally optimised with a procedure described in Sect. 5.1. In order to increase the detector surface for the FT-ICR system, the ring electrode is segmented into two 40° and two 140° segments where the larger ones are used for detection and the smaller ones for the excitation of the ion motion (Fig. 4.16).

Fig. 4.17 shows a cut drawing of the precision trap as well as the relative changes of the magnetic field due

⁷Polytetrafluoroethylene.

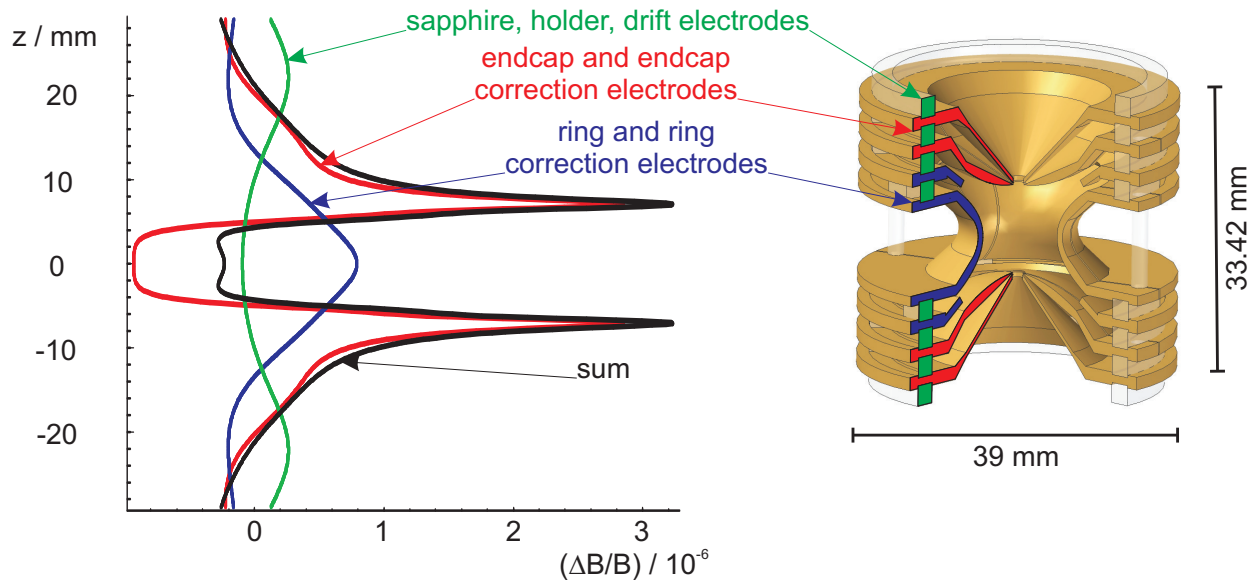


Figure 4.17: (Colour) Hyperbolic precision Penning trap with ring and ring correction electrodes (blue), endcap and endcap correction electrodes (red), insulated by sapphire rings (green) on the right. The graph on the left shows the relative changes of the magnetic field due to the magnetisation of the different parts. The black line is the sum of all contributions. Graph on the left taken from [Webe2004].

to the different electrodes. The sum of all contributions leads to a distortion of only $|\Delta B/B| \approx 2 \cdot 10^{-7}$ in a region of ± 2 mm around the trap center at $z = 0$. This could be achieved by a special design of the back-sides of the electrodes, which are not contributing to the electric potential inside the trap.

4.6 Ion detection systems

At TRIGA-TRAP the mass is measured via a determination of the true cyclotron frequency of the ion of interest stored in the precision trap. The basics of the two detection schemes applied, TOF-ICR and FT-ICR, have been discussed in Sect. 3.3. This section deals with the implementation of the techniques including the required detectors and electronics. An overview on the developments that have been made at TRIGA-TRAP in the field of ion detection techniques can be found in [Kete2009].

Time-of-flight detection: As described in Sect. 3.3.1, the TOF-ICR detection method is based on the measurement of the ion's flight time from the precision trap to a detector as a function of the quadrupolar excitation frequency. For the ion detection, two types of electron multipliers are used. Microchannelplates (MCP) consist of about 10^6 parallel channels with a diameter of 5-100 μm and a length-to-diameter ratio between 40 and 100 [Wiza1979]. The arrangement of the channels is done with a small angle ($< 10^\circ$) between the channel axes and the normal of the MCP front surface. Usually, coated lead-glass is used to fabricate MCPs which has a good secondary electron emission capability. An ion impact at the front surface starts a secondary electron avalanche towards the back surface that can be detected by a current measurement on an anode plate behind the MCP. Electron multiplication factors of $10^3 - 10^4$ are possible. At TRIGA-TRAP all

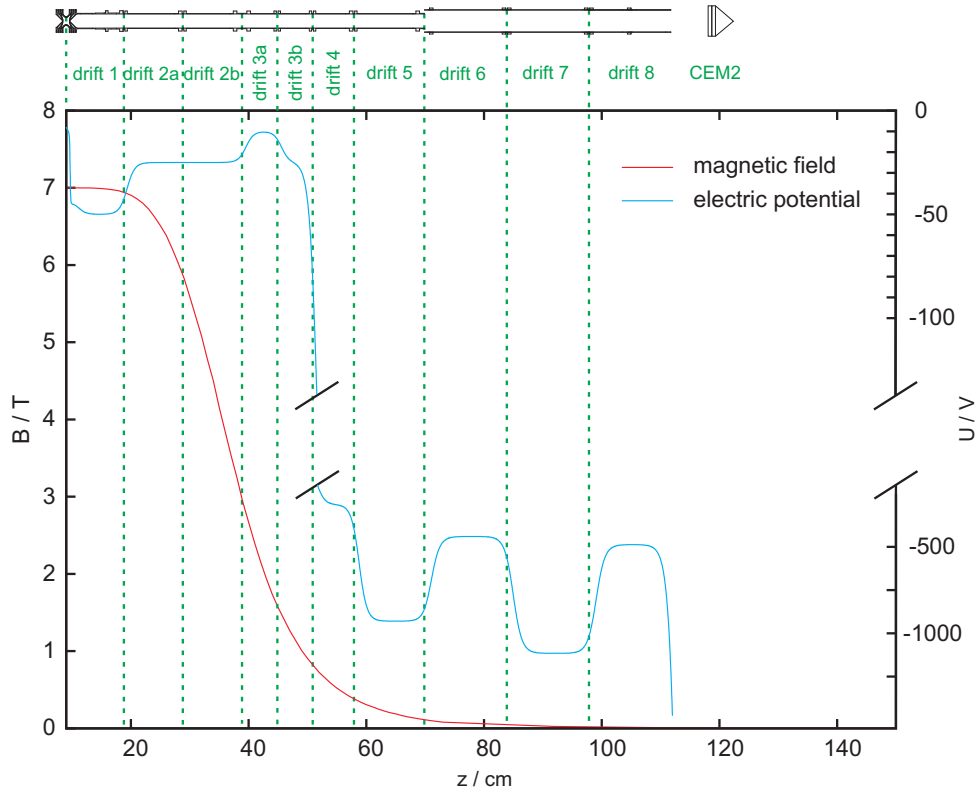


Figure 4.18: (Colour) Time-of-flight section beginning with the precision trap centre at $z = 9$ cm (the z -scale is identical to Fig. 4.13). The magnetic field is given by the red and the electric potential by the blue line. Drift electrode 3a is used to decelerate the ions at the position of the strongest gradient of the magnetic field. For more details see text.

MCP detectors are built up in a so-called ‘Chevron’ configuration, where two MCP plates are cascaded in a way that the tilt direction of the channel axes of the second plate is rotated by 90° with respect to the front plate. The time resolution of this detector is usually better than 100 ps and the detection efficiency for the conditions at on-line Penning trap mass spectrometers with ion energies around 2 keV is typically 30-50% [Ferr2007a]. However, due to the channel structure of MCPs only a fraction of about 60% is sensitive to ions giving a practical upper limit for the detection efficiency. The advantage of using MCP detectors is the large detection surface, since they are available with many different diameters of the plates and can be chosen that they cover the entire cross-section of the ion optics in front. They also provide a low dead-time of about 10 ns.

Nevertheless, the limited detection efficiency is a drawback for Penning trap mass spectrometry on very exotic nuclides since those have only very low production rates. Recently, a Channeltron[®] electron multiplier (CEM) has been introduced to this application [Yazi2006b]. A single horn-shaped coated lead-glass channel is used to create a secondary electron avalanche started by an ion impact on the front surface. At TRIGA-TRAP, the CEM detector is used in combination with a conversion dynode which releases electrons upon the ion impact to be multiplied by the horn afterwards [Bur] so that typically 10^7 electrons can be collected at the anode. The detection efficiency depending on the electron energy reaches 90% [Olse1979]⁸. A direct

⁸The electron energy can be adjusted to reach the maximum detection efficiency by tuning the voltage on the conversion dynode. It is independent from the energy of the incoming ions.

comparison of the detection efficiency of an MCP and a CEM detector as used similarly at TRIGA-TRAP has been done in [Yazi2006b, Ferr2007a, Kete2008], where an efficiency gain of the CEM with conversion dynode compared to the MCP of about 3 has been observed for ions in the low energy range (≤ 100 eV). CEM with conversion dynode are used at TRIGA-TRAP at the laser ion source, since the horn is mounted off-axis to suppress the background from neutral particles and to allow the laser beam pass through to the target, and in combination with the time-of-flight measurement.

Besides the standard ion detectors mentioned above, a delay line detector *DLD40* from ROENTDEK [Jagu2002] is used as well behind the precision trap [Eite2007]. Two MCP plates in Chevron configuration with an active diameter of about 42 mm are used for the secondary electron multiplication. The standard anode to measure the current is replaced in this case by the delay line: two coils with wires along the x and the y -axis (perpendicular to the ion beam direction) enable a position-sensitive ion detection. Here, the electrons from the MCP hit the wires at a certain position and create a current pulse which drifts towards the ends of the coils. By using the ion impact on the MCP front as a start trigger and knowing the drift velocity of the current pulse, the impact position can be calculated from the time information with a spatial resolution of $70 \mu\text{m}$ [Roen2009]. The detection efficiency for typical ion energies at TRIGA-TRAP is 30 – 40 %, the maximum count-rate 10^6 events/s. Detailed simulations and experimental studies have been performed at SHIPTRAP which showed that the position information on the detector can be used to obtain information on the ion motion in the precision trap [Eite2009]. These studies will be continued at TRIGA-TRAP.

Fig. 4.18 shows the electric potential and the magnetic field strength along the time-of-flight drift section starting with the centre of the precision trap at $z = 9$ cm. For an adiabatic conversion of the radial energy the ions gained during the quadrupolar excitation in the precision trap into axial energy due to the interaction between the magnetic moment of the ions and the gradient of the magnetic field, the ions are slowed down at the position of the strongest gradient. Therefore, the voltage on drift electrode 3a is on the same level as the ring electrode. The voltages before are tuned to optimise the line width in the time-of-flight spectrum, which directly determines the contrast [Raut2007a]

$$\bar{c} = \frac{t_{\text{off}} - t_{\text{on}}}{\sqrt{\sigma_{\text{off}}^2 + \sigma_{\text{on}}^2}}. \quad (4.2)$$

Here, $t_{\text{off,on}}$ denote the mean flight times for ions off resonance and on resonance, respectively, and $\sigma_{\text{off,on}}$ the corresponding line widths. The contrast is a measure to describe the quality of a TOF-ICR resonance. Detailed studies on the optimisation of \bar{c} by tuning the voltages in the drift section have been performed at SHIPTRAP [Raut2007a]. Fig. 4.19 gives an example with $^{133}\text{Cs}^+$ ions recorded during the commissioning phase of TRIGA-TRAP with different voltage settings for the precision trap and the drift section. The drift electrodes after ‘drift 3’ are used to transport the ions and to focus them onto the detector. In case of TRIGA-TRAP the time-of-flight drift section is rather long compared to other Penning trap mass spectrometers for short-lived nuclides since additional space is required for the liquid helium cryostat for the FT-ICR detection, which has to be close to the precision trap.

Image current detection systems: Both Penning traps at TRIGA-TRAP have a non-destructive image current detection system connected which differ in the sensitivity aimed for. A broad-band system is attached to the purification trap in order to monitor the trap content and to identify contaminations in amounts of about hundred ions. Unwanted ion species can be selectively removed by the application of a mass dependent dipolar

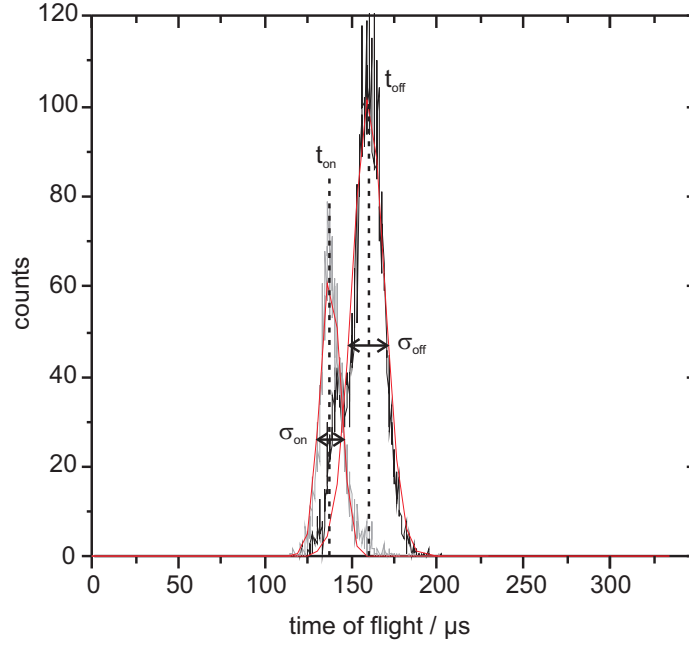


Figure 4.19: Time-of-flight contrast example for $^{133}\text{Cs}^+$ ions and an excitation time of 300 ms. The line centres are on resonance at $t_{\text{on}} = 138 \mu\text{s}$ and off resonance at $t_{\text{off}} = 160 \mu\text{s}$, the line widths are $\sigma_{\text{on}} = 12 \mu\text{s}$ and $\sigma_{\text{off}} = 18 \mu\text{s}$, leading to a TOF contrast of 1. The data has been recorded during the commissioning phase of TRIGA-TRAP where about 30 V higher potential on the precision trap and the drift section was used.

excitation at the modified cyclotron frequency ν_+ . For the image current detection, a combination of a newly developed ultra-low noise cryogenic amplifier and a low-noise commercial amplifier at room-temperature is used. The latter has been chosen after detailed investigations performed in [Repp2008]. The FET amplifier *SA-220F5* from NF CORPORATION has a voltage noise of only $0.4 \text{ nV}/\sqrt{\text{Hz}}$ and a current noise of $29.8 \text{ fA}/\sqrt{\text{Hz}}$. The frequency range from 10 kHz to 100 MHz covers the complete mass range of interest at TRIGA-TRAP. The amplifier in use has an input capacitance of 65 pF and an input resistance of $1 \text{ M}\Omega$. In a first attempt, the room-temperature amplifier should be connected directly to one of the 140° segments of the ring electrode of the purification trap. In this case, the wire length between detection electrode and amplifier was about 1.5 m leading to an additional capacitance of about 100 pF drastically reducing the signal-to-noise ratio (see Eq. (3.57)). Thus, a cryogenic amplifier developed at the experiment to determine the electron g -factor in Mainz [Scha2007] has been tested at TRIGA-TRAP as well [Knut2009]. It has an input capacitance of $< 8 \text{ pF}$ and is mounted close to the ring electrode to keep the wire connection as short as possible (Fig. 4.15). The voltage noise has been determined in an off-line experiment to be about $0.5 \text{ nV}/\sqrt{\text{Hz}}$ at $T = 77 \text{ K}$. Further information can be found in [Knut2009]. The concept of broad-band FT-ICR detection with hundreds of simultaneously stored charged particles is common in chemistry [Mars1998].

The second image current detection system developed in [Kete2006] is dedicated to high-precision mass measurements on nuclides with very low production rates. To get a sufficient signal-to-noise ratio (Eq. (3.65)) for the detection of a single singly charged ion with induced image currents i_{ion} of only a few 10-100 fA, the effective parallel resistance \hat{R}_p has to be maximised. In case of the narrow-band FT-ICR this is achieved by a high- Q superconducting helical coil (Fig. 4.20) which is connected to the 140° segments of the precision trap

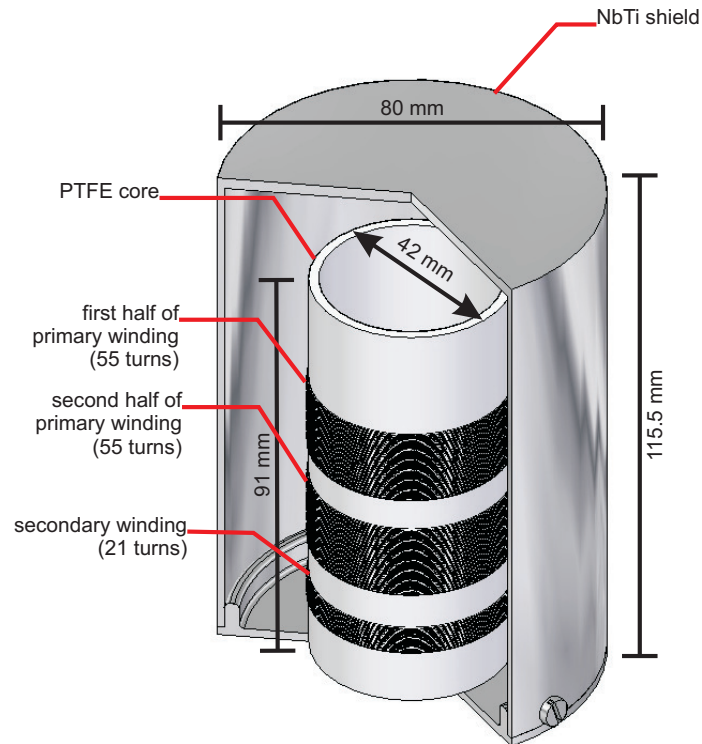


Figure 4.20: Drawing of the helical resonator used for the narrow-band FT-ICR detection in the precision trap. A primary winding of NbTi wire separated into two packages of 55 turns each and a secondary winding with 21 turns are held by a PTFE core. The coil is mounted inside an NbTi shield. The connection of the different parts of the coil to the trap and the following amplifier is done via copper wires.

ring electrode as shown in Fig. 4.21. It consists of a primary winding of PTFE-insulated NbTi wire around a hollow PTFE core which are connected to the detection electrodes, and a secondary winding to couple the signal to the following cryogenic amplifier. Fig. 4.20 shows the dimensions and gives the turn numbers for a test coil, which matches the cyclotron frequency of the easily available rubidium isotopes $^{85,87}\text{Rb}$. The coil is mounted inside a polished NbTi shield. This concept has been taken from helical resonators used in radio communications as high- Q filters [Maca1959]. As discussed in Sect. 3.3.2, the inductance L of the coil forms a tuned circuit with the parasitic capacitance of the trap and the wires. Thus, the detection bandwidth $\Delta\nu$ is reduced and the signal-to-noise ratio is improved. Further noise reduction is achieved by operating the trap at $T = 77\text{ K}$. Fig. 4.21 gives an overview on the different temperature zones in which the signal processing circuits are placed. The primary side of the coil has a center tap to connect the DC voltage to the ring electrode segments which is required for the trapping potential. In addition, tuning circuits are attached to both ends of the winding. By using varactor diodes, the parallel capacitance of the tuned circuit can be varied such that the resonance frequency of the narrow-band detection system matches the cyclotron frequency of the ion of interest. With a test configuration, the mass range covered by this system was about 10 atomic mass units [Kete2008]. The Q -value of the unloaded superconducting coil is about 15 000 and it reduces to 1 000 in case the coil is attached to the trap and the resonance tuning circuit. The intrinsic capacitance of the resonator is about 6 pF and its inductance about 340 μH . A new coil has been developed to be used

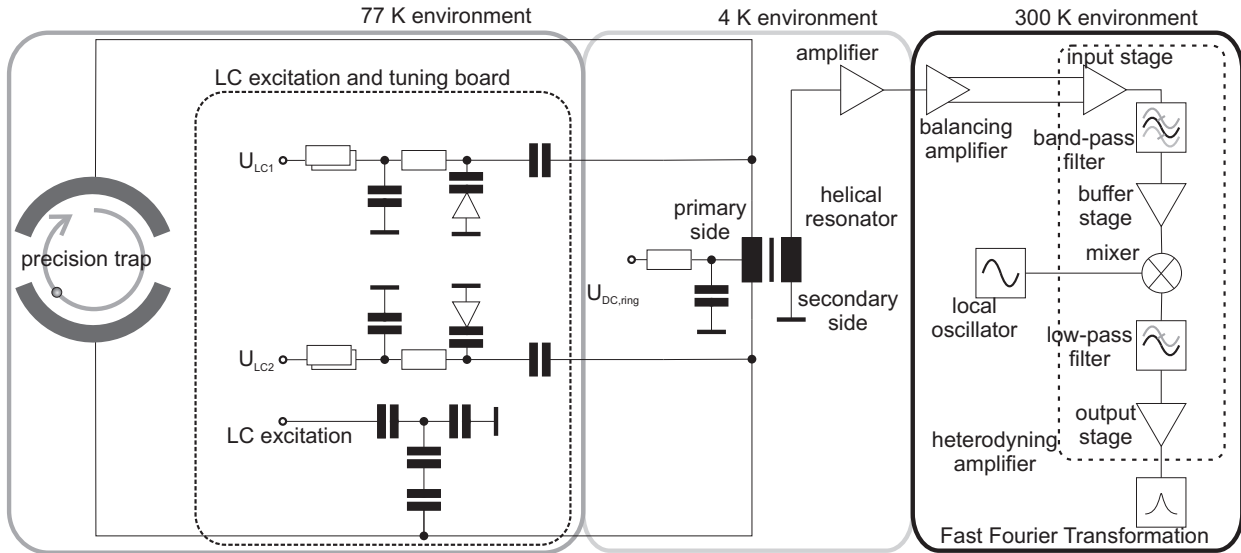


Figure 4.21: Signal processing circuit for the narrow-band FT-ICR. The induced image current is detected via two 140° segments of the ring electrode, which are connected to the primary side of the superconducting coil. Both packages of the primary side are connected via a center tap to apply the DC voltage for the ring electrode segments. The resonance frequency of the coil can be shifted to match the ion frequency by two circuits using varactor diodes. The signal is coupled to a 4-K amplifier via the secondary side. For details about the further signal processing see text.

in the frequency range required for nuclides above uranium [Kett2009]. Further tests are presently ongoing [Eiba2012].

A transistor amplifier at $T = 4\text{ K}$ is connected to the secondary side of the superconducting coil, which feeds an operational amplifier at room-temperature. The latter creates a differential output signal which is less sensitive to external distortions outside the vacuum chamber. A heterodyning amplifier follows subsequently, which shifts down the signal frequency (500 kHz-1 MHz) to frequencies below 10 kHz. Prior to a discrete Fourier Transformation the analogue signal is sampled by an analogue-to-digital converter (ADC), which has a limited number of samples in the transient. Thus, the product of the sampling rate and the number of samples determines the transient length, which is the inverse of the frequency-domain bin width after the Fourier Transformation. To obtain a maximum resolution the sampling rate has to be at the limit allowed by the Nyquist theorem, which is twice as large as the highest frequency component in the signal. Therefore, the signal frequency is reduced by the heterodyning amplifier. Band-pass and low-pass filters ensure that the correct frequency component is transferred to the ADC.

The sampling and the discrete Fourier Transformation are carried out for both narrow-band and broad-band FT-ICR by the same NATIONAL INSTRUMENTS data acquisition card *NI PCI-4551*. This card provides two analogue inputs with a maximum frequency of 102.4 kHz. To perform the Fourier Transformation a Fast Fourier Transformation (FFT) algorithm is used.

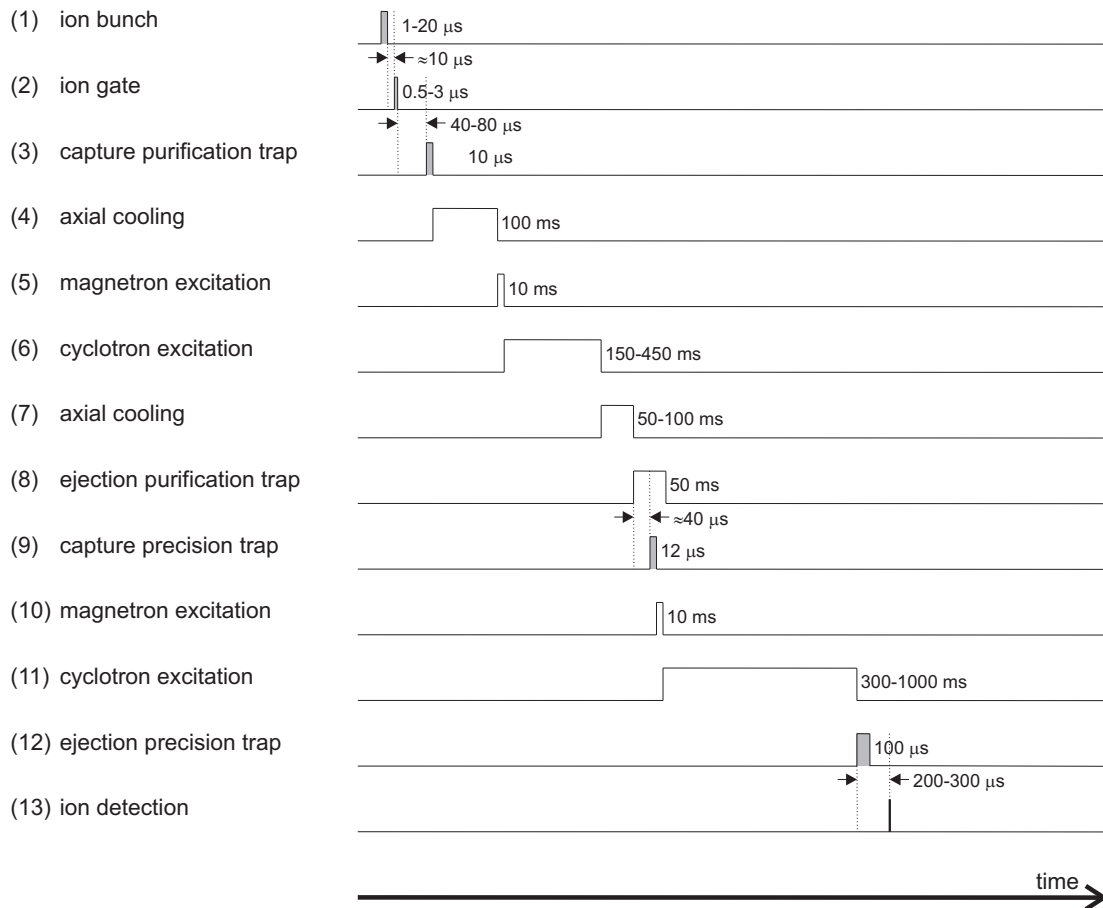


Figure 4.22: Typical measurement cycle for a time-of-flight mass measurement. The grey pulses are enlarged for a better visibility. The delays given by the distances between the dashed lines are charge-to-mass dependent and have to be adapted for each ion species. For more details see text.

4.7 Measurement procedure

A typical timing scheme for a TOF-ICR measurement cycle (with time steps (1)-(13)) is shown in Fig. 4.22. It starts with the ion creation (1) labeled by ‘ion bunch’. In principle, three different ion sources are coupled to TRIGA-TRAP, which are the surface ion source, the laser ablation source, and the on-line ECR source. Each of them can be operated to obtain ion bunches with a width of typically a few μs . After a flight time of about $10 \mu\text{s}$ the ions reach the ion gate (2), which allows transmission only for a short time. Thereby, unwanted ion species can be already suppressed to a certain fraction. The entrance electrodes of the purification trap (left endcap and left correction electrodes) are lowered after a q/m specific delay for $10 \mu\text{s}$ to capture the ions (3). First, the axial motion is damped in the buffer-gas for about 100 ms (4). Subsequently, a mass independent dipolar excitation increases the magnetron radius of all stored ion species simultaneously (5). In the next step, a quadrupolar excitation at the cyclotron frequency of the ion of interest is used to centre the desired ion species in the purification trap (6). The duration of this excitation is a compromise between a high mass resolving power and a cycle length appropriate for short half-lives. Before the ions are ejected (8) by lowering the exit electrodes (right correction electrodes and right endcap), they are stored in the buffer-gas

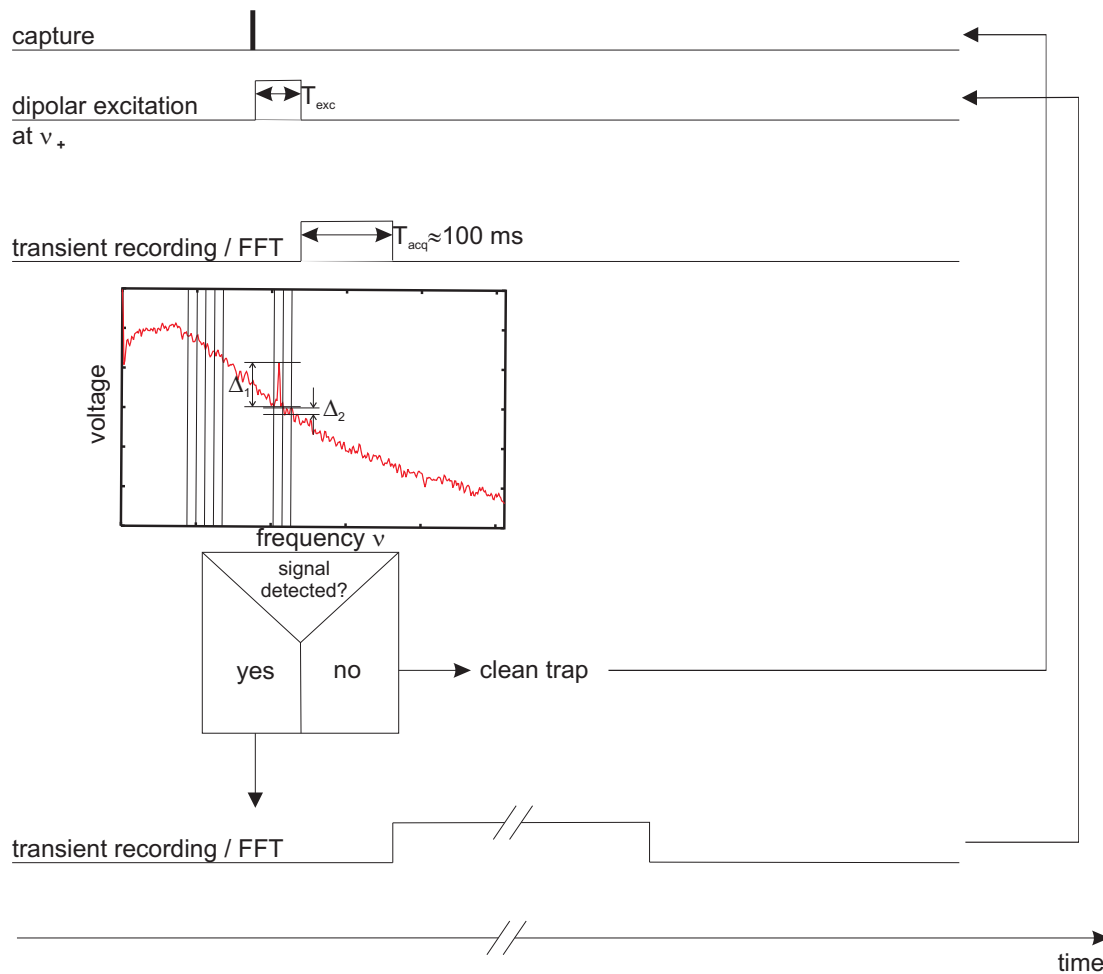


Figure 4.23: Simplified narrow-band FT-ICR measurement procedure in the precision trap. The cyclotron amplitude of the ion of interest is increased by a short dipolar excitation pulse at ν_+ . In a next step, a transient of about 100 ms length is taken to apply the stopping condition on the spectrum. At this point, the decision is made whether to clean and reload the trap or to continue the transient recording. For details see text.

for additional 50-100 ms to damp away the remaining cyclotron motion (7). The transfer to the precision trap takes about $40 \mu\text{s}$ (9). Here, the actual time-of-flight mass measurement is performed as described in detail in Sect. 3.3.1. The magnetron excitation is again 10 ms (10) and the cyclotron excitation time can be varied between 300 ms and 1 s, or even longer (11). For the Ramsey technique (see Sect. 3.3.1), the timing structure is similar with the difference that the cyclotron excitation is splitted into two pulses interrupted by a certain waiting time. After ejection from the precision trap (12), the ions need about $200\text{-}300 \mu\text{s}$ (using the voltage settings in Tab. 5.1) to reach the detector located at the end of the drift section (13). The complete cycle described here is repeated while changing the frequency of the cyclotron excitation in the precision trap, to obtain the typical time-of-flight resonance profile.

In case of an FT-ICR measurement, the scheme differs only in the excitation steps in both traps and the final ion detection. In the purification trap, the standard procedure of mass-selective buffer-gas cooling is also applied. It has to be mentioned that the broad-band image current detection system will be only used

to get complete mass spectra of the ion bunch coming from the source. In this case, only a broad-range dipolar excitation is applied to increase the cyclotron orbits of all ions before the image current transient is recorded. For a high-precision mass measurement on a single ion, the ion of interest is prepared and transferred to the precision trap similar to Fig. 4.22. After capturing in the precision trap, a short dipolar excitation at the modified cyclotron frequency ν_+ is applied to increase the cyclotron amplitude for a better signal-to-noise ratio. Subsequently, a transient of about 100 ms length is recorded. The measurement program decides whether an ion is in the trap and the transient recording can be continued or not. This stopping condition is obtained by dividing the spectrum into frequency intervals. Within each interval i , the difference Δ_i between the maximum and the minimum signal levels is determined. In the inset of Fig. 4.23 this is done for two intervals ($i = 1, 2$). In case an ion is stored in the trap, for one or more intervals the value of Δ_i will be significantly larger than for the remaining ones due to a peak. In this case, the transient recording is continued. If no ion is detected, the trap is cleaned (all electrodes are switched down for a short time) and loaded again. The same measurement cycle is applied to the ion of interest as well as to the reference ions. To calibrate the magnetic field B and the trapping potential V_0 , reference measurements with two different carbon cluster species are needed before and after the measurement of the ion of interest (see Eq. (3.54)).

For both, the TOF-ICR and the FT-ICR measurement, the observation time⁹ is limited by the half-life of the ion of interest. The typical coherence time in a Penning trap at a pressure of better than 10^{-8} mbar is longer than the half-life of the short-lived nuclides under investigation ($T_{1/2} \approx 1$ s), so it does not set a limit here. For the FT-ICR method, the damping constant for energy losses due to the measurement process is again much longer than typical half-lives.

4.8 The TRIGA-TRAP control system

Medium-sized experiments with a limited amount of available beam-times like TRIGA-TRAP require a stable and reliable control system that can handle all process variables. Moreover, a distributed system is needed to share the CPU load and to enable remote control of the experiment. A simple and unambiguous data acquisition should be included as well, which links all measured data to an individual setting of the process variables. Finally, the maintenance and the expansion for new pieces of hardware should be simple tasks that can be done by PhD students with typically three years working period. Since other facilities comparable to TRIGA-TRAP faced the same problems and already found a solution in the *LabView* based CS from GSI [Beck2004], the choice was easy to join this community. In a close collaboration with D. Beck from the DVEE¹⁰ department of GSI and the SHIPTRAP experiment, the CS was adapted and implemented at TRIGA-TRAP. Other Penning trap facilities using the CS are CLUSTER TRAP [Schw2006], ISOLTRAP [Mukh2008], SHIPTRAP [Raha2006], and LEBIT [Schw2003].

CS is an object-oriented, multi-threaded, and event-driven framework based on the NATIONAL INSTRUMENTS *LabView* development system and is designed to handle up to 10 000 process variables. The different elements of CS are distributed over several computers grouped to a domain, which is configured and controlled by a client-server application called Domain Management System (DMS). Hardware devices and software modules are represented by objects being instances of classes created during run-time. The defi-

⁹Observation time means the cyclotron excitation time in case of a TOF-ICR measurement and the transient length for the FT-ICR method.

¹⁰Datenverarbeitung und Experimentelektronik = Data processing and experiment electronics.

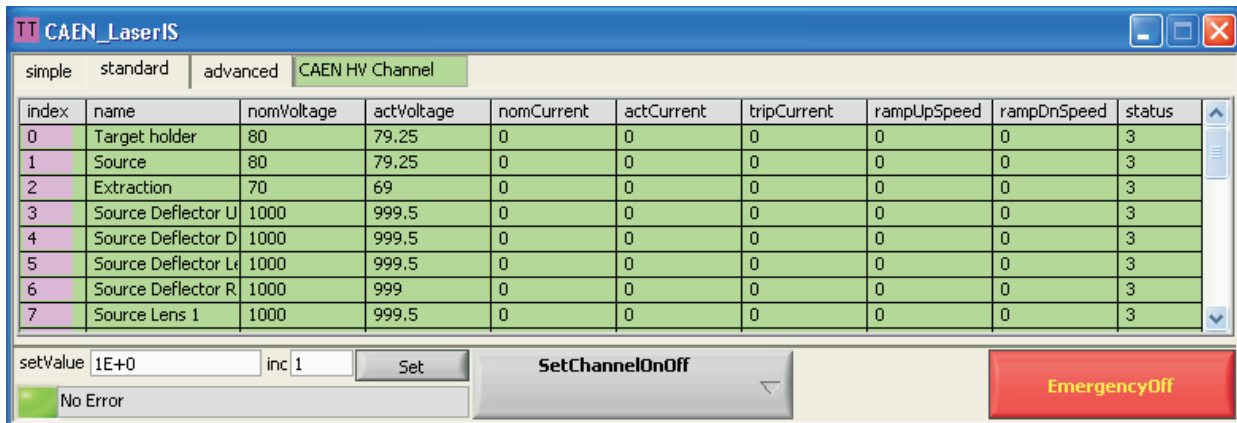


Figure 4.24: Sample screenshot of a voltage control panel of the laser ion source. The front panel itself is part of the CS developed at GSI Darmstadt [Beck2004]. All voltages for the ion sources and the transport sections have been implemented in such control panels.

nition of objects is done via an SQL¹¹ based database, which also contains the required configuration data used at the initialisation. The communication between the objects is handled via the Distributed Information Management (DIM) system developed at CERN [Gasp1993], which implements a publisher-subscriber architecture and leads to an event-driven communication. Each object in the CS publishes data via a so-called DIM service registered at a Domain Name Server (DIM DNS) so that the data can be accessed by other objects. To communicate with a hardware device, a graphical user interface (GUI) object (GUI layer) is used within CS, which addresses the device object providing all necessary methods (application layer). The communication to the device is finally established via a third-party driver library supplied by the hardware manufacturer (device layer). The CS framework provided by GSI already contains basic GUI objects, so that the main focus within this work in adapting the CS to TRIGA-TRAP was to implement device classes which were not available before. In total, the fully implemented system controls 115 voltages for the ion transport and storage, 4 frequencies, and 16 TTL pulses for the timing. In addition, the pressure of up to 12 gauges at different positions of vacuum chamber can be monitored. Moreover, stepper motors and engines are controlled which put the various detectors into the beam line and rotate the target of the laser ion source. Thus, the CS at TRIGA-TRAP enables fully remote operation of the complete mass spectrometer. Fig. 4.24 gives an example of a front panel for the voltage settings.

To control the time-of-flight measurement cycle as described in Sect. 4.7 a special GUI has been developed at LEBIT, which is called MM6. This GUI provides access to all devices required for the measurement and allows for the on-line analysis of the recorded data during the cycle. Fig. 4.25 shows a simplified diagram of the part of the TRIGA-TRAP control system used for the TOF-ICR measurement cycle. In this case, a sequencer object within CS is used to control the cycle: the user starts a measurement using the MM6 GUI and passes over full control to the sequencer, which communicates with the involved objects. Like this, the FPGA¹² card is triggered generating a TTL pulse pattern controlling the cycle. The sequencer sets the voltages on the high-voltage switches providing the trapping potentials as well as the frequencies and amplitudes of the arbitrary function generators (AFG) required for the excitation of the ion motion. Finally, the sequencer

¹¹Structured Query Language.

¹²Field Programmable Gate Array.

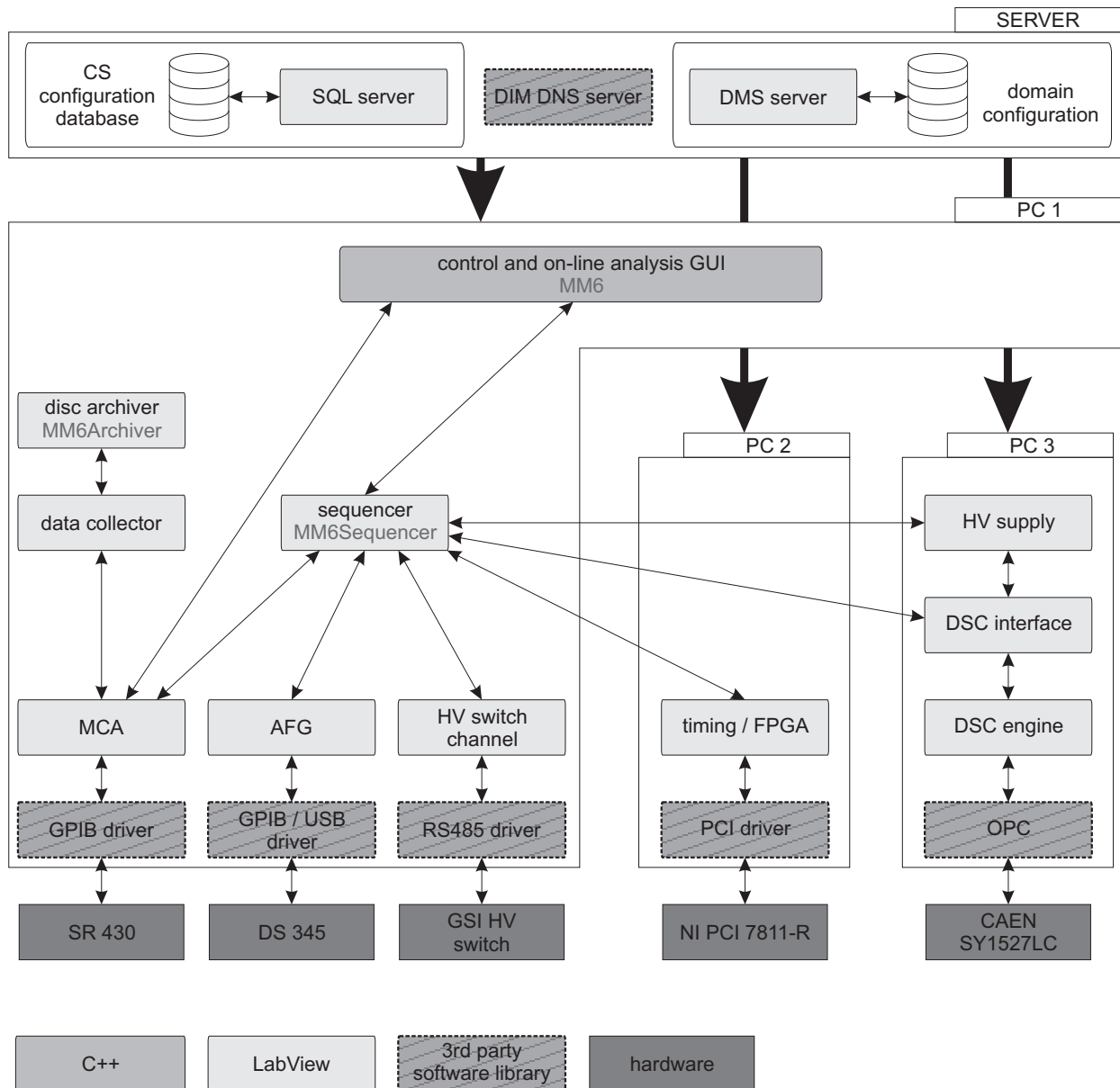


Figure 4.25: Part of the TRIGA-TRAP control system architecture as used for the TOF-ICR measurement cycle. For details see text.

triggers the read-out of the data acquisition device (in this case the multichannel-analyser (MCA)) by the data collector. The disc archiver module saves the data into a file for further analysis. Besides a time-of-flight measurement, MM6 can also start different other cycles needed for the preparation and optimisation of the complete setup prior to a mass measurement. For example, this includes any type of DC voltage scans for the beam transport via a multichannel high-voltage supply from CAEN. In Fig. 4.25, all non-standard modules for the cycle control which have been developed at other Penning trap facilities are labeled in light grey. It has to be mentioned, that a similar architecture has to be applied to the FT-ICR measurements which gets presently developed at the Max-Planck-Institute for Nuclear Physics in Heidelberg. In principle, the parts GUI, sequencer and disc archiver have to be modified or re-programmed and the data acquisition module has to be exchanged. Since CS is modular, the remaining parts can be kept without any change.

Part III

Results and discussion

5 Commissioning of the mass spectrometer

The commissioning of TRIGA-TRAP at the research reactor started in spring 2008 with the investigation of the field of the superconducting magnet as described in [Repp2008]. In parallel to the assembling of the vacuum system, the ion optics, and the Penning traps, extensive simulation studies were performed to determine the optimal configuration for the ion transport (see Sect. 5.1). The vacuum tube inside the magnet has been aligned versus the magnetic field direction using a narrow electron beam generated by a miniature cathode. The best adjustment is achieved if the electron beam is coaxially centred inside the tube, since the axis is parallel to the magnetic field direction in this case [Repp2008]. A residual tilt angle between the trap axis and the magnetic field vector leads to a mass-independent shift of the cyclotron frequency (see Sects. 3.4 and 5.3) and, thus, has to be minimised. After that the trap electrode stack has been inserted. All remaining electrode structures (see Fig. 4.11) were subsequently aligned versus the traps using a theodolite.

After successfully storing ions in the purification trap, the parameters required for mass selective buffer-gas cooling, such as excitation times, frequencies, and amplitudes were optimised. The helium gas flow was fixed to 1×10^{-5} mbar l/s in order to ensure good vacuum conditions in the precision trap which is only separated by a differential pumping channel (see Sect. 4.5). To achieve sufficient cooling of the ion cloud, the storage time in the buffer-gas volume was increased instead (see Fig. 4.22 for a typical timing pattern). Prior to the actual mass measurement, the electric field in the precision trap had to be optimised using correction voltages as described in Sect. 5.1 and in [Beck2009]. Subsequently, all remaining influences on the frequency measurement in the precision trap leading to uncertainties in the mass measurement were investigated using carbon cluster ions (see Sects. 5.2 and 5.3) similar to studies at other facilities [Kell2003, Chau2007, Elom2009]. This chapter is closed by presenting the results of the direct mass measurement on ^{197}Au , demonstrating the accuracy of TRIGA-TRAP [Kete2010].

5.1 Simulation studies and electric field optimisation

In the ion trajectory simulation program SIMION 8.0, a so-called potential array representing the complete electrode structure shown in Fig. 4.11 has been implemented. For each point of this three-dimensional grid the electric potential is calculated by numeric relaxation using a fourth-order Runge-Kutta algorithm dependent on the voltages applied to the areas specified as electrodes [Dahl2000]. The magnetic field of the superconducting magnet has been included as well in the ion trajectory simulations, by using a rather simple model consisting of three pairs of Helmholtz coils for which the field magnitude can be calculated analytically [Verd2003, Verd2006]. The geometric parameters such as the positions of the coils, their radius and length, as well as the current, have been adjusted to the measured points on axis of the magnet bore (see Fig. 4.13) [Repp2008]. Since superconducting magnets consist of a complex coil geometry optimised to provide a very homogeneous field within a certain volume, only the general trend could be reproduced, which is sufficient for the simulation studies performed here.

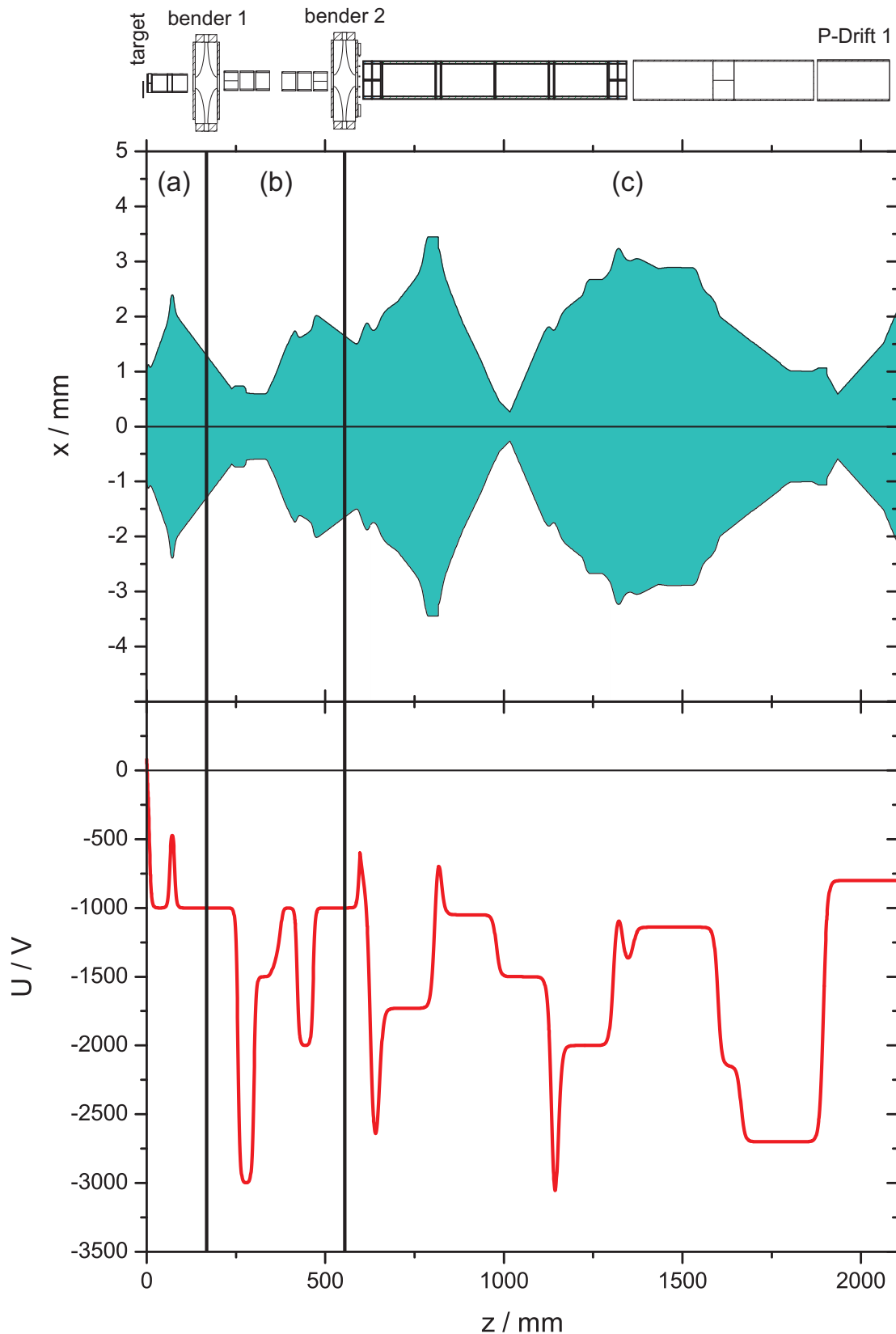


Figure 5.1: Simulation of the ion transport from the laser ion source to the superconducting magnet. (a) consists of all optical elements between the laser ion source and the first bender, (b) reaches until the second bender, and (c) until the magnet. All parts have been simulated individually but with ion starting conditions matching the previous section. The upper graph shows the beam diameter x as a function of the position z , the lower graph displays the corresponding electric potential U . For details see text.

A first crucial point is the ion transport from the off-line sources to the magnet. To ensure a high transport efficiency, the ion energy is increased to about 1 keV in this region, which is achieved by lowering the electric potential of all optical elements by 1 kV. The ion energy versus ground is always kept below 100 eV to be able to capture the ions in the purification trap. At this point it has to be mentioned that the results of simulation studies and their applicability to the real situation heavily depend on the knowledge of the starting conditions of the particles and of possible alignment errors in the setup. To this end, the optimal voltage settings obtained in the simulation are always taken as a starting point for further optimisation in the experimental setup. Fig. 5.1 shows the result of the simulation obtained for singly charged $^{12}\text{C}_{20}^+$ ions produced in the laser ion source with an initial energy of 0.1 eV and a maximum release angle versus the beam axis of 45° . Here, the magnetic field is neglected. In Fig. 5.1 the three parts, the ion source (a), the transfer between both benders (b), and the ion optics in front of the magnet (c) have been simulated individually. At the end of each part, the ion position and the velocity vector have been determined to use them as starting conditions for the following section. Like this, the complete ion transport to the magnet could be simulated. The upper graph in Fig. 5.1 shows the beam diameter as a function of the position along the axis. Since all optical elements are of cylinder symmetry, the beam profile exhibits the same symmetry. This statement is, of course, only true for the ideal case, where no alignment errors have to be corrected and, thus, the deflectors are kept on identical potential. Moreover, the benders are not of cylinder symmetry in general, but for this simulation -1 kV was applied to all electrodes, so that the error introduced by this approximation should be small. The electric potentials shown in the lower graph are the results of an iteration between simulation and optimisation in the real setup, which is carried out by maximising the count-rate on MCP1 (see Fig. 4.11).

Further simulations of the complete setup have been performed including the injection into the Penning traps located in the strong magnetic field, and the ejection of the ions through the drift section towards the detector. The total transport efficiency has been studied in SIMION for $^{133}\text{Cs}^+$ ions produced in the surface ion source resulting in a value between 15-25% [Smor2008] for the operation mode without trapping. In this case, the pumping barrier channel limits the efficiency whereas almost no ion losses occur due to the remaining parts of the setup. The diameter of the channel used in the simulation was 3 mm, while the diameter used presently in the real setup is only 1.5 mm. Of course, alignment errors in the real setup will further decrease this number. For the laser ablation ion source, the transport efficiency should be similar, since the studies shown in Fig. 5.1 indicate no ion losses until the second bender. In the real setup, studies have been performed using $^{197}\text{Au}^+$ produced by the laser ion source, since gold has only one stable isotope which can be ionised using a thin foil as target. Here, the efficiency between the laser ion source and MCP1 was 22%, and between MCP1 and CEM2 14%. This leads to a total transport efficiency of about 3%, which is similar to other Penning trap mass spectrometers [Raha2006]. It has to be mentioned that the total efficiency is certainly much higher in case the ions are first stored and cooled in the purification trap during a normal measurement run. Thus, all ions reaching the first trap pass the narrow pumping barrier. A list of all voltages used in the setup, which are a result of simulation studies and on-line optimisation, is given in Tab. 5.1.

An important step towards a time-of-flight resonance obtained with the precision trap is to tune the voltages of the two sets of correction electrodes (see Fig. 4.17) such that higher order perturbations to the ideal quadrupole potential are minimised (compare Eq. (3.21)). Higher order contributions to the magnetic field (see Eq. (3.24)) have been reduced during the shimming process of the superconducting magnet using correction coils [Repp2008] and no further changes are possible. Prior to the E-field optimisation, the delay

electrode	voltage / V	electrode	voltage / V	electrode	voltage / V
LIS target holder	+80	Ion gate	-200 V / +600 V	P-Ring	-10
LIS source	+80	Deflector 1 up	-800	P-RIC	-20 / -0.9
LIS extraction	-140	Deflector 1 down	-800	P-ROC	-20 / +34.8
LIS deflector up	-1000	Deflector 1 left	-800	P-RE	-20 / +60
LIS deflector down	-1000	Deflector 1 right	-800	Funnel	-20 / +180
LIS deflector left	-1000	Deflector 2 up	-2890	Drift 0	-20
LIS deflector right	-1000	Deflector 2 down	-2890	LEC	-20 / 1.86
LIS lens 1	-1000	Deflector 2 left	-2890	LE	-20 / -3
LIS lens 2	-400	Deflector 2 right	-2890	LRC	-20 / -7.94
LIS lens 3	-1000	Lens 1.1	-1730	Ring	-10
Bender 1.1	-2350 / -1000	Lens 1.2	-410	RRC	-14 / -7.94
Bender 1.2	-50 / -1000	Lens 1.3	-1050	RE	-14 / -3
Bender 1 house	-1000	Lens 2.1	-1500	REC	-50 / 1.86
Source defl. 1 up	-1000	Lens 2.2	-3690	Drift 1	-60
Source defl. 1 down	-1000	Lens 2.3	-2000	Drift 2a	-60
Source defl. 1 left	-1000	Deflector 3 up	-1064	Drift 2b	-60
Source defl. 1 right	-1000	Deflector 3 down	-1000	Drift 3a	-10.5
Source lens 2	-3000	Deflector 3 left	-940	Drift 3b	-60
Source lens 3	-1500	Deflector 3 right	-1050	Drift 4	-256
Source lens 4	-1000	Deflector 4 up	-1098	Drift 5	-930
Source lens 5	-2000	Deflector 4 down	-1479	Drift 6	-440
Source defl. 6 up	-1000	Deflector 4 left	-1465	Drift 6 up	-345
Source defl. 6 down	-1000	Deflector 4 right	-1615	Drift 6 down	-385
Source defl.6 left	-1000	Lens 3.1	-1140	Drift 6 left	-350
Source defl. 6 right	-1000	Deflector 5 up	-2237	Drift 6 right	-385
SIS source	+102	Deflector 5 down	-2071	Drift 7	-1116
SIS extraction	-660 / +200	Deflector 5 left	-2230	Drift 8	-487
SIS deflector up	-1000	Deflector 5 right	-2141	Drift 9	-1400 / 0
SIS deflector down	-960	Lens 3.3	-2700		
SIS deflector left	-1000	P-Drift 1	-801		
SIS deflector right	-1012	P-Drift 2	-550		
SIS lens 1	-1000	P-Drift 3	-500		
SIS lens 2	-3000	P-LE 1	0		
SIS lens 3	-1000	P-LE 2	+50 / +200		
Bender 2.1	-2000 / -1000	P-LE 3	-10 / +60		
Bender 2.2	0 / -1000	P-LOC	-10 / +34.8		
Bender 2 house	-1000	P-LIC	-10 / -0.9		

Table 5.1: List of all voltages used on the transport and trap electrodes from the ion sources to the final detector. The settings for the purification trap are marked in light gray, those of the precision trap in dark gray. In total, more than 100 voltage settings have to be optimised. For switchable electrodes both voltage values are given. See Fig. 4.11 for an explanation of the labels.

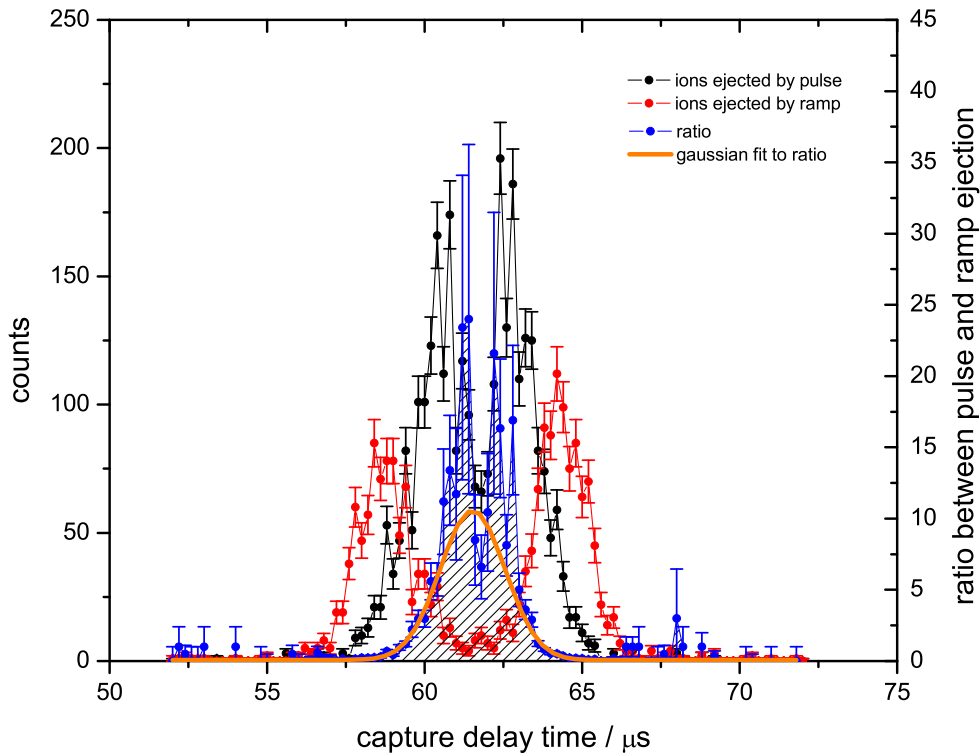


Figure 5.2: Optimisation of the capture delay time in the precision trap for $^{12}\text{C}_{20}^+$ ions. The different data sets represent the hot ions ejected by ramping the ring electrode voltage (red), the cold ions ejected by pulsing the endcap (black), as well as the ratio of both (blue). The optimal capture delay time $t_{\text{opt}} = 61.52(2) \mu\text{s}$ is determined by a Gaussian fit to the ratio values. For details see text.

between the ion ejection from the purification trap and the capturing in the precision trap has been determined as described in [Beck2009]. Here, the ring voltage is ramped up from the nominal value¹ of -10 V to -100 mV within a time of 16 ms to eject hot (high energetic) ions. Only 1 ms later, the endcap and endcap correction voltage are pulsed down to 220 mV below the present ring voltage to release the cold (low energetic) ions which still remained in the trap. The result is shown in Fig. 5.2, giving the number of ejected ions as a function of the capture delay separately for the ramp and the pulse ejection. This procedure allows to capture the ions at the lowest possible energy ($t_{\text{opt}} = 61.52(2) \mu\text{s}$), when the trap is closed with the ions exactly in the potential minimum². The curve for the ions ejected by the pulse shows a minimum for the optimal capture delay time which is due to the fact that the voltage of ‘drift3a’ has to be slightly lowered not block the low energy ions. To probe electric field imperfections, ν_+ is an ideal candidate since the frequency is rather high

¹During this test, the trapping potential was set to 10 V leading to an endcap voltage of 0 V. The trap depth was later changed to the final value of 7 V which does not affect the capture delay.

²Since the deviation between the capture delays obtained with the more complicated procedure in [Beck2009] and with simply looking for a maximum of the ion number as function of the capture delay without ramping the ring voltage is negligible, the latter is routinely applied at TRIGA-TRAP.

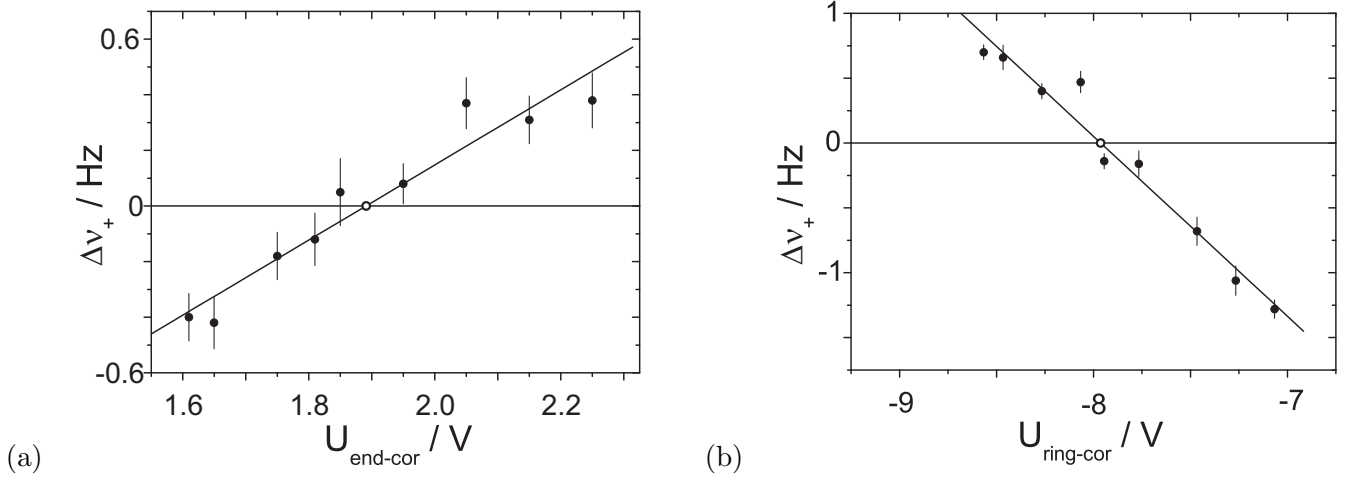


Figure 5.3: Shift of the reduced cyclotron frequency $\Delta\nu_+$ between two different capture times $t_{\text{opt}} = 61.52 \mu\text{s}$ and $t_{\text{off}} = 60.52 \mu\text{s}$ in the precision trap as a function of the endcap-correction (a) and the ring-correction voltage (b). For the optimal correction voltages, the shift vanishes (open circles). For details see text.

endcap correction voltage	1.86(30) V
ring correction voltage	-7.94(82) V

Table 5.2: Best tuning voltages of the precision trap for a ring offset of -10 V and a trap depth of 7 V.

and dependent on the potential (see Eq. (3.17)). To this end, ν_+ has been measured for two different capture delay times corresponding to different ion energies versus the bottom of the trap, obtained for the optimal capture delay t_{opt} (minimum energy) and for $t_{\text{off}} = 60.52 \mu\text{s}$. The difference $\Delta\nu_+ = \nu_+(t_{\text{opt}}) - \nu_+(t_{\text{off}})$ is plotted in Figs. 5.3(a,b) as a function of the endcap and the ring correction voltage, which are symmetrically applied to both electrodes of the individual sets. The best tuning given in Tab. 5.2 is obtained by a linear interpolation to $\Delta\nu_+ = 0$ for both electrode sets³.

5.2 Stability of the magnetic field

Reasons for changes in the magnetic field have been discussed in Sect. 3.1.2. To this end, the stability of the magnetic field at TRIGA-TRAP has been investigated by repeated cyclotron-frequency measurements with $^{12}\text{C}_{20}^+$ ions in the precision trap [Kete2010]. Here, a Ramsey excitation profile with two 100 ms pulses and a waiting time of 800 ms was used. The result is presented in Fig. 5.4 by the relative deviation of the cyclotron frequency $\Delta\nu_c/\nu_c$ as a function of time. In addition, the temperature of the air side wall of the vacuum trap tube is shown, exhibiting a strong correlation. The lower graph in Fig. 5.4 displays the environmental temperature and the air pressure inside the reactor hall for completeness. Due to the strong

³In the literature a tuning ratio is defined for 5-pole traps (with only one set of correction electrodes) as the ratio between correction and ring voltage. To avoid confusion with this definition, the absolute voltages for the 7-pole trap are given here instead.

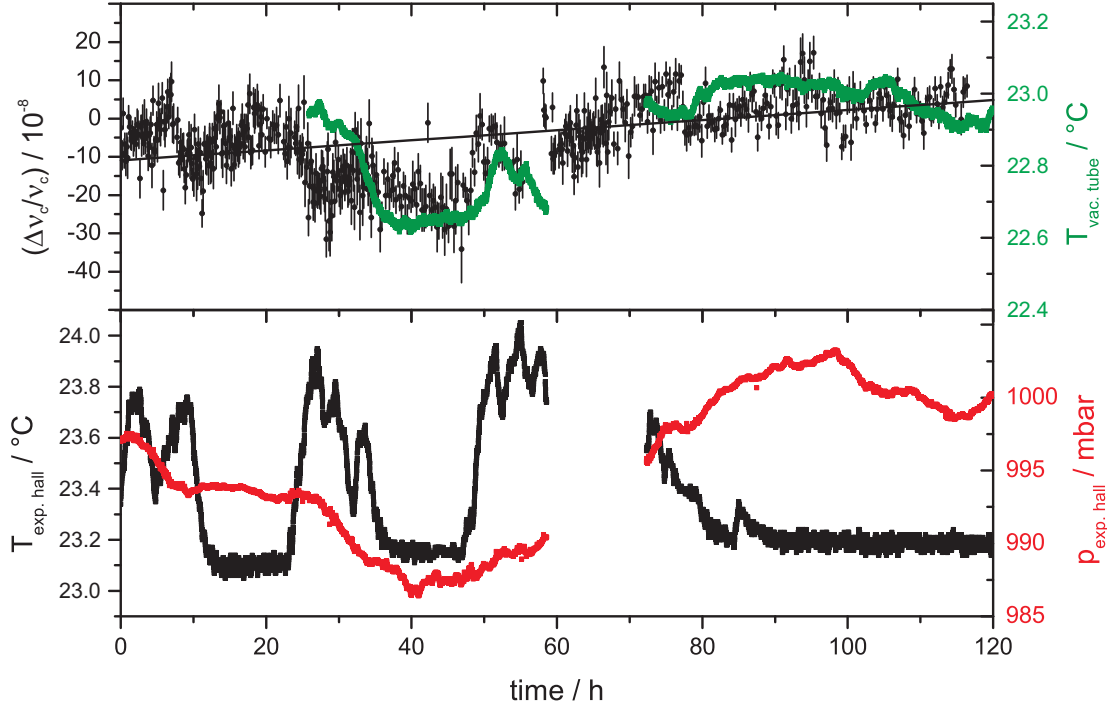


Figure 5.4: Relative deviation of the cyclotron frequency $\Delta\nu_c/\nu_c$ as a function of time (upper graph). The solid line is a fit to the frequency data points to estimate the linear trend. In addition the temperature $T_{\text{vac.tube}}$ of the air side of the vacuum tube housing the Penning traps is given. The environmental temperature $T_{\text{exp.hall}}$ and air pressure $p_{\text{exp.hall}}$ in the reactor hall are also shown (lower graph) for comparison. Due to a failure in the automatic logging system, no data is available for a certain time period. For details see text.

correlation between the vacuum tube temperature and the frequency drift, the trap environment will later be temperature-stabilised using the liquid nitrogen reservoir. To this end, a pressure stabilisation system gets presently installed to reduce pressure fluctuations of the nitrogen exhaust, and, thus, to further suppress temperature changes. The linear trend of the magnetic field⁴

$$\frac{\Delta B}{B} \frac{1}{\Delta t} = 1.3(4) \times 10^{-9} / \text{h}, \quad (5.1)$$

which is already mentioned in Sect. 4.5, is estimated by a linear fit to the data points. Due to the correlation between magnetic field and bore temperature, this number can be only regarded as an estimate. In an earlier measurement with $^{133}\text{Cs}^+$ ions and a 300-ms standard cyclotron resonance, about a factor of 4 larger drift has been found but here the small temperature-induced effects were completely covered by the large uncertainty of each frequency point. However, the absolute number of the linear magnetic field drift does not enter any data evaluation as described in the following. Non-linear fluctuations are superimposed on the continuous change of the frequency, thus, causing an uncertainty in the determination of the cyclotron frequency of the reference ion $\nu_{c,\text{ref}}$ (compare Eq. (3.46)). Since $\nu_{c,\text{ref}}$ cannot be measured simultaneously to the cyclotron frequency of the ion of interest ν_c , a reference measurement is performed before and after the determination of ν_c . Finally, a linear interpolation yields $\nu_{c,\text{ref}}$ at the time of the measurement which enters Eq. (3.46).

⁴According to Eq. (3.7) the relative deviations are identical for the cyclotron frequency and the magnetic field.

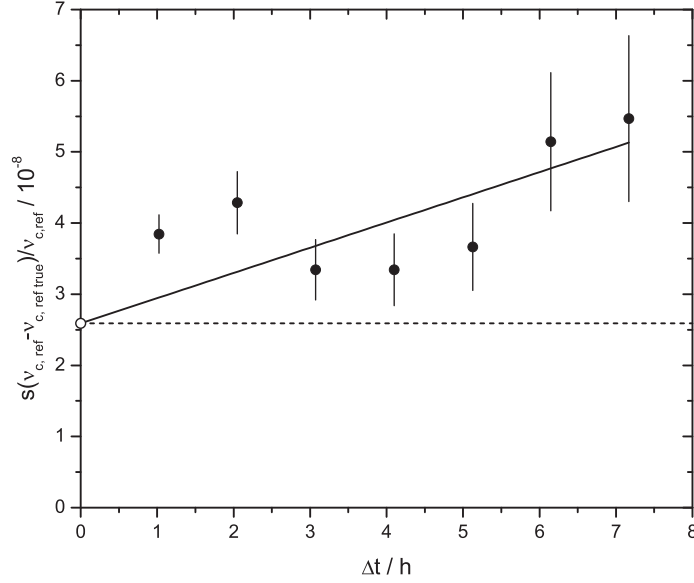


Figure 5.5: Relative deviation of the interpolated cyclotron frequency $\nu_{c,\text{ref}}$ from the measured true value $\nu_{c,\text{ref true}}$ as a function of the time interval Δt between the two reference measurements. The offset of the line is fixed to 2.59×10^{-8} , which is the mean relative uncertainty of a frequency measurement of 30 minutes length.

To account for non-linear fluctuations of the cyclotron frequency of the reference ion, the data displayed in the upper graph of Fig. 5.4 is subdivided into packages of about 30 minutes. This provides enough statistics for an individual evaluation of the cyclotron frequency of each package and the length is similar to the situation in a real mass measurement. Two blocks separated by⁵ Δt are taken as reference measurements to obtain the interpolated cyclotron frequency $\nu_{c,\text{ref}}$. The true reference frequency $\nu_{c,\text{ref true}}$ can be obtained from the package located in the center of the interval Δt . Fig. 5.5 shows the relative standard deviation $s(\nu_{c,\text{ref}} - \nu_{c,\text{ref true}}) / \nu_{c,\text{ref}}$ as a function of the time interval Δt . The offset of the linear fit corresponds to the mean relative statistical uncertainty of 2.59×10^{-8} of a single frequency measurement of 30 minutes length. The additional uncertainty of the interpolated reference frequency due to non-linear frequency fluctuations is given by the slope

$$\frac{u_f(\nu_{c,\text{ref}})}{\nu_{c,\text{ref}}} = 6(2) \times 10^{-11} / \text{min} \times \Delta t \quad (5.2)$$

and has to be added quadratically to the uncertainty of the interpolation. This value is similar to the ones obtained at other Penning trap mass spectrometers [Kell2003, Raut2007a, Raha2007].

5.3 Data analysis procedure and accuracy studies

Before the accuracy studies determining the uncertainties present at TRIGA-TRAP are discussed, the data analysis procedure based on TOF-ICR resonances as shown in Fig. 5.6 is briefly described. As discussed in Sect. 3.3.1, each point represents the mean time of flight of the ions corresponding to the frequency value. The error bars are calculated using the width of the total time-of-flight distribution and the number of ions

⁵The timings always refer to the center of each package.

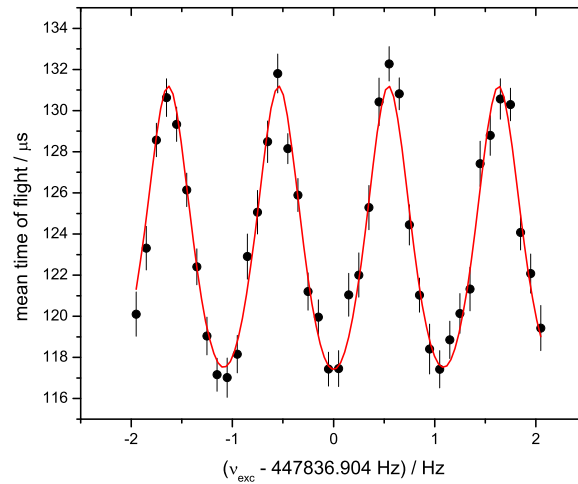


Figure 5.6: TOF-ICR resonance with $1626 \text{ }^{12}\text{C}_{20}^+$ ions using a Ramsey excitation profile of two 100 ms pulses and a waiting time of 800 ms. The centre frequency is $\nu_c = 447836.904(5) \text{ Hz}$, obtained by a fit (solid line) of the theoretical line shape [Kret2007] to the data.

for the individual points. In principle, also the individual time-of-flight distributions should be used, but due to a lack of statistics in usual mass measurements, the width has to be estimated based on all ions.

Data analysis procedure:

- To determine the damping coefficient $A_{\text{damp}} = \delta/m$, i.e. the parameter describing the ion mobility with rest gas atoms present in the trap, in a first step the appropriate theoretical line shape (see Sect. 3.3.1) is fitted to the data of each reference measurement using the analysis program *EVA* developed at LEBIT [Ring2009]. The mean damping obtained is then used as a fixed parameter for all following fits to the measured data. In most cases, the fit would not converge in case A_{damp} is free as well [Yazi2006a]. To assume a mean damping is justified by the fact that the residual gas pressure inside the precision trap always reaches an equilibrium level which stays constant during a complete mass measurement.
- A least-squares fitting of the theoretical line shape to the measured data of the ions of interest as well as the reference ions yields the cyclotron frequencies ν_c and the corresponding statistical uncertainties $\delta\nu_{c,\text{stat}}$ (see Fig. 5.6). In order to identify and eliminate the influences of contaminant ions on the results, the analysis is performed separating the available data into count-rate classes [Kell2003]. Here, the events in one TOF-ICR resonance measurement are grouped in 3-5 classes of similar total event number according to the number of ions which were simultaneously detected, and the cyclotron frequency is determined for each class individually. Finally, the cyclotron frequency is extrapolated to a single ion stored in the precision trap, corresponding to 1 detected ion in case a CEM with conversion dynode is used (or 0.3 detected ions for an MCP due to the lower detection efficiency) [Yazi2006b]. This count-rate analysis is at least possible for the reference measurements where the statistics is large enough.
- The cyclotron frequency of the reference ion is interpolated to the time of the measurement of the

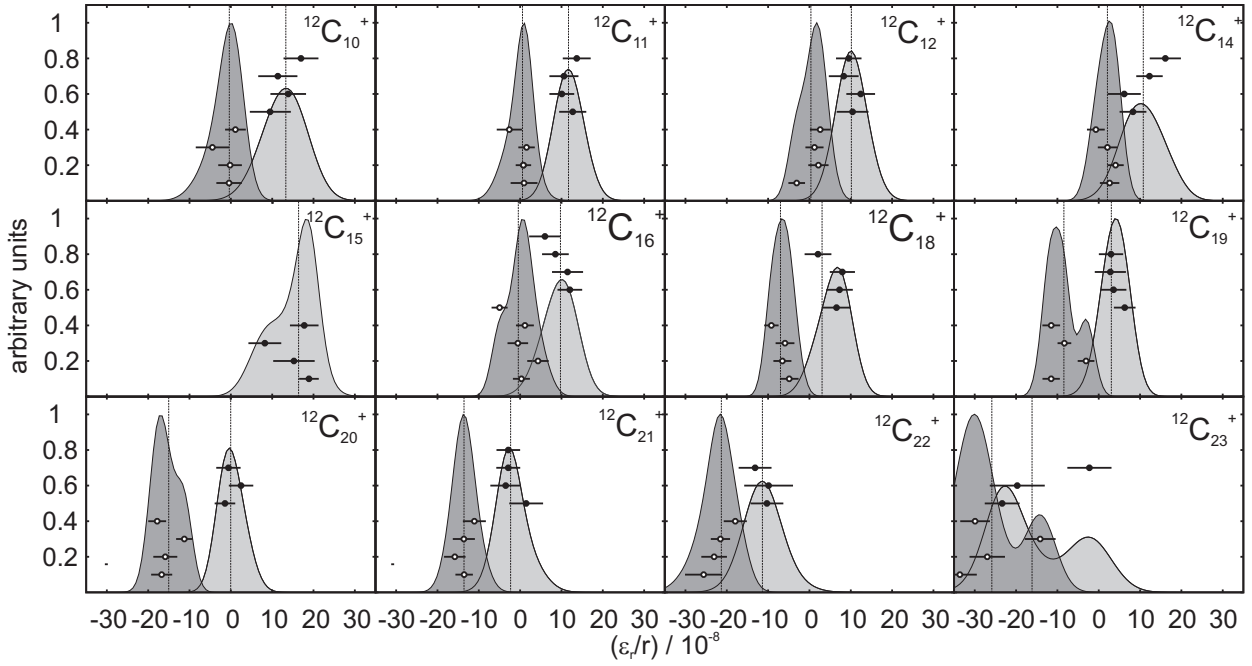


Figure 5.7: Ideograms of all 90 cluster cross-reference measurements with $^{12}\text{C}_{15}^+$ (open circles) and $^{12}\text{C}_{20}^+$ (filled circles) as reference ions. The measurements are represented by their relative deviation given in Eq. (5.6). The vertical dashed lines represent the mean values of the corresponding distributions. For details see text.

ion of interest as described in Sect. 5.2. This interpolated reference frequency is used to calculate the frequency ratio r_i (see Eq. (3.46)) for each individual measurement. To account for non-linear fluctuations of the magnetic field, the uncertainty given in Eq. (5.2) is added quadratically leading to the statistical uncertainty σ_i of the frequency ratio r_i .

- The mean frequency ratio r is calculated from all measurements of the same nuclide. To account for possible point scattering of the N individual frequency ratios r_i around the mean value, the statistical uncertainty of the mean value $(\delta r)_{\text{stat}}$ is always taken as the maximum of internal and external error defined as

$$\sigma_{\text{int}} = \frac{1}{\sqrt{\sum_i \frac{1}{\sigma_i^2}}} \quad (\text{internal error}), \quad (5.3)$$

$$\sigma_{\text{ext}} = \sqrt{\frac{1}{N-1} \sum_i \frac{(r_i - r)^2}{\sigma_i^2}} \times \sigma_{\text{int}} \quad (\text{external error}). \quad (5.4)$$

It has to be mentioned that frequency ratios strongly deviating from the mean value are excluded from the data evaluation if a certain experimental reason can be identified for the failure. This can be due to sudden changes in the environmental conditions like temperature or air pressure as well as in any step of the measurement procedure.

- Finally, systematic effects are accounted for which are identified by the studies reported in the following to ensure an accurate mass measurement.

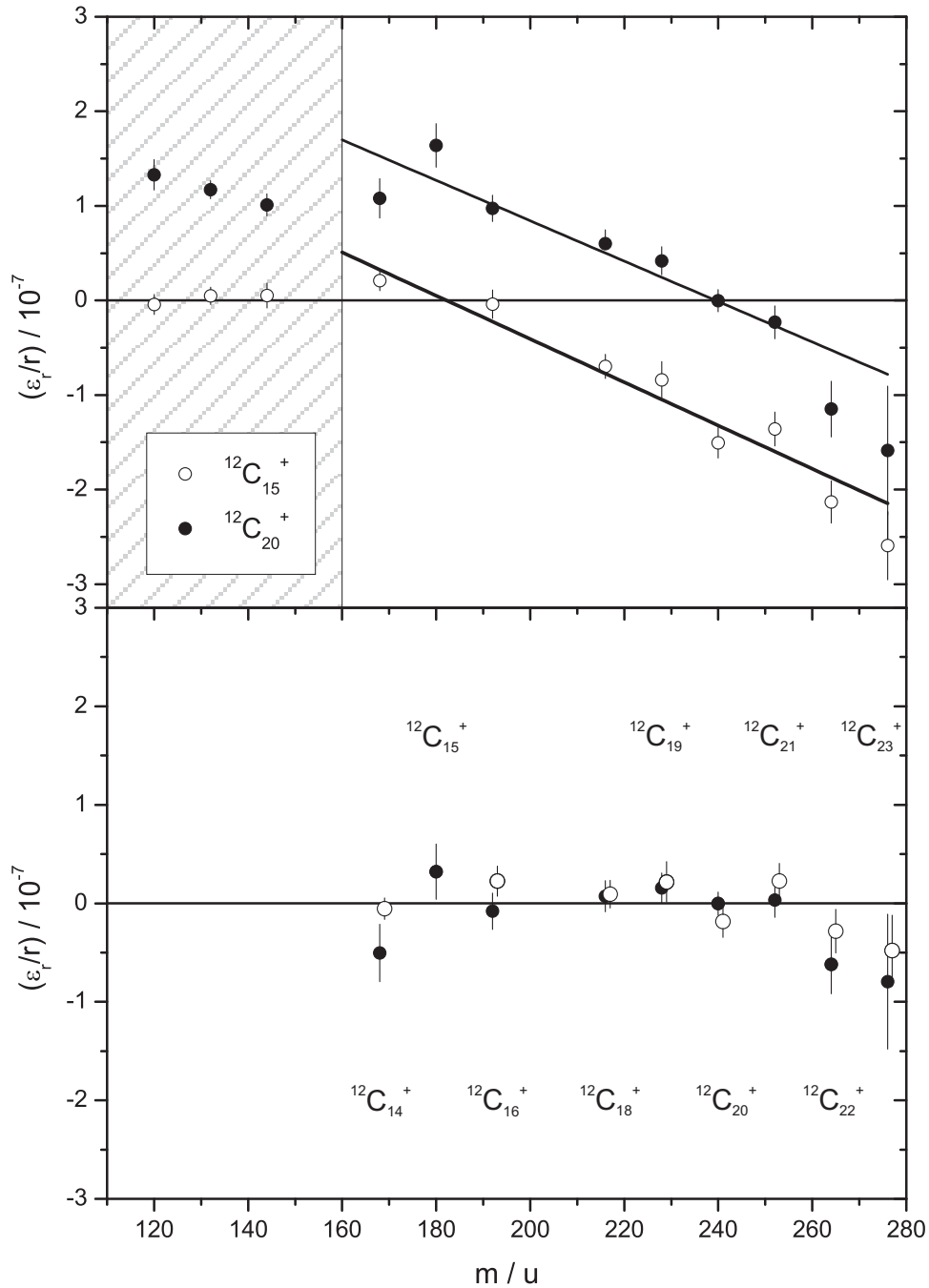


Figure 5.8: Relative deviation between the known and the weighted means of the measured frequency ratios as a function of the mass for two series with different reference ions (upper graph). The grey area represents the mass region not taken into account for the analysis reported here (for details see text). After correction of the mass dependent systematic shift, which is given by the average slope of both straight lines in the upper graph, the relative deviations are eliminated (lower graph).

Accuracy studies: The cyclotron frequency ratio between singly charged carbon cluster ions is exactly known

$$\frac{\nu_c(^{12}\text{C}_{n_1}^+)}{\nu_c(^{12}\text{C}_{n_2}^+)} = \frac{12\text{u } n_2 - m_e}{12\text{u } n_1 - m_e}, \quad (5.5)$$

since the the electron binding energy ($\approx 6\text{ eV}$) [Lark1977], the binding energy of the carbon atoms in the cluster ($\approx 10\text{ eV}$) [Lifs2000], and the uncertainty of the electron mass m_e ($< \text{meV}$) [Beie2001] can be neglected for our purpose. To this end, carbon clusters are an ideal tool to test the accuracy of mass measurements at TRIGA-TRAP by comparing the measured frequency ratios to the expected values [Kete2010]. The studies have been performed using a Ramsey excitation scheme with two 100 ms pulses and a waiting time of 800 ms producing time-of-flight resonances as shown in Fig. 5.6 for $^{12}\text{C}_{20}^+$ as an example. The results of 90 cross-reference measurements of cluster ions from $^{12}\text{C}_{10}^+$ to $^{12}\text{C}_{23}^+$ are displayed in Fig. 5.7, where $^{12}\text{C}_{15}^+$ and $^{12}\text{C}_{20}^+$ have been taken as reference ions. Each data point represents the relative difference between the known and the measured frequency ratio

$$\frac{\epsilon_r}{r} = \frac{r_{\text{known}} - r_{\text{measured}}}{r_{\text{measured}}}. \quad (5.6)$$

In addition, a Gaussian distribution with the uncertainty taken as the width is assigned for simplicity to each of the points. The sum of all distributions for a certain reference ion is displayed in the figure together with the mean value of the deviation ϵ_r/r , where a normalisation has been performed such that the larger sum distribution reaches one at its maximum. The complete setup is optimised for mass $A = 240$, which is especially true for the cooling of the ion bunch, the transport to the precision trap, and the electric potential of this trap (see Sect. 5.1). Thus, a mass dependent frequency shift becomes significant in case much lighter or heavier ions are used. To identify the problematic mass region, the cross-references are represented in the upper graph of Fig. 5.8 by the mean values of the distributions shown in Fig. 5.7 as a function of the mass for the two different reference ions. It can be clearly seen that clusters which differ by more than about 80 u from the mass the trap is optimised for, in this case clusters between $^{12}\text{C}_{10}^+$ and $^{12}\text{C}_{12}^+$, do not follow the general trend and, thus, are not considered in the following discussion. This low-mass region is anyhow not relevant for the results reported within this region. The slopes of the linear fits to both series of remaining data points are $-2.1(3) \times 10^{-9} / \text{u}$ for $^{12}\text{C}_{20}^+$ and $-2.3(2) \times 10^{-9} / \text{u}$ in case of $^{12}\text{C}_{15}^+$. The facts that both slopes agree with each other and that the horizontal zero line is crossed for the corresponding reference mass can be explained by a mass independent frequency shift introduced by imperfections of the electric field and a misalignment of the trap axis versus the magnetic field direction as discussed in Sect. 3.4. As shown in Eq. (3.75), this leads to a relative mass-dependent systematic shift of the frequency ratio. The value obtained by the average of the two slopes is

$$\frac{\epsilon_m(r)}{r} = -2.2(2) \times 10^{-9} \times (m - m_{\text{ref}}) / \text{u}. \quad (5.7)$$

At this point, the big advantage of carbon clusters as reference ions becomes obvious since $|m - m_{\text{ref}}|$ is limited to only 6 atomic mass units at maximum, thus, minimising the mass dependent effect. Moreover, since the absolute shift has been determined through the cross-references, each frequency ratio measured at TRIGA-TRAP will be corrected. The error given in Eq. (5.7) is quadratically added to the uncertainty. This mass dependent shift has been first investigated systematically using carbon clusters at ISOLTRAP, where the value determined is about one order of magnitude lower than at TRIGA-TRAP [Kell2003]. If the complete mass independent frequency shift leading to the effect observed is assigned to a misalignment of the trap axis versus

ion	reference	meas.	BR	r	$ME_{\text{TRIGA-TRAP}}$ / keV	ME_{AME2003} / keV	$\Delta\overline{ME}$ / keV
$^{197}\text{Au}^+$	$^{12}\text{C}_{16}^+$	5	2.37	1.0258676107(282)	-31142.58(5.04)	-31141.06(0.56)	-1.53(5.07)
$^{12}\text{C}_{15}^+$	$^{12}\text{C}_{16}^+$	6	1.19	0.9374998132(109)	-1.48(1.94)	0(0)	-1.48(1.94)

Table 5.3: Result of the mass measurement of ^{197}Au [Kete2010]. The columns contain the ion of interest, the reference ion, the number of individual measurements, the Birge ratio $BR = \sigma_{\text{ext}}/\sigma_{\text{int}}$, the mean frequency ratio r (see Eq. 3.46), the measured value $ME_{\text{TRIGA-TRAP}}$, the literature value of the mass excess ME_{AME2003} [Waps2003b] and the difference $\Delta\overline{ME} = ME_{\text{TRIGA-TRAP}} - ME_{\text{AME2003}}$.

the magnetic field direction which is more likely than a large perturbation of the electric field, the tilt angle would be about 0.3° (see Eq. (3.27)). At SHIPTRAP and JYFLTRAP a similar superconducting magnet with a horizontal bore and a similar holder system for the vacuum trap tube is used as at TRIGA-TRAP. The mass dependent shift is zero within the uncertainty at SHIPTRAP [Chau2007] and about half the value determined within this thesis work in case of JYFLTRAP [Elom2009]. To further increase the precision of the alignment and to correct the small tilt angle at TRIGA-TRAP as a future improvement, the procedure presently used at all facilities employing an electron beam [Repp2008] is no longer suited. Thus, the frequency shift (Eq. (3.27)) has to be investigated directly using stored ions while moving the trap tube inside the magnet bore in order to be much more sensitive. However, the present value of the mass dependent shift does not limit the accuracy of mass measurements at TRIGA-TRAP since it can be corrected.

After correcting the mass dependent systematic shift (Eq. (5.7)), the measured frequency ratios should be equal to the expected ones for all values of m (see lower graph in Fig. 5.8). In other words, the reduced chi-square

$$\frac{\chi^2}{N} = \sum_{i=1}^N \left[\frac{(\epsilon_r/r)_i}{\delta(\epsilon_r/r)_i} \right]^2 \approx \sum_{i=1}^N \left[\frac{r_{\text{true}} - r_{\text{measured}}}{\delta_{\text{measured},i}^{\text{total}}} \right]^2 \quad (5.8)$$

has to be one. In the studies reported here, a value of 1.15 was found, indicating that no further systematic uncertainty is present at TRIGA-TRAP at the present level of precision. At SHIPTRAP a residual systematic uncertainty of 4.5×10^{-8} has to be added [Chau2007], whereas the systematic limit at ISOLTRAP as well as at JYFLTRAP is only about 8×10^{-9} . In the case of JYFLTRAP only data with $|m - m_{\text{ref}}| \leq 24$ u has been used for the evaluation [Elom2009]. To ensure that the uncertainties determined within this work stay valid and no further error is introduced, frequency ratios between one or two additional carbon cluster ions will be always compared in each mass measurement.

To test the evaluation procedure and the uncertainties discussed above in a first high-precision mass measurement at TRIGA-TRAP, the nuclide ^{197}Au was used. Gold is an ideal candidate to demonstrate the accuracy of Penning trap mass spectrometers besides using carbon cluster ions, since only one stable isotope exists that can be easily ionised by the laser ablation ion source from a metallic foil target. Moreover, the mass of ^{197}Au is known with an uncertainty of only a few hundred eV, which is better than the precision aimed for in typical mass measurements of short-lived nuclides at TRIGA-TRAP. Tab. 5.3 shows the results

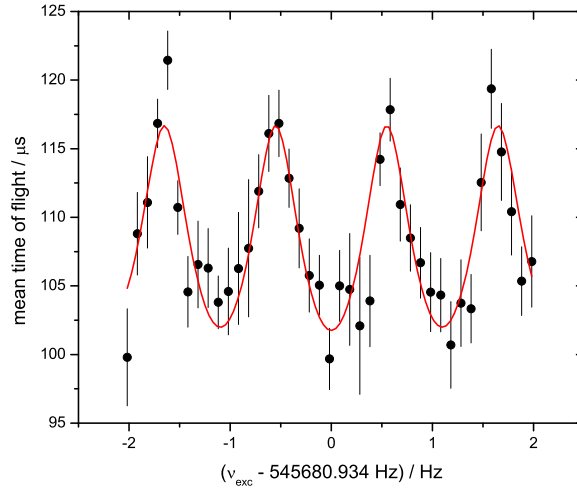


Figure 5.9: TOF-ICR resonance with 576 $^{197}\text{Au}^+$ ions using a Ramsey excitation profile of two 100 ms pulses and a waiting time of 800 ms. The centre frequency is $\nu_c = 545680.934(13)$ Hz.

for the mean frequency ratios⁶ obtained in the mass measurements of ^{197}Au (see Fig. 5.9 for a TOF-ICR resonance) and $^{12}\text{C}_{15}$ using $^{12}\text{C}_{16}$ as the reference with the mean damping determined to be $0.01(1)/\text{s}$ in this run. Moreover, the literature values of the mass excess

$$ME = (m_{\text{atom}} - A \times u)c^2 \quad (5.9)$$

taken from the Atomic-Mass Evaluation 2003 [Waps2003b] and the deviations $\Delta\overline{ME} = ME_{\text{TRIGA-TRAP}} - ME_{\text{AME2003}}$ of the values obtained at TRIGA-TRAP are also given. The Birge ratio as an indication for point scattering between the individual measurements is acceptable due to the low statistics. Fig. 5.10 graphically displays the deviations of the mass excesses, showing an excellent agreement between the literature values and the measurement reported here. As mentioned above, the binding energy of the carbon atoms in the cluster is neglected in case of $^{12}\text{C}_{15}$, thus, the literature value has no uncertainty.

Besides the demonstration of the accuracy of TRIGA-TRAP the mass measurement of ^{197}Au was also of high interest for ISOLTRAP since the isotope was used as the mass reference in the investigation of short-lived nuclides important for neutrino physics [Elis2010]. For these studies an independent confirmation of the present literature value for ^{197}Au was needed, since it changed by 15.9 keV between the Atomic-Mass Evaluations from 1995 [Audi1995] and 2003 [Waps2003b] (see Fig. 5.10).

5.4 Phase shift in the Ramsey excitation

As discussed in Sect. 3.3.1, the Ramsey excitation with two separated oscillatory fields can be used instead of a single continuous pulse. In mass spectrometry, this technique is so far only used with the second excitation pulse in phase with the first one. To generate this pattern, the output of a single frequency generator is

⁶For the mean frequency ratios within this work always three significant digits are given since this is the requirement for an implementation in the Atomic-Mass Evaluation.

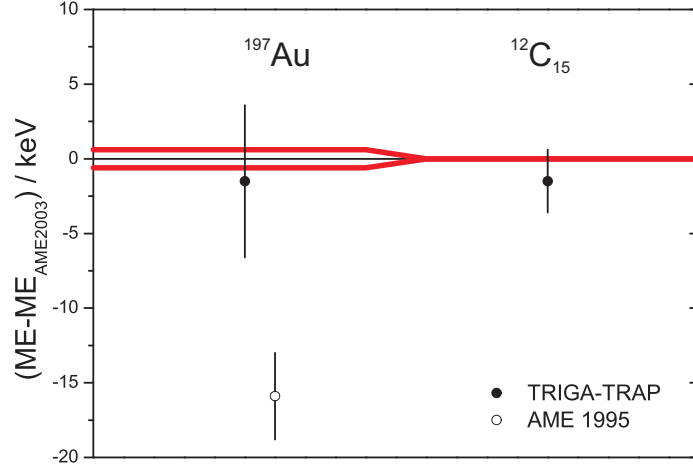


Figure 5.10: Mass excess differences between the TRIGA-TRAP (filled circles) and the literature values [Waps2003b] as given in Tab. 5.3. The horizontal zero line is defined by the literature values and their uncertainties are marked by the red lines, which is zero in case of the cluster ion. For completeness, the difference of the previous literature value [Audi1995] from the present one is also given for ^{197}Au (open circle). The error bars are one standard deviation of the literature value.

simply amplitude modulated as shown in Fig. 3.8(a). However, the theoretical line shape is discussed in the literature more generally, also allowing for a phase shift between the two pulses [Kret2007]. In case the ion is prepared in a pure magnetron orbit with radius $\rho_-^{(0)}$, the magnetron and cyclotron amplitudes after an excitation with a pulse pattern shown in Fig. 3.8(a) is given by

$$\begin{aligned}\rho_+^2 &= F_2(\rho_-^{(0)})^2, \\ \rho_-^2 &= (1 - F_2)(\rho_-^{(0)})^2,\end{aligned}\quad (5.10)$$

with the conversion probability [Kret2007]

$$F_2(\delta, T_1, T_0, g, \chi) = \frac{4g^2}{\omega_R^2} \left[\cos\left(\frac{\delta T_0}{2} + \frac{\chi}{2}\right) \sin(\omega_R T_1) + \frac{\delta}{\omega_R} \sin\left(\frac{\delta T_0}{2} + \frac{\chi}{2}\right) \{\cos(\omega_R T_1) - 1\} \right]^2. \quad (5.11)$$

Here, $\delta = 2\pi(\nu_{\text{exc}} - \nu_c)$ is the detuning of the excitation frequency, g the excitation amplitude, and χ the phase difference between the second and the first excitation pulse. Using Eqs. (5.10,5.11) in Eq. (3.41) finally leads to the theoretical line shape of the TOF-ICR resonance (Eq. (3.44)).

At TRIGA-TRAP the line shape was tested for three different non-zero phase shifts with $T_1 = 100$ ms and $T_0 = 800$ ms as shown in Fig. 5.11. For this purpose a second frequency generator was set to the appropriate phase, and a radiofrequency switch selected the proper signal for both pulses. The theoretical line shape could be experimentally confirmed for $\chi = 0, \pm\pi/2, \pi$. Small frequency deviations as visible in Fig. 5.11 originate from fluctuations of the magnetic field during the measurements as explained in Sect. 5.2. In [Dwor2006], it has been discovered that the data points at the position of the largest slope in the standard TOF-ICR resonance have the largest weight on the uncertainty of the cyclotron frequency. It has been speculated whether the use of a phase shifted Ramsey profile with $\chi = \pm\pi/2$ would lead to a further reduction of the uncertainty without enlarging the excitation time. To this end, TOF-ICR resonances with Ramsey

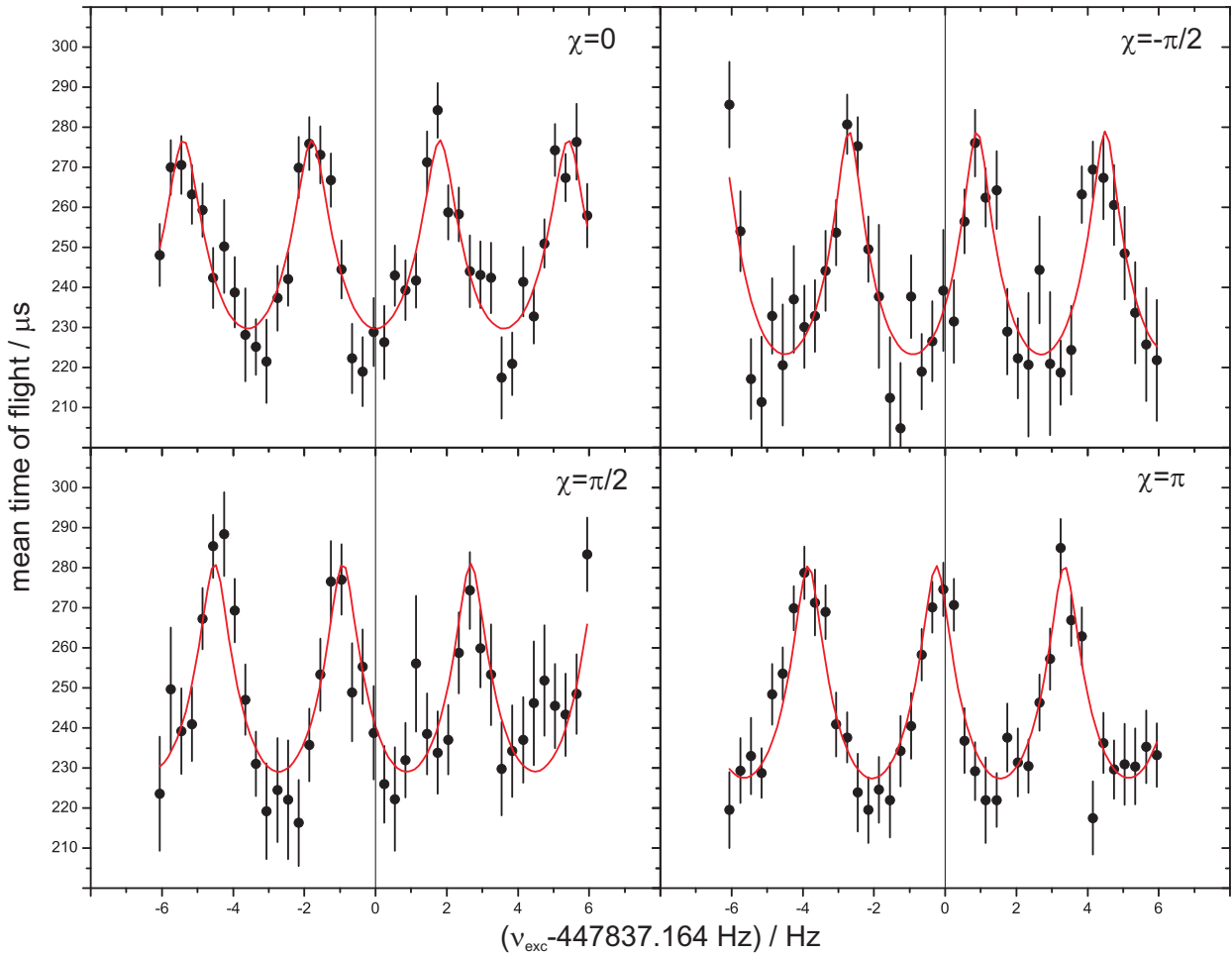


Figure 5.11: TOF-ICR resonances of $^{20}\text{C}_{12}^+$ ions with four different phase shifts χ between the first and the second excitation pulse of a Ramsey pattern. The red lines are fits of the theoretical line shape [Kret2007]. For details see text.

patterns of $T_1 = 100$ ms and $T_0 = 800$ ms and phase differences of $\chi = 0$ and $-\pi/2$ were recorded with about 5000 ions in both cases. The cyclotron frequencies obtained from a fit of the theoretical line shape were $\nu_c = 447836.609(13)$ Hz and $447836.655(10)$ Hz. Obviously, the uncertainty did not improve and the frequencies agree besides a shift of 46 mHz caused by magnetic field fluctuations. In conclusion, the Ramsey method will be applied at TRIGA-TRAP with $\chi = 0$. However, the phase shifted Ramsey excitation could be useful, e.g. for the detection of isomers, but detailed simulations and further tests are required to investigate other possible fields of application.

6 First direct mass measurements at TRIGA-TRAP

Prior to the on-line coupling to the research reactor TRIGA Mainz, which will make neutron-rich fission products available for high-precision mass measurements, stable nuclides as well as long-lived actinoids can and have been investigated using the laser ablation ion source (see Sect. 4.3). Within this thesis work one of the objectives was to study the rare-earth region, since certain of those elements and actinoids form chemical homologue pairs, e.g. gadolinium and curium. Stable rare-earth nuclides are easily available in natural compositions (see Sect. 6.1). Targets with up to 10^{18} atoms could be produced enabling further optimisation of the complete measurement cycle including the ion production and the beam transport. Another important aspect apart from the technical reasons mentioned so far, is a detailed study of the mass surface in this region of the nuclear chart. Nuclides are linked through several nuclear reactions, mainly of the (n, γ) -type, as well as some mass doublets causing a complicated network of data determining the masses. This issue will be addressed in Sect. 6.1.3. Sect. 6.1.4 deals with an important application of the measured mass values for nuclear structure studies, manifesting experimental evidence of deformation.

One of the main aims of TRIGA-TRAP are direct mass measurements of actinoids heavier than uranium, since so far no such experimental data exists. Besides SHIPTRAP, no other mass spectrometer worldwide is investigating nuclides in this region of the nuclear chart. Nevertheless, direct data is required to unambiguously determine the masses of heavy elements which is so far only done via decay reactions. After the mass measurements on three nobelium isotopes at SHIPTRAP [Bloc2010a, Bloc2010b, Dwor2010] it was also possible to obtain the very first results on actinoids at TRIGA-TRAP within this thesis work. During the commissioning phase of the experimental setup in Mainz, the mass of ^{241}Am could be measured directly for the very first time (see Sect. 6.2).

6.1 Investigation of stable isotopes in the rare-earth region

Masses of 15 stable rare-earth nuclides could be measured within this thesis work, providing anchorpoints for the mass surface which are linked to the atomic-mass standard ^{12}C . In most cases, no direct mass measurement has been performed before. As it will be discussed in Sect. 6.1.3, a shift in the order of a few keV is introduced for a large number of nuclides linked in a complicated network of reactions and mass measurements to the 15 species under investigation here. The literature values of the new Atomic-Mass Evaluation (AME) are determined in most cases by about 5-20% by the new TRIGA-TRAP results.

6.1.1 Ion production

The ions of interest as well as the reference ions were produced by the non-resonant laser ablation ion source [Smor2009] as described in Sect. 4.3. Sigradur[®] has been chosen as the target material being suitable to get carbon clusters and to serve as a backing for a layer of the rare-earth element under investigation. In

element	A	natural abundance / %	total nuclear angular momentum and parity (J^Π)
Eu	151	47.81(3)	$5/2^+$
	153	52.19(3)	$5/2^+$
Gd	152	0.20(1)	0^+
	154	2.18(3)	0^+
	155	14.80(12)	$3/2^-$
	156	20.47(9)	0^+
	157	15.65(2)	$3/2^-$
	158	24.84(7)	0^+
	160	21.86(19)	0^+
Lu	175	97.41(2)	$7/2^+$
	176	2.59(2)	7^-
Hf	174	0.16(1)	0^+
	176	5.26(7)	0^+
	177	18.60(9)	$7/2^-$
	178	27.28(7)	0^+
	179	13.62(2)	$9/2^+$
	180	35.08(16)	0^+

Table 6.1: Natural abundances of the stable rare-earth nuclides under investigation [Rosm1998]. For completeness, total angular momenta and parities of the nuclear ground states are also given [Audi2003]. The masses of all isotopes in the list besides ^{151}Eu and ^{174}Hf have been measured within this work.

principle, foils are available for rare-earth elements and can be used on the target similar to the case of ^{197}Au . For the measurements reported here, a layer with an atom density of about $10^{17}/\text{mm}^2$ was deposited on a sandblasted circular spot with 4 mm diameter on the Sigradur[®] surface (see Fig. 4.10). This approach is more general with respect to the later application for actinoids (see Sect. 6.2). Despite the disadvantage of an inhomogeneous layer the targets were produced by drying drops of the corresponding element solution in 1 molar nitric acid. Tests with molecular plating in case of gadolinium showed an inefficient ion production which is not fully understood yet and still under investigation [Reni2010]. A possible explanation might be that the deposited layer is electrically insulating and, therefore, distorts the electric potential required for the ion extraction. This problem is in principle the same for the drying method but due to the inhomogeneities the insulation layer is reduced to only a fraction of the spot surface, which turned out to enable a reliable and efficient ion production. Moreover, the target preparation is simpler and also allows to prepare mixed targets with different rare-earth elements on different spots of the Sigradur[®] target surface.

In most cases, the natural isotope mixture was sufficient to deliver ions for the mass measurements. Tab. 6.1 shows the natural abundances of the isotopes for the elements under investigation within this work. To prepare the targets, either the hydrated nitrate or the (hydrated) chloride of the rare-earth element was dissolved in 1 molar nitric acid: $\text{EuCl}_3 \cdot x\text{H}_2\text{O}$ for europium, $\text{Gd}(\text{NO}_3)_3 \cdot x\text{H}_2\text{O}$ for gadolinium, $\text{Lu}(\text{NO}_3)_3 \cdot x\text{H}_2\text{O}$

for lutetium, and HfCl_4 for hafnium. The number of water molecules x in the complex was about 5-6. A natural abundance of about 2% was sufficient to obtain an ion production rate of the isotopes suitable for a mass measurement. In the case of ^{152}Gd with a natural abundance of 0.2% this rate was insufficient. Tests to improve the ion count-rate by increasing the atom density on the target failed, since no prefiltering with a resolution in the order of one mass unit could be performed, and an isotope mixture always entered the purification trap. Space charge effects in general set a limit to the maximum ion number (~ 100) where mass-selective buffer gas cooling is still working, which did not allow to increase the total ion number sufficiently. To overcome this difficulty, a sample of Gd_2O_3 with about 35% enrichment¹ was used for the mass measurement of ^{152}Gd .

Depending on the natural abundance, the atom density on the surface irradiated by the laser and the width of the ion gate (see Sect. 4.4), a count-rate of 0.1-1 ions per shot was adjusted, leading to a few hundred up to about 1000 ions in a single measurement running for 1-2 hours. For each of the elements under investigation, the monoxide ions were the most abundant species and, thus, used instead of the pure elements. It should be mentioned that employing a foil for the ion production avoids the oxidation. However, since the mass of ^{16}O is known to a relative uncertainty of about 1×10^{-11} [Waps2003b], the natural abundance is 99.8% [Rosm1998], and the energy in the vibrational and rotational modes of the molecule is negligible, using the monoxides does not introduce any further uncertainty in the mass measurements reported here.

Contaminations: During the mass measurements on stable isotopes in the rare-earth region, contaminations did not represent a problem. For each element, a different target - at least a different target spot - was prepared to avoid isobaric contaminations. However, part of the ablated atoms do not get ionised and are deposited mainly on the extraction electrode surface and may be also accidentally released by the laser again. To this end, all possible combinations of nuclides of the rare-earth species involved as well as typically present elements (H, He, C, N, O, Na, Al, Cl, K, Fe, Cu, Kr, Rb, Ag, Xe, Cs, Au) with a cyclotron frequency within a ± 5 Hz window around the frequencies of the oxide molecular ions under investigation were determined in a simple combinatorial analysis. Each combination found could be discarded due to chemical reasons, or the probability of its presence was negligible since the abundance of a nuclide involved was well below 1%.

It should be mentioned that the isobaric selection in the purification trap could be easily applied, since the cyclotron frequencies between isobars of neighbouring elements differed by about 300 Hz, thus requiring a mass resolving power of only 2000. Even in case the trap was tuned to obtain maximum transmission, the width of the quadrupolar cyclotron excitation used in the mass-selective buffer-gas cooling process (see Sect. 3.2.2) was at maximum in the order of 20-30 Hz, leading to a resolving power of at least 20 000. Moreover, the rare-earth nuclides under investigation were in the nuclear ground state since the energy transferred by the laser was of course not sufficient to excite an isomeric state of a nucleus. Rotational and vibrational states of the molecules did not play a role for the results of the mass measurements either, since the energy scale is at least one order of magnitude smaller than the uncertainties of a few keV claimed here.

¹The sample also contained the other stable gadolinium isotopes. The only one used here is ^{158}Gd with an abundance of about 11%.

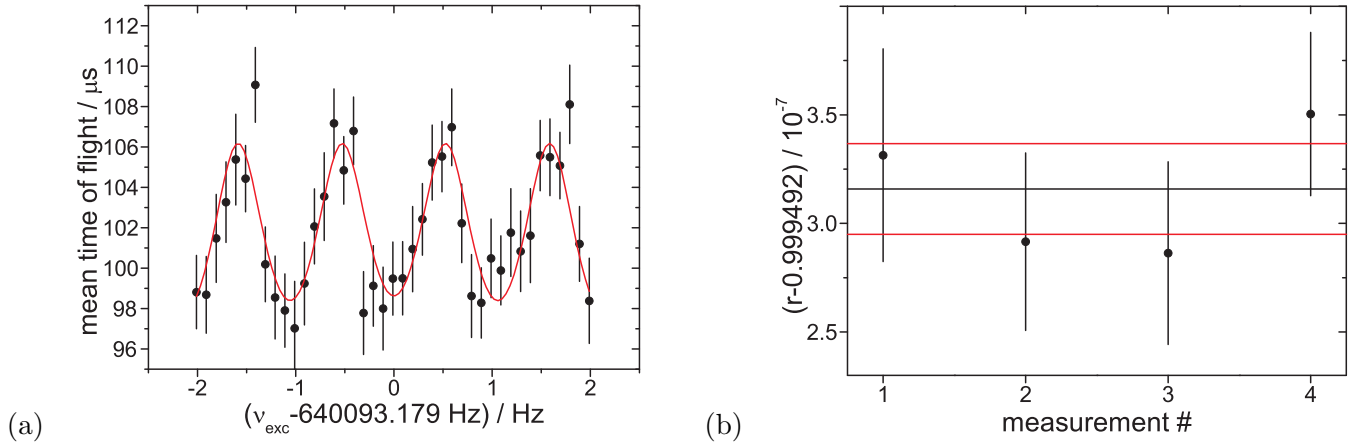


Figure 6.1: (a) TOF-ICR resonance with 858 $^{152}\text{Gd}^{16}\text{O}^+$ ions using a Ramsey excitation pattern of two 100 ms pulses and a waiting time of 800 ms. The centre frequency obtained by a fit of the theoretical line shape (red line) [Kret2007] is $\nu_c = 640093.179(18)$ Hz. (b) Frequency ratios r_i of all individual measurements of $^{152}\text{Gd}^{16}\text{O}^+$ with $^{14}\text{C}_{12}^+$ as the reference ion. The black line marks the weighted mean value of $r = 0.9994923158(209)$ and the red lines indicate its statistical uncertainty. Here, only the additional uncertainty due to fluctuations of the magnetic field is quadratically added.

6.1.2 Measurements and results

All mass measurements reported here have been performed using the TOF-ICR technique. Moreover, a Ramsey excitation profile with two 100 ms pulses and a waiting time of 800 ms was employed since the statistical uncertainty of the cyclotron frequency was found to be between a factor of 2 to 3 lower than for a continuous excitation of 1 s duration in agreement with [Geor2007b]. The measurements were grouped into four individual runs starting in November 2009 with the six stable gadolinium isotopes $^{154-158,160}\text{Gd}$. As mentioned before, singly charged monoxide ions of the rare-earth nuclides were produced by the laser ablation ion source. The carbon cluster ion $^{12}\text{C}_{15}^+$ was used as the reference ion in all cases, and $^{12}\text{C}_{14,16}^+$ were taken as cross-checks to test the accuracy of the mass measurements. This is done in each experimental run at TRIGA-TRAP since the mass of carbon clusters is exactly known by definition besides the negligible molecular and atomic binding energies. The number of individual measurements of the gadolinium isotopes was chosen to be 3-4 in order to achieve a relative mass uncertainty $\delta m_{\text{atom}}/m_{\text{atom}}$ of better than 2×10^{-8} . Four individual TOF-ICR resonances of the monoxide ion of the less abundant isotope ^{152}Gd have been recorded in a second experimental run in February 2010 using the enriched target which was not available earlier. The reference ion was $^{12}\text{C}_{14}^+$ due to the identical mass number compared to $^{152}\text{Gd}^{16}\text{O}^+$. In addition, a single resonance of $^{158}\text{Gd}^{16}\text{O}^+$ was measured here again as a consistency check between this measurement and the one performed in November 2009. Moreover, $^{12}\text{C}_{15}^+$ served as a further cross-check.

As an example, Fig. 6.1(a) shows a TOF-ICR resonance of $^{152}\text{Gd}^{16}\text{O}^+$ with a fit of the theoretical line shape. The number of ions varied between a few hundred up to about 1000 in a single resonance. In principle, a measurement was stopped after $\delta m/m$ was sufficiently low (see above), but in case the target was used up, only less statistics could be accumulated. Following the data analysis procedure described in Sect. 5.3, the frequency ratios of the individual measurements were determined for each isotope, as given in Fig. 6.1(b) for

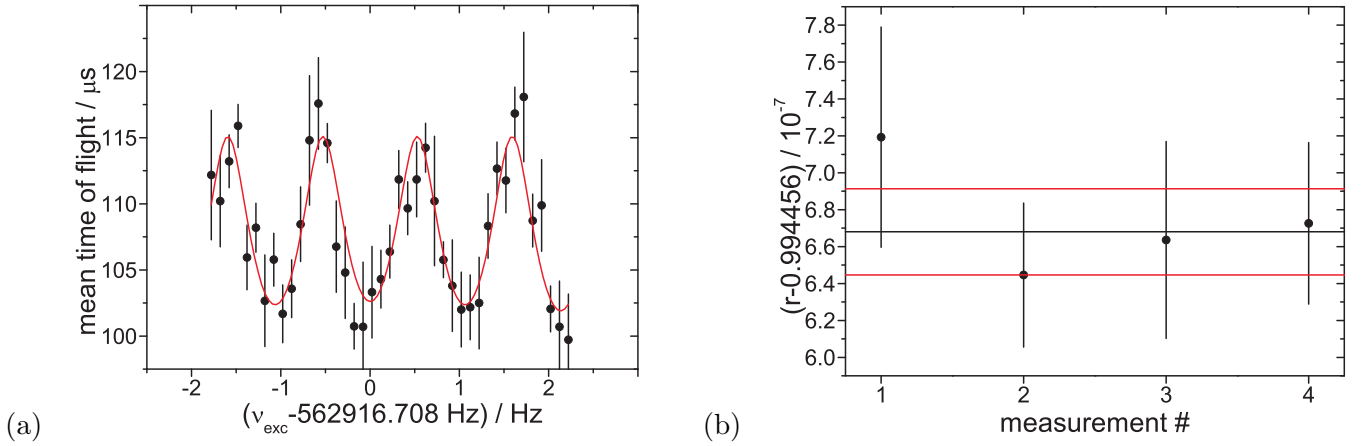


Figure 6.2: (a) TOF-ICR resonance with 177 $^{175}\text{Lu}^{16}\text{O}^+$ ions with a centre frequency of $\nu_c = 562916.708(14)$ Hz under similar conditions to Fig. 6.1(a). (b) Frequency ratios r_i of the 4 individual measurements of $^{175}\text{Lu}^{16}\text{O}^+$ with $^{16}\text{C}_{12}^+$ as the reference ion. The mean value is $r = 0.9944566680(235)$ (black line). For further details see Fig. 6.1(b).

$^{152}\text{Gd}^{16}\text{O}^+$ as an example. The error bars denote the statistical uncertainties corrected for the contribution of the magnetic field fluctuations (see Eq. (5.2)). The weighted mean of the frequency ratios is finally calculated taking point scattering into account by using the largest of the internal or external error (see Eqs. (5.3,5.4)). During all mass measurements reported here, no individual frequency ratio was discarded, since no crucial instability of the experimental conditions was detected. The air pressure and temperature in the reactor hall as well as the temperature of the vacuum tube housing the Penning traps was permanently monitored for this purpose. While the air pressure fluctuated² by up to 2.5 Pa over a typical measurement time of 5 hours, the air temperature was stable to 0.1-0.5 K depending on the day time, and the temperature of the tube to better³ than 0.25 K in 30 hours. A measure indicating point scattering is the Birge ratio $BR = \sigma_{\text{ext}}/\sigma_{\text{int}}$. The largest values of 2.2 and 2.3 were obtained for $^{154,156}\text{Gd}^{16}\text{O}^+$, which is still acceptable considering the low number of individual frequency ratios. The expected value for BR is 1 ± 1 in case of ^{154}Gd and 1 ± 0.8 for ^{156}Gd . For all other isotopes the ratios agreed with the expected values given by $1 \pm \sqrt{2(N-1)/(N-1)}$ with N denoting the number of individual measurements (see Tab. 6.2).

In March 2010, the masses of the five stable hafnium isotopes $^{175-180}\text{Hf}$ were measured using the monoxide ions $^{175-180}\text{Hf}^{16}\text{O}^+$. An enriched target with ^{174}Hf was not available. $^{12}\text{C}_{16}^+$ served as the reference ion and $^{12}\text{C}_{15}^+$ as a cross-check. Four individual measurements have been performed for each nuclide to obtain relative mass uncertainties between $\delta m_{\text{atom}}/m_{\text{atom}} = 3.6 \times 10^{-8}$ and 5.6×10^{-8} . There was no scattering between the individual frequency ratios, leading to Birge ratios within the expected range. During the experiment on hafnium, the so-called TOF-effect TE dropped from about 10% in the gadolinium measurements to 4-7%. The TOF-effect

$$TE = \frac{t_{\text{off}} - t_{\text{on}}}{t_{\text{off}}} \quad (6.1)$$

is another possibility to quantify the quality of a TOF-ICR resonance besides the contrast defined in Eq. (4.2),

²The air pressure inside the reactor hall is not stabilised but only kept a certain offset below the outside air pressure.

³For the duration of a typical mass measurement of about 5 hours, the fluctuations of the tube temperature were mostly well below 0.1 K.

and only takes the temporal separation of excited (t_{on}) and non-excited ions (t_{off}) into account. The contrast could not be calculated for most cases, since this would require to determine the width of the time-of-flight distributions for excited (σ_{on}) and non-excited (σ_{off}) ions separately, which is only possible in case of sufficient statistics. However, the drop of TE is sometimes assigned to contaminations present, but this has been already ruled out in case of TRIGA-TRAP (see the discussion in Sect. 6.1.1). The reason is rather an initial magnetron motion likely due to not optimal injection and capturing, which has been investigated during the experiment. It is not fully understood yet, why the magnetron excitation in the precision trap could not be phase locked for hafnium isotopes but in order to perform the mass measurement, it was sufficient to disable this excitation completely here and to get TOF-ICR resonances based on the initial magnetron motion on the expense of slightly increased statistical uncertainties from the fits of the theoretical line shape.

Directly after the hafnium experiment, the masses of the two stable lutetium isotopes $^{175,176}\text{Lu}$ as well as of ^{153}Eu were measured. The frequency ratios were taken between the singly charged monoxide ions and the references $^{12}\text{C}_{16}^+$ in case of lutetium, and $^{12}\text{C}_{14}^+$ for europium, respectively. $^{12}\text{C}_{15}^+$ served as a cross-check in both cases. ^{153}Eu was only investigated to compare the TRIGA-TRAP result to a value from ISOLTRAP [Beck2000] for consistency reasons. 3-4 individual TOF-ICR resonances were recorded for the lutetium isotopes (see Tab. 6.2). As an example, a resonance of $^{175}\text{Lu}^{16}\text{O}^+$ is shown in Fig. 6.2(a), demonstrating the very good performance of TRIGA-TRAP in this case since already 177 ions were sufficient to obtain a relative statistical uncertainty of 2.5×10^{-8} . The Birge ratio between the individual frequency ratios shown in Fig. 6.2(b) is 0.4 for $^{175}\text{Lu}^{16}\text{O}^+$, and 1.1 for $^{176}\text{Lu}^{16}\text{O}^+$, respectively.

Tab. 6.2 summarizes all mass measurements performed within this work including the cross-checks with carbon cluster ions. The mean frequency ratios for each monoxide ion species were calculated and corrected for the mass-dependent systematic shift as described in Sect. 5.3. Thus, the total uncertainty for r including all contributions from the procedure discussed in Sect. 5.3 is given. Using Eq. (3.46), the mass of the neutral monoxide molecule is obtained⁴. Tab. 6.2 lists the atomic mass of the isotopes under investigation, which is calculated subtracting the mass value 15.99491461956(16) u [Waps2003b] of ^{16}O , neglecting the molecular binding energy in the order of $\sim\text{eV}$. Moreover, the atomic-mass excesses $ME_{\text{TRIGA-TRAP}}$ obtained in the measurements reported here, the latest published literature values ME_{AME2003} as well as their differences are given.

As already mentioned in Sect. 5.3, a cross-check measurement is always performed at TRIGA-TRAP to ensure the accuracy of the results. To this end, frequency ratios of certain carbon cluster ions have been determined using the same reference ions as for the rare-earth isotopes in the individual experimental runs. The mean ratios obtained are also given in Tab. 6.2. In these cases, only the mass excesses of the clusters are compared to the expected values, showing an excellent agreement with zero in all cases. Thus, the accuracy of all results presented here is confirmed and no residual uncertainty is identified at the present level of precision after the shift discussed in Sect. 5.3 has been corrected. For completeness, it should be noted that the mean damping determined through the reference measurements was only 0.01(1)-0.02(1)/s for all experimental runs on elements in the rare-earth region.

element	Z	N	A	ion	reference	meas.	BR	τ	m_{atom} / μ	$\delta m_{\text{atom}} / m_{\text{atom}} / 10^{-8}$	$ME_{\text{TRIGA-TRAP}} / \text{keV}$	$ME_{\text{AME2003}} / \text{keV}$	$\Delta ME / \text{keV}$
Eu	63	90	153	$^{153}\text{Eu}^{16}\text{O}^+$	$^{12}\text{C}_{14}^+$	2	< 0.01	1.0054532942(343)	152.921235.8(5.8)	3.77	-73368.37(5.37)	-73373.5(2.5)	-5.13(5.92)
				$^{12}\text{C}_{15}^+$	2	1.0714288017(371)	-	-	-0.47(5.81)	0(0)	0.47(5.81)		
Gd	64	88	152	$^{152}\text{Gd}^{16}\text{O}^+$	$^{12}\text{C}_{14}^+$	4	0.60	0.9994923158(209)	151.919794.7(3.5)	2.31	-74710.75(3.27)	-74714.2(2.5)	-3.45(4.11)
				$^{154}\text{Gd}^{16}\text{O}^+$	$^{12}\text{C}_{15}^+$	3	2.20	0.9439764595(237)	153.920878.8(4.3)	2.77	-73700.91(3.97)	-73713.2(2.5)	-12.29(4.69)
				$^{155}\text{Gd}^{16}\text{O}^+$	$^{12}\text{C}_{15}^+$	4	0.60	0.9495417784(147)	154.922633.2(2.7)	1.71	-72066.73(2.47)	-72077.1(2.5)	-10.37(3.51)
				$^{156}\text{Gd}^{16}\text{O}^+$	$^{12}\text{C}_{15}^+$	4	2.30	0.9550946098(200)	155.922139.8(3.6)	2.31	-72526.34(3.35)	-72542.2(2.5)	-15.86(4.18)
				$^{157}\text{Gd}^{16}\text{O}^+$	$^{12}\text{C}_{15}^+$	3	0.01	0.9606603600(183)	156.923971.8(3.3)	2.10	-70819.85(3.07)	-70830.7(2.5)	-10.85(3.96)
				$^{158}\text{Gd}^{16}\text{O}^+$	$^{12}\text{C}_{14}^+$	1	-	1.0352324681(491)	157.924120.7(8.3)	5.21	-70681.12(7.68)	-70696.8(2.5)	-15.64(8.08)
				$^{158}\text{Gd}^{16}\text{O}^+$	$^{12}\text{C}_{15}^+$	3	0.10	0.9662167424(179)	157.924117.5(3.2)	2.04	-70684.06(3.00)	-70696.8(2.5)	-12.74(3.91)
					-	-	average	157.924118.0(3.0)	1.90	-	-	-	-
				$^{160}\text{Gd}^{16}\text{O}^+$	$^{12}\text{C}_{15}^+$	4	1.63	0.9773442650(199)	159.927065.5(3.6)	2.24	-67938.03(3.34)	-67948.6(2.6)	-10.57(4.23)
					$^{12}\text{C}_{14}^+$	4	0.11	0.9333331419(148)	-	-	1.97(2.48)	0(0)	-1.97(2.48)
*	64	96	160	$^{12}\text{C}_{15}^+$	$^{12}\text{C}_{15}^+$	4	1.11	1.0714287811(277)	-	-	-3.69(4.33)	0(0)	3.69(4.33)
				$^{12}\text{C}_{16}^+$	4	1.58	1.0666668629(216)	-	-	-1.17(3.16)	0(0)	1.17(3.16)	
Lu	71	104	175	$^{175}\text{Lu}^{16}\text{O}^+$	$^{12}\text{C}_{16}^+$	4	0.37	0.9944566701(234)	174.940769.1(4.5)	2.57	-55173.24(4.18)	-55170.7(2.2)	2.54(4.73)
				$^{176}\text{Lu}^{16}\text{O}^+$	$^{12}\text{C}_{16}^+$	3	1.14	0.9996750300(394)	175.942691.3(7.6)	4.39	-53382.70(7.05)	-53387.4(2.2)	-4.70(7.39)
*	72	104	176	$^{176}\text{Lu}^{16}\text{O}^+$	$^{12}\text{C}_{16}^+$	4	0.94	0.9374998460(217)	-	-	4.40(3.87)	0(0)	-4.40(3.87)
				$^{176}\text{Lu}^{16}\text{O}^+$	$^{12}\text{C}_{15}^+$	4	0.41	0.9996683922(511)	175.941416.9(9.9)	5.58	-54569.85(9.14)	-54577.5(2.2)	-7.65(9.40)
Hf	72	105	177	$^{177}\text{Hf}^{16}\text{O}^+$	$^{12}\text{C}_{16}^+$	4	0.65	1.0048862367(375)	176.943240.1(7.2)	4.07	-52871.46(6.71)	-52889.6(2.1)	-18.14(7.03)
				$^{178}\text{Hf}^{16}\text{O}^+$	$^{12}\text{C}_{16}^+$	4	0.90	1.0100970872(414)	177.943720.6(8.0)	4.47	-52423.94(7.40)	-52444.3(2.1)	-20.36(7.69)
*	72	107	179	$^{179}\text{Hf}^{16}\text{O}^+$	$^{12}\text{C}_{16}^+$	4	0.68	1.0153163888(336)	178.945823.6(6.5)	3.61	-50464.96(6.01)	-50471.9(2.1)	-7.94(6.37)
				$^{180}\text{Hf}^{16}\text{O}^+$	$^{12}\text{C}_{16}^+$	4	0.95	1.0205285770(340)	179.946560.9(6.5)	3.63	-49778.19(6.08)	-49788.4(2.1)	-10.21(6.43)
*	72	108	180	$^{12}\text{C}_{15}^+$	$^{12}\text{C}_{16}^+$	4	0.99	0.9374998408(213)	-	-	3.47(3.80)	0(0)	-3.47(3.80)
				$^{12}\text{C}_{15}^+$	-	-	average	0(0)	-	-0.12(1.58)	-	0.12(1.58)	

Table 6.2: Results of the mass measurements in the rare-earth region. The columns from left to right represent the element, the proton, neutron, and mass numbers, the ion of interest, the reference ion, the number of individual measurements, the Birge ratio $BR = \sigma_{\text{ext}}/\sigma_{\text{int}}$, the mean frequency ratio τ (see Eq. (3.46)) with the total uncertainty, the atomic mass of the nuclide, the relative mass uncertainty, the atomic mass excess $ME_{\text{TRIGA-TRAP}}$ obtained at TRIGA-TRAP, the literature value ME_{AME2003} [Waps2003b] and the difference $\Delta ME = ME_{\text{AME2003}} - ME_{\text{TRIGA-TRAP}}$. Rows labeled with (*) contain cross-reference measurements with carbon clusters which have been performed as accuracy checks. In these cases, the mass excess values refer to the cluster and not to the ^{12}C atom. The last row gives the mass excess for $^{12}\text{C}_{15}^+$ averaged over all individual measurements within three different experimental runs. For details see text.

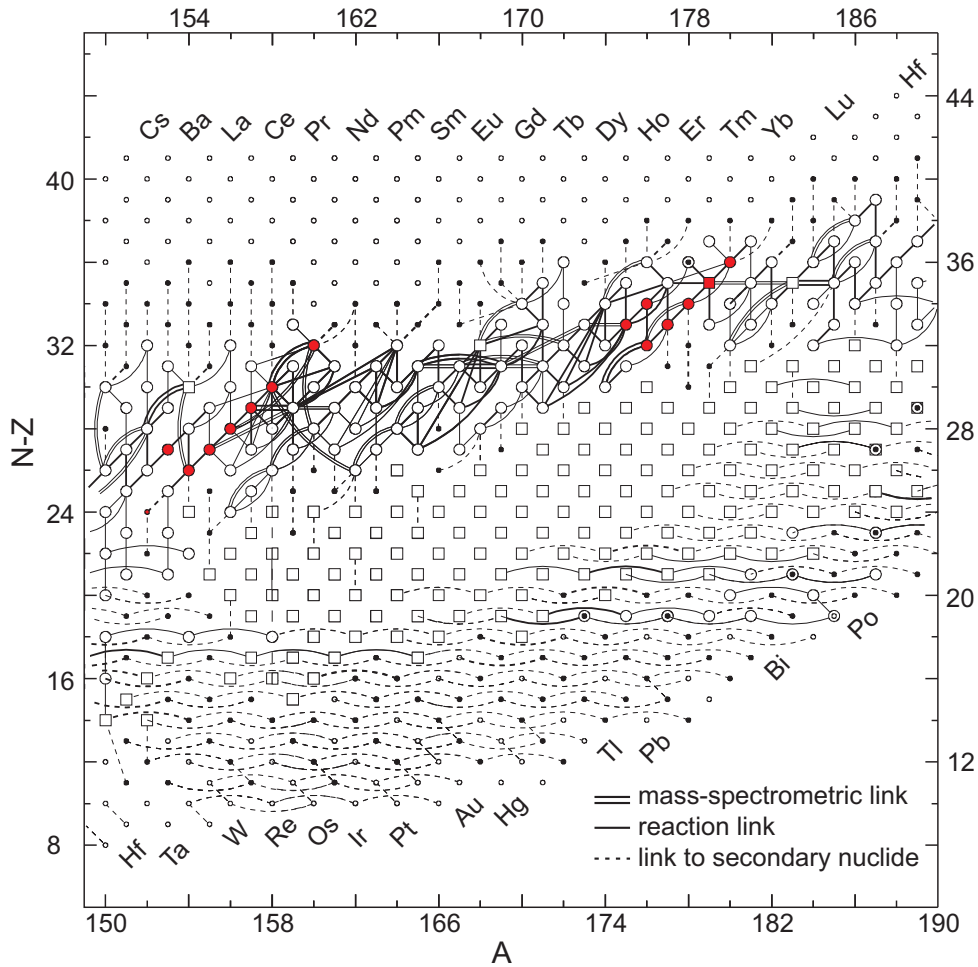


Figure 6.3: Network of experimental links originating from mass spectrometric measurements as well as from nuclear reaction studies prior to the TRIGA-TRAP results. The masses of the nuclides in this network are determined by these connections. Squares (\square) denote nuclides directly linked to ^{12}C or $^{35,37}\text{Cl}$, open circles (\circ) stand for other nuclides with at least two connections to the remaining mass surface. Small open circles (\circ) mark nuclides with only a single connection, and small filled circles (\bullet) nuclides for which the mass is estimated from systematic trends. Masses of the 15 red coloured nuclides have been measured within this work. For details and discussion see text. Figure taken from [Waps2003a] and modified.

6.1.3 The Atomic-Mass Evaluation in the rare-earth region

The mass of a nuclide can be determined by many different ways: direct mass measurements in Penning traps such as performed at TRIGA-TRAP are only one possibility. In case of the rare-earth elements, neighbouring isotopes are typically linked via (n, γ) reactions⁵. Other significant contributions come from β^+ , β^- , and electron-capture (EC) decays. Nuclear reactions like (t, p) , (d, t) , and (α, t) have minor influences on the mass surface in this region. Each nuclide is part of a complicated network based on the mass links just mentioned

⁴Note that the index “atom” in Eq. (3.46) refers to the neutral species of the ion used in the mass measurement, which is in case of the experiments reported here a monoxide molecule.

⁵The notation is a short form of $A(n, \gamma)B$ meaning that a nucleus A captures a neutron, leading to nucleus B in the final state after a photon emission.

(see Fig. 6.3) which leads to an over-determination of the atomic masses. In order to take all connections into account, the AME [Waps2003a] is based on a least-squares fit to the experimental data, described by a set of linear equations of the type

$$\sum_{\mu=1}^M k_i^{\mu} m_{\mu} = q_i. \quad (6.2)$$

Here, M is the number of masses which are linked, k_i^{μ} is a constant related to the explicit nuclear reaction or mass measurement, m_{μ} is the (unknown) mass of the nuclide μ , and q_i is the experimental input data with the uncertainty δq_i . The treatment of data from Penning trap mass spectrometers, such as TRIGA-TRAP, is described in detail in [Beck2000]. Prior to the actual least-squares fit, all parameters (i.e. masses) which occur only once as well as the corresponding equations are removed in an iterative process until each parameter has at least two occurrences in the remaining set. The data removed are called secondaries, the remaining primaries. This treatment does not change the results of the fit but simplifies the computational approach used [Waps2003a]. Moreover, secondary nuclides are assigned a degree l expressing the number of links l needed to reach a primary nuclide in the mass surface, which has degree 1 by definition.

Fig. 6.3 shows that besides ^{179}Hf none of the nuclides measured within this work (marked in red) have been connected to the atomic mass standard ^{12}C before. The TRIGA-TRAP results provide new anchor points to the mass surface and directly test the mass values mainly obtained by nuclear reaction energy measurements. Moreover, ^{152}Gd now changes its status from a secondary to a primary nuclide since the connection to ^{12}C has been added.

An overview on the mass excesses obtained within this work (see Tab. 6.2) in comparison to the previous literature values from 2003 and 2010 [Waps2003b, Audi2010] is shown in Fig. 6.4. The TRIGA-TRAP results define the horizontal zero line and the differences $\Delta ME = ME_{\text{AME}} - ME_{\text{TRIGA-TRAP}}$ are given with an error bar representing one standard deviation of the literature values. The red lines mark the band of uncertainty for the experimental results of TRIGA-TRAP. In general the masses adjusted using the experimental input data available in 2003 suggest a too strong binding by about 10-20 keV. New measurements until spring 2010 shifted the masses of all nuclides besides the Hf isotopes by about 5 keV so that the discrepancy to the TRIGA-TRAP data decreased. In the following, the masses are discussed in detail. The influence of the results presented within this work on the upcoming AME is given in Tab. 6.3.

^{153}Eu : This nuclide was taken as a cross-check of the complete series of rare-earth measurements, since there was a previous Penning trap mass value available from ISOLTRAP [Beck2000]. Taking the published frequency ratio from ISOLTRAP the atomic mass is $m_{\text{ISOLTRAP}}(^{153}\text{Eu}) = 152.9212426(159)$ u which agrees very well with the TRIGA-TRAP result of $m_{\text{TRIGA-TRAP}}(^{153}\text{Eu}) = 152.9212358(58)$ u (see Tab. 6.2). The literature value of 2010 is only determined by the reactions $^{152}\text{Eu}(n, \gamma)^{153}\text{Eu}$ [Egid1985] and $^{153}\text{Eu}(n, \gamma)^{154}\text{Eu}$ [Balo1987, Fire2007], and it agrees as well with the TRIGA-TRAP result as it can be seen in Fig. 6.4.

$^{152,154-158,160}\text{Gd}$: As already mentioned, a connection between the mass of ^{152}Gd and ^{12}C was added by TRIGA-TRAP, which created a new primary anchorpoint of the mass surface. Many different nuclear reactions have been investigated involving ^{152}Gd , among those α , β^+ , β^- decays or (d,t) reactions. Besides this, mass spectrometric measurements have been performed determining the mass difference between different Gd isotopes. However, the uncertainties of all those experimental results are typically a few 10 keV, so

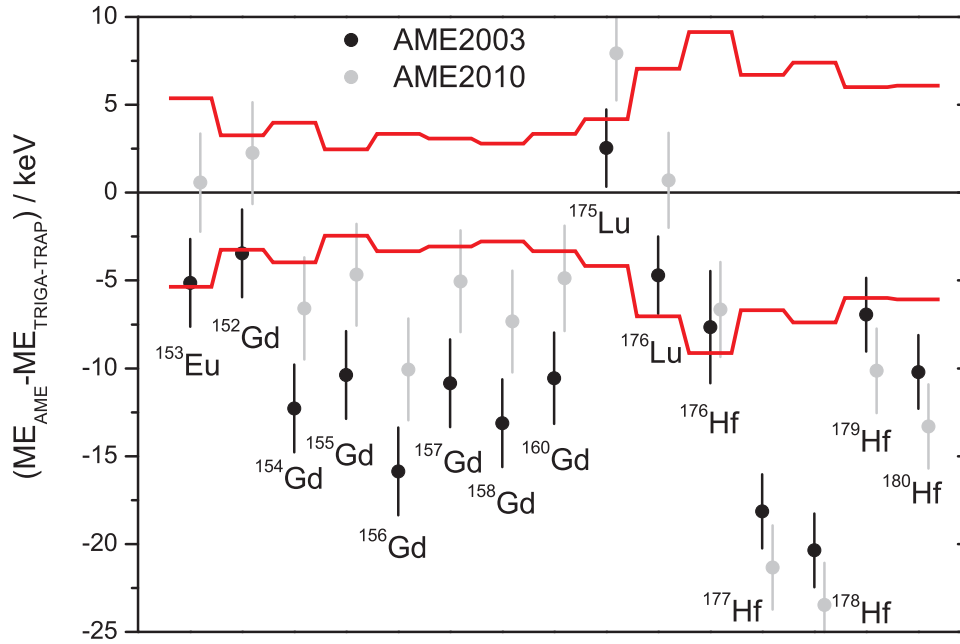


Figure 6.4: Differences between the measured mass excesses $ME_{\text{TRIGA-TRAP}}$ (zero line) and the literature values ME_{AME} from the last published Atomic-Mass Evaluation in 2003 (solid black dots) [Waps2003b] and from an intermediate evaluation in spring 2010 (solid grey dots) just before the TRIGA-TRAP data was included [Audi2010] for nuclides in the rare-earth region. The red lines indicate the uncertainty of the TRIGA-TRAP results, while the error bars are one standard deviation of the literature value. For discussion and further details see text.

there is no significant impact on the adjusted mass. The AME value has been solely determined by the $^{152}\text{Gd}(n, \gamma)^{153}\text{Gd}$ reaction energy averaged over 3 individual measurements [Egid1985, Spit1993, Fire2007]. The average neutron-separation energy obtained in the (n, γ) measurements cannot be checked, since the mass of ^{153}Gd could not be measured within this work. A direct mass measurement of ^{153}Gd is required to identify a wrong (n, γ) Q -value, either in $^{152}\text{Gd}(n, \gamma)^{153}\text{Gd}$, or $^{153}\text{Gd}(n, \gamma)^{154}\text{Gd}$, because the TRIGA-TRAP result for ^{152}Gd obviously agrees with the adjusted AME mass (see Fig. 6.4) and the mass values of ^{154}Gd disagree significantly at least in case of the AME 2003. This problem is also visible in a comparison of $S_{2n}(^{154}\text{Gd})$, which shows a discrepancy of 1.9 standard deviations between the AME and the TRIGA-TRAP data. The new literature value of the ^{152}Gd mass is determined to 9.8% by the TRIGA-TRAP result.

For the nuclides $^{154-158}\text{Gd}$, the situation is rather similar, since their masses have been mainly determined by $^{153-157}\text{Gd}(n, \gamma)^{154-158}\text{Gd}$ reaction measurements. Fig. 6.5 shows a comparison between the neutron separation energies calculated from the masses measured within this work and the values from the (n, γ) reaction studies as used in the AME. For $^{154,157}\text{Gd}(n, \gamma)^{155,158}\text{Gd}$ these are averages over two individual measurements which are each in agreement [Isla1982, Schm1986, Fire2007], whereas for $^{155,156}\text{Gd}(n, \gamma)^{156,157}\text{Gd}$ only single measurements enter the evaluation [Isla1982, Bond2003]. In general, there is a good agreement between the TRIGA-TRAP values and the reaction-experiment results for S_n . However, the measurements performed within this work suggest a slightly stronger binding of the last neutron for odd- A nuclides and a slightly weaker binding for even- A . Perfect agreement on the level better than 0.7 standard deviations is also found for $S_{2n}(^{156-160}\text{Gd})$. Other significant contributions in the previous AME came from the decays

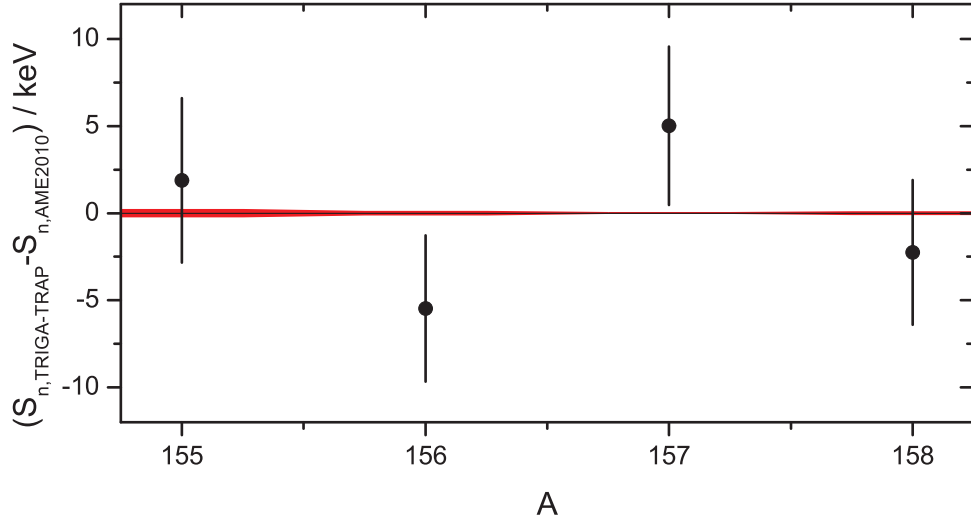


Figure 6.5: Comparison between the neutron separation energies S_n from (n, γ) studies used as input parameters in the AME2010 [Audi2010] (zero line) to the values obtained through the TRIGA-TRAP mass measurements (data points) for gadolinium isotopes. The red band denotes the uncertainties of the literature data, the error bars are one standard deviation of the calculated values based on the experimental results.

$^{154,155}\text{Eu}(\beta^-)^{154,155}\text{Gd}$ (average in [Waps2003a]) and from the measurement $^{154}\text{Sm}-^{154}\text{Gd}$ [Kais1975].

The mass adjustment for ^{160}Gd was different in a way that no (n, γ) reaction entered here, but instead $^{160}\text{Gd}(\alpha, t)^{161}\text{Tb}$ [Burk1975]. There are also measurements of mass differences, $^{160}\text{Gd}-^{35}\text{Cl}-^{158}\text{Gd}-^{37}\text{Cl}$ [Kais1975, Dyck1985] and $^{160}\text{Gd}-^{160}\text{Dy}$ [Barb1972]. The average mass difference $m(^{160}\text{Gd}) - m(^{158}\text{Gd})$ from the AME 2003 of 2.0029499(11) u agrees with the TRIGA-TRAP result of 2.0029475(47) u.

In general, the measurements reported here contribute by 10-17% to the masses of the stable gadolinium nuclides in the upcoming AME, supposed that nobody will re-measure these nuclides with a higher precision in the meantime. However, the TRIGA-TRAP result of ^{154}Gd is not used since its influence is only 6.4%, providing too little significance.

$^{175,176}\text{Lu}$: The results reported in Tab. 6.2 lead to a neutron separation energy of $S_n(^{176}\text{Lu}) = 6280.8(8.2)$ keV which agrees with the value from a $^{175}\text{Lu}(n, \gamma)^{176}\text{Lu}$ reaction measurement of 6288.0(0.2) keV [Klay1991] used to determine the masses of $^{175,176}\text{Lu}$ in the previous AME by about 50%. Furthermore, the Q_{β^-} -value of the decay $^{176}\text{Lu}(\beta^-)^{176}\text{Hf}$

$$Q_{\beta^-} = [m(^{176}\text{Lu}) - m(^{176}\text{Hf})] c^2 \quad (6.3)$$

obtained with the data in Tab. 6.2 of 1187.1(11.7) keV agrees well with 1194.1(1.0) keV derived from a decay study of the 1^- isomeric state $^{176\text{m}}\text{Lu}$ [Werf1973] together with a correction of the corresponding excitation energy [Klay1991]. However, this Q_{β^-} value does not contribute any more to the new literature values of the two lutetium masses, which has been decided by the AME evaluators due to a conflict in the links between the four nuclides $^{175,176}\text{Lu}$, $^{175,176}\text{Hf}$. Major contributions in the AME besides those discussed above come from the decay $^{175}\text{Yb}(\beta^-)^{175}\text{Lu}$ (average value published in [Waps2003a]), from the nuclear reaction

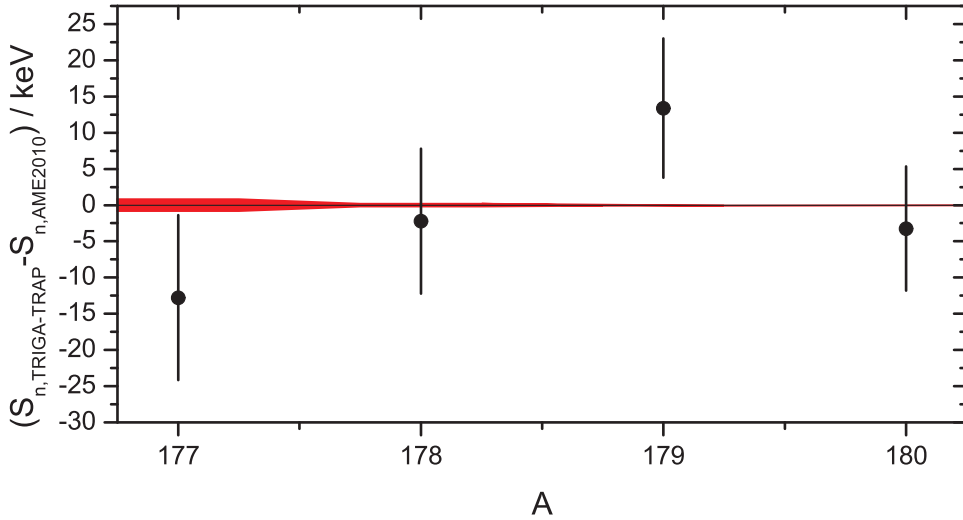


Figure 6.6: Same as Fig. 6.5 just for hafnium isotopes.

$^{176}\text{Lu}(n, \gamma)^{177}\text{Lu}$ (average value [Waps2003a]) and from the mass spectrometric measurement $^{176}\text{Lu}^{37}\text{Cl}$ - $^{143}\text{Nd}^{35}\text{Cl}_2$ [Sout1977]. While the TRIGA-TRAP results have a comparably large impact on ^{175}Lu (8.9%), the uncertainty of the value for ^{176}Lu is already too large to compete with the other contributions mentioned leading to an impact of only 3.1%, which means this result from TRIGA-TRAP is not used in the AME.

176-180Hf: Fig. 6.6 compares the neutron separation energies obtained from (n, γ) measurements for the isotopes $^{177-180}\text{Hf}$ [Bush1974, Hagu1986, Rich1989, Fire2007] with the values calculated from the masses in Tab. 6.2. In general there is an agreement on the level of 1.5 standard deviations for all of the given cases. However, a remarkable difference to gadolinium (see Fig. 6.5) is the missing odd-even regularity. The binding of the last neutron seems to be weaker for ^{177}Hf than indicated by the reaction study results, whereas in the case of gadolinium all odd- A nuclides tended to have a larger separation energy S_n . Also the values for S_{2n} are in good agreement, which is not shown explicitly. In order to draw further conclusions and to identify possibly wrong (n, γ) results, mass measurements with a higher precision would be needed to reach a final uncertainty better than 1 keV. The mass of ^{176}Hf was determined to 36% by the decay $^{176}\text{Lu}(\beta^-)^{176}\text{Hf}$ in the AME, which was already discussed in the preceding paragraph. The TRIGA-TRAP result of ^{176}Hf agrees with the literature value (see Fig. 6.4) since it is directly linked to ^{176}Lu . Similar to the lutetium case, this decay energy was also discarded in the new AME calculation. Significant contributions are now the α -decay of ^{180}W [Cozz2004] (60%) and the mass difference $^{176}\text{Hf}^{35}\text{Cl} - ^{174}\text{Hf}^{37}\text{Cl}$ [Shar1977] (35%). In this respect the other measured stable hafnium isotopes $^{177-180}\text{Hf}$ are different since their masses have been mainly determined by $^{177-180}\text{Hf}(n, \gamma)^{178-181}\text{Hf}$ reaction studies as mentioned above. There is also a mass difference available ($m(^{180}\text{Hf}) - m(^{179}\text{Hf}) = 1.0007308(47)$ u) measured in a magnetic mass spectrometer [Halv1979], which agrees with the TRIGA-TRAP result of $1.0007373(92)$ u. Moreover, the nuclides $^{179,180}\text{Hf}$ are the only ones with a direct link to the carbon mass independent from the TRIGA-TRAP studies. The isobaric mass doublets $^{12}\text{C}_{14}^{1}\text{H}_{11} - ^{179}\text{Hf}$ ($\Delta m_1 = 0.1402603(18)$ u) and $^{12}\text{C}_{14}^{1}\text{H}_{12} - ^{180}\text{Hf}$ ($\Delta m_2 = 0.1473566(48)$ u) [Halv1979] do not both agree to the differences calculated from the TRIGA-TRAP results, which are $\Delta m_1 = 0.1402518(65)$ u and $\Delta m_2 = 0.1473395(65)$ u, leading to an offset of 2.1 standard deviations for Δm_2 . The latter magnetic

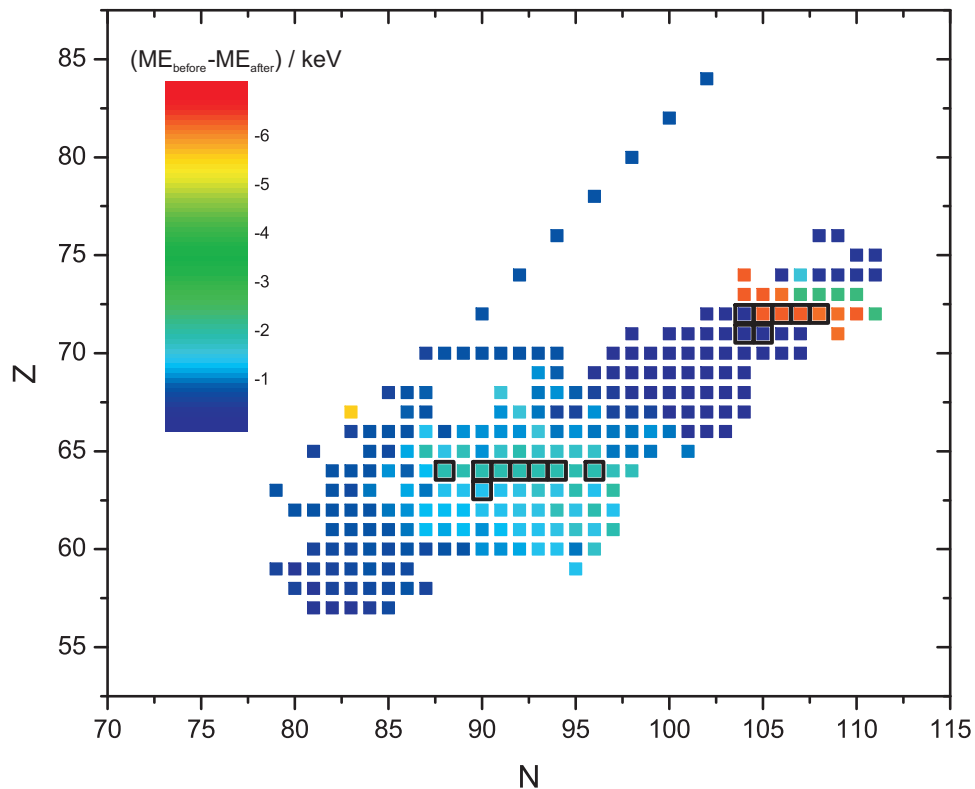


Figure 6.7: Shift of the mass surface due to the TRIGA-TRAP results presented within this work. The colours encode the difference of the mass excess ME_{before} just before the TRIGA-TRAP data was entered into the AME adjustment and the mass excess ME_{after} including this data [Audi2010]. The black squares mark those nuclides which have been measured within this work. Note that only those about 100 nuclides are included in the figure for which the mass changed. For further details see text.

mass spectrometer result was also discarded in the AME 2003 due to conflicts with other experimental values. The influences of the TRIGA-TRAP results on the new literature values are between 3 and 7% according to the larger uncertainties as compared to the gadolinium or lutetium measurements. Due to the AME policy, some values are not used in the adjustment, since they provide too little significance compared to other input data for the same nuclide.

General remarks: The discussion of the measurement results in comparison to existing data used to determine the present literature mass values showed that no significant discrepancy could be identified when looking on particular mass differences or reaction energies. Fig. 6.4 shows more a general trend of the mass surface to shift towards larger values by a few keV (see also Fig. 6.7). Comparing the AME mass excesses from 2003 and from 2010 for the nuclides under investigation within this work, it is obvious that meanwhile a similar shift has been already introduced by other measurements. It should be stressed again that regarding mass determination all nuclides are strongly connected to their neighbours forming the complicated network displayed in Fig. 6.3. Thus, the measurements reported here have an influence on more than 100 other nuclides, as shown in Fig. 6.7, and the uncertainties of about 50 nuclides improved by more than 10%. Prior to the TRIGA-TRAP measurements, besides ^{179}Hf no other nuclide had a direct connection within the AME

element	Z	N	A	ME_{before} / keV	ME_{after} / keV	$ME_{\text{before}} - ME_{\text{after}}$ / keV	influence / %
Eu	63	90	153	-73367.8(2.8)	-73366.4(1.7)	-1.4(3.3)	4.6*
Gd	64	88	152	-74708.5(2.9)	-74706.6(1.5)	-1.9(3.3)	9.8
	64	90	154	-73707.5(2.9)	-73705.6(1.5)	-1.9(3.3)	6.4*
	64	91	155	-72071.4(2.9)	-72069.5(1.5)	-1.9(3.3)	17.4
	64	92	156	-72536.4(2.9)	-72534.6(1.5)	-1.8(3.3)	9.1
	64	93	157	-70824.9(2.9)	-70823.1(1.5)	-1.8(3.3)	10.8
	64	94	158	-70691.0(2.9)	-70689.1(1.5)	-1.9(3.3)	11.5
	64	96	160	-67942.9(3.0)	-67941.1(1.6)	-1.8(3.4)	10.4
Lu	71	104	175	-55165.3(2.7)	-55167.1(1.9)	1.8(3.3)	8.9
	71	105	176	-53382.0(2.7)	-53383.8(1.9)	1.8(3.3)	3.1*
Hf	72	104	176	-54576.5(2.7)	-54578.0(3.6)	1.5(4.5)	7.0*
	72	105	177	-52892.8(2.4)	-52886.5(1.9)	-6.3(3.1)	3.4*
	72	106	178	-52447.4(2.4)	-52441.2(1.9)	-6.2(3.1)	2.8*
	72	107	179	-50475.1(2.4)	-50468.9(1.9)	-6.2(3.1)	4.2
	72	108	180	-49791.5(2.4)	-49785.3(1.9)	-6.2(3.1)	4.2

Table 6.3: Comparison between the mass excess values of the AME just before (ME_{before}) and after (ME_{after}) the data from the measurements within this work have been included [Audi2010]. The last column gives the influence of the TRIGA-TRAP data on the new literature values. (*) Note that input data with too little significance compared to others is not used in the AME. For details see text.

framework to a well-known mass, preferably to ^{12}C , since the mass doublet $^{12}\text{C}_{14} \text{ } ^1\text{H}_{12} - ^{180}\text{Hf}$ was not used. In this context, it can be understood why the mass values of a complete region in the nuclear chart are affected by a few measurements as shown in Fig. 6.7. The consistency of the complete data set used in the AME is tested by

$$\chi_n \equiv \sqrt{\frac{1}{f} \sum_i \left[\frac{\bar{q}_i - q_i}{\delta q_i} \right]^2}, \quad (6.4)$$

with the experimental input q_i , the adjusted value \bar{q}_i , and the number of degrees of freedom f . In case the TRIGA-TRAP data was implemented with the uncertainties given in Tab. 6.2 and the adjustment was performed, χ_n for the set of TRIGA-TRAP measurements became 1.9, which is far outside the expectation range of 1 ± 0.5 [Waps2003a]. However, χ_n can be also calculated for all cross-checks using carbon cluster ions which have been performed in each individual experimental run, leading to a value of 0.9. Obviously, there is a discrepancy between other older measurements implemented in the AME, not necessarily among the nuclides investigated here, and the TRIGA-TRAP data. Increasing the experimental uncertainty for the values given in Tab. 6.2 by a factor of 1.5, which is the standard procedure in the AME [Waps2003a], would reduce χ_n to the acceptable number of 1.5. However, the accuracy studies carefully performed at TRIGA-TRAP (see Sects. 5.2 and 5.3) as well as several more consistency tests during the rare-earth measurements and the data evaluation showed no hint of the presence of an additional uncertainty for the apparatus. To this end, the increase of the error bars is only a conservative standard treatment of the AME evaluators until other measurements at TRIGA-TRAP as well as at SHIPTRAP confirm the present results once more or simply more data of this apparatus are available. The fact that all mass excesses from the individual carbon cluster measurements (see Tab. 6.2) agree with the expected value zero, ensures the accuracy of mass measurements

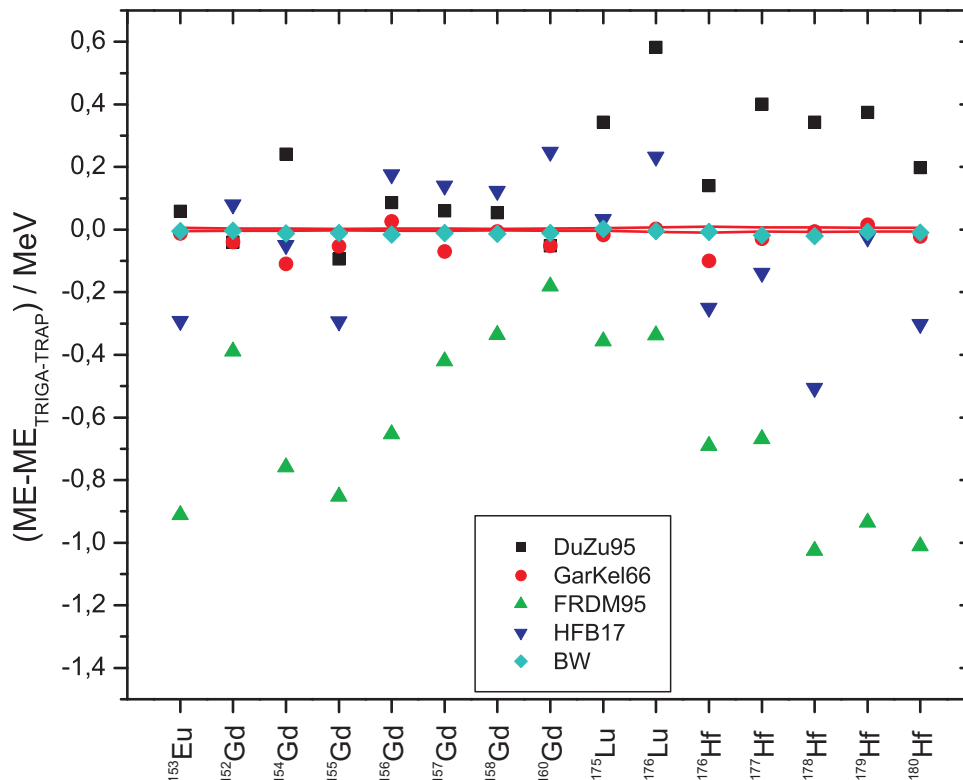


Figure 6.8: Comparison between mass models and the TRIGA-TRAP results, which define the horizontal zero line. The red lines mark the uncertainty of the experimental mass excesses. Note the MeV scale here compared to the keV uncertainties obtained in this work. Theoretical mass excesses are calculated by the Duflou-Zuker model (DuZu95), Garvey-Kelson relations (GarKel66), the Finite-Range Droplet Model (FRDM), the Hartree-Fock-Bogoliubov algorithm number 17 (HFB17), and by the Bethe-Weizsäcker mass formula (BW) (see Sect. 2.1). For discussion see text.

at TRIGA-TRAP and the reliability of the uncertainties claimed.

The impact of the TRIGA-TRAP mass measurements reported here on the literature values in the rare-earth region is mainly to provide new anchorpoints and to test the existing data based to a large extent on nuclear reaction studies. Moreover, the mass of ^{152}Gd is now determined by a second independent measurement, which makes it a primary nuclide in the language of the AME. Moreover, the uncertainty for the gadolinium, lutetium and hafnium isotopes improved by up to a factor of 2 (see Tab. 6.3), which is the result of the mass adjustment with the complicated network shown in Fig. 6.3.

6.1.4 Discussion of the new mass values with respect to nuclear structure studies

Comparison to theoretical mass models: The measured masses are compared with five selected mass models in Fig. 6.8, which have been discussed in detail in Sect. 2.1. It is remarkable how well the experimental masses are reproduced by the liquid-drop model (Eq. (2.10)) with the parameters given in Tab. 2.1. The rms deviation⁶ $\tilde{\sigma}_{\text{rms}}$ (Eq. (2.4)) of only 11 keV in this case can be explained looking at Fig. 2.5: the nuclides under

⁶The label $\tilde{\sigma}_{\text{rms}}$ is only used to make clear that the values in this section refer to a limited data set and not to all known nuclides.

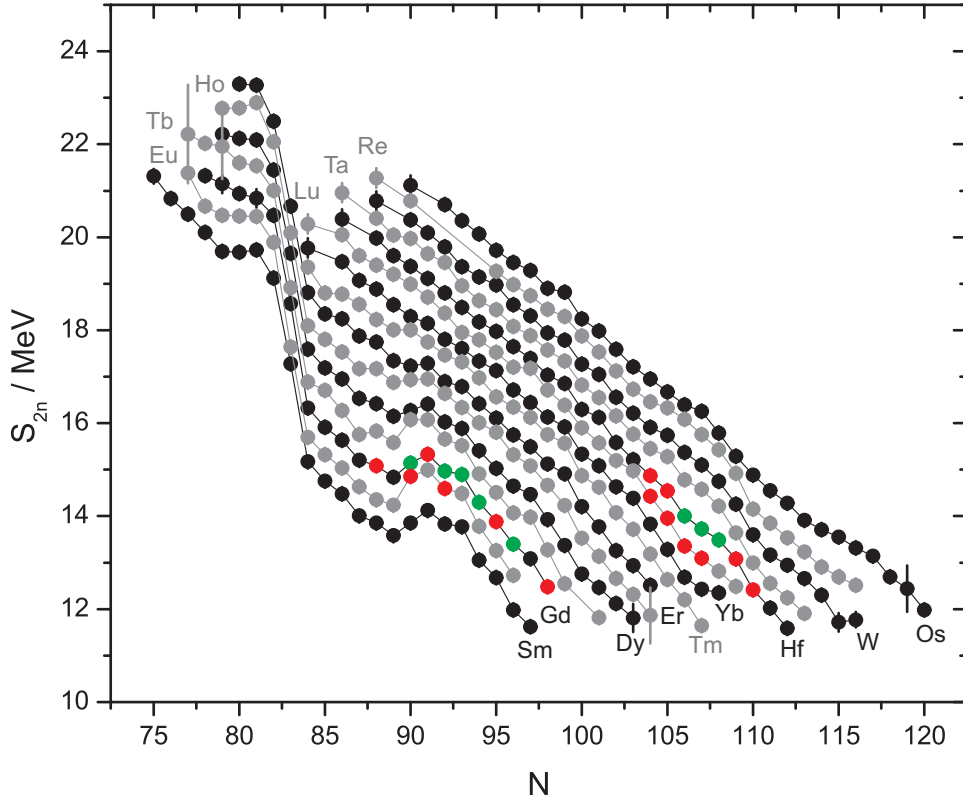


Figure 6.9: Two-neutron separation energies S_{2n} as a function of the neutron number N for nuclides in the rare-earth region. The latest adjusted values from the AME [Audi2010] were used for the calculation including the TRIGA-TRAP results as listed in Tab. 6.3. Red points mark values partly based, green points those fully based on nuclides which have been also investigated here. Besides the neutron-shell closure at $N = 82$ and the general linear trend of S_{2n} , the strongly deformed nuclei between $N = 90$ and 94 for $Z = 62 - 68$ show enhanced neutron binding. For details see text.

investigation are not close to a magic number and, moreover, are part of the valley of stability. The large discrepancies of the Bethe-Weizsäcker formula occur for magic and exotic nuclei due to the negligence of shell-effects. As already discussed in Sect. 2.1.4, Garvey-Kelson relations linking neighbouring nuclides (see e.g. Eq. (2.28)) perform very well in the region of known masses, leading to $\tilde{\sigma}_{\text{rms}} = 49$ keV in Fig. 6.8. The model by Duflo and Zuker ($\tilde{\sigma}_{\text{rms}} = 261$ keV) as well as the HFB17 algorithm ($\tilde{\sigma}_{\text{rms}} = 230$ keV) reproduce the experimental results similarly well with rms deviations within the ranges of their total values given in Sect. 2.1. However, while the Duflo-Zuker model in general overestimates the masses, the HFB17 leads to an underestimation for europium and hafnium. In this case, ^{155}Gd is exceptional since the theoretical prediction by HFB17 is about 300 keV below the experimental value while the other gadolinium isotopes show a positive offset and ^{154}Gd agrees quite well. The FRDM ($\tilde{\sigma}_{\text{rms}} = 691$ keV) with a parameter set from 1995 [Möll1995] is not appropriate in this mass region since it underestimates the experimental values by 0.5-1 MeV. The general problem in this comparison is the low precision of theoretical predictions in comparison to experimental uncertainties, which is also visible in Fig. 6.8.

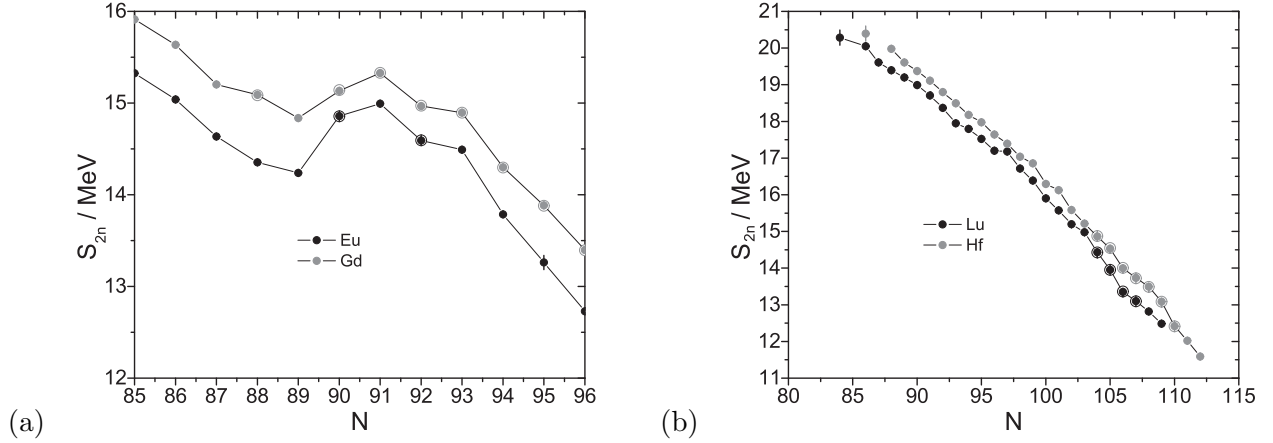


Figure 6.10: Two-neutron separation energies calculated by replacing the mass values of the AME with the data given in Tab. 6.2 for the nuclides under investigation here. For those cases where TRIGA-TRAP data was used in the calculation the open circles denote the corresponding result from the literature values. (a) Zoom into the region of deformed nuclei around $N \sim 90$. (b) General linear trend for lutetium and hafnium. For details see text.

Deformation in the region $N \sim 90$ and collective effects: Besides looking at the masses, or mass excesses, respectively, of the nuclides under investigation within this work, one should also pay attention to the binding energies. Fig. 6.9 shows the two-neutron separation energy S_{2n} (Eq. (2.2)) in the rare-earth region as a function of the neutron number N . The values are calculated using the latest AME [Audi2010] including the TRIGA-TRAP results (see Sect. 6.1.3). Points where mass values measured within this work entered are marked in red and green, even- Z chains have black circles, odd- Z chains grey ones. The sudden drop of S_{2n} after $N = 82$ has been already identified in Chap. 2 as a neutron shell closure for magic nuclides. However, the liquid-drop model suggests a linear behaviour which is also interrupted by slight curvatures e.g. at $N \sim 90$. The S_{2n} lines for the elements europium ($Z = 63$) and gadolinium ($Z = 64$) are shown for this region in Fig. 6.10(a). Here, the binding energies (Eq. (2.1)) calculated from the results in Tab. 6.2 replace the AME values for the nuclides under investigation within this work. The sudden increase in S_{2n} when the neutron number exceeds 89 characterises a well-established region of quadrupolar-prolate deformed nuclei [Barb1964], which will be discussed in more detail later in this section.

Inspecting Fig. 6.9 more carefully, additional slight deviations from the expected linear behaviour of S_{2n} are also noticed for higher values of N , e.g. at hafnium. This region is shown in Fig. 6.10(b) for the elements lutetium ($Z = 71$) and hafnium ($Z = 72$), which have been investigated at TRIGA-TRAP (the values have been calculated similarly to Fig. 6.10(a)). In [Caki2009] the authors report on calculations employing one of the collective models, the Interacting-Boson Approximation (IBA)⁷ (see e.g. [Cast2000]), for deformed rare-earth nuclides to determine contributions of collective correlations among valence nucleons to $S_{2n, \text{coll}}$, which differs from S_{2n} by only a linear term⁸. An enhanced sensitivity of the ground-state binding energy measured, e.g. at TRIGA-TRAP, to collective excitations is discovered. In [Caki2009], the lowest experimental intrinsic 0^+ levels of Er, Yb, and Hf were fit with the IBA assuming each level to be the lowest collective intrinsic

⁷The IBA - also referred to as IBM - treats valence nucleons as boson pairs of protons and neutrons in even-even nuclei.

⁸Linear contributions to S_{2n} originate from the average nucleon potential as well as standard interactions (e.g. pairing).

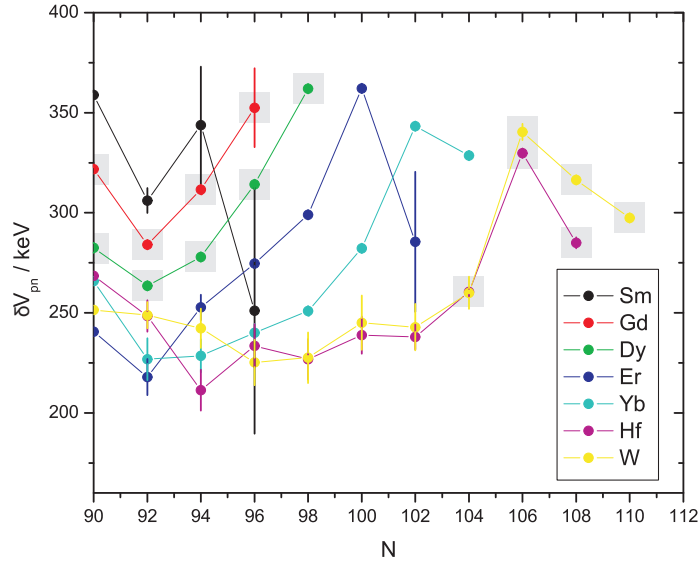


Figure 6.11: δV_{pn} values for even-even rare-earth nuclei. The calculation is based on the latest AME [Audi2010] including the mass data presented within this work. Values where TRIGA-TRAP data contributed are marked with grey boxes. For details see text.

0^+ state. For ^{176}Hf , these two levels are separated by only 140 keV, but the IBA calculations gave about 1 MeV difference in $S_{2n,\text{coll}}$ (for ^{168}Er this difference is even about 4 MeV). This demonstrated the sensitivity of the ground-state binding energies to nuclear structure including the nature of the intrinsic states. Despite the fact that this approach is still not fully developed and tested, this method may be of use in studying collective excitations requiring further high-precision mass measurements (e.g. at TRIGA-TRAP).

p-n interaction among valence neutrons: The ground-state masses - or nuclear binding energies - can be also interpreted on the basis of proton-neutron interactions among valence nucleons. In case the two-neutron separation energies are regarded as first derivatives of the binding energy surface $B(N, Z)$, one can also define double differences approximating the second derivatives. To obtain the average interaction between the last protons and the last neutrons, the δV_{pn} values can be defined as follows [Isac1995]:

$$\delta V_{pn} = \begin{cases} \frac{1}{4} [B(N, Z) - B(N-2, Z) - B(N, Z-2) + B(N-2, Z-2)] & N \text{ even, } Z \text{ even,} \\ \frac{1}{2} [B(N, Z) - B(N-2, Z) - B(N, Z-1) + B(N-2, Z-1)] & N \text{ even, } Z \text{ odd,} \\ \frac{1}{2} [B(N, Z) - B(N-1, Z) - B(N, Z-2) + B(N-1, Z-2)] & N \text{ odd, } Z \text{ even,} \\ [B(N, Z) - B(N-1, Z) - B(N, Z-1) + B(N-1, Z-1)] & N \text{ odd, } Z \text{ odd.} \end{cases} \quad (6.5)$$

For the commonly considered case of even-even nuclides δV_{pn} is the interaction between the last two protons and the last two neutrons, for even-odd, odd-even, and odd-odd nuclei it is only between the last nucleon of each type. Fig. 6.11 shows the values for even Z and even N as a function of N using the latest AME mass excesses including the TRIGA-TRAP data. There is a striking regularity visible, showing an increase of δV_{pn} with N until a maximum is reached. Obviously, more experimental data is required to calculate the values for ^{162}Gd and ^{166}Dy for a confirmation of the general trend. However, a simple qualitative understanding is possible when taking the deformed Nilsson orbits occupied by the valence nucleons into account (see

Z/N		92	94	96	104	106	108
64	p	5/2[413]	5/2[413]	5/2[413]			
	n	3/2[521]	3/2[521]	3/2[521]			
72	p				7/2[404]	7/2[404]	7/2[404]
	n				5/2[512]	7/2[514]	9/2[624]

Table 6.4: Ground-state Nilsson orbits for protons (p) and neutrons (n) for the even-even gadolinium and hafnium isotopes under investigation within this thesis work [Okte2006].

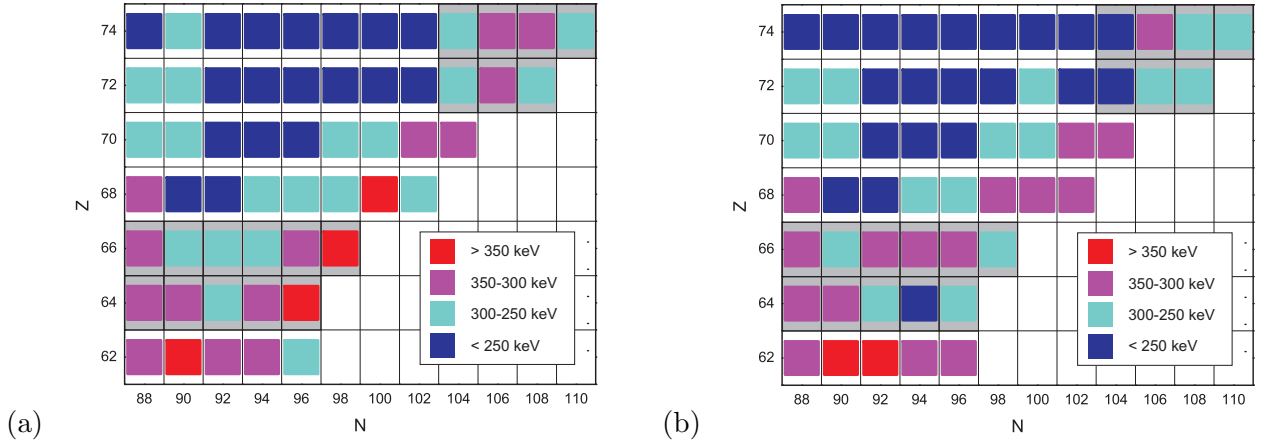


Figure 6.12: (a) Experimental δV_{pn} values for even-even rare-earth nuclides calculated similarly to Fig. 6.11. (b) Theoretical δV_{pn} values for the same nuclides shown in (a) obtained using a Density-Functional Theory (DFT) model, values taken from [Stoi2007]. In both cases nuclides are shaded in grey if TRIGA-TRAP data contributed to the corresponding experimental δV_{pn} .

Sect. 2.1.3) [Bren2006]. Taking the Nilsson diagram [Gust1967] (Fig. 2.7(b) shows the level splitting only for a single shell model orbit) the even-even nuclides in Fig. 6.11 mainly fill up those proton Nilsson orbits which are relatively flat in energy as a function of the deformation α_{20} , e.g. 5/2[413] in case of $^{156,158,160}\text{Gd}$ [Okte2006] since the proton number $Z = 64$ is close to mid-shell. The p-n interaction will be largest in case protons and neutrons occupy orbits with similar inclinations θ ($\sin \theta \sim K/j$, see Fig. 2.7(a)) to the symmetry axis. The neutrons fill up the lower half of the shell starting with $N = 83$, so K will vary from low to high values as the neutron number increases for a certain element. The increasing p-n interaction expressed by the δV_{pn} values for even-even nuclides is visible in Fig. 6.11. The parallel slopes for different elements can be also explained by the overlap of Nilsson orbits since for each subsequent (even) Z the protons fill up the next level in the Nilsson diagram, leading to a slightly more positive slope of the energy as a function of deformation.

This qualitative argumentation has been also checked through calculations based on the Nilsson orbits (some examples for isotopes under investigation here are given in Tab. 6.4) [Okte2006]. The general trend as well as the correct order of magnitude (a few hundred keV) could be reproduced, especially the sudden drop in δV_{pn} for hafnium and other elements. However, looking at the orbits for the three gadolinium isotopes, it is obvious that the simple overlap model cannot explain the increase in δV_{pn} since the levels are identical due to level crossing as a function of the deformation. A microscopic calculation has been also performed using Density-Functional Theory (DFT) based on a self-consistent solution of the Hartree-Fock-Bogoliubov

equations and an approximate pairing treatment [Stoi2007]. Fig 6.12 presents a comparison between the experimental δV_{pn} determined with the help of the latest AME including the mass measurements reported within this work and corresponding DFT calculations. It is remarkable that most of the values are predicted with an accuracy on the 100 keV-level while DFT in general reproduces binding energies with rms errors in the order of 1 MeV. This is due to δV_{pn} being a quantity based on binding energy differences on which DFT usually performs much better. As discussed in [Stoi2007], the agreement between DFT calculations and experimental values is best for deformed regions, as this is the case for the nuclides under investigation here. This impressive level of agreement can be used for local mass extrapolations in such regions where three of four binding energies required in the δV_{pn} are known.

Within this section, the importance of high-precision mass data in the region of rare-earth nuclides with respect to nuclear structure studies was discussed. The mass measurements at TRIGA-TRAP helped to confirm the structure of the mass surface and its derivatives which differs significantly from a linear behaviour. This is especially important since all previous studies were only based on reaction energy measurements, which have shown in the past to be sometimes wrong due to, e.g. missing lines. The data given in Tab. 6.2 fixes the missing links of the mass surface not only to a well-known mass but directly to the atomic-mass standard ^{12}C , confirming the nuclear structure effects also on the absolute energy scale.

6.2 First direct mass measurement of ^{241}Am

During the commissioning of the TRIGA-TRAP setup in the beginning of 2009 it was already possible to measure the mass of ^{241}Am for the first time directly in a doublet with the atomic-mass standard ^{12}C . At this point it should be already mentioned that a large residual pressure in the precision trap (and, thus, only short possible excitation times) and problems with the ion count-rate lead to a comparably large uncertainty of $\delta m/m = 2.5 \times 10^{-7}$, which requires a repetition of this experiment with the completed setup. It is important to note that above uranium only the masses of $^{252-254}\text{No}$ [Bloc2010a] have been measured directly besides ^{241}Am so far.

6.2.1 Mass measurements and results

Ion production and contaminations: The ions of interest as well as the carbon clusters for the calibration of the magnetic field and accuracy cross-checks have been produced similarly to the rare-earth nuclides as described in Sect. 6.1.1. Also the target production using a solution of $\text{Am}(\text{NO}_3)_3$ in 1 molar nitric acid was identical. The atom density on the Sigradur[®] surface was about $8 \times 10^{13} / \text{mm}^2$ leading to an activity of roughly 50 kBq ($t_{1/2} = 432.2 \text{ y}$ [Audi2003]). For the mass measurement $^{241}\text{Am}^{16}\text{O}^+$ ions were used, $^{12}\text{C}_{21}^+$ served as the reference, $^{12}\text{C}_{20,22}^+$ as cross-checks. The mean count-rate for americium was 0.1-0.5 ions per shot, which was sufficient to accumulate 700-1000 ions in a single resonance during 2-3 hours.

In order to determine possible contaminations from molecules created in the setup, a similar combinatorial analysis as described in Sect. 6.1.1 was performed showing no molecular ion within a frequency window of $\pm 5 \text{ Hz}$. Since americium has only one long-lived isotope and the mass is more than 50 u away from the species investigated so far, contaminations are in general no issue. Furthermore, all $^{241}\text{Am}^{16}\text{O}^+$ ions can be considered to be in the nuclear ground-state (see also Sect. 6.1.1).

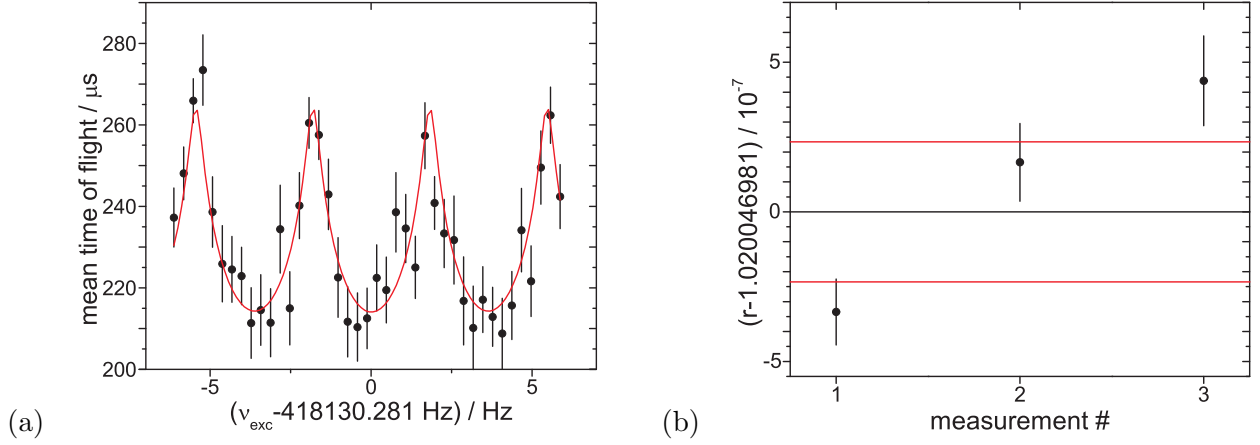


Figure 6.13: (a) TOF-ICR resonance with 677 $^{241}\text{Am}^{16}\text{O}^+$ ions with a centre frequency of $\nu_c = 418130.281(29)$ Hz using a Ramsey excitation profile of two 30 ms pulses and a waiting time of 240 ms. (b) Frequency ratios r_i of the 3 individual measurements of $^{241}\text{Am}^{16}\text{O}^+$ with $^{21}\text{C}_{12}^+$ as the reference ion. The black line marks the mean value of $r = 1.020046981(234)$ and the red lines indicate its statistical uncertainty, only including the additional uncertainty due to fluctuations of the magnetic field.

Result of the mass measurement: The mass measurement on americium reported here was performed with an earlier design of the pumping barrier [Neid2008] between both Penning traps (see Fig. 4.15 for the new improved design used already during the rare-earth measurements) with a channel diameter of about 4 mm. To this end, the residual pressure in the precision trap was about one order of magnitude worse compared to the present situation after the replacement of the differential pumping barrier. This led to large damping effects (mean damping determined for the reference resonances of $0.12(2) / \text{s}$) limiting the excitation time to two 30 ms pulses and an intermediate waiting period of 240 ms. Fig. 6.13(a) shows one of the three individual TOF-ICR resonances recorded for $^{241}\text{Am}^{16}\text{O}^+$. The evaluation leading to a mean frequency ratio was done according to Sect. 5.3.

During the commissioning phase accuracy studies to determine the contributions to the uncertainty listed

nuclide	ion	ref.	#	BR	r	m_{atom} / μu	$ME_{\text{TRIGA-TRAP}}$ / keV	ME_{AME2003} / keV	ΔME / keV
$^{241}_{95}\text{Am}$	$^{241}\text{Am}^{16}\text{O}^+$	$^{12}\text{C}_{21}^+$	3	9.42	1.020046981(234)	241 056914(59)	53015(55)	52936.0(1.8)	-79(59)
*	$^{12}\text{C}_{20}^+$	$^{12}\text{C}_{21}^+$	1	-	0.9523808633(996)	-	3.4(23.4)	0(0)	-3.4(23.4)
*	$^{12}\text{C}_{22}^+$	$^{12}\text{C}_{21}^+$	2	0.76	1.047619027(123)	-	-29.3(29.0)	0(0)	29.3(29.0)

Table 6.5: Result of the mass measurement of ^{241}Am . The columns contain the nuclide, the ion of interest, the reference ion (ref.), the number of individual measurements (#), the mean frequency ratio r (see Eq. (3.46)), the atomic mass of the nuclide, the atomic mass excess $ME_{\text{TRIGA-TRAP}}$ obtained at TRIGA-TRAP, the literature value ME_{AME2003} [Waps2003b] and the difference $\Delta ME = ME_{\text{AME2003}} - ME_{\text{TRIGA-TRAP}}$. Rows labeled with (*) contain cross-reference measurements with carbon clusters which have been performed as accuracy checks. In these cases, the mass excess values refer to the cluster and not to the ^{12}C atom.

in Sects. 5.2 and 5.3 have been performed as well. At this point, the statistical uncertainty gained with a 300 ms total excitation time was larger than the effects introduced by magnetic field fluctuations and the mass-dependent shift, which could not be determined. For consistency, the values obtained in the accuracy studies after the replacement of the pumping barrier (see Sect. 5.3) are used. This is justified since the magnetic field fluctuations as well as the mass-dependent shift do not depend on this particular change to the setup.

Fig. 6.13(b) shows the three individual frequency ratios for $^{241}\text{Am}^{16}\text{O}^+$ as well as the mean value and its uncertainty. Obviously, point scattering is an issue in this measurement (Birge ratio 9.42), which apparently did not originate from any environmental influence. Those have been monitored during the rare-earth measurement and no impact was observed on a precision-level of one order of magnitude better than obtained here in case of americium. The reason for the point scattering is rather the comparably large count-rate fluctuation: due to the low atom density on the target, the count-rate dropped to zero already after a few shots. Rotating the target lead to a sudden increase of up to 10 ions per shot, followed by a drop again. It has been observed in many tests with carbon clusters that such a highly fluctuating count-rate leads to point scattering between the individual frequency ratios in a mass measurement. The problem is accounted for by using the external error as given in Eq. (5.4).

The result of the mass measurement of ^{241}Am is given in Tab. 6.5 including the two sets of cross-checks with carbon clusters to confirm the accuracy. The values have been calculated similarly to Tab. 6.2. As already mentioned the final relative uncertainty of the atomic mass of ^{241}Am is about a factor of 10 larger than reported for measurements after the completion of the setup (see Sect. 6.1), which is due to the residual pressure limiting the total excitation time to only 300 ms as well as the count-rate problem. To this end, the TRIGA-TRAP value will not be used in the upcoming AME until the measurement is repeated with a

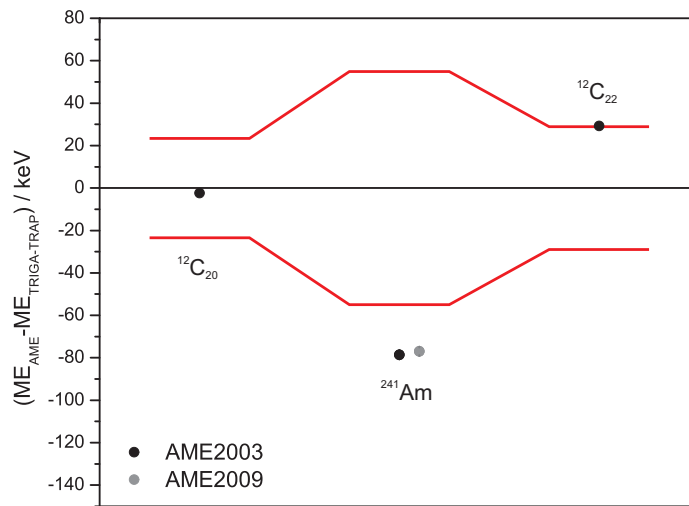


Figure 6.14: Result of the mass measurement of ^{241}Am . The difference $\Delta ME = ME_{\text{AME2003}} - ME_{\text{TRIGA-TRAP}}$ of the mass excesses between the literature [Waps2003b] and the TRIGA-TRAP values is shown (data points) as well for two cross-checks with carbon clusters. The error bars denoting the uncertainty of the AME value are included but hardly visible, the red lines mark the uncertainty of the measurement result. For completeness, the slightly shifted mass excess from the AME 2009 [Audi2009] is also given. For details see text.

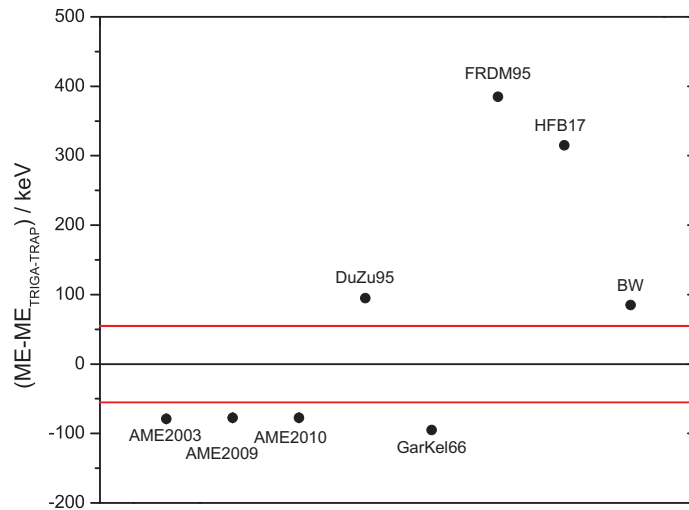


Figure 6.15: Comparison of the experimental mass excess (zero line) to the latest three AME values [Waps2003b, Audi2009, Audi2010] and theoretical calculations by the Duflo-Zuker model (DuZu95), Garvey-Kelson relations (GarKel66), the Finite-Range-Droplet-Model (FRDM95), a Hartree-Fock-Bogoliubov algorithm (HFB17), and the Bethe-Weizsäcker formula (BW). The red lines mark the uncertainty of the experimental value obtained at TRIGA-TRAP. The error bars of the experimental values are too small to be visible. For discussion see text.

similar performance of the setup than reported in Sect. 6.1 since the uncertainty of other contributions is more than an order of magnitude smaller. Fig. 6.14 compares the literature values from 2003 and 2009 of the mass excess with the TRIGA-TRAP result, showing an agreement on the level of 1.3 standard deviations. For completeness, the cross-checks are also given in this figure.

6.2.2 Discussion

Fig. 6.15 compares the TRIGA-TRAP mass excess of ^{241}Am to calculations based on different theoretical mass models. The last three values available from the AME are also included. In principle, the Garvey-Kelson and the Duflo-Zuker model reproduce the experimental mass excess similarly well. However, only the Garvey-Kelson relations seem to agree with the present literature value of the ^{241}Am mass, whereas the Duflo-Zuker model shows an offset of about 170 keV in this case. Also the Bethe-Weizsäcker result lies within 100 keV of the TRIGA-TRAP and 170 keV of the AME mass excess, which can be understood since americium is far away from a shell closure and, moreover, the rather long-lived nuclide with $N = 146$ lies on the imaginary prolongation of the valley of stability. FRDM and HFB calculations are already 300-400 keV off which can be also expected due to their overall rms error (see Sect. 2.1). It is remarkable that all mass models besides the local Garvey-Kelson relations overestimate the mass excess, or underestimate the binding energy. However, the argument given in Sect. 6.1.4 stays valid that the present uncertainties of theoretical mass predictions are in general several hundred keV, which makes it impossible to draw further conclusions. Furthermore, the comparison for a single nuclide is not sufficient for a general analysis of the performance of mass models in this region of the nuclear chart.

Mass measurements at the upper end of the nuclear chart are important, since the masses for elements

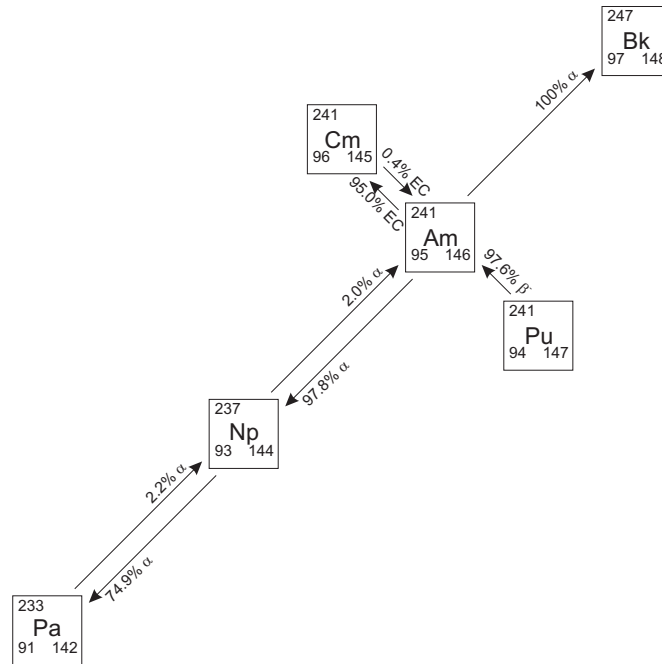


Figure 6.16: Part of the network to determine the atomic masses with ^{241}Am embedded [Waps2003a]. The numbers on the arrows denote the influence of a mass on another. For discussion see text.

heavier than uranium are in general only determined by reaction energies (apart from the measurement reported here and the SHIPTRAP experiment on nobelium isotopes already mentioned). Part of this network embedding ^{241}Am is displayed in Fig. 6.16. So far the mass of ^{241}Am is mainly determined by a β^- decay from ^{241}Pu and, in turn, has large influences on the masses of a complete chain of nuclides via α decays and EC.

7 Conclusion and Outlook

For the first time, a Penning trap setup has been installed at a nuclear reactor within this thesis work to perform highly precise and accurate mass measurements on neutron-rich fission products and actinoids. The concept based on two ion traps, one for ion cooling and isobaric selection, the second for the actual mass measurement, is similar to existing facilities like SHIPTRAP and JYFLTRAP, but TRIGA-TRAP goes even beyond [Kete2008]. Technical developments discussed within this thesis will improve accuracy and sensitivity also at other experiments such as SHIPTRAP. The complete vacuum system of TRIGA-TRAP has been set up, employing a cryogenic trap tube for the first time in an on-line mass spectrometer for short-lived ions. This leads to a thermal noise reduction necessary for a newly developed non-destructive ion detection system, which will ultimately allow for a high-precision mass measurement on a single singly charged ion. Part of this system is already completed and first test results of the components like a superconducting resonator have been discussed showing very promising results [Kete2009]. Besides this, a position-sensitive delay line detector has been implemented at TRIGA-TRAP and tested extensively beforehand at SHIPTRAP, which enables monitoring of the ion motion in the Penning trap using the position information of the ion impact on the detector [Eite2009].

Simulations of the electrostatic ion transport from the sources to the Penning traps and to a detector used in the TOF-ICR measurements have been performed including about 100 voltage parameters and the field of the superconducting magnet. Ion optics consisting of cylinder lenses, xy-deflectors, and drift tubes were designed and assembled together with the double-Penning trap system. A crucial part was the development of a new differential pumping barrier suppressing the helium gas flow from the purification trap to the precision trap, which allowed for a better alignment of the channel versus the axis of the system.

A new non-resonant laser ablation ion source has been developed and commissioned which is based on a simple and reliable design [Smor2009]. Extensive tests of the ion production with several different target materials showed that this is a universal tool to deliver carbon cluster ions for absolute mass measurements as well as ions of certain stable or long-lived actinoid nuclides. TRIGA-TRAP can perform off-line experiments without the reactor, important for tests of the mass values known commonly from reaction studies and for nuclear structure investigations independently from beam-time schedules.

Based on the CS framework developed at GSI and a measurement program from LEBIT (Michigan State University, East Lansing USA), a distributed control system with more than 150 parameters has been set up to enable full remote control of the complete experiment. To this end, devices like voltage supplies and frequency generators were implemented into the framework and movable parts along the beamline like linear manipulators are operated by stepper motors. Besides the capability of remote control this also reduced the probability of mistakes since, e.g., detectors are moved into the ion beam with a precision of sub- μm , or automated switches replace manual changes of signal cables.

Extensive accuracy studies have been performed using carbon cluster ions of various sizes since their mass is exactly known by definition besides the negligible contributions of the binding energies [Kete2010]. The

contribution of magnetic field fluctuations to the final uncertainty of a mass measurement at TRIGA-TRAP is $u_f(\nu_{c,\text{ref}})/\nu_{c,\text{ref}} = 6(2) \times 10^{-11} / \text{min} \times \Delta t$. Due to an unavoidable small misalignment of the trap axis versus the magnetic field, a mass-dependent systematic shift of $\epsilon_m(r)/r = -2.2(2) \times 10^{-9} \times (m - m_{\text{ref}}) / u$ of the frequency ratio r is observed, which can be corrected. Unlike other facilities, no further residual systematic uncertainty has to be added at TRIGA-TRAP at the present level of precision.

Besides the commissioning of TRIGA-TRAP and the technical developments mentioned above, first direct mass measurements have been performed within this thesis work. One focus was on the well-established deformed region of rare-earth nuclides around $N \sim 90$. 15 stable isotopes of the elements europium ($Z = 63$), gadolinium ($Z = 64$), lutetium ($Z = 71$), and hafnium ($Z = 72$) could be measured with a relative precision of a few times 10^{-8} using the Ramsey technique which reduces the uncertainty by up to a factor of 3 without increasing the excitation time. For most of the nuclides the results reported here provide the very first link to the atomic-mass standard ^{12}C , whereas previous literature mass values were determined mainly by (n, γ) reaction energies. Moreover, for ^{152}Gd the measurement within this work was the only independent confirmation besides such a nuclear reaction experiment. In comparison to the previous literature values, a general offset in the order of 5-10 keV has been determined, which will be confirmed by further measurements at TRIGA-TRAP and SHIPTRAP. The derivatives of the mass surface, S_{2n} and δV_{pn} , and thus, the nuclear structure effects in this region of the chart of nuclides have been confirmed. As discussed in Sect. 6.1.4 p-n interactions among valence nucleons can be investigated using the ground-state binding energies from high-precision mass measurements as performed, e.g., at TRIGA-TRAP. Furthermore, these experimental results in certain rare-earth nuclides like ^{176}Hf show an enhanced sensitivity to collectif effects in the nucleus.

Since at TRIGA-TRAP the long-lived actinoids will be studied, the very first direct mass measurement on ^{241}Am has been performed within this thesis. However, since the experiment already took place during the early commissioning phase, the final uncertainty is 55 keV, about a factor of 10 larger than possible with the completed setup as demonstrated with the rare-earth elements. The Am measurement will be repeated soon to provide a new accurate anchorpoint of the mass surface for heavy elements. Presently, literature values in this region are only obtained through decay energies besides the isotopes $^{252-254}\text{No}$ measured at SHIPTRAP [Bloc2010a, Dwor2010]. With the present result of ^{241}Am at TRIGA-TRAP, no large discrepancy to the literature value is observed.

In the near future, TRIGA-TRAP has to be coupled to the research reactor to enable mass measurements on neutron-rich fission products [Eiba2010]. This project is presently ongoing within the TRIGA-SPEC collaboration, which also includes a collinear laser-spectroscopy beamline. Neutron-rich ion beams will be delivered by a system of an ECR ion source [Smor2010], a magnetic mass separator and an RFQ cooler-buncher [Beye2012] at an energy of 30 keV. A pulsed drift tube has been developed to reduce the energy to below 100 eV and to enable storage in the Penning traps. The first nuclides to be investigated will be ^{93}Sr , $^{94,95}\text{Y}$, ^{101}Mo , and ^{104}Tc since the transport yields after the gas-jet system are in the order of $10^3 - 10^4$ [Eiba2010]. Their mass uncertainty of presently about or more than 10 keV could also be easily improved at TRIGA-TRAP.

Even before the on-line coupling, some improvements to the TRIGA-TRAP setup will be done. First of all, a pressure stabilisation system will be implemented to the nitrogen dewar cooling the trap tube to enable a temperature stabilised operation of the Penning traps at 77 K. Tests at SHIPTRAP with a stabilisation at 300 K showed promising results, so excitation times of several seconds should be possible at TRIGA-TRAP, which could help to improve the uncertainty for stable elements significantly. Moreover, an upgrade of the

laser ablation ion source is presently developed in the group of Prof. Klaus Wendt in Mainz, which consists of a miniature RFQ to accumulate and cool the ions directly in front of the target [Schw2010]. This will dramatically improve the efficiency of the ion transport to the purification trap. Furthermore, mass selection on the level of a few mass units will reduce the number of ions prior to the mass-selective buffer gas cooling and thus, increase the efficiency for rare ions like actinoids even further. It is also considered to use a second laser pulse to resonantly ionise the ablated atoms in the volume of the RFQ for the future. This upgrade as well as implementing an electrostatic quadrupole lense will improve the efficiency of TRIGA-TRAP in combination with the laser ion source to enable mass measurements on actinoids like ^{252}Cf where orders of magnitude less atoms are available to produce a target.

Bibliography

- [Abzo1991] A. Abzouzi, E. Caurier, and A. P. Zuker, Phys. Rev. Lett. **66** (1991) 1134.
- [Adam1971] A. Adams and F. H. Read, J. Phys. E **5** (1971) 150.
- [Ande1962] P. W. Anderson, Phys. Rev. Lett. **9** (1962) 309.
- [Ande1982] E. Anders and M. Ebihara, Geochim. Cosmochim. Act. **46** (1982) 2363 .
- [Anto1978] K. R. Anton, S. L. Kaufman, W. Klempt *et al.*, Phys. Rev. Lett. **40** (1978) 642.
- [Asto1920] F. W. Aston, Nature **105** (1920) 9.
- [Audi1995] G. Audi and A. H. Wapstra, Nucl. Phys. A **595** (1995) 409.
- [Audi2003] G. Audi, O. Bersillon, J. Blachot *et al.*, Nucl. Phys. A **729** (2003) 3.
- [Audi2009] G. Audi, private communication (2009).
- [Audi2010] G. Audi and M. Wang, private communication (2010).
- [Balo1987] M. K. Balodis, P. T. Prokofjev, N. D. Kramer *et al.*, Nucl. Phys. A **472** (1987) 445 .
- [Barb1964] R. Barber, H. Duckworth, B. Hogg *et al.*, Phys. Rev. Lett. **12** (1964) 597.
- [Barb1972] R. C. Barber, R. L. Bishop, J. O. Meredith *et al.*, Can. J. Phys. **50** (1972) 34.
- [Bard1957] J. Bardeen, L. N. Cooper, and J. R. Schrieffer, Phys. Rev. **108** (1957) 1175.
- [Bare2005] J. Barea, A. Frank, J. G. Hirsch. *et al.*, Phys. Rev. Lett. **94** (2005) 102501.
- [Bare2008] J. Barea, A. Frank, J. G. Hirsch *et al.*, Phys. Rev. C **77** (2008) 041304.
- [Beas1969] M. R. Beasley, R. Labusch, and W. W. Webb, Phys. Rev. **181** (1969) 682.
- [Beck2000] D. Beck, F. Ames, G. Audi *et al.*, Eur. Phys. J. A **8** (2000) 307.
- [Beck2004] D. Beck, K. Blaum, H. Brand *et al.*, Nucl. Instrum. Meth. A **527** (2004) 567.
- [Beck2009] D. Beck, K. Blaum, G. Bollen *et al.*, Nucl. Instrum. Meth. A **598** (2009) 635 .
- [Beie2001] T. Beier, H. Häffner, N. Hermanspahn *et al.*, Phys. Rev. Lett. **88** (2001) 011603.
- [Bend2001] M. Bender, W. Nazarewicz, and P. Reinhard, Phys. Lett. B **515** (2001) 42.
- [Bend2002] M. Bender, T. Cornelius, G. A. Lalazissis *et al.*, Eur. Phys. J. A **14** (2002) 23.

- [Bend2003] M. Bender, P. H. Heenen, and P. G. Reinhard, *Rev. Mod. Phys.* **75** (2003) 121.
- [Beth1936] H. A. Bethe and R. F. Bacher, *Rev. Mod. Phys.* **8** (1936) 82.
- [Beth1971] H. A. Bethe, *Ann. Rev. Nucl. Sci.* **21** (1971) 93.
- [Beth2008] K. Bethge, G. Walter, and B. Wiedemann, *Kernphysik*, Springer (2008).
- [Beye2012] T. Beyer, Ph.D. thesis, Ruprecht-Karls-Universität Heidelberg (2012), in preparation.
- [Bill2005] J. Billowes, *Hyperfine Interact.* **162** (2005) 63.
- [Blau2002] K. Blaum, G. Bollen, F. Herfurth *et al.*, *Eur. Phys. J. A* **15** (2002) 245.
- [Blau2003a] K. Blaum, G. Audi, D. Beck *et al.*, *Phys. Rev. Lett.* **91** (2003) 260801.
- [Blau2003b] K. Blaum, G. Bollen, F. Herfurth *et al.*, *J. Phys. B* **36** (2003) 921.
- [Blau2006a] K. Blaum, *Phys. Rep.* **425** (2006) 1.
- [Blau2006b] K. Blaum and H. Schatz, *Physik Journal* **2** (2006) 35.
- [Bloc2010a] M. Block, D. Ackermann, K. Blaum *et al.*, *Nature* **463** (2010) 785.
- [Bloc2010b] M. Block, D. Ackermann, K. Blaum *et al.*, *Hyperfine Interact.* **196** (2010) 225.
- [Bogu1977] J. Boguta and A. R. Bodmer, *Nucl. Phys. A* **292** (1977) 413 .
- [Bohr1939] N. Bohr and J. A. Wheeler, *Phys. Rev.* **56** (1939) 426.
- [Boll1992] G. Bollen, H. J. Kluge, M. König *et al.*, *Phys. Rev. C* **46** (1992) R2140.
- [Boll1996] G. Bollen, S. Becker, H. J. Kluge *et al.*, *Nucl. Instrum. Meth. A* **368** (1996) 675.
- [Boll2001] G. Bollen, *Nucl. Phys. A* **693** (2001) 3.
- [Bond2003] V. Bondarenko, A. V. Afanasjev, F. Becvar *et al.*, *Nucl. Phys. A* **726** (2003) 175.
- [Borc1993] C. Borcea and G. Audi, *Rev. Roum. Phys.* **38** (1993) 455.
- [Brac1973] M. Brack and H. C. Pauli, *Nucl. Phys. A* **207** (1973) 401 .
- [Brad1936] N. E. Bradbury and R. A. Nielsen, *Phys. Rev.* **49** (1936) 388.
- [Bren2006] D. S. Brenner, R. B. Cakirli, and R. F. Casten, *Phys. Rev. C* **73** (2006) 34315.
- [Brow1971] G. E. Brown, *Unified Theory of Nuclear Forces and Models*, North Holland, Amsterdam (1971).
- [Brow1982] L. S. Brown and G. Gabrielse, *Phys. Rev. A* **25** (1982) 2423.
- [Brow1986] L. S. Brown and G. Gabrielse, *Rev. Mod. Phys.* **58** (1986) 233.
- [Brue1955] K. A. Brueckner and C. A. Levinson, *Phys. Rev.* **97** (1955) 1344.

- [Bur] Burle Technologies Inc., *Channeltron Electron Multiplier handbook for mass spectrometry applications*.
- [Burb1957] E. M. Burbidge, G. R. Burbidge, W. A. Fowler *et al.*, *Rev. Mod. Phys.* **29** (1957) 547.
- [Burk1975] J. M. Burke, D. G. and Balogh, *Can. J. Phys.* **53** (1975) 948.
- [Bush1974] D. L. Bushnell, D. J. Buss, and R. K. Smither, *Phys. Rev. C* **10** (1974) 2483.
- [Caki2009] R. Cakirli, R. Casten, R. Winkler *et al.*, *Phys. Rev. Lett.* **102** (2009) 82501.
- [Cast2000] R. Casten, *Nuclear structure from a simple perspective*, Oxford University Press, USA (2000).
- [Cham2009] N. Chamel, S. Goriely, and J. M. Pearson, *Phys. Rev. C* **80** (2009) 065804.
- [Chau2007] A. Chaudhuri, M. Block, S. Eliseev *et al.*, *Eur. Phys. J. D* **45** (2007) 47.
- [Comi1974] M. B. Comisarow and A. G. Marshall, *Chem. Phys. Lett.* **25** (1974) 282.
- [Comi1978] M. B. Comisarow, *J. Chem. Phys.* **69** (1978) 4097.
- [Cowa2004] J. J. Cowan and F. K. Thielemann, *Phys. Today* **57** (2004) 47.
- [Cozz2004] C. Cozzini, G. Angloher, C. Bucci *et al.*, *Phys. Rev. C* **70** (2004) 64606.
- [Dahl2000] D. A. Dahl, *Int. J. Mass Spectrom.* **200** (2000) 3.
- [Dech1980] J. Decharge and D. Gogny, *Phys. Rev. C* **21** (1980) 1568.
- [Dehm1990] H. Dehmelt, *Rev. Mod. Phys.* **62** (1990) 525.
- [Deu2009] Deutsches Kupferinstitut e.V., *Werkstoff-Datenblatt Cu-OFE* (2009).
- [Dick1992] W. H. Dickhoff and H. Muther, *Rep. Prog. Phys.* **55** (1992) 1947.
- [Doba1994] J. Dobaczewski, I. Hamamoto, W. Nazarewicz *et al.*, *Phys. Rev. Lett.* **72** (1994) 981.
- [Duff1995] J. Dufflo and A. P. Zuker, *Phys. Rev. C* **52** (1995) 23.
- [Dunb1984] R. C. Dunbar, *Int. J. Mass. Spectrom. Ion Proc.* **56** (1984) 1.
- [D'Ur2005] B. D'Urso, R. v. Handel, B. Odom *et al.*, *Phys. Rev. Lett.* **94** (2005) 113002.
- [Dwor2006] M. Dworschak, diploma thesis, Bayerische Julius-Maximilians-Universität Würzburg (2006).
- [Dwor2008] M. Dworschak, G. Audi, K. Blaum *et al.*, *Phys. Rev. Lett.* **100** (2008) 72501.
- [Dwor2009] M. Dworschak, Ph.D. thesis, Johannes Gutenberg-Universität Mainz (2009).
- [Dwor2010] M. Dworschak, M. Block, D. Ackermann *et al.*, *Phys. Rev. C* **81** (2010) 064312.
- [Dyck1985] G. R. Dyck, R. J. Ellis, K. S. Sharma *et al.*, *Phys. Lett. B* **157** (1985) 139.
- [Dyck2004] R. S. v. Dyck Jr, S. L. Zafonte, S. v. Liew *et al.*, *Phys. Rev. Lett.* **92** (2004) 220802.

- [Eber2000] K. Eberhardt and A. Kronenberg, *Kerntechnik* **65** (2000) 269.
- [Egid1985] T. von Egidy, H. Börner, and F. Hoyler, *Z. Phys. A* **322** (1985) 669.
- [Eiba2009] M. Eibach, diploma thesis, Johannes Gutenberg-Universität Mainz (2009).
- [Eiba2010] M. Eibach, T. Beyer, K. Blaum *et al.*, *Nucl. Instrum. Meth. A* **613** (2010) 226.
- [Eiba2012] M. Eibach, Ph.D. thesis, Ruprecht-Karls-Universität Heidelberg (2012), in preparation.
- [Eite2007] G. Eitel, diploma thesis, Johannes Gutenberg-Universität Mainz (2007).
- [Eite2009] G. Eitel, M. Block, A. Czasch *et al.*, *Nucl. Instrum. Meth. A* **606** (2009) 475.
- [Elis2007] S. Eliseev, M. Block, A. Chaudhuri *et al.*, *Int. J. Mass Spectrom.* **262** (2007) 45.
- [Elis2010] S. Eliseev *et al.*, *Phys. Rev. Lett.* (2010) submitted.
- [Elom2008] V. V. Elomaa, T. Eronen, U. Hager *et al.*, *Nucl. Instrum. Meth. B* (2008).
- [Elom2009] V. V. Elomaa, T. Eronen, J. Hakala *et al.*, *Nucl. Instrum. Meth. A* **612** (2009) 97 .
- [Engl1993] T. R. England and B. F. Rider, technical report LA-UR-94-3106, ENDF-349, Los Alamos National Laboratory (1993).
- [Ferr2007a] R. Ferrer, Ph.D. thesis, Johannes Gutenberg-Universität Mainz (2007).
- [Ferr2007b] R. Ferrer, K. Blaum, M. Block *et al.*, *Eur. Phys. J. Spec. Top.* **150** (2007) 347.
- [Fire2007] R. B. Firestone, S. F. Mughabghab, and G. L. Molnár, *Database of prompt gamma rays from slow neutron capture for elemental analysis*, chapter 5, International Atomic Energy Agency (2007), pages 45–64.
- [Fröh2006] C. Fröhlich, G. Martínez-Pinedo, M. Liebendörfer *et al.*, *Phys. Rev. Lett.* **96** (2006) 142502.
- [Gabr1983] G. Gabrielse, *Phys. Rev. A* **27** (1983) 2277.
- [Gabr2009] G. Gabrielse, *Int. J. Mass Spectrom.* **279** (2009) 107.
- [Garv1966] G. T. Garvey and I. Kelson, *Phys. Rev. Lett.* **16** (1966) 197.
- [Garv1969a] G. T. Garvey, *Ann. Rev. Nucl. Sci.* **19** (1969) 433.
- [Garv1969b] G. T. Garvey, W. J. Gerace, R. L. Jaffe *et al.*, *Rev. Mod. Phys.* **41** (1969) S1.
- [Gasp1993] C. Gaspar and M. Donszelmann, *Proc. IEEE* (1993).
- [Gell1990] R. Geller, *Ann. Rev. Nucl. Part. Sci.* **40** (1990) 15.
- [Geor2007a] S. George, S. Baruah, B. Blank *et al.*, *Phys. Rev. Lett.* **98** (2007) 162501.
- [Geor2007b] S. George, K. Blaum, F. Herfurth *et al.*, *Int. J. Mass Spectrom.* **264** (2007) 110.
- [Goep1950] M. Goeppert-Mayer, *Phys. Rev.* **78** (1950) 16.

- [Gori2000] S. Goriely, AIP Conf. Proc. **529** (2000) 287.
- [Gori2007] S. Goriely, M. Samyn, and J. M. Pearson, Phys. Rev. C **75** (2007) 064312.
- [Gori2009a] S. Goriely, N. Chamel, and J. M. Pearson, Phys. Rev. Lett. **102** (2009) 152503.
- [Gori2009b] S. Goriely, S. Hilaire, M. Girod *et al.*, Phys. Rev. Lett. **102** (2009) 242501.
- [Gräf1980] G. Gräff, H. Kalinowsky, and J. Traut, Z. Phys. A **297** (1980) 35.
- [Gros1991] P. B. Grosshans, P. J. Shields, and A. G. Marshall, J. Chem. Phys. **94** (1991) 5341.
- [Guan1995] S. Guan and A. G. Marshall, Int. J. Mass. Spectrom. Ion Proc. **146** (1995) 261.
- [Gust1967] C. Gustafson, I. L. Lamm, B. Nilsson *et al.*, Ark. Fys. **36** (1967) 613.
- [Häff2003] H. Häffner, T. Beier, S. Djekić *et al.*, Eur. Phys. J. D **22** (2003) 163.
- [Hage2006] U. Hager, T. Eronen, J. Hakala *et al.*, Phys. Rev. Lett. **96** (2006) 42504.
- [Hagu1986] A. M. I. Hague, R. F. Casten, I. Förster *et al.*, Nucl. Phys. A **455** (1986) 231.
- [Halv1979] J. E. Halverson and W. H. Johnson Jr, Phys. Rev. C **20** (1979) 345.
- [Hamp2006] G. Hampel, K. Eberhardt, and N. Trautmann, ATW **51** (2006).
- [Haxe1950] O. Haxel, J. H. D. Jensen, and H. E. Suess, Z. Phys. A **128** (1950) 295.
- [Herf2001a] F. Herfurth, J. Dilling, A. Kellerbauer *et al.*, Nucl. Instrum. Meth. A **469** (2001) 254.
- [Herf2001b] F. Herfurth, J. Dilling, A. Kellerbauer *et al.*, Phys. Rev. Lett. **87** (2001) 142501.
- [Hofm2000] S. Hofmann and G. Münzenberg, Rev. Mod. Phys. **72** (2000) 733.
- [Ili2007] C. Iliadis, *Nuclear Physics of Stars*, Wiley-VCH (2007).
- [Isac1995] P. v. Isacker, D. D. Warner, and D. S. Brenner, Phys. Rev. Lett. **74** (1995) 4607.
- [Isla1982] M. Islam, T. J. Kennett, and W. V. Prestwich, Phys. Rev. C **25** (1982) 3184.
- [Jagu2002] O. Jagutzki, J. S. Lapington, L. B. C. Worth *et al.*, Nucl. Instrum. Meth. A **477** (2002) 256.
- [Jane1988] J. Janecke and P. Masson, At. Data Nucl. Data Tab. **39** (1988) 265.
- [John1928] J. B. Johnson, Phys. Rev. **32** (1928) 97.
- [Joki2006] A. Jokinen, T. Eronen, U. Hager *et al.*, Int. J. Mass Spectrom. **251** (2006) 204.
- [Kais1975] D. C. Kaiser and W. H. Johnson, Phys. Rev. C **12** (1975) 1054.
- [Kauf1976] S. L. Kaufman, Opt. Comm. **17** (1976) 309.
- [Kell2003] A. Kellerbauer, K. Blaum, G. Bollen *et al.*, Eur. Phys. J. D **22** (2003) 53.

- [Kete2006] J. Ketelaer, diploma thesis, Johannes Gutenberg-Universität Mainz (2006).
- [Kete2008] J. Ketelaer, J. Krämer, D. Beck *et al.*, Nucl. Instrum. Meth. A **594** (2008) 162.
- [Kete2009] J. Ketelaer, K. Blaum, M. Block *et al.*, Eur. Phys. J. A **42** (2009) 311.
- [Kete2010] J. Ketelaer, T. Beyer, K. Blaum *et al.*, Eur. Phys. J. D **58** (2010) 47.
- [Kett2009] J. Ketter, diploma thesis, Johannes Gutenberg-Universität Mainz (2009).
- [Kirc1981] R. Kirchner, K. H. Burkard, W. Huller *et al.*, Nucl. Instrum. Meth. **186** (1981) 295.
- [Kirc1990] R. Kirchner, Nucl. Instrum. Meth. A **292** (1990).
- [Klay1991] N. Klay, F. Käppeler, H. Beer *et al.*, Phys. Rev. C **44** (1991) 2801.
- [Klug2003] H. J. Kluge and W. Nörtershäuser, Spectrochim. Act. B **58** (2003) 1031.
- [Knut2009] K. Knuth, diploma thesis, Johannes Gutenberg-Universität Mainz (2009).
- [Kolh2008] V. S. Kolhinen, M. Bussmann, D. Habs *et al.*, Nucl. Instrum. Meth. B **266** (2008) 4547.
- [Köni1995] M. König, G. Bollen, H. J. Kluge *et al.*, Int. J. Mass. Spectrom. Ion Proc. **142** (1995) 95.
- [Kour2000] H. Koura, M. Uno, T. Tachibana *et al.*, Nucl. Phys. A **674** (2000) 47.
- [Krac2007] H. Kracke, diploma thesis, Johannes Gutenberg-Universität Mainz (2007).
- [Kret1991] M. Kretzschmar, Eur. J. Phys. **12** (1991) 240.
- [Kret2007] M. Kretzschmar, Int. J. Mass Spectrom. **264** (2007) 122.
- [Kret2008] M. Kretzschmar, Eur. Phys. J. D **48** (2008) 313.
- [Kret2009] M. Kretzschmar, private communication (2009).
- [Lang1925] I. Langmuir and K. H. Kingdon, Proc. Royal Soc. London A (1925) 61.
- [Lark1977] F. P. Larkins, At. Data Nucl. Data Tab. **20** (1977) 311 .
- [Li2006] Z. H. Li, U. Lombardo, H. J. Schulze *et al.*, Phys. Rev. C **74** (2006) 47304.
- [Lieb2008] D. Liebe, K. Eberhardt, W. Hartmann *et al.*, Nucl. Instrum. Meth. A **590** (2008) 145.
- [Lieh1992] M. Liehr, R. Trassl, M. Schlapp *et al.*, Rev. Sci. Instrum. **63** (1992) 2541.
- [Lifs2000] C. Lifshitz, Int. J. Mass Spectrom. **200** (2000) 423 .
- [Lind1991] M. Lindinger, S. Becker, G. Bollen *et al.*, Z. Phys. D **20** (1991) 441.
- [Lunn2003] D. Lunney, J. M. Pearson, and C. Thibault, Rev. Mod. Phys. **75** (2003) 1021.
- [Lunn2009] D. Lunney, C. Bachelet, C. Guénaut *et al.*, Nucl. Instrum. Meth. A **598** (2009) 379.

- [Maca1959] W. W. Macalpine and R. O. Schildknecht, Proc. IRE **47** (1959) 2099.
- [MacF1969] R. D. MacFarlane, R. A. Gough, N. S. Oakey *et al.*, Nucl. Instrum. Meth. **73** (1969) 285.
- [Mach2001] R. Machleidt and I. Slaus, J. Phys. G **27** (2001) R69.
- [MAG2006] MAGNEX Scientific Ltd., *Technical specifications for a 7.0 Tesla / 160 mm actively shielded room temperature bore magnet system for ion trap application* (2006).
- [Majo2004] F. G. Major, V. N. Gheorghe, and G. Werth, *Charged particle traps: physics and techniques of charged particle field confinement*, Springer (2004).
- [Mari2008] M. Marie-Jeanne, J. Alonso, K. Blaum *et al.*, Nucl. Instrum. Meth. A **587** (2008) 464.
- [Mars1998] A. G. Marshall, C. L. Hendrickson, and G. S. Jackson, Mass Spectrom. Rev. **17** (1998) 1.
- [Mend2008] J. Mendoza-Temis, I. Morales, J. Barea *et al.*, Nucl. Phys. A **812** (2008) 28.
- [Möll1981] P. Möller and J. R. Nix, Nucl. Phys. A **361** (1981) 117.
- [Möll1988] P. Möller and J. R. Nix, At. Data Nucl. Data Tab. **39** (1988) 213 .
- [Möll1994] P. Möller and J. R. Nix, J. Phys. G **20** (1994) 1681.
- [Möll1995] P. Möller, J. R. Nix, W. D. Myers *et al.*, At. Data Nucl. Data Tab. **59** (1995) 185.
- [Mukh2008] M. Mukherjee, D. Beck, K. Blaum *et al.*, Eur. Phys. J. A **35** (2008) 1.
- [Myer1966] W. D. Myers and W. J. Swiatecki, Nucl. Phys. **81** (1966) 1 .
- [Myer1969] W. D. Myers and S. W. J., Ann. Phys. **55** (1969) 395.
- [Myer1996] W. D. Myers and W. J. Swiatecki, Nucl. Phys. A **601** (1996) 141.
- [Navr2000] P. Navrátil, J. P. Vary, and B. R. Barrett, Phys. Rev. Lett. **84** (2000) 5728.
- [Naya1999] R. C. Nayak, Phys. Rev. C **60** (1999) 64305.
- [Neid2006] D. Neidherr, diploma thesis, Johannes Gutenberg-Universität Mainz (2006).
- [Neid2008] D. Neidherr, K. Blaum, M. Block *et al.*, Nucl. Instrum. Meth. B **266** (2008) 4556.
- [Neug1981] R. Neugart, Nucl. Instr. Meth. **186** (1981) 165 .
- [Niem2001] A. Nieminen, J. Huikari, A. Jokinen *et al.*, Nucl. Instrum. Meth. A **469** (2001) 244.
- [Niko1985] E. N. Nikolaev and M. V. Gorshkov, Int. J. Mass Spectrom. Ion Proc. **64** (1985) 115.
- [Nyqu1928] H. Nyquist, Phys. Rev. **32** (1928) 110.
- [Odom2004] B. C. Odom, Ph.D. thesis, Harvard University Cambridge (2004).
- [Ohsh2006] S. Ohshima, A. Fujisawa, A. Shimizu *et al.*, Rev. Sci. Instrum. **77** (2006) 03B704.

- [Okte2006] Y. Oktem, R. Cakirli, R. Casten *et al.*, Phys. Rev. C **74** (2006) 27304.
- [Olse1979] J. Olsen, J. Phys. E **12** (1979) 1106.
- [Otte1989] E. W. Otten, Treatise on Heavy-Ion Science **8** (1989) 519.
- [Ozaw2000] A. Ozawa, T. Kobayashi, T. Suzuki *et al.*, Phys. Rev. Lett. **84** (2000) 5493.
- [Pano2005] I. V. Panov, E. Kolbe, B. Pfeiffer *et al.*, Nucl. Phys. A **747** (2005) 633 .
- [Paul1990] W. Paul, Rev. Mod. Phys. **62** (1990) 531.
- [Penn1936] F. M. Penning, Physica **3** (1936) 873.
- [Pfei2001] B. Pfeiffer, K. L. Kratz, F. K. Thielemann *et al.*, Nucl. Phys. A **693** (2001) 282.
- [Pier1954] J. R. Pierce, *Theory and design of electron beams*, D. Van Nostrand Company (1954).
- [Pine2007] D. B. Pinegar, S. L. Zafonte, and R. S. v. Dyck, Hyperfine Interact. **174** (2007) 47.
- [Pyle2002] M. C. Pyle, A. García, E. Tatar *et al.*, Phys. Rev. Lett. **88** (2002) 122501.
- [Raha2006] S. Rahaman, M. Block, D. Ackermann *et al.*, Int. J. Mass Spectrom. **251** (2006) 146.
- [Raha2007] S. Rahaman, J. Hakala, V. V. Elomaa *et al.*, Eur. Phys. J. A **34** (2007) 5.
- [Rain2004] S. Rainville, J. K. Thompson, and D. E. Pritchard, Science **303** (2004) 334.
- [Raut2007a] C. Rauth, Ph.D. thesis, Ruprecht-Karls-Universität Heidelberg (2007).
- [Raut2007b] C. Rauth, D. Ackermann, G. Audi *et al.*, The European Physical Journal-Special Topics **150** (2007) 329.
- [Rein1989] P. G. Reinhard, Rep. Prog. Phys. **52** (1989) 439.
- [Remp1986] D. L. Rempel, S. K. Huang, and M. L. Gross, Int. J. Mass. Spectrom. Ion Proc. **70** (1986) 163.
- [Reni2010] D. Renisch, diploma thesis, Johannes Gutenberg-Universität Mainz (2010), in preparation.
- [Repp2008] J. Repp, diploma thesis, Johannes Gutenberg-Universität Mainz (2008).
- [Reus1983] U. Reus and W. Westmeier, At. Data Nucl. Data Tab. **29** (1983) 193.
- [Rich1989] R. Richter, I. Förster, A. Gelberg *et al.*, Nucl. Phys. A **499** (1989) 221.
- [Ring2007] R. Ringle, G. Bollen, P. Schury *et al.*, Int. J. Mass Spectrom. **262** (2007) 33.
- [Ring2009] R. Ringle, G. Bollen, A. Prinke *et al.*, Nucl. Instrum. Meth. A **604** (2009) 536 .
- [Rodr2003] D. Rodríguez, Ph.D. thesis, Universidad de València (2003).
- [Rodr2010] D. Rodríguez, K. Blaum, and W. Nörtershäuser, Eur. Phys. J. Spec. Top. (2010) submitted.
- [Roen2009] RoentDek Handels GmbH, *MCP Delay Line Detector Manual, version 9.17.205.2* (2009).

- [Rolf1988] C. E. Rolfs and W. S. Rodney, *Cauldrons in the Cosmos*, The University of Chicago Press (1988).
- [Rosm1998] K. J. R. Rosman and P. D. P. Taylor, *Pure Appl. Chem.* **70** (1998) 217.
- [Sara2000] F. Sarazin, H. Savajols, W. Mittig *et al.*, *Phys. Rev. Lett.* **84** (2000) 5062.
- [Sava1991] G. Savard, S. Becker, G. Bollen *et al.*, *Phys. Lett. A* **158** (1991) 247.
- [Scha2006] H. Schatz and K. Blaum, *Europhysicsnews* **37** (2006) 16.
- [Scha2007] B. Schabinger, J. Alonso, K. Blaum *et al.*, *J. Phys.* **58** (2007) 121.
- [Schm1986] H. H. Schmidt, W. Stoffl, T. Egidy *et al.*, *J. Phys. G* **12** (1986) 411.
- [Schw1989] L. Schweikhard, M. Blundschling, R. Jertz *et al.*, *Rev. Sci. Instrum.* **60** (1989) 2631.
- [Schw1991] L. Schweikhard, *Int. J. Mass. Spectrom. Ion Proc.* **107** (1991) 281.
- [Schw2003] S. Schwarz, G. Bollen, D. Lawton *et al.*, *Nucl. Instrum. Meth. B* **204** (2003) 507.
- [Schw2006] L. Schweikhard, M. Breitenfeldt, A. Herlert *et al.*, *AIP Conf. Proc.* **862** (2006) 264.
- [Schw2010] F. Schwellnus, K. Blaum, R. Catherall *et al.*, *Review of Scientific Instruments* **81** (2010) 02A515.
- [Shar1977] K. S. Sharma, J. O. Meredith, R. C. Barber *et al.*, *Can. J. Phys.* **55** (1977) 1360.
- [Shi2005] W. Shi, M. Redshaw, and E. G. Myers, *Phys. Rev. A* **72** (2005) 22510.
- [Shoc1938] W. Shockley, *J. Appl. Phys.* **9** (1938) 635.
- [Sick2003] G. Sickler, Ph.D. thesis, Ruprecht-Karls-Universität Heidelberg (2003).
- [Smit2008] M. Smith, M. Brodeur, T. Brunner *et al.*, *Phys. Rev. Lett.* **101** (2008) 202501.
- [Smor2008] C. Smorra, diploma thesis, Johannes Gutenberg-Universität Mainz (2008).
- [Smor2009] C. Smorra, K. Blaum, K. Eberhardt *et al.*, *J. Phys. B* **42** (2009) 154028.
- [Smor2010] C. Smorra, T. Beyer, K. Blaum *et al.*, *AIP Conf. Proc.* **1224** (2010) 544.
- [Smor2011] C. Smorra, Ph.D. thesis, Ruprecht-Karls-Universität Heidelberg (2011), in preparation.
- [Sout1977] F. C. G. Southon, J. O. Meredith, R. C. Barber *et al.*, *Can. J. Phys.* **55** (1977) 383.
- [Span1988] L. Spanier and S. A. E. Johansson, *At. Data Nucl. Data Tab.* **39** (1988) 259 .
- [Spie2005] H. Spieler, *Semiconductor detector systems*, Oxford University Press (2005).
- [Spit1993] A. M. Spits, P. H. M. Van Assche, H. G. Borner *et al.*, *JYFL Annual Report* (1993) 95.
- [Stöc2000] H. Stöcker, *Taschenbuch der Physik*, Verlag Harri Deutsch (2000).
- [Stoi2000] M. V. Stoitsov, J. Dobaczewski, P. Ring *et al.*, *Phys. Rev. C* **61** (2000) 34311.

- [Stoi2007] M. Stoitsov, R. B. Cakirli, R. F. Casten *et al.*, Phys. Rev. Lett. **98** (2007) 132502.
- [Thib1975] C. Thibault, R. Klapisch, C. Rigaud *et al.*, Phys. Rev. C **12** (1975) 644.
- [Vaut1972] D. Vautherin and D. M. Brink, Phys. Rev. C **5** (1972) 626.
- [Vaut1973] D. Vautherin, Phys. Rev. C **7** (1973) 296.
- [Verd2003] J. Verdú, Ph.D. thesis, Johannes Gutenberg-Universität Mainz (2003).
- [Verd2006] J. Verdú, private communication (2006).
- [Viol1966] V. Viola and G. T. Seaborg, J. Inorg. Nucl. Chem. **28** (1966) 741 .
- [Waps2003a] A. H. Wapstra, G. Audi, and C. Thibault, Nucl. Phys. A **729** (2003) 129.
- [Waps2003b] A. H. Wapstra, G. Audi, and C. Thibault, Nucl. Phys. A **729** (2003) 337.
- [Webe2004] C. Weber, Ph.D. thesis, Ruprecht-Karls-Universität Heidelberg (2004).
- [Webe2008] C. Weber, V.-V. Elomaa, R. Ferrer *et al.*, Phys. Rev. C **78** (2008) 054310.
- [Weiz1935] C. F. v. Weizsäcker, Z. Phys. A **96** (1935) 431.
- [Werf1973] S. Y. Van der Werf, Z. Phys. A **259** (1973) 45.
- [Wert2006] G. Werth, J. Alonso, T. Beier *et al.*, Int. J. Mass Spectrom. **251** (2006) 152.
- [Wiza1979] J. L. Wiza, Nucl. Instrum. Meth. **162** (1979) 587.
- [Yazi2006a] C. Yazidjian, Ph.D. thesis, Université de Caen / Basse-Normandie (2006).
- [Yazi2006b] C. Yazidjian, K. Blaum, R. Ferrer *et al.*, Hyperfine Interact. **173** (2006) 181.

Acknowledgements

I would like to thank my supervisor, Prof. Dr. Klaus Blaum, first of all, for giving me the opportunity to join his research group and to take part in the TRIGA-TRAP project, one of the most exiting experiments in Penning trap mass spectrometry for the near future. He always supported me in every respect, not only concerning the research but also in gaining some reputation in the scientific community. Klaus, I am so grateful for all that.

I also want to thank my local supervisor, Dr. Szilard Nagy, for many fruitful discussions about physics and beyond, for his help which I could count on whenever needed. He joined the TRIGA-TRAP project from the very beginning and I cannot think of anyone else to commission and start up the experiment with, to fight against all the problems that go along with such a project.

Thanks are also due to the other members of the TRIGA-TRAP team, Thomas Beyer, Martin Eibach, and Christian Smorra. It was always a pleasure to work with you in the lab and see the fast progress in setting up a new facility. I am also grateful to my present or former colleagues Dr. Michael Block, Dr. Michael Dworschak, Dr. Klaus Eberhardt, Dr. Rafael Ferrer, Dr. Sebastian George, Dr. Christopher Geppert, Jochen Ketter, Holger Kracke, Jörg Krämer, Dr. Dennis Neidherr, Prof. Dr. Wilfried Nörtershäuser, Dennis Renisch, Julia Repp, Christian Roux, Birgit Schabinger, Sven Sturm, Stefan Ulmer, Anke Wagner, and Dr. Christine Weber for many scientific discussions, shared lab-work, beam-time shifts, and nice social events besides physics.

For their support in the data analysis and the physics discussion of the mass measurements within this thesis, I want to thank Dr. R. Burcu Cakirli from the Max-Planck-Institute of Nuclear Physics in Heidelberg, as well as Prof. Dr. Georges Audi and Dr. Meng Wang from the Atomic Mass Data Centre in Orsay (France).

Prof. Dr. H.-Jürgen Kluge supported my application for the Wolfgang-Paul student award of the German Mass Spectrometry Society as well as for the Gutenberg-Akademie. I would like to thank him for his help.

I would also like to thank Prof. Dr. Reinhold Schuch and the SMILETRAP team, Matthias Hobein, Dr. Markus Suhonen, and Andreas Solders, for giving me the opportunity to join their experiment in Stockholm for three months.

Not to forget to thank the technical staff and the members of the workshops at the institutes of physics and nuclear chemistry of the University of Mainz for their help in all issues around the experiment. Especially I would like to mention Jörg Runke and Petra Thörle-Pospiech whom I could always count on when dealing with new targets for the laser ion source. Thanks are also due to Prof. Dr. Norbert Trautmann for his support and his advice.

Last but not least I want to thank my family for an incredible support in everyday life without which I could not have concentrated so much on my physics studies as well as the PhD work.

List of Publications

Penning trap mass measurements on nobelium isotopes

M. Dworschak, M. Block, D. Ackermann, G. Audi, K. Blaum, C. Droese, S. Eliseev, T. Fleckenstein, E. Haettner, F. Herfurth, F.P. Heßberger, S. Hofmann, J. Ketelaer, J. Ketter, H.-J. Kluge, G. Marx, M. Mazzocco, Yu.N. Novikov, W.R. Plaß, A. Popeko, S. Rahaman, D. Rodríguez, C. Scheidenberger, L. Schweikhard, P.G. Thirolf, G.K. Vorobyev, M. Wang, and C. Weber
Phys. Rev. C, in print (2010).

Accuracy studies with carbon clusters at the Penning trap mass spectrometer TRIGA-TRAP

J. Ketelaer, T. Beyer, K. Blaum, M. Block, K. Eberhardt, M. Eibach, F. Herfurth, C. Smorra, and S. Nagy
Eur. Phys. J. D 58, 47-52 (2010).

High-Precision Mass Measurements At TRIGA-TRAP

C. Smorra, T. Beyer, K. Blaum, M. Block, K. Eberhardt, M. Eibach, F. Herfurth, J. Ketelaer, K. Knuth, W. Nörtershäuser, and Sz. Nagy
AIP Conf. Proc. 1224, 544-551 (2010).

Penning trap mass measurements of transfermium elements with SHIPTRAP

M. Block, D. Ackermann, K. Blaum, C. Droese, M. Dworschak, M. Eibach, S. Eliseev, T. Fleckenstein, E. Haettner, F. Herfurth, F. P. Heberger, S. Hofmann, J. Ketelaer, J. Ketter, H.-J. Kluge, G. Marx, M. Mazzocco, Yu. N. Novikov, W. R. Plaß, A. Popeko, S. Rahaman, D. Rodríguez, C. Scheidenberger, L. Schweikhard, P. G. Thirolf, G. K. Vorobyev, and C. Weber
Hyp. Interact. 196, 225-231 (2010).

First direct mass measurements above uranium bridge the gap to the island of stability

M. Block, D. Ackermann, K. Blaum, C. Droese, M. Dworschak, S. Eliseev, T. Fleckenstein, E. Haettner, F.P. Heßberger, S. Hofmann, J. Ketelaer, J. Ketter, H.-J. Kluge, G. Marx, M. Mazzocco, Yu.N. Novikov, W.R. Plaß, A. Popeko, S. Rahaman, D. Rodríguez, C. Scheidenberger, L. Schweikhard, P.G. Thirolf, G.K. Vorobyev, and C. Weber
Nature 463, 785-788 (2010).

Transport of fission products with a helium gas-jet at TRIGA-SPEC

M. Eibach, T. Beyer, K. Blaum, M. Block, K. Eberhardt, F. Herfurth, C. Geppert, J. Ketelaer, J. Ketter, J. Krämer, A. Krieger, K. Knuth, Sz. Nagy, W. Nörtershäuser, and C. Smorra
Nucl. Instr. Meth. A 613, 226-231 (2010).

Recent developments in ion detection techniques for Penning trap mass spectrometry at TRIGA-TRAP

J. Ketelaer, K. Blaum, M. Block, K. Eberhardt, M. Eibach, R. Ferrer, S. George, F. Herfurth, J. Ketter, Sz. Nagy, J. Repp, L. Schweikhard, C. Smorra, S. Sturm, and S. Ulmer
Eur. Phys. J. A 42, 311-317 (2009).

Position-sensitive ion detection in precision Penning trap mass spectrometry

G. Eitel, M. Block, A. Czasch, M. Dworschak, S. George, O. Jagutzki, J. Ketelaer, J. Ketter, Sz. Nagy, D. Rodríguez, C. Smorra, and K. Blaum
Nucl. Instr. Meth. A 606, 475-483 (2009).

A carbon cluster laser ion source for TRIGA-TRAP

C. Smorra, K. Blaum, K. Eberhardt, M. Eibach, J. Ketelaer, J. Ketter, K. Knuth, and Sz. Nagy
J. Phys. B 42, 154028 (2009).

TRIGA-SPEC: A setup for mass spectrometry and laser spectroscopy at the research reactor TRIGA Mainz

J. Ketelaer, J. Krmer, D. Beck, K. Blaum, M. Block, K. Eberhardt, G. Eitel, R. Ferrer, C. Geppert, S. George, F. Herfurth, J. Ketter, Sz. Nagy, D. Neidherr, R. Neugart, W. Nörtershäuser, J. Repp, C. Smorra, N. Trautmann, and C. Weber
Nucl. Instr. Meth. A 594, 162-177 (2008).

Measurement and simulation of the pressure ratio between the two traps of double Penning trap mass spectrometers

D. Neidherr, K. Blaum, M. Block, R. Ferrer, F. Herfurth, J. Ketelaer, Sz. Nagy, and C. Weber
Nucl. Instr. Meth. B 266, 4556-4559 (2008).

Development of a Fourier-Transform Ion-Cyclotron-Resonance detection for short-lived radionuclides at SHIP-TRAP

R. Ferrer, K. Blaum, M. Block, F. Herfurth, J. Ketelaer, Sz. Nagy, D. Neidherr, C. Weber, and the SHIP-TRAP Collaboration
Eur. Phys. J. ST 150, 347-348 (2007).

Curriculum Vitae

Personal Information

Name: Jens Ketelaer
Date of Birth: 10.01.1982
Place of Birth: Bingen am Rhein, Germany
Nationality: German
Marriage Status: unmarried
Address: Gaulsheimer Weg 7
55411 Bingen-Kempton

Education

07.06.2001 Abitur at the Stefan-George-Gymnasium Bingen am Rhein

01.10.2001 - 18.09.2006 Study of Physics at the Johannes Gutenberg-Universität Mainz
04.09.2003 Pre-Diploma in Physics
18.09.2006 Diploma in Physics passed with distinction

since 23.10.2006 Scientific Assistant in the group of Prof. Dr. Klaus Blaum
since 25.10.2006 Phd student at the Institute of Physics,
Johannes Gutenberg-Universität Mainz

04.03.2009 - 15.05.2009 Visiting research scientist at the
AlbaNova University Physics Centre in Stockholm (Sweden)

23.09.2010 Doctoral examination in Physics (summa cum laude)

Scholarships and Awards

01.04.2006 - 30.09.2006 Scholastic scholarship from the
Johannes Gutenberg-Universität Mainz

06.03.2007 Award 2006/2007 of the Verein Deutscher Ingenieure
- Rheingau Bezirksverein e.V.

13.03.2007 Wolfgang-Paul-Award for Student Research of the
German Society for Mass Spectrometry

21.04.2008 - 12.05.2010 Junior member of the Gutenberg-Academy

